Form-finding of Arch Structures

By

Asal Pournaghshband

A thesis submitted in partial fulfilment of the requirements for the

degree of

Doctor of Philosophy in Engineering

University of Warwick, School of Engineering

May 2016

Table of Contents

List of Figures

List of Tables

Acknowledgements

Special thanks should be given to my supervisor Dr Theodore L. Karavasilis for his support, guidance and encouragement. Dr Karavasilis supervised this work for the last six months and helped me writing and organising my thesis. A thank goes to my colleague Amin Najafi back in Iran for his assistance and long discussion on the analytical model. I would also like to thank Dr Fabio Freddi for his assistance in numerical part using *OpenSees* software. A thank should be given to Professor Roger Johnson in Civil Engineering department for taking his time and share his opinion with me. Many thanks to the staff of School of Engineering for their feedbacks and supports, I am extremely grateful.

Last, I thank my mother, Pari, my husband, Amir, and my friend Chrysoula Voulgari who helped me through this process by their understanding, patience, love and supports.

Declaration

The present thesis *Form-finding of arch structures* is submitted to the University of Warwick in support of my application for the degree of Doctor of Philosophy. It has been composed by myself and has not been submitted in any previous application for any degree. The work was carried out at the School of Engineering in the Civil Engineering department, and it was commenced under the main supervision of Professor Wanda J. Lewis. This work has been completed under the main supervision of Associate Professor of Structural Engineering Theodore L. Karavasilis and second supervision of Associate Professor of Structural Engineering Jonathan Pearson since October 2015.

Abstract

In this thesis, the optimal shape of two-pin arches of constant cross-section is found analytically using a novel form-finding technique. To find the purely compressed arches built of masonry and concrete material, the state of static equilibrium is applied. As the main finding, the momentless two-pin arch shape is derived for the arches with any span-to-height ratio subjected to its self-weight (*SW*) and uniformly distributed load (*UDL*). The contribution of using momentless arches is shown through comparing their maximum displacements to those of parabolic shape. The first failure of the cross-section of the momentless and parabolic arches was then compared for the same loading. This work is conducted practising the knowledge of arch response to loading as a function of the chosen form. In this regard, a comprehensive study of the behaviour of different arch shapes considering different ratios of uniformly distributed load to self-weight (*UDL:SW*) is also carried out. The ideal common arch shape is investigated for minimum combined axial and bending stresses using the commercial software *GSA*. The optimal range of span-to-height ratio of common two-pin arch shapes is also suggested. In general, the best arch performance is exhibited for the parabolic and catenary arch with span-to-height ratios between 2–4 when *UDL:SW*≥1 and *UDL:SW*<1 respectively. However, the circular arch demonstrates the least desirable performance with the optimum range of span-to-height ratio between 4–6. Moreover, approximate methods of two-pin arch analysis are evaluated, including the masonry design method and virtual work method suggested by Megson (2006). The effect of the assumptions made by these methods on the result of analysing two-pin arches is investigated through comparing their results to those obtained by the second theorem of Castigliano, including full structural action and the *GSA* results.

Symbols

A	Area of Arch Cross-section
a and b and c	Constants in arch Equations Found Using Boundary Conditions
A' and $Acat$	Catenary Arch Constant
a'	Flexibility Coefficient of the Arch
Ai	Load Case Indicator
b_a	Wide of Arch Cross-section
C	Indicate Concrete Material
C_i	Integral Constant
D	Denominator
d	Arch Thicknesses
d_a	Effective Depth of the Arch Cross-section
ds	Infinitesimal Piece of Arch length
E	Young's Modulus
{**f**}	Load or Force Vector
F	Shear Force
$f(x)$	Arch Function
f'_c	Concrete Compressive Strength
f_{cd}	Concrete Design Stress in Compression
F_x	Horizontal Force
F_y	Vertical Force
f_{yk}	Steel Strength
g	Radius of Gyration of the Arch Cross-section
G	Shear Modulus
h	Arch Height
H	Horizontal Reaction Force
I	Second Moment of Area
I_0	Second Moment of Area at the Arch Crown
k	Shear Reduction Factor
[**K**]	Stiffness Matrix of the Arch
L	Arch Span
l	Horizontal Distance between Arch Support and Arch Crown
m	Midpoint of the Arch
M	Bending Moment

M_d	Design Bending Moment
M_{rd}	Ultimate Bending Moment
n	Number
N	Numerator
P	Arbitrary Point along the Arch
q	Self-weight of Arch per unit Arc Length
q_k	Uniformly Distributed Load from Traffic Load
r	Span-to-height Ratio
R	Radius of Curvature of the arch Structure
s	Indicate Steel Material
S	Arch Length
S'	Length of the Parabolic Arch
t	Derivative of Arch Function
T	Thrust
u	Displacement
U	Strain Energy
V	Vertical Reaction Force
w	Deck Weight per unit Span
w_{cr}	Critical Value of the Intensity of Loading
W_e	External Virtual Work
W_i	Internal Virtual Work
Wi	Point Loads from *UDL +SW*
X	Location of Maximum Structural Response along Arch Span
x and y	Arch Coordinates
z	Lever Arm for Flexure
z'	Distance of the Surface from Neutral Axis
α	Arch Slope at any Point along the Arch
α_q	Adjustment Factor for Traffic Load
β	Angle
γ	Slope of Arch at the Support
γ_2	Numerical Factor Depends on the *L:h* Ratio
γ_c	Concrete Partial Factor of Safety
$\Delta_{,h,}$	Horizontal Displacement at Arch Support
δs	Elemental Length of the Arch
η and ζ	Horizontal Distance of Elemental arch length *ds* from Arch Support
θ	Angle

υ'	Rib shortening Coefficient in Gaylord Equation
σ	Maximum Combined Compressive Stresses
υ	Poisson's Ratio

Abbreviations

2D	Two-dimensional
3D	Three-dimensional
ADS	Advanced Design System
AMPL	A Mathematical Programming Language
DDA	Discontinuous Deformation Analysis
DEM	Discrete Element Method
FDM	Force Density Method
FE	Finite Element
GA	Genetic Algorithm
LM	Load Model
LP	Linear Programming
MEXE	Military Engineering Experimental Establishment
NCE	New Civil Engineer
NFDM	Natural Force Density Method
SW	Self-weight
Tcl	Tool Command Language
TNA	Thrust Network Analysis
TRRL	Transport and Road Research Laboratory
UDL	Uniformly Distributed Load
ULS	Ultimate Limit State
URS	Updated Reference Strategy

Chapter 1 : Introduction

The form of arch structures and its effects on structural action is explored in this thesis. This study concerns an analytical determination of an optimal form of arch structures that are momentless, and their application. The methodology will be developed for any span (*L*) to height (*h*) ratios (*L:h*) and three different ratios of uniformly distributed load (*UDL*) to self-weight (*SW*). Three categories of loading comprises *UDL:SW*>1, *UDL:SW*=1, and *UDL:SW*<1, in which each category gives one functional relationship for the arch shape. The work is preceded by a comprehensive study of the behaviour of known shapes of arches including catenary, parabolic and circular forms. Also, different methods of analysis were investigated. In this regard, approximate methods of analysis, such as the masonry design (Curtin et al. 2006) and virtual work or energy methods suggested by Megson (Megson 2006) are evaluated by comparing their results with those obtained by the finite element analysis using *GSA* software (http://www.oasys-software.com/products/engineering/GSA-suite.html), in addition to an accurate method of analysis that includes full structural action, i.e., strain energy due to bending, shear, thrust and coupling of bending and thrust (Timoshenko 1986).

1.1. Framework and Motivation

One of the oldest forms of structures in the engineering field is the arch structure. Masonry arches were first used by the ancient Romans and continue to today with different applications in many diverse fields. Transporting goods, vehicles and people from one place to another place has played a significant role in human history. At times, rivers, mountains and valleys were major barriers for transportation. This is one of the remarkable reasons why bridges and tunnels have been regularly used and developed. Since arches support a large amount of applied load in compression,

arch structures are widely used in constructing bridges and tunnels. Other than spanning rivers and mountains for a transportation system, arches were used to form the roofs of large buildings, which is considered at the heart of the evolution of the vault.

There are about 75,000 masonry arch bridges in the United Kingdom, most of which are around 100 years old and still in service (Ng 1999). As the transportation system ages, arch structures may not be fit to withstand the speed, dimensions, loads, and volume of modern traffic conditions. Because of the increase in traffic load and speeds, a reliable assessment of the structural response of arch structures is required. In this regard, the behaviour of known shapes of arches are analysed and compared with each other. This comparison confirms the best shape from the known shape of arches based on the applied load. Also, the optimal range of span-to-height ratio for each shape of the arch is proposed in this study. The criterion of choosing the best arch and optimal span-to-height ratio causes the structural action within the arch material to be minimised. Moreover, different methods of analysis are evaluated. As a result, the accuracy of the approximate methods of analysis is explored through comparing with the most accurate method, i.e., the Castigliano approach based on full structural action.

The structural determinacy of arches and type of arch supports plays a determining role in the analysis of arch structures. Only three-pin arches can be analysed simply using static. A complicated analysis is required for most arches including two-pin and fixed ones. The connection of arches at the abutment is of a fixed type and pin-ended. The first type was more common in traditional design, while the latter is becoming widespread because of the developing technology in building deliberate pins. The pin-ended arches can deflect more under loading than fixed-ended arches with the easier design process for pin-ended arches. Also, arches may be built with either a variable or constant cross-section. However, not only can designing arches

with a constant cross-sectional area ease the complexity of design, but also, the cost of the construction can be reduced. In traditional design, arches were widely constructed as a filled barrel arch using masonry material. This kind of arch with very large self-weight could be counted as a brace that would keep the arch from buckling. The arch can carry the applied load, while the arch rib and the loading are connected through columns. The reason for great stability and durability of most of the historical arches was the large self-weight using masonry material as filled barrel arches that serve to brace it. Therefore, the shape of the arch was not a problem in the ancient design of arches.

Finding a desirable form of arches has recently become a significant issue in designing this classical form of structure. The shape of the arch has a direct effect on the stress that an arch structure will experience under the loading. Also, the cost of construction and the beauty of arches are directly related to their shape. Apart from designing suitable arches of known shapes, finding the optimal arch shape leads to low maintenance cost and favours the construction of new arch structures, both structurally and aesthetically. Since arch forms transfer dead load as compression forces, the optimal shape of the arch is one that can carry the loading in pure compression along the arch axis. However, there is only one optimal arch shape for any specific loading configuration that may be considered a limiting condition. Also, because of the behaviour of arch structures in transferring the loads, arch shapes are well suited to materials with high compressive strength such as masonry and concrete.

The form of structures was determined from the outset in conventional design (Curtin et al. 2006; Millais 2005). Nevertheless, a more efficient structure can be shaped if the form of the structure is considered as a core of the design. The significance of the shape effect on the behaviour of the structure can be displayed when analysing the Gerrard Cross tunnel. This tunnel collapsed in 2005. Applying surcharge loading in a

different sequence was determined as the cause for this failure. Hence, the failure could have been prevented if the arch had been of a shape less sensitive to disproportionate loading.

In previous practice, arch forms and their three-dimensional (*3D*) equivalents, i.e., vaults (tunnels), were designed to follow either a parabolic, circular, or catenary shape. None of these shapes represent an optimal form for the real case of self-weight plus uniformly distributed load, or variable, imposed loading. Although it is not possible to optimise the form (shape) for every practical load case, this proposed research will demonstrate that much improved design recommendations and analysis methods can be produced. Consequently, the best form of pin-ended rib concrete arches with constant cross-section in which the arch carries the loading in pure compression is a focus of this study. Hence, the optimal shape of an arch is proposed, using a novel form-finding technique.

1.2. Research aims and objectives

A principal aim of this research is to use a form-finding method for arch structures to obtain a momentless shape of arches and to present the application of the optimal arch shape. It involves analytical calculations and computational modelling aimed at producing durable and sustainable design solutions. The grounding of this work is shaped through a comprehensive study of the effects of the structural form of arches on their structural behaviour. In this regard, the behaviour of the known shapes of arches are analysed and compared with each other. Also, different methods of analysis are evaluated. This assessment of the known shape of arches advances the knowledge of arch response to loading as a function of a chosen arch form. As a result, designers can make informed decisions concerning which forms and span-to-height ratios to use in arch design, in order to minimise the magnitude of structural

action effects. The aim can be accomplished by specific set of objectives, listed below.

- To explore the effect of arch form on structural actions and a complete assessment of arch behaviour.

- To compare the behaviour of the known shapes of arches including, parabolic, catenary, and circular arches with each other.

- To find the optimum range of span-to-height ratio of the known shapes of arches in which the stress from the combination of bending stress and axial one reaches its minimum.

- To evaluate approximate methods of analysis of arches by comparing them with the most accurate method of analysis, i.e., the Castigliano approach based on full structural action.

- To find momentless two-pin arches for any span-to-height ratio and any ratios of unifomly distributed load to self-weight.

- To illustrate the application of the momentless arch as the optimal arch shape.

The novelty of this research is composed of three aspects. Firstly, there is no comprehensive study of the effects of arch forms and span-to-height ratio on structural action. Secondly, the credibility of the approximate methods of analysis currently in use is evaluated, and their inaccuracies are highlighted. Finally, the form-finding of arch structures itself has not been practised mathematically for two-pin arches with a constant cross-section. This is because of the inherent complexity of mathematical representation for an optimal structure. The analytical solutions mainly offer high accuracy. Therefore, the optimal momentless shape of arches is

investigated analytically in this research. The advantage of momentless arch is also assessed numerically.

1.3. Structure of the thesis

This thesis consists of six chapters starting with an introduction chapter and ending with a conclusion chapter. Both the first and last chapters outline the main points covered in other chapters.

In Chapter 2, current knowledge from and literature on common shapes of arches, methods of arch analysis and optimal arch form is reviewed. The form-finding technique is reviewed in this chapter.

Chapter 3 presents a numerical assessment of the known shapes of arches, namely parabolic, circular, and catenary, using *GSA* finite element software. The studied arches are pin-ended concrete ones with a constant cross-section. The optimum range of span-to-height ratio for each arch is then investigated. Therefore, the best shape amongst the known shapes of arches and optimal *L:h* ratio are obtained when the combined stress is at a minimum.

Chapter 4 presents a comparison of different methods of analysis for arch structures. These methods are mainly linear elastic ones applied to pin-ended arches to calculate their reaction forces. The methods consist of an accurate analytical method (the Castigliano approach) and approximate methods such as numerical method applying *GSA* software, the virtual work method described by Megson, and masonry design method. Therefore, the validity of the approximate methods is explored.

Chapter 5 presents the analytical calculation of a momentless arch using equations of equilibrium. The optimal shape of the arch is then achieved for any *L:h* ratio and *UDL:SW* ratio. This will be followed by the application of the momentless

arch presented numerically through comparing its deflection and first failure load with the ones of the parabolic arch. Hence, the merit of the momentless arch is confirmed.

Finally, the main conclusions from the conducted study in this research project are reported in chapter 6.

This thesis also includes an Appendix section containing:

- Theoretical analysis of the two-pin circular arch using the Castigliano approach (Appendix A).

- Theoretical analysis of two-pin parabolic arch using the Castigliano approach (Appendix B).

- *MATLAB* scripts of programming the shape of the momentless arch (Appendix C).

Chapter 2 : Literature review

2.1. Introduction

The aim of this research project is to investigate the optimal shape of arch structures that are momentless, together with their application. This work is carried out via an analytical form-finding technique for arches with any span-to-height ratio (*L:h*) and any ratio of uniformly distributed load to self-weight (*UDL:SW*). Investigation of the optimal arch shape is grounded in a comprehensive study of the behaviour of different arch shapes. Hence, the effect of the form and span-to-height ratio of arches on their structural actions is studied in detail. The focus of this study is on two-pin arches with a constant cross-section which are built of masonry or concrete material and subjected to static loading. Furthermore, different methods of arch analysis involving approximate analytical and numerical methods and the accurate analytical method are explored.

This literature review presents a background on the recent knowledge of the performance of arch shapes under applied loading and eventually finding an optimal arch shape. Firstly, the arch history is reviewed in Section 2.2. In Section 2.3, ways of finding the optimal range of span-to-height ratio and the optimal arch amongst common arch shapes are reviewed, followed by multiple analysis methods of arch structures in Section 2.4. Then, the current understanding of finding the optimal arch shape is provided in parallel with a review of some form-finding and optimization methods in Section 2.5. Finally, the findings from the review that inform the author's research are presented in Section 2.6.

2.2. History of arches

The arch is a curved structure with a variety of applications mostly to support or strengthen a building by transmitting compressive forces. Historically, arches have been made of masonry, then concrete, and lately of steel. The Romans can be considered the forerunners in appreciating the benefits of the arch in Europe, possibly building the first in the world (Ambrose and Tripeny 2011). Rounded arches, also called circular arches, are commonly found in ancient buildings. The Roman building constructions relied upon circular arches to span large, open areas. One of the Roman Empire's most impressive works of engineering is the Aqueduct of Segovia (Figure 2.1). It was built in the first century AC in Spain and comprised 166 semi-circular brick-like stone arches (Ambrose and Tripeny 2011).

Figure 2.1. The Aqueduct of Segovia, Spain (http://whc.unesco.org/en/list/311)

Concerning arch bridges, one of the oldest stone arch bridges having a single span is found near Smyrna in Turkey, and dates back to the ninth century (Barker and Puckett 2007). Mediaeval arches built over rivers in Europe in chronological order are: the arch over the river Tagus in Toledo-Spain around 900, over the Main river in Wurzburg-Germany around 1140, the Danube in Regensburg-Germany around 1140, the Moldova in Prague-Czech Republic about 1160, the Thames in London

around 1180, the Rhone in Avignon-France about 1180, and the Elbe in Dresden-Germany around 1200 (Proske and Pieter 2009).

Proske and Pieter (2009) stated that the use of circular arches was remarkable during the 14th and 15th centuries in the shape of filled barrel stone arch. In the late 16th century, the arch building industry entered a new stage of development, when new spans exceeded those achieved by the Romans by a large margin. Building arches with large spans was practised using other arch forms, although circular arches were still being widely used. Arches with large spans were found to be feasible when constructed of steel. The development of the knowledge of steel arches began in England during the mid-18th century. The first steel bridge was built at Coalbrookdale Ironbridge in England in 1781. This bridge was made of a semi-circular cast-iron rib with constant rectangular cross-section (published in the State of Maryland website, 2015).

2.3. Study of the behaviour of arches

Researching into the impact of the *L:h* ratio of two-dimensional parabolic, circular and catenary arches on buckling loads, Austin and Ross (1976) produced a comprehensive numerical study. In their assessment, the arches were assumed to be slender with a constant cross-section, and axial and shear deformations were ignored. For this reason, the studied arches could buckle elastically. The authors illustrated that the critical horizontal reactions for the asymmetrical buckling modes were sensitive to changes in the *L:h* ratios. Their findings concerned both two-pin and fixed arches under vertical point load at the crown and *UDL* applied across the arch axis. They showed that, for *L:h* ratios between 2 and 5, parabolic arches could carry 10–48% higher buckling loads than circular forms, and 9–30% higher buckling loads than catenary arches. Hence, from their study it is concluded that parabolic arches are preferable to circular and catenary ones when buckling loads are

evaluated. Moreover, it was seen that the buckling load of the arches is affected by the *L:h* ratios and the arch shape.

Later, Harvey and Smith in 1987 defended semi-circular arches as sound and aesthetic forms, when they are subjected to surcharge due to ground fill exerting horizontal forces. This case is an exception to the general findings, including the results presented in this thesis that confirm a circular arch form to be less efficient than parabolic or catenary shapes. Since finding the origin and direction of the thrust line of arches required difficult calculations for actual loading conditions, a microcomputer programme was developed by Harvey and Smith. The program was based on the mechanism analysis method in which Rankine's concept of fill pressure was used to design a smooth vertical wall. As an elaborated example, they pointed to the test bridge at Bargower, which performed properly under different fill pressures. Further, their method, based on the thrust line analysis, is analogical to the masonry design method that produces inaccurate results, as discussed in Chapter 4 of this thesis. The authors concluded that an ideal arch shape did not exist, and that an optimal arch form may be found for each specific loading configuration.

Fairfield and Ponniah (1994) used a series of timber model tests to study the behaviour of backfilled arch bridges. In their experimental investigation most of the tests carried out involved a parametric study of circular arches, considering various fill depths. The research was done to find the impact of the surrounding fill and earth pressures on the buried arch bridges. The fill depth at the crown and the load location were considered as variables. To achieve this, multiple small timber circular arches were constructed in which, to resist a frictional force, a high collapse load was applied. They found the collapse load, at the *L:h* ratio of 2 (semi-circular form), to be 20– 45% of the collapse load at the *L:h* ratio of 4. Thus, the circular arch was more efficient at higher *L:h* ratio, as far as the collapse load's tolerance of circular

arches was concerned. Unfortunately, their assessment was limited to arches with *L:h* ratios of 2 and 4, respectively. In order to compare model tests in the study with full-scale bridge tests, Bridgemill and Bargower bridges tested by the University of Edinburgh were used. Therefore, the relationship between the model tests and full-scale bridges was obtained in terms of the collapsed loads, arch densities of the model, arch prototype and the linear dimension scale factor. The model tests demonstrated that by increasing the fill density, the collapse load increased too because of raising the dead weight and the support stiffness.

Investigating the span-to-height ratio of arches, Bensalem et al. (1998) tested circular arches with a constant cross-section and different span-to-height ratios subjected to various load conditions. To do so, three finite element analyses were applied which found the relationship of the collapse load and the modal characteristics of the arches such as; arches' resonant frequency and mode shapes. By disregarding the problem of buckling, steel circular arches with a range of span-to-height ratio between 2 and 8 were analysed under different load regimes. Firstly, natural frequency analysis was implemented to acquire the natural frequency and mode shape of each arch. Then, implicit dynamic analysis was carried out to study the behaviour of arches under transient impact loading. These two tests investigated the dynamic behaviour of arches that are not of relevance to this study. Lastly, a non-linear static analysis was conducted to estimate the load-carrying capacities and deflections of arches under vertical loads. It was also noted that, as long as the level of loading remains that much lower than the serviceability limit, the analysis can be expanded to arches built of other materials. Although the concept of collapse load is not in the scope of this research, it is interesting to compare the behaviour of circular arches with different *L:h* ratios. It was shown that the minimum collapse load occurred at the *L:h* ratio of 2 when the arches were subjected to a vertical uniformly distributed load. Also, the collapse load of a semi-circular arch

was about half of the collapse load when the *L:h* ratio of the arch was 3. This finding shows the sensitivity of the behaviour of the circular arch with a changing *L:h* ratio. The maximum collapse load was found for a *L:h* ratio between 4 and 5. Moreover, because of the low level of loading in their tests, which could not exceed the linearity state, they compared their results with those obtained from tests on masonry or concrete arches. The comparison demonstrated a fairly good correlation for the range of span-to-height ratio which has the highest collapse load. In spite of the remarkable findings for the optimal range of span-to-height ratio with the criterion of maximum collapse load, only the arches of circular shapes were analysed.

In order to find the actual limits for the *L:h* ratio of concrete arches in which the arch behaviour is assured, Salonga and Gauvreau (2010) studied the behaviour of fixed-ended rib concrete arch bridges under permanent loading. Although the behaviour of fixed-ended arches is not investigated in this research, studying the difference between shallow and deep fixed-ended arches is of particular interest. They studied the limit of the *L:h* ratio in the construction of shallow concrete arches which are sensitive to axial deformations. Hence, they proposed the limit of the *L:h* ratio in which the efficient arch behaviour was guaranteed. In this regard, the influence of the axial deflections and the bending moments on the shallowness of arches was studied. The limit of the shallowness was considered as a conversion between the behaviour of fixed arches and fixed beams in their study. Regarding the conversional behaviour, a force method was implemented to determine a dimensionless ratio which was dependent on axial and flexural rigidity and the arch's height. It was demonstrated that the shallowness ratio was related directly to the arch height and had an inverse relation to the radius of gyration of the system. The system consisted of a deck plus arch, ignoring the effect of the spandrel column. To simplify the analytical calculations of this indeterminate structure, they

assumed that the spandrel columns were connected to the arch and deck with pins. Also, it was assumed that the flexural rigidity at the crown of the arch is equal to the flexural rigidity of the arch projected on the horizontal axis. The lowest shallowness ratio to guarantee the effectiveness of the arch was found to be 20. This threshold showed that the fixed-ended arch carried most of the uniform loads in axial compression.

2.4. Study of the analysis methods of arches

The methods of structural analysis have been developing in recent years. Many researchers developed assessment tools based on plastic principles, including Heyman (1966 and 1969), Harvey and Smith (1987-1991), Blasi and Foraboschi (1994), and Gilbert (2007). Other researchers such as Pippard et al. (1936-1968), Crisfield (1984), Bridle and Hughes (1989), and Choo and Coutie (1991) analysed arches based on “elastic” principles. Many of these methods were based on Castigliano’s energy method (1876; 1879). As Harvey et al. (1990) stated the most recognized analysis methods were mainly classified as: *MEXE*, mechanism and finite element.

The *MEXE* method was an elastic analysis method, initially introduced by the Military Engineering Experimental Establishment, using a semi-empirical approach based on Castigliano’s theorem and the work carried out by Pippard et al. (1936, 1938, 1951). A formula was developed based on the arch dimensions to estimate the strength of a masonry arch. The arch is required to be parabolic with the *L:h* ratio of 4. The method does not fully capture the spandrel fill strength, or arch “thinning”. Moreover, its results were viewed as very conservative and the modification factors mainly affected the results from the method. However, the *MEXE* method is categorised as an easy-to-use analysis method in which the results can be obtained fast (Harvey et al. 1991). The mechanism method was

developed by Heyman (1966 and 1969) and was a straightforward approach for plastic analysis of arches (Harvey et al. 1991). The mechanism method identifies the location of four hinges with the associated loads applied to the arch. Hence, the mechanism related to the minimum load can be found using the equations of the equilibrium of forces through an iterative process. Heyman believed that an accurate failure load could be achieved in the mechanism method if the input parameters had sufficient accuracy. The method also presumed negligible tensile strength, infinite Young's modulus and infinite compressive strength and finally stiff abutments. The thrust line was the main means to estimate the maximum load in this method. The mechanism method later became the basis of the programme used in Archie software (Smith 1991). The location of the thrust line under the applied load was given using Archie. Hence, the mechanism could be determined when the thrust line touched the edge of the arch. The load-carrying capacity, internal forces, zone of thrust, and the worst location for the load to produce the fourth hinge were given using this software. The effect of the soil–structure interaction was also a programme feature. The programme was easy to use for finding collapse load, but all the variable loads and reactions needed to be determined proportionally (Ng 1999). Later, Harvey and Smith (1988) extended the Heyman method to estimate the minimum arch thickness under a given loading condition by introducing the 'thrust zone' instead of the term 'thrust line'. Nowadays, finite element (*FE*) methods dominate structural analysis and it is claimed that their use in the analysis of two-pin arches provides solutions in a shorter period of time than the classical methods. The finite method provides information regarding: a) cracks; b) the stress and deflections history of the arch at design or maximum loading condition; c) the spandrel filling effect; d) geometric non-linearity, unlike the mechanism and *MEXE* methods (Ng 1999). Since this review of different methods of arch analysis is mostly accompanied with a review of the arch behaviour, some arch assessment methods are summarised next.

One of the well-known researchers in the field of analysing masonry arch structures is Heyman. He (1969) studied the importance of the location of the thrust line within the arch on the arch stability. As noted, setting the thrust line entirely in the masonry arch rib under all loading conditions leads the purely compressive forces to transmit between each two adjacent cross-sections. Additionally, if the thrust line acts at the surface, the entire cross-section would have no stress. Otherwise, the cross-section of the masonry would experience a tensile force. However, there was a probability of hinging action that could lead to a failure when the cross-section involved the thrust line completely. Consequently, creating a pattern of hinges which were related to the failure mechanism resulted in understanding how the arch could develop instability. Hence, the focus of both the theory and experiments in his research was to collapse. In this regard, Heyman applied limit principles to the masonry arch. After reviewing collapses of some historical masonry arches, it turned out that the arch failure caused by the stresses of voussoir arches; however, the stresses in voussoir arches were low. The reason of such failure, while stresses in arch material are low, is the lack of an appropriate geometrical factor of safety for containing a thrust line properly within the arch depth. To demonstrate this notion, the pattern of hinges of semi-circular and incomplete circular arches was plotted and the required minimum thickness of the arch was determined. As a result, he defined a geometrical factor of safety as the ratio of the actual thickness of the arch to the minimum one for containing the thrust line. Although this factor had a major influence, it was not sufficient to confirm the stability of the arch in which pattern of hinges does not lead to a mechanism of collapse. Thus, the strength and the resistance of the arch to an imposed load were tested. This could be highlighted when a travelling point load was applied to the arch, which could alter the position of the thrust line. Heyman illustrated that, by assuming the shape of the arch to have an ideal thrust line instead of the existing shape of the arch, a simple analysis could be carried out on the influence of moving the point loads. The assumption of this

method was that the arch material had an infinite compressive strength. As a consequence, the geometrical factor of safety and the thickness of the arch became respectively infinity and zero. These properties were known as the plastic theory hypothesis. The purpose was to obtain a distance between the thrust line and centre-line caused by a travelling load. In this regard, the calculations of simple plastic theory were used with the consideration of the formation of hinges which turned the arch into a mechanism. The calculations resulted in equality of the work done under all loadings on a small motion of the mechanism to the work dissipated in the hinges. He then applied this theory to analyse the stone bridge of Lincoln Cathedral with a constant cross-section and Ponte Mosca, in Turin, with a variable cross-section.

Bridle and Hughes (1990) explored a tool for elastic assessment of the maximum strength of unreinforced arches. In this regard, they proposed a new computer programme based on Castigliano's second theorem to analyse the arches. They assumed that the strain energy has contribution from bending action and tangential forces. Ideally, the method would be capable of modifying load limits and identifying the status of collapse under different loading arrangements in a cost-effective way. This could facilitate the durability and maintenance of arches, especially with the modern material used in masonry. The programme could calculate the forces, bending moments, and deflections according to different load configurations. This computer numerical integration technique was also used to evaluate deflection integrals under each load increment in an iterative process. The technique addressed the non-linearity effect as well. Moreover, an incremental load was added to the live load at the end of each convergence and the iteration was re-run till the maximum load was found. The method had been tested for Bridgemill arch in Girvan. The findings demonstrate that earth forces could be modelled more realistically than in the mechanism method. Furthermore, the support's movement

could be considered in the calculations if the initial dead load conditions were known. The loading history of the masonry arch could be estimated with evaluation of the arch geometry and used in the analyses.

Smith et al. (1990) introduced an innovative way of arch analysis in the same year as Bridle and Hughes. They proposed a practical method, named the three-hinge method, for analysing masonry arches subject to working loads. As they cited, there are different reasons for the movement of the thrust line from the centre in masonry arches, such as shortening of the arch because of the great compression forces or the spread of abutment next to the springing. Therefore, masonry arches are likely to deform even under permanent actions. This indicated the possibility of the formation of three hinges across the arch whose locations are unknown. However, the location of the hinges was affected by the magnitude of the live load because of producing various lines of thrust. These locations were varied by affecting the traffic loads in real arch bridge cases with time. By increasing the magnitude of the load, a fourth hinge could be formed, which causes the structure to turn into a mechanism, and eventually the arch would collapse. It was stated that the three-hinge method and four-hinge mechanism method have the same solution for the ultimate load state. Nevertheless, the proposed three-hinge method concentrated on the definition and measurement of the serviceability limits in preference to ultimate limits. In the three-hinge analysis method, the vertical and horizontal thrust components were calculated using static equilibrium at any hinge. The applied loading in their calculations involved the fill weight, live loads, and pressure forces because of the arch movement. Thus, different lines of thrust could be drawn for the entire arch by determining the size and direction of the thrust line at any hinge. Consequently, there would be different acceptable static solutions, especially in the case of shallow arches. In this regard, the case which produced the minimum horizontal thrust by the springing was used in their computer program. The chosen

thrust line was also related to the minimum energy in the structure. As a practical example, the three-hinge method was applied to the Torksey Bridge in Lincolnshire. The results of the three-hinge method showed that the measured collapse load was in accordance with the one obtained by the full-scale tests by the *UK* Transport and Road Research Laboratory (*TRRL*). However, the three-hinge method illustrated the behaviour of the arch before its failure. They also simulated the collapses for Torksey Bridge due to local crushing by expanding the three-hinge method. Moreover, they showed that by decreasing the arch ring thickness, the load that causes a mechanism to be formed would be reduced. As another example, the Preston-upon-the-Weald Moors Bridge, containing hunching above the springing, was simulated using the three-hinge method programme numerical predictions were compared with the test results from *TRRL*. In this example, a significant horizontal movement was observed when the load was increased, which indicated the action of hunching as an abutment. This caused the height of springing to rise effectively. The fourth hinge could not be formed in this case and the structure would survive until a significantly large load causes a failure through crushing at the hinge. Again, there was a good correlation between the programme and *TRRL* results. An advantage of the three-hinge method is that it can calculate the position and magnitude of the thrust line on each abutment. It was shown that the ultimate capacity of the arch was greatly influenced by the abutment movements.

In spite of the existence of plenty of investigations on the methods of arch analysis including finding collapse loads, no study before 1994 was found presenting analytical methods to estimate the collapse mechanism and relevant loads. At that time, Blasi and Foraboschi (1994) offered an analytical collapse approach that assumed negligible tensile and shear strengths for a masonry arch based on a no-tension elastic constitutive model. The minimum principal strain was considered to be always positive in their research. Additionally, the strain tensor was the sum of

the elastic strain and the inelastic one; the inelastic strain was because of the cracking in the arch material by dilatations. They presumed a hinge to be elastic when the line of thrust was tangent to the boundary. This thrust line was significantly affected by the horizontal thrust at the skewback because of the thrusting function of the arch structure. Therefore, the lower and upper horizontal thrust limits of a semi-circular arch under its own weight, and an *UDL*, were calculated to prevent collapse. The lower and the upper thrust were considered as the minimum and maximum values of the thrust. They are obtained by calculating the rotational equilibrium equation of any point on the arch. The resultant equation of each thrust was the function of the angle of the collapsed hinge. It was also dependent on the span and thickness of the arch. There was a possibility of arch collapses when the line of thrust lay inside or tangential to the boundary. The former could occur when the applied load increased significantly and the latter when a hinge was formed at the tangential point. Subsequently, the collapse mechanisms and the intensity of the relevant horizontal limit thrusts at the arch's skewback were regenerated. The relation between the spandrel fill and the vertical dead load was shown in their analyses when the relevant horizontal action was much smaller than the weight. In so doing, they suggested some applicable analytical functions, such as the minimum magnitude of the thickness-to-span ratio, the safety margin, and the maximum value of uniformly distributed load. They indicated that both the collapse mechanism and the limit of the horizontal thrust were defined as a function of the loads and the geometry of the arch. Hence, it can be concluded from their study that the arch's geometry has a major impact on the horizontal thrust. To obtain the minimum permissible value of the thickness-to-span ratio of the arch, they set the lower thrust equal to the upper one. The safety margin of the masonry arch was calculated based on the difference from having the upper or lower thrust. Finally, to demonstrate the accuracy of this approach, they compared the results of their

analytical method with the results of *FE* analysis. Furthermore, they stated that the collapse approach was more reliable than *FE* for complex boundary conditions.

Later, Clemente et al. (2001) analysed arch numerically when in pure compression and designing the structure by having a series of cells which had a linear elastic behaviour in compression, joined with rigid voussoirs. They applied Castigliano's approach and established the equilibrium equations. They used an iterative process to find the cross-section of each cell. To study the arch structural behaviour, they applied a computational programme to an arch subjected to *UDL* up to the point of collapse when the contribution of the fill material to the arch lateral support was ignored. Thus, the arch was divided into *n* voussoirs with the same length and, therefore *n*+1 joining cells. It was assumed that the two cells near both supports behave in the same way as the other cells and that the depth of the arch was constant. Therefore, arch stiffness was constant along the arch. Then the bending stiffness of the i^{th} cell was written in terms of the modulus of elasticity, the length of the rigid voussoir and the thickness of the arch for the unit width of the arch. Thus, the equilibrium equation was defined in Lagrangian coordinates. This equation was only adaptable for linear elastic structures. It was shown that the cells would be cracked when the eccentricity went over 1/6 of the arch depth. The stiffness of cracked cells was relevant to the compressed part of the cross-section, i.e., the height of the effective cross-section. Furthermore, the effective depth of each cell was obtained by iteration. Subsequently, the solution was dependent on the weight of the backfill, the shape of the arch involving the thickness-to-span ratio of the arch and the arch height. As they concluded, the final solution from this numerical method was achieved in a short time and its results were related to the strength and modulus of elasticity of the material without using complicated computational procedures.

Hughes and Pitchard (1998) investigated the impact of dead loads and stresses due to serviceability loads on masonry arch bridges, based on both actual measurements and the numerical analysis using a cracking elastic model. The authors explained how load conditions and the masonry material have change with the time. Since the vehicle loads – especially on rail lines – were increased; the bridges could have been subjected to a heavier load. On the other hand, the material used in the masonry has been deteriorating. As a result, an assessment method for masonry arches needed to be developed. The initial stress state, deflection and cracking (joint opening) were regarded as the fundamental knowledge of a bridge's serviceability condition. Based on the numerical methods used by previous researchers prior to Hughes et al. the initial state of masonry arches was not a decisive factor in the estimation of critical load for arch failure. However, Hughes and Pitchard declared the possibility of the pre-existence of hinges at the abutments in the recent arch assessment theories, in which the initial state of the arch was regarded as an important input in the assessment. In this regard, an experimental test, named "flatjack", was carried out in their research. This test was initially designed to measure stress in rocks and then extended for masonry arches in Italy. The test equipment consisted of a frame and voltage displacement transducers. The flatjack test provided information about the arch's initial state. The authors showed the starting stress state on a real arch bridge for the first time. Hughes et al. modelled the arch one-dimensionally assuming no tension for a geometrically non-linear structure. Consequently, a numerical method considering the cracking elastic model with initial stress states was developed. The authors compared the experimental findings with numerical results. In conclusion, Hughes and Pitchard regarded the initial stress state as an essential parameter for masonry arch assessment. Moreover, the model was validated with the measurement values. They believed that complex non-linear arches could be properly assessed by the elastic cracking analysis method.

To find the proper material properties for three specific full-scale masonry arch bridges, Fanning and Boothby (2001) analysed the available test results of those in-service arch bridges. To do so, they applied the three-dimensional non-linear *FE* tool, *ANSYS V*5.5, to the three masonry arches. The authors referred to difficulties in assessing masonry arch bridge behaviour based on empirical formulation in the past. One of the reasons was the limitation of the information about the condition of masonry arch bridges. Secondly, there was no globally agreed method to assess the behaviour of bridges. The first issue was not considered to be a major challenge since the observable parameters such as stone quality and geometric profile were more important for assessment. The authors address the second issue by using a three-dimensional commercial non-linear *FE* analysis, while reviewing the existing assessment methods of masonry arch bridges. They replaced the masonry material with a solid element having the same stiffness in modelling the arch bridges. Also, significant bending moments were produced because of the distribution of fill pressure. Therefore, they included cracks and crushing in the modelling of the masonry arches as results of the bending moments that could change the structural response to loading. Later, they assessed a structure's behaviour under different load conditions, highlighting the response of the bridges to "truck loading" and the need to consider the three-dimensional effects. They compared the results of the deflection and displacement of the arch based on the distance of the front axle or truck position from the arch crown from their findings with the available results of three studied arches. The comparison showed a good agreement between the test results and the numerical method. Hence, Fanning et al. concluded that the three-dimensional *FE* was an appropriate analysis tool to assess masonry arch bridge behaviour with the consideration of fill material, cracking, and crushing of the material.

Ng and Fairfield (2004) modified the conventional mechanism method using the deflection-dependent pressure updating algorithm. They assessed Bargower stone arch bridge to show the validity of their modification. The reason for this modification was triggered by the significant change in the arch profile at the time of failure. Ng and Fairfield reviewed the previous research carried out to assess masonry arch bridges with the soil material interaction. The authors believed Heyman ignored the arch shape deformation and only considered the lateral soil pressure distributed on the extrados, whereas the arch profile at the time of the arch failure was different from its original shape. Ng and Fairfield modified the four-hinge method assuming infinite strength for the arch compression with no tensile stresses. The authors plotted the collapse loads of the Bargower arch bridge against its vertical deflection under different load lines. The effects of the backfill's weight, different ultimate passive deflection, the backfill's angle, live dispersal angle and different arch unit weights were also analysed. They used the results of centrifuge tests on the soil–arch system obtained from Hughes et al. (1998) and Burroughes et al. (2001), when analysing the effect of changes in the live load dispersal angle. The authors concluded that the collapse-load estimation was largely affected by arch deflections. Consequently, the weight, angle of shearing resistance, and the ultimate passive deflection of the backfill influenced the predicted collapse load.

For the assessment of the historical masonry arch structures, Gencturk and Kilic (2006) used the Discrete Element Method (*DEM*). They applied *DIANA* software which used a finite element non-linear solver to explore a first century stone arch named Titus Tunnel Bridge. This is a semi-circular arch with no filling material for binding the stones and it is located in Antakya city in southern Turkey. This bridge was built for pedestrians only. Using the *DEM*, voussoirs were divided into finite elements connected by contact surfaces which acted as non-linear finite elements. Since adjacent voussoirs were not joined robustly by a binding material, the

application of this method to masonry arch and vault analysis was justified. The results of *DIANA* software were compared with the analytical solutions. As a benchmark of analytical solutions, the snap-through truss method was used. This analytical approach gives two solutions to analyse the problem: one for shallow trusses (when $Sin\theta=\theta$, and θ is the internal angle of truss at the support with horizontal axis) only and the other for both shallow and deep trusses. The results from *DIANA* were compared with results from the snap-through truss work. From the information in plots of force-displacement for the different methods they concluded that, for problems including geometric non-linearity, *DIANA* could be suitable as long as large rotations were not included (shallow truss). Regarding the analytical investigation of masonry arch structures, they considered the geometrical factor of safety along with the thrust line. For the line of thrust, they applied Heyman's theory (1982) that assumed the stability of a pure compression structure under all possible loads when the line of thrust lies entirely within the masonry section. According to Heyman, to contain the entire thrust line within an arch ring, a minimum thickness should be determined for the arch cross-section. The minimum thickness was also required to find the exact collapse load. To calculate the collapse load, two different methods were implemented, the mechanism method for asymmetrical loading and the virtual work method for symmetrical loading. To check the precision of the arch depth, the thrust line was drawn by programming it into *MATLAB*, as well as the calculations of the collapse load. Their investigation indicated that the geometrical factor of safety for Titus Tunnel Bridge was 2.06, which confirmed the durability of the bridge. Also, because of its high self-weight and low live loads, the semi-circular geometry of this bridge could satisfy the loading conditions. Regarding the symmetry of Titus Tunnel Bridge, when a point load was applied at the crown, a five-hinge collapse mechanism was estimated. Finally, the graphs of the thrust line using the mechanism method and the thickness of the arch ring against the collapse load for crown loading for the bridge were presented.

Gilbert (2007) highlighted the limit analysis in verifying the arch safety that has been transferred from hand calculation into computer-based assessment. The two main methods for arch analysis i.e., elastic and plastic, were considered in his research. The elastic method was not regarded as a straightforward approach since there was no unique computable equilibrium state existing for masonry arches. On the other hand, there was only one ultimate state of arch considered whilst assessing the plastic method. As a result, there were considerably fewer parameters and initial stress input data required. The specific conditions of the arch plastic limit state were defined by the “equilibrium”, “mechanism” and “yield” defined. The conditions demonstrated the state of the arch when a load (multiplied by a load factor) was applied. Ideally, the “uniqueness theorem” required all three pre-defined conditions to be satisfied. The resultant factor is for the minimum collapse load factor. There was an emphasis on the thrust line, the number of releases for the mechanism and the geometrical factors for safety whilst estimating the maximum loading factor. Line of thrust and rigid block had been the recognised techniques for masonry arch stability analysis until then. The backfill method was branded as the latest computational procedure capable of modelling the masonry and soil components. Moreover, they stated that three-dimensional masonry arch analysis was a potential area for investment in the future because the technique was still expensive and difficult to adopt in computer-based analysis.

Most of the preceding investigations of the behaviour of arches were conducted on circular arches. However, the buckling of parabolic arches was studied in many cases. In this regard, Moon et al. in 2007 studied the elastic buckling of two-pin shallow parabolic arches under vertically distributed loads. Considering a probable symmetric mode, which was called the symmetric snap-through mode, for buckling of the shallow arches, the conventional buckling hypothesis could expect the buckling load to be much higher than the actual buckling of the arch. The reason for

this overestimation was because of the large value of the ratio of the pre-buckling deformation to the arch's height. Therefore, the buckling formula for the symmetric snap-through mode of a two-pin shallow parabolic arch was found from the non-linear principal equilibrium equation of it. To obtain the equation of shallow parabolic arches subjected to a vertically distributed load, the static mathematical method was used. Thus, the common non-linear equilibrium equation of the arch was reformulated to achieve the equation of an incremental form for the shallow parabolic arch. Also, to find the symmetric buckling load, the shape of the arch was assumed to deform symmetrically. Following the reformulation of the equilibrium equation, the load–displacement relationship was acquired. Additionally, the threshold of different symmetric and asymmetric in-plane buckling modes was obtained in terms of the slenderness ratio and the height-to-span ratio. To find the threshold of different buckling modes, the dimensionless height term (H) was defined as $4h/\pi^2 g$, in which h is the arch height and g is the radius of gyration of the arch cross-section. Thus, the stability, symmetric snap-through, and asymmetric buckling of the two-pin parabolic arch were determined for the range of dimensionless rise H. Hence, the arch is presumed to be stable for $H<\pi/4$, and the parabolic arch may have symmetric snap-through buckling for $\pi/4<H<1.85$, and finally asymmetric buckling may occur when $H>1.85$. To assess the accuracy of the suggested formula, numerical finite element examples were applied, although the interactive buckling was ignored. Hence, the findings from the buckling load via this novel formula and threshold were in accordance with the results of the numerical method.

Audenaerta et al. (2008) proposed a two-dimensional assessment approach to identify distribution of internal forces and displacements in single-span masonry bridges under different load conditions. They emphasised the challenges that bridges were facing with regard to their complex structure and loading pattern. The

authors were trying to develop an assessment algorithm to estimate the ultimate load capacity of the structure. Previous attempts to evaluate arch behaviour with different load conditions is summarised in their work. The researchers applied both two-dimensional and three-dimensional finite element models to investigate the structure's response to vehicle loadings. The transverse distribution of stresses across the arch barrel was not considered in the two-dimensional studies. Audenaerta et al. compared the two-dimensional assessment method with the three-dimensional one. The former was considered as a convenient and efficient tool for arch capacity assessment, whereas the latter was more suitable for detailed stress distribution and displacements quantification, with more complex arch information and resources. The abutment movement and stress distributions under different load conditions were also addressed in the approach. Additionally, the stiffness loss in masonry cracks was taken into account. This led to more stability in their numerical computations. Audenaerta et al.'s approach was called "elasto-plastic". There were horizontal, vertical and moments equilibrium equations within the analytical model. To limit the horizontal, vertical and abutment movement, a set of boundary conditions was also defined. Additionally, the material properties were included in the model to capture the initiation of cracks and hinges. Audenaerta et al. applied this analytical method to identify the critical point load on the arch, ultimate load factor, location of plastic hinges formation, stress distribution and abutment displacements levels. The method was validated through comparison with numerical results from an elastic/plastic and continuum finite element analysis methods. The authors believed that their proposed analytical method was a simpler version of two-dimensional plastic analysis and had a more complex finite element modelling procedure compared to the existing methods. In other words, the hinges formation, in addition to the cross-sectional normal stresses under an increasing load factor, was achievable with the proposed analytical model. The method was

used in computer software to investigate an arch's behaviour under both vertical and horizontal displacements.

Drosopoulos et al. (2008) identified the load factor for stone arch failure by using finite element work. The modelling methodology considered the contact interfaces, while coping with potential cracks. To realize arch non-linearity, the structure was modelled as a unilateral contact friction representing that no tension forces can be transmitted. Furthermore, they assumed the stone arch bridge material to have no tension strength in order to satisfy limit analysis criteria. To indicate crack formation, the discretized model of a bridge with a number of interfaces was simulated. The authors emphasised the application of iterative techniques for the numerical solution. The research also summarised the Heyman collapse mechanism theory and limit analysis carried out for discrete structures with a frictional contact boundary. Drosopoulos et al. demonstrated how the geometry parameters could impact on the mechanical behaviour of the arch. The authors assessed the mechanical behaviour of stone arch bridges against two main principles: the arch geometry impact on the load factor, and the impact of abutment movement on the structure's behaviour. The applicability of the unilateral contact model to execute limit analysis was also proved in the paper. In summary, Drosopoulos et al. modelled the structure as a unilateral contact-friction, then estimated the maximum load for arch failure, and finally depicted the optimal shape of the arch from the parametric analysis results, based on studies carried out on 19 different bridges. They also suggested that the approach was applicable for multi-span arches and even more complicated structures. The findings of the research were validated against Heyman's results (1982). Drosopoulos et al. concluded that lowering the height of the arch leads to the limitation of the arch load factor with a rise in the compressive arch failure, whilst deep structures failed according to the fourth-hinge

collapse mechanism theory. The authors recommended a study of backfill influence on an optimal arch shape as the way forward for future arch studies.

Pintucchi and Zani (2009) determined the impact of geometric non-linearity on the collapse mechanism of circular masonry arches. In their study, the material was assumed to have no tension strength and negligible compressive strength. Pintucchi and Zani evaluated the collapse load of arches under their self-weight and a uniformly distributed load or a vertical load applied at the structure crown. As they stated, the slenderness and the equivalent strength of the arch were two decisive factors in determining the collapse load. The former was the relation between the radius and thickness of the circular arch, and the latter was the relationship of the arch geometry to the compressive strength a weight of the arch. An algorithm was defined to estimate the critical load condition. The algorithm was developed into computational code. Pintucchi and Zani concluded that the resultant value of the collapse load was not dependent only on the slenderness and equivalent strength parameters but also on something called equivalent stiffness derived from modulud of elasticity (*E*). Thus, the authors applied the limit analysis method to circular arches to calculate the multiplier of the collapse load. Moreover, it was presented that a collapse load would be reduced because of the destabilizing effect of forces such as a decreasing *E* value, which is in accordance with increasing the size of the arch. Furthermore, the reduction of the collapse load would be greater if the slenderness of the arch was greater.

Toth et al. (2009) used the *DEM* to investigate the impact of the backfill on the mechanical behaviour of a multi-span masonry arch. The main applications of multi-span arches are found in railway and road bridges operating in Europe and around the world. The load conditions on these arches have been increasing and, as a result, there is a requirement to re-assess the load-bearing capacity of existing structures. They assumed a high compressive strength for masonry arch with no

tension strength. Both simple conservative (such as *MEXE*) and computerised (such as mechanism and *FEM*) methods were applied to investigate arch loading capacity. The conservative methods usually estimated a loading factor lower than the actual value, hence they were not a cost-effective solution. Additionally, Toth et al. believed that the conservative method was not suitable in the case of non-standard geometries. The computerized method such as the *FE* has been applied in two- and three-dimensional arch assessments. However, the computerized method was relatively expensive and complicated input data was required. The *DEM* was recognised to have advantages over previous methods since it modelled the arch through a “collection of separate blocks”. To achieve an appropriate method of masonry analysis, initially the geometry and mechanical properties of a one-span bridge model were defined based on experimental results. Then, Toth el al. developed a multi-span model from the one-span model using new material. In other words, they validated the parameters and mechanical behaviour of the Nishida one-span arch bridge using a discrete element *FE* method to generate the multi-span arch model. Then they compared the results of the multi-span structures with different backfill materials. The deflections, normal stresses, and plastic mode of backfill under different live load cases were estimated. Toth et al. concluded that the structure capacity was dependent on the stiffness, friction angle, and cohesion of the backfill.

Gibbons and Fanning (2010) compared five different analysis methods for masonry arch bridges. They suggested that these structures needed to be regularly reassessed to make sure their loading requirements and material strength were fit for purpose. However, there was no globally agreed framework. The modified *MEXE* method, a three-hinge plastic method, a rigid block method and *2D* and *3D* elastic methods were considered amongst the common practices of masonry arch bridge assessment. They applied five methods to analyse 10 bridges with spans

ranging from 2.4 to 15.2 m in Ireland. The modified *MEXE* method focused on the relation of the arch span and the crown thickness, based on the work of Pippard. However, there were some concerns regarding the span length, span-to-height ratios, depth of fill and its applicability to short-span bridges. Gibbons and Fanning added that the three-hinge plastic and rigid block methods both fell into the plastic method category defined by Heyman. The formation of the fourth hinge leading to the structure failure was the main principle of the plastic methods. *Archie-M* and *Ring* were regarded as existing commercial software for the three-hinge plastic method and the rigid block method, respectively. The three-hinge plastic method was based on the formation of the three-hinge principle developed by Harvey. On the other hand, the rigid block method was based on the failure load factor criterion, which is for the loading required to form the fourth hinge in the arch, as developed by Gilbert and Melbourne (1994). The other assessed method was the elastic one. This involved two-dimensional and three-dimensional elastic analyses. In elastic method, an equation for the compressive strength to withstand the axial forces and bending moments, while having a limited tensile capacity, was used. Consequently, the axial forces and bending moments and compressive strength within the arch material were calculated. This was an iterative process and continued until the maximum axle load was identified. The vertical structural behaviour of the arch was also considered in three-dimensional analyses. Consequently, loads and loads factor, transverse load distribution, and the earth pressures were evaluated using the above-mentioned assessment methods. They concluded that the rigid block method and the *3D* elastic method provide the user with the best results. Gibbons also recommended the impact of the earth's pressure on *2D* and *3D* elastic methods for future work in this field.

Oliveira et al. (2010) investigated the ultimate load capacity of 59 masonry arch bridges in Spain and Portugal. They also compared the historical experimental rules

with the geometrical data from the assessed bridges. In this regard, the authors chose eight reference bridges to represent the sample. They assumed three classes for *L:h* ratios in which the arch was shallow if $L:h \geq 4$, semi-shallow for $2.5 \leq L:h < 4$, and finally deep when $L:h < 2.5$. It was shown that most of the 59 studied arches were in the 'deep' category, with spans between 7.5 m and 15 m. More than half of the chosen arches were built before the 15th century. However, identifying the history and as a result the classification of the arches was sometimes difficult, mainly due to maintenance and repair carried out in the past. On the other hand, the authors explained that the load conditions of the arches had been changing and their materials had been deteriorating. As a result, the ageing bridges might not be safe anymore. Oliveira et al. summarised the past two decades activities to assess the mechanics of masonry arch bridges in Spain and Portugal. Once the geometric profile of arches for one geographical area was identified, the structure's safety was scrutinised, based on their geometry and a simple numerical method. The numerical analysis was based on the maximum load that the masonry arch could carry and load distribution. They discussed the result of geometrical surveys of eight bridges and eventually identified the parameters required to estimate the maximum load capacity of both single- and multi-span masonry arch bridges. The shape of the arch, thickness of the arch and width of the piers were introduced as empirical rules. The paper reviewed the available numerical analysis methods. Oliveira et al. chose the rigid block limit analysis as a numerical method for their study. This method recognises the load distribution. However, the load capacity of the bridges needed to be calculated. Therefore the Ring software was used for masonry arch limit analysis. The authors concluded that the crown thickness of the short-span arches and the pier width values were greater than the empirical rules had suggested. The width of the cross-section-to-span ratio was considered constant for larger span arches. Oliveira et al. also concluded that the arch thickness and fill material properties had a significant impact on the structure's load capacity. Having definition

of load factor as the ratio of collapse load to live load, assuming a standard vehicle, the load factor was greater than 7 for the chosen single- and multi-span arches. Hence, the sample was relatively sound against the safety criteria.

To analyse the single- and multi-ring masonry arches at both ultimate limit and load serviceability states, Casas (2011) proposed a methodology for a reliability-based format assessment. He reviewed the research into the assessment of masonry arch behaviour. The author listed *MEXE*, maximum stress analysis, the mechanism method, Castigliano method and discrete element analysis amongst the numerical and semi-empirical ways of estimating the load-carrying capacity of masonry arches. Furthermore, he indicated that there were also some developments in computer-based analysis such as *Archie-M*, *RING*, and *DIANA*. The static loads, self-weight plus *UDL*, and the arch ring were considered for load condition analysis, not the cyclic loading. Moreover, the described methods were all based on a deterministic approach. As a result, neither the impact of traffic loads on the masonry arch bridges nor other uncertainties were taken into account. An assessment method was proposed by the author to investigate the “fatigue failure” under normal traffic load. The fatigue failure under cyclic loading was assumed to be lower than the ultimate load and its main objective was to assess the long-term operability of masonry arch bridges. Casas developed his assessment as a way to address uncertainties. He classified the failure of masonry structures into: the formation of a fourth hinge, separation of rings in multi-ring arches and finally slipping at the foundation. The last item was not discussed in the paper because of the lack of the material data and modelling. Casas proposed a reliability method to assess masonry arch limit analysis based on the fourth hinge formation and mechanism theory. The author validated the proposed methodology findings against a single-ring brick masonry bridge in Spain which is composed of five barrel vaults of 20m each span.

Rizzi et al. (2014) studied the failure mode of a circular masonry arch with a recently developed analytical solution. The aim of the study was to investigate the Couplet–Heyman problem when the circular masonry arch thickness was at its minimum under self-weight. They used both analytical and numerical analysis to estimate the purely-rotational failure mode. The paper was part of a wider research program initiated at the University of Bergamo in 2006. The classical Heyman (1969, 1982) solution was an analytical method based on masonry arch limit analysis. The solution presented the essential parameters of the five-hinge mechanism failure method. On the other hand, the numerical analysis was also developed by the *DEM* within a discontinuous deformation analysis (*DDA*) framework. There were two other *DEM* categories developed by Cundall and Hart (1992). Rizzi et al. (2014) chose *DDA* mainly because of its efficiency in the static modelling of masonry arches and they summarised existing *DDA* techniques in their paper. The results agreed with the analytical solutions. The authors compared the masonry arch critical condition of minimum thickness resulting from the analytical method with Heyman's solution and validated their technique against *DDA* numerical computations. In summary, the analytical solutions presented in the paper signified how the minimum masonry arch thickness led to the maximum point on the curve in rotational equilibrium.

2.5. Optimization and form-finding survey

As a widely accepted fact, decision-making has played a major role in any field of human activity. As concerns structural design, optimization techniques facilitate the way for a designer to make a decision that achieves the highest advantage from the existing resources. Efficient and architecturally appealing arch structures can be produced if the form of the structure is set at the heart of the design. Searching for the optimum arch shape is necessary to prevent the collapse and deficiency of structures such as the collapsed tunnel at Gerrards Cross in 2005 (*NCE* 2005).

Moreover, finding an optimal arch shape leads to a cost-effective structure with high strength and efficiency.

Many researchers have defined structural form-finding. Otto and Rasch (1995) described form-finding as a technique which uses optimization methods to find the optimal form under a particular load condition. Millais (2005) and Megson (2006) defined form-finding as a technique for finding the most efficient shape of a structure under a specific load condition. The proposed technique involves physical and numerical modelling, and has been applied to a variety of structures, such as shells, domes, cable, and fabric membrane structures (Millais 2005). Coenders and Bosia (2006) defined form-finding as a “proper architectural and structural shape”. Later, Bletzinger (2011) expressed form-finding as “shape finding of equilibrium of forces in a given boundary considering specific stress state”. As a popular definition for form-finding, the optimal shape of a structure is in a state of static equilibrium.

One of the basic form-finding methodologies in the field of arch structures is the application of hanging models. It was Robert Hooke who first stated an anagram in Latin translated as “as hangs the flexible line, so but inverted will stand the rigid arch” (Osserman 2010). This philosophy was put into practice by Gaudi (Tomlow et al. 1989). Gaudi was well known for his novel forms of vertical and inverted catenaries (see Figure 2.2).

Figure 2.2. Antonio Gaudi’s hanging model (http://memetician.livejournal.com)

To shape catenaries when creating a vault or natural curved arch, Gaudi hung different weights on a series of strings and then photographed the shape and inverted it to get the required form. Many architects have applied this method in their work. Finnish-American architect Eero Saarinen and German-American structural engineer Hannskarl Bandel in 1947 designed the Gateway Arch in St. Louis as an inverted catenary (Osserman 2010). The stability of catenary arches subjected to self-weight only that can transfer only axial forces was explored at the University of Stuttgart (Tomlow et al. 1989). Catenary arches subjected to self-weight only showed great stability while being rocked in their experimental investigation. Inspired by physical hanging models, Kilian and Ochsendorf (2005) applied a well-known programme named the particle-spring system to find a funicular form that could transmit axial forces only. The hanging model was represented by lumped masses linked using axial springs in the computational model. Later, they used an iterative solver to find the equilibrium state of each mass. Thus the optimal structural form was achieved once the whole system was in equilibrium. The technique started with two-dimensional funicular forms and expanded to three-dimensional networks.

In physical modelling, Isler (1994) is renowned for his free-form shell structures. To obtain free-form surfaces, Isler has drawn on three novel methods which are: the membrane under pressure, the freely-shaped hill, and the hanging cloth reversed. He made physical models without using computers and obtained calibrated measurements. For shell structures in three dimensions, he used the theory of the inverted catenary arch and inflated membrane (Chilton 2012). Some of his works are: the creative triangular shells of the Deitingen Sud Service Station in 1968, the linked shells on seven supports for the Sicli factory in Geneva in 1969, the hooded shells of the air museum at Dübendorf in 1987, and oft-repeated tennis hall and swimming pool shells (Oxman and Oxman 2010).

Arch form-finding can also be carried out analytically, using mathematical equations. One of the early analytical studies into the optimization of arches was carried out in 1973 by Tadjbakhsh and Farshad. They investigated the possibility of the optimal shape of funicular arches when both the bending moment and shear forces are zero. The general shape of the arch was defined from the beginning in their study. Moving toward form-finding of arches, Farshad (1976) obtained different parametric functions for the shape of an optimal arch under static loading, defining multiple objectives. The objectives in his research comprised minimizing the arch length, arch thrust, and volume of the arch material separately. Consequently, the shape of the arches with minimum thrust and minimum length was found individually when the arches were of a constant cross-section. In the case of arches with a variable cross-section, the objectives were minimized the thrust and the volume of the arch material respectively. Later on, Tadjbakhsh (1981) obtained the geometry of a momentless arch subjected to self-weight and the deck weight, assuming constant axial stress in arches with a variable cross-section. Tadjbakhsh showed that the arch shape was independent of the magnitude of the loading in the case of uniformly distributed load. However, the cross-sectional area varied in proportion to the loading.

In 1986, Haftka and Grandhi reviewed the optimization methods of two- and three-dimensional structures. The authors started the survey with a numerical optimization that was mainly based on the sizing variable of a structure. Later, Haftka and Grandhi considered optimization with shape design variables as a more difficult procedure compared to optimization with sizing variables. The authors assumed changing in finite element model when the optimization was running. This includes changing in coordinate of boundary nodes in finite element model. Haftka and Grandhi highlighted the requirement to develop an automated optimization tool which took account as the necessary design parameters. Additionally, they

emphasised the significance of sensitivity analysis for an optimization. Haftka and Grandhi considered calculating accurate stress at the boundary as important parameters in shape design optimization. To obtain valid optimization results, the design variables had to be selected carefully, especially when they were selected as coordinates of boundary nodes. The shape design variables were chosen so as to reducing the stresses at the boundary. Their work dealt with changing mesh in finite element model when the boundary is changing. The optimization with shape design variables controlled the geometry of the structure. They noted to the significant impact of changes in shape on the structure performance. The importance of the shape effect on the structural action is investigated in the third chapter of this thesis.

Ding (1986) reviewed the numerical and analytical methods of shape optimization. Structural optimization started with model identification, followed by structure variables, objective function and boundary determination. He also emphasised the shape optimization difference with sizing optimization. Ding reviewed the sizing design optimization in which the structure shape was fixed. In other words, sizing parameters such as bar cross-sectional or arch thickness were used in the optimization to identify the structural shape. Additionally, he extended his research to shape optimization, in which the structure's displacements, stresses and other constraints were involved in establishing the boundary for the material in the arch. The shape optimization requires extra care since the boundary conditions must be chosen in a way to satisfy finite element analysis, while addressing the structure's change during the design process. Ding believed that there was no unique method for shape optimization and described different shape optimization methods. He referred to analytical methods used for such optimization since 1904 and Michell's works, as well as recently developed numerical methods. There, the design variables were node coordinates. He noted to the impact of the arch shape on its performance. The finding has assisted researchers in structure design and shape

optimization. In Ding's shape optimization survey, first the objective function was defined. Then, different ways of shape representation were summarised. Thirdly, the finite element mesh generation and methods of refinement were described. Next, the sensitivity analysis and solution methods were offered, and finally the author assessed the shape optimization of eight actual structures. Ding emphasised shape representation as a decisive factor for shape optimization. The structure could be modelled by boundary nodes. The application of coordinates of boundary nodes as shape variables was the first method of shape representation mainly practised in the finite element method. Although this approach was straightforward, the design variables were sometimes too large or there was incompatibility amongst boundary nodes. Hence the approach was not regarded as the preferred option. Ding named a second way of shape representation by boundary shape as "polynomial". This used control nodes for shape representation, which requires fewer design variables. However, there was a possibility of numerical instability in high-order polynomial shapes. Finally, Ding introduced "spline function" as another way of boundary shape description for shape representation. The advantage of splines over polynomials was in high-order polynomials. In other words, a spline took advantage of low-order polynomial modelling. As a result, the chance of numerical instability was very low. Following the finite element method and refinement, Ding explained two ways of sensitivity analysis: discretized finite element system differentiation and continuum equations continuation. The sensitivity analysis was required to assess the structure's response when the design variables changed. Ding chose the approach relied on differentiation of the discretized finite element system in his work. The author used six numerical methods to find the optimal shape of different structures such as design of bridge. Linear programming (*LP*), optimality criteria, and the sequence of the approximate problem were some of the numerical methods explained. In conclusion, Ding explained the applicability of shape optimizing, ranging from dams and bridges to

shoulder fillets. The author drew a flow chart describing “the design process of the shape optimization”.

Dopker et al. (1988) developed a structural design sensitivity analysis of an arch’s shape. They reviewed curved structures, especially arch bridges, and highlighted the challenge of their curvature design. In other words, such structures need to be designed in such a way as to satisfy constraint requirements under stress and displacement forces. They believed an appropriate “shape design sensitivity analysis” would assure the structure’s performance. The shape sensitivity method used mathematical programming methods to improve structural design for a given boundary and stress state. Dopker et al. explained the past attempts to form a unique method for shape design sensitivity analysis, including different design variations such as truss, beam, and plate components. As they indicated, Choi and Seong (1986) initially formulated the shape design sensitivity for built-up structures. However, the curved component was still missing. Moreover, the previous shape design sensitivity analyses could not offer a comprehensive method to address more than one design component and they were only applicable for one specific form of arch. The authors developed the unique method of shape design sensitivity analysis to cover the curved component. Dopker et al. used the continuum mechanics principle to derive the domain and boundary parameters of a structure based on the shape change. They derived shape design sensitivity information and analysed the displacement fields. The former was based upon curved beam theory and the latter developed according to beam/truss theory. Dopker et al. applied a theory of beam-truss to estimate the displacement fields. The authors emphasised the good accuracy of straight beam-truss approximation method for displacement fields in the case of shallow arches. Dopker et al. concluded that design sensitivity analysis was an appropriate method for built-up structures.

Vanderplaats and Han (1990) used the force approximation method to optimize the shape of both fixed and two-hinged rib arches subjected to combined stress constraints, by minimizing the volume of the structures. The ribs of the two-dimensional arches were assumed to be designed with a finite number of straight members. So, the member area and the nodal coordinates were taken as the variables in the optimization process. They propounded the necessity of developing a new approach for the optimization algorithms because the extent of the number of variables and the degree of non-linearity were remarkable in optimization problems. Thus, they proposed an iterative optimization approach including two separate sizing and coordinate spaces. In this approach, optimization of the member area under a predetermined geometry was simultaneous with the optimization of the arch geometry. Hence, there was a continuous iteration alternating between area and coordinates. For the constraint condition, the calculated combined stress due to the bending moment and axial force was set as equal to or smaller than the allowable stress. Therefore, an approximate structural analysis was obtained by expanding the first-order Taylor series for the axial forces and bending moments at the end of the member alongside applying the relevant gradients. To achieve this, a finite element analysis was used with the initial structure for the calculation of the gradients of axial forces and bending moments. Also, the gradients of member end forces, which were integrated into the finite element analysis, were calculated using the equation of element stiffness with respect to the considered variables. To solve the optimization problem, they used a numerical optimizer programmed in *ADS* by Vanderplaats and Sugimoto in 1986. In order to illustrate the reliability of the force approximation method, they presented three numerical examples for both fixed and two-hinged arches. The first example showed the optimal shape of two-hinged arches with point load at the crown, which became a triangle. For the second example, they found an optimal shape of parabolic arches under uniformly distributed load for both fixed and two-hinged arches. By assuming the height of the

arch as the only geometric variable, they minimized the volume of the parabolic arch in this case. The last example was the optimization of the fixed-ended arch under a uniformly distributed load having the same variable as the second example. In this case, they compared the optimal arch shape from their analysis with the parabolic shape. As the result, it was demonstrated that the parabola is the optimal shape of arches under uniformly distributed load. Furthermore, the new results for the three examples were compared with the findings of the two design space methods conducted by Byun and Han in 1984. A plot of the iteration history of the force approximation method showed a swift rate of convergence through few finite element analyses. This was an advantage of the approach by Vanderplaats and Han over the approach of Byun and Han.

Serra (1994) proposed analytical and numerical approximate solutions for the optimal form of funicular arches as a uniformly compressed structure. Serra found the shape of the arch with variable cross-section subjected to uniform horizontal and vertical loading analytically. It was assumed that the *L:h* ratio is a minimum in the analytical solution, while the limit for this ratio was not given.

Hsu (1994) investigated the methods of structural shape optimization and identified a comprehensive framework to address geometrical modelling, structural assessment and optimization. In other words, a computer-based programme was formulated to minimize the self-weight of two- or three-dimensional arches. They could be analysed with varying geometrical parameters for the structural responses of stresses and displacements, to arrive at the optimal structural shape. Ideally, the designer is seeking a method to translate structural optimization analysis into a mechanical form. The developed optimization algorithms paved the way for systematically optimizing structure shapes. Hsu introduces the zero-order algorithm in which only function values of the implicit constraints are required to assess three-dimensional shape optimization.

The application of the form-finding process in architecture was done by Otto and Rasch (1995) in the second half of the 20th century. Otto is well-known because of his lightweight tensile and membrane structures. As he believed, the optimal architecture is ethical architecture, including an aesthetic viewpoint, and his works were considered as artistic and innovative masterpieces, such as the West German Pavilion at the Montreal exhibition in 1967 and the roof of the Munich Olympic Arena in 1972. He considered form-finding as a research technique and a way of designing natural systems without destruction in nature. Moreover, his main tool for working was physical modelling that could be used to simulate the optimized solution. He concentrated on tents with a minimal surface area, including soap-film experiments, pressure-loaded vault forms, and grid shells stabilized by tension lines through careful construction and experimental physical models. Earlier, in 1964, Otto established the famous Institute for Lightweight Structures at the University of Stuttgart. Accomplished experiments in that Institute have provided detailed information for the description of forces, as well as their transpositions, which were regarded as the explanation of the form principle. Then, by consuming minimum material and energy, any new structure was fitted into its environment. Many form-finding experiments to obtain natural forms of arches and their three-dimensional equivalents such as domes continue to be conducted in the University of Stuttgart. They demonstrated a great stability of a natural arch shape subjected to self-weight only, which is turned out to be a catenary arch with the momentless shape.

In 1998 Habbal, used a direct non-smooth analysis method to minimize the maximal stress in arch structures. To achieve this, he developed an arch equation for formulation of optimum design, using the linear elastic thin shell approach. Firstly, he considered the arch structure as an infinite three-dimensional cylindrical body. Then, by assuming the arch thickness to be very small with constant loading applied across the cylinder axis, the problem became a one-dimensional one using the thin

shell theory of Kirchhoff–Love. The stress distribution was obtained from the elastic energy function and displacements constraints, which were defined for both fixed and simply supported arch ends. Hence, the compliance of the elastic energy functional was achieved from the equilibrium equation in terms of the geometrical description of the arch and the loading. To optimize the arch structure regarding displacements and stress distribution, he modified the shape of the arch structures. This optimization process was carried out by applying the cost function theorem to two different minimization areas. Cost parameters one was the minimization of the maximum stress distribution of the upper surface and the second was the minimization of the maximum displacement. In this process, a parabola form was first considered, and the optimal shape was identified, when the method converged after a number of iterations. Habbal showed that the optimal arch shape obtained under uniform and non-uniform distributed loading for the maximum displacement cost is different from the one for the maximum stress cost.

Choi (2002) used a curved beam principle in a linear elastic analytical method to assess the design sensitivity of plane arches. He emphasises the importance of curved beams in the optimization of different structural shapes. He developed a design sensitivity method to analyse the optimization of these structures, and called it the “continuum approach” which results in closed-form solution. Choi compared the continuum approach with other types for sensitivity analysis such as the finite dimensional method in which the sensitivity formula for structural optimization was mainly derived from a discrete element. He reviewed the work of Dopker et al. (1988) and Chenais et al. (1988). They introduced another method for sensitivity analysis using Cartesian coordinates. This time the sensitivity formula was derived based on an explicit model of an arch which can move in normal direction. Choi explained the drawback of the Dopker et al. and Chenais et al. model in its flexibility. In other words, due to variation limitation in the axial direction, the approach was

only suitable for shallow arches. He also indicated that Kim and Kwak (1993) had taken one further step and tackled the Dopker et al. and Chenais et al. generality issue by considering the structure in different segments, each segment representing a shallow arch. The continuum approach developed by Choi was initially introduced by Dems and Mroz in 1987. First, the curved beam “variational equation”, that is the derivation of the variational theory of the equilibrium equation, was formulated, followed by the shape variation sensitivity formula using continuum mechanics. Next, the resultant sensitivity coefficients were used in a parametric study. In summary, the author defined the design sensitivity formulation when stress was applied at a local segment of the structure. Choi believed that the proposed shape design sensitivity method could be solved numerically, giving accurate results. Additionally, the method thoroughly described the shape and its variation. The arch length variation was also considered in the analysis. As a result, such comprehensive analysis presented better optimal design parameters for complex shapes. Lastly, the proposed shape design sensitivity analysis was not limited to shallow arches. It could be expanded from linear elements to higher order elements. Choi also tried to validate the findings of his sensitivity assessment method with a number of examples. He applied the *ANSYS* finite element analysis tool with just a straight line representation. As he stated, *ANSYS* was more accurate compared to other tools in terms of numerical assessment. The author carried out shape optimization using his method of analysis for two design problems.

Griva and Vanderbei (2003) reviewed the recent modelling algorithms and assessment methods embedded in modern optimization software. The focus of their study was on the large-scale constrained case studies having a large number of discretization points. They highlighted the applications of catenary arches in the world. The arch optimization was examined analytically against convex and non-convex formulation. The authors added that the structure should be modelled in a

unique mathematical formulation available for numerical traceability. To address the curvature problem, they used programme *AMPL* as a modelling language and also *LOQO* as a non-linear optimization solver. Because it took *LOQO* a few seconds to search for the solution it is the optimization solver. The findings suggested that convex optimization was more numerically traceable for an arch with an identified mass function. Furthermore, the role of proper modelling in the optimization process was emphasised. In other words, the effective arch modelling resulted in a simpler and much quicker optimization process.

Megson (2006) and Millias (2005) noted that when an arch is subjected to only a uniformly distributed load, a parabolic form shows zero bending moment, while an arch with self-weight only will have a zero bending moment if it follows a catenary form. However, in reality, both kind of loads are imposed on the structure, so the form in between might present the zero bending moment solution. By reducing the bending moment, an arch will resist loading by developing mostly compressive forces. The important engineering fact is that tensile forces cannot transfer in the case of masonry arches reliably. As bending moments are reduced in masonry arches, the internal tensile forces are decreased and it leads to have a more durable structure.

Taysi et al. (2008) proposed a method to optimize arch structures considering stress, displacement and weight constraints. They explained the necessity of the shape optimization of structures to design a cost-effective arch with large spans and the capability to carry heavier loads. On the other hand, smaller cross-sections were considered for the beams. Additionally, the authors defined an objective function with certain constraints to achieve a more economical solution. It was a challenging process for complex structures, since solving optimization with conventional solving techniques was almost impossible. Moreover, some of the functions were not analytically modelled. The evaluation of functions was carried out point-by-point as

far as computer-based programs are concerned. Hence the authors recommended evolutionary algorithms (e.g. genetic algorithm (*GA*)) in the optimization. Such techniques evaluate the constraint function and design variables separately. Hence they can incorporate discrete variables, such as cross-sections in the optimization process. The *GA*, which works on the basis of the survival of the fittest and adaptation, was developed into Lagrangian, hybrid algorithms with fuzzy system and neural network forms. Taysi et al. described the optimization method as an automated procedure. It incorporates the finite element analysis with parametric cubic spline geometry definition, Mindlin–Reissner theory, automatic mesh generation and genetic algorithm methods. Moreover, the authors used the structure's thickness and shape variables in the optimization procedures. Such parameters were used to identify the natural line of the arch. Ideally, their optimization tool produced the best arch thickness and curvature under the maximum loading. They scrutinised "bending", "membrane" and "shear strain energy" while running an optimization program. The computer program developed based on the proposed method could optimize variable thickness curved beams and arches. The authors presented several examples to demonstrate the proposed arch optimization method.

Tyas et al. (2011) proposed a precise geometry for optimal structural arch form carrying a uniform load between pinned supports. They found the least-volume hybrid structure as an optimal form encompasses a central parabolic section and networks of truss bars commencing from the supports. The authors pointed to the previous investigations about structural optimization, suggesting that the best structural form to carry a uniformly distributed load was the two-pin parabolic arch. It was considered that the loads were directly applied either to an arch (in compression) or a suspended cable (in tension). Under these conditions, the least-volume form of structure was achieved when the parabolic funicular made an angle

of 30 degrees to the vertical at the support. They set the tensile strengths of material and compressive to be the same. The authors assumed that the structure was subjected to the *UDL* and they ignored the structure's self-weight. The authors analytically presented the geometry, stress and displacement fields within the structure. They achieved a precise analytical relation for the geometry having minimum volume.

Veendendaal and Block (2012) compared some of the existing form-finding methods with each other. The authors first explained how the shape of the structure was dependent on the applied forces and then emphasised the significance of form-finding to address the optimal form. Moreover, they reviewed computational form-finding that has been developing since 1960. The authors listed "stiffness matrix, geometric stiffness and dynamic relaxation" as the three form-finding methods for their comparison framework. The basis of stiffness matrix method was the standard elastic and geometric stiffness matrices which were formed by the real material parameters. The geometric stiffness method was independent of the structural material and resulted from the force density method, in which the essential parameter in the mathematics was the ratio of force to length. The dynamic relaxation method was based on the motion that considered dynamic equilibrium at a steady-state. There, the forces transformed to velocities and their acceleration was determined by the nodal mass. The authors believed most of the previous comparison approaches were qualitative. Additionally, some of them were no longer fit for purpose. As they stated, Barnes (1977) compared dynamic relaxation with the stiffness matrix method with regard to the "storage requirement" per iteration. The findings suggested that dynamic relaxation had better storage capability. Veendendaal and Block identified a gap in the accuracy of comparing form-finding methods. They tried to find a straightforward comparison framework. Their framework was based on "sparse-branch node data". The way each method

identified the internal forces and eventually the stiffness were presented. The internal forces and stiffness were considered for both linear and triangular surface elements. Moreover, the framework describes the “solver” that each method applied in form-finding. In conclusion, Veendendaal and Block introduced an efficient comparison framework which assessed the existing form-finding methods based on their operating criteria and programming language. Finally, they applied their framework to compare the performance of different form-finding methods; firstly to a saddle-shaped minimal-length net, secondly to a high-point net, and lastly to a minimal surface. They did not consider arch structures in their investigation.

Concerning the computational form-finding method in conjunction with the construction technique, the work of innovative funicular tile vaulting was advanced by a group of researchers at the Institute of Technology in Architecture, *ETH* Zurich (Davis et al. 2012). The prototype vault’s form was achieved by the computational form-finding method using interactive software *Rhino VAULT* for thrust network analysis (*TNA*). In doing so, the free-form shapes for funicular vaults that were purely in compression were obtained by setting boundary conditions in the software. The required boundary conditions to be specified to generate a three-dimensional equilibrium solution for the self-weight of the vault were listed as: the general in-plane form of the structure; the position of the footings; the internal distribution of thrust; and the shape of open edge arches. To show the validity of the *TNA* form-finding method, they made a three-dimensional full-scale vault prototype from a cardboard box falsework system, based on the surface obtained from the *TNA* form-finding. Lightweight sandwich constructions of three layers were used as thin tiles in compression. They concluded that an artistic shape of compression-only shell constructions can be produced by applying simple technology without using excessive material. Hence, the method could be applied to the design of new optimal funicular masonry structures.

Foglar and Křístek (2012) investigated centre line optimization of the buried arch bridges. They historically reviewed arches and their applications and highlighted the fact that even some Roman-built arch bridges are still in use today. Then, they described buried arch bridges and their application in roads and railways. They believed that buried bridges with span lengths between 2 and 40 m have frequently been used. As they stated, buried arch bridges are cheaper and last longer. The loading conditions of buried arch bridges were also described in their research. Initially, in the fill compaction stage the arch was subjected to the vertical load of self-weight. Then the traffic load was expected to be added to the weight of the fill. Foglat and Křístek considered the lateral load condition resulting from soil–structure interaction. The authors tried to introduce an optimization method using theoretical derivation for the buried arch bridges centre line. Moreover, the geotechnical software *PLAXIS* was applied to numerically model the soil interaction with the structure. The calculated soil–structure stresses were used in the format of interaction vectors in the method. It was shown that the bending moments reduced by 22% in a quarter of the arch span. That reduction was 25% at the arch crown. The soil interaction with the structure did not allow Foglar and Křístek to propose a uniform reduction of bending moments. The bending moment reduction itself led to a decrease of deflection.

Another research into the optimization of arch structures was conducted by Houšt et al. (2013). They used numerical modelling to optimize the shape of buried concrete arches. To do so, they applied non-linear finite element simulation with *ANSYS*. The construction layers were situated sequentially through 8 or 9 layers to cover the top crown of the arch with agiven geometry. The compaction of the soil and the sequential process of construction were considered. Since the self-weight of the soil is important to the design of the arch's cross-section, modelling concluded the interaction of the soil and the construction procedure. The objective function was set

to reduce the bending moment and bending stresses. They assumed the ideal shape for the centre line of an arch is when the arch is momentless. In the case of buried arches, because of the combination of horizontal and vertical applied load, the bending moment cannot be completely eliminated. Houšt et al. sought the geometry for the centre line to produce the minimum bending moment. They used a two-dimensional model with the assumption that the permanent load was dominant. The live load for traffic was considered to be negligible. Additionally, they ignored longitudinal displacements of the arch. As an optimization process, they parameterized the arch centre line with a third-degree Bezier curve for half of the arch, owing to symmetry. Thus, the problem was analysed by finding the Bezier curve for arch's coordinates. This calculation led to the summation of the maximal tangent stresses of the arch to be minimized. They applied a non-linear finite element model to specified centre line geometry in order to extract the tangent stresses in the arch subjected to live load and loading resulting from erection, placement and compaction of backfill. In order to reduce the maximum tensile stresses, firstly a genetic algorithm using a *MATLAB* was implemented to acquire a global minimization. Then, the Levenberg–Marquardt method was employed to refine the final solution. The optimal shape of buried arch was found parametrically for different span-to-height ratios, types of soil, and depths of backfill. It was shown that, for any span-to-height ratio, when the dead load was higher than live load and the subsoil was sufficiently stiff, the most curved part of the optimal shape of the arch was at the crown and the straighter parts were at the bottom of the arch. Additionally, the tensile stresses reduced significantly towards finding the optimal shape of the arch, when the subsoil was stiffer. Finally, the tensile stresses decreased more noticeably in arches with a small span-to-height ratio using this optimization method. Furthermore, they applied this method to optimize the shape of a reinforced concrete arch culvert which was physically tested at the University of Massachusetts. They also compared the bending moment and axial forces of

optimal shapes for arches with different thickness. They showed that by reducing the arch thickness by about 30%, the maximum tensile stresses reduced to half of their initial magnitude. It was demonstrated that by further shape optimization of the centre line of the thin arch, the tensile stresses decrease and the upper fibres of the arch ring experiences pure compression.

Koohestani (2014) proposed a new form-finding method by applying discrete models and the non-linear force density method for tension membranes. He introduced different methods of form-finding for tension membrane structures and summarised previous activities such as Veenendaal and Block's form-finding survey. Koohestani believed that the geometric stiffness method is the most favourable of the method. Koohestani named other alternatives in the geometric stiffness method, such as the updated reference strategy (*URS*) and natural force density method (*NFDM*). As he stated, the force density method (*FDM*) was the earliest form-finding method in the category of the geometric stiffness approaches. The *FDM* method was initially developed by Linkwitz and Schek and first used for form-finding a cable net. The author introduced triangular and quadrilateral finite element meshes for his form-finding modelling of the minimal surface membrane**.** The triangular model had been practised by structural designers, while the quadrilateral one was proposed as a novel form-finding approach by Koohestani. The principle of the quadrilateral computational model was membrane form-finding with a non-linear force density method. The structure form-finding was introduced as a way of defining a self-equilibrated state of the structure before imposing any stress in his study. Koohestani also reviewed fixed point and Newton–Raphson iteration methods for discrete modelling and offered a combination method as a useful solution. Koohestani eventually validated his method with some popular minimal surfaces compared against analytical solutions.

Regarding form-finding and optimization investigations, Descamps (2014) proposed an optimization method that can manage different design parameters efficiently for lightweight structures. First, the author explained the basics of truss layout optimization. Then, a method to optimize the structural sizes and system connectivity at the same time was programmed. The combined mathematical programming and structural mechanics were used to estimate the optimal truss geometry and topology in his study. The optimization process was formulated separately according to plastic and elastic principles under different loading conditions. The method was relatively fast and the optimized solution was obtained within 18 minutes in *MATLAB* with 1414 iterations. The author validated the approach against a number of realistic design problems and proved the method's applicability with varying design parameters.

2.6. Concluding remarks

Despite the wealth of literature on arch analysis methods, to the best of the author's knowledge, a comprehensive assessment of known shape arches has not been done before. In other words, there is no pervasive study of the effects of arch forms and span-to-height ratios on structural action. As demonstrated in Section 2.3, previous studies concentrated mostly on circular arches. The comparison of the response of different arch shapes has not been studied in detail. The optimal range of span-to-height ratios at which the combined stress of the bending moment and axial force is at the minimum has also not been explored in the literature. However, designing the arch with an appropriate shape using the optimum span-to-height ratio leads the structure to be more durable and safe in reality. This solution will thereby reduce the cost of maintenance. This Section aims to acquire an in-depth understanding of the response of known arch shapes to loading and to find the optimal range of span-to-height ratios.

As reviewed in Section 2.4, there is plethora of methods for arch analysis that are based on both elastic and plastic theories. There is also much user-friendly software provided to analyse arch structures in a short time. However, there is no investigation of the existing approximate analysis methods for arch structures such as the masonry design method, and the virtual work method suggested by Megson. These two methods of arch analysis are currently in use to analyse two-pin arches. However, the assumptions made in these approximate analysis methods lead to varying degrees of reliability.

As far as structural optimization is concerned, there are a large number of investigations available using different methods of optimization and form-finding. As reviewed in Section 2.5, the form-finding methods have been used for various structures, mainly consisting of tensile members such as cables and shells structures. Finding the optimal structure shapes has also been developed for compressive members such as trusses and arches. In the case of arch shape optimization, there has been more concentration on the study of arch dams, buried arches, and arches of variable cross-section, which are expensive in practical terms. There has been no effort on the analytical investigation of optimal shapes of rib two-pin arches with constant cross section. This problem might be due to the essential difficulties of mathematical analysis. The novel aspect of the author's PhD work is to develop an optimal shape of arches for any ratio of uniformly distributed load to the self-weight. This work involves analytical form-finding, in which the principle of zero bending action will be implemented. As the bending moments are minimized, the stresses resulting from bending and axial forces are reduced in the arch material. A lower level of stress, as the result of an optimal shape, will reduce the amount of material required and the cost of the structure. It was seen in the literature that most researchers looked for structures with the minimum bending moment. However, their attempts were mostly focused on buried arches and arches of variable cross-section. This study aims to fill the gap in form-finding of

compression structures i.e. two-pin arches. Also, the applicability of the momentless arch as the optimum arch shape has not been studied in the literature.

Chapter 3 : Analysis of two-pin arches

3.1. Introduction

An arch is an impressive structure from an aesthetic point of view and also has good durability under environmental loading. It dates back to ancient times but is still in wide use today. Despite the extensive literature on arches, there is no comprehensive study of the influence of arch forms and the span (*L*) to height (*h*) ratio (*L:h*) on their structural action effects. Previous studies (Chapter 2) focused predominantly on circular arches or arches with variable cross-sections, which are expensive in view of the complexity of construction.

A comprehensive review of two-pin arches of various forms and their response to loading is presented in this chapter. Rib arches of catenary, parabolic and circular form respectively are investigated using four typical load cases and *L:h* ratios ranging from 2 to 10. The study is mainly conducted for arches made of concrete or masonry material. The effects of form on the structural response of each type of arch are presented using finite element analysis provided using *GSA* software. This investigation permitted conclusions to be drawn as to which *L:h* ratio and shape is preferable in design. A crucial goal of this analysis is to give an in-depth understanding of the influence of structural form on structural actions.

3.2. Theory of common arch shapes

It is possible, using computational or physical form-finding experiments, to show that the optimum shape of an arch depends on the predominant loading applied to it (Figure 3.1). Thus, provided the arch has a constant cross-section, a circular arch (Figure 3.1 (*a*)) represents the optimum form for the case of a constant radial load, a parabolic arch (Figure 3.1 (*b*)) for a weightless structure under a uniformly

distributed load (*UDL*), and a catenary arch (Figure 3.1 (*c*)) for the case of self-weight (*SW*) only (Proske and Pieter 2009).

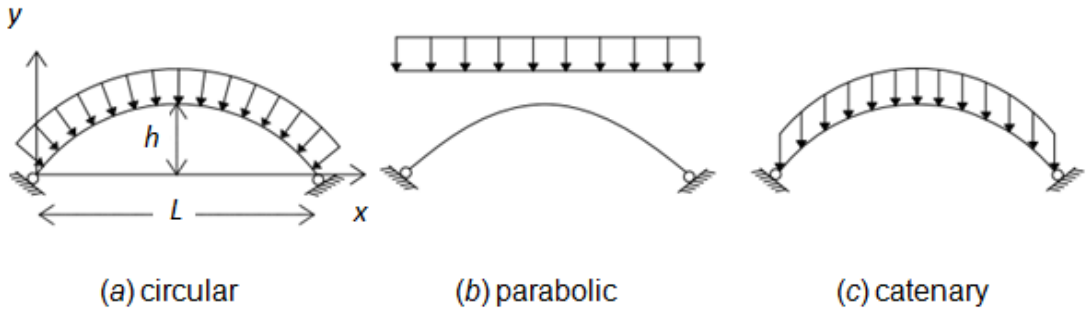

Figure 3.1. Optimal arch shape according to different loading patterns (Proske and Pieter 2009)

3.2.1. Derivation of arch equations

By considering *L* as the span of each arch shape and *h* as the height of the arch, each curve is derived starting with the general equation for the curve, so that the arch starts at (0, 0), passes through (*L/2*, *h*) and ends at (*L*, 0), as shown in Figure 3.2.

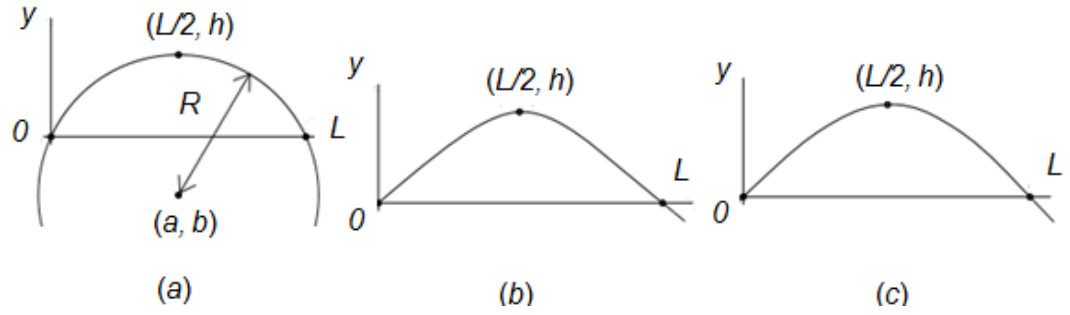

Figure 3.2. Circular (*a*), parabolic (*b*) and catenary (*c*) arch shapes

3.2.1.1. Circular form equation

Starting with the general equation for a circular form (mathwold.wolfram.com):

$$(x-a)^2+(y-b)^2=R^2 \tag{3.1}$$

To represent the governing equation for a circle, related to *L* and *h* as shown in Figure 3.2, constants *a*, *b* and *R* are obtained in terms of *L* and *h*.

Differentiating the general equation of the circle leads to Equ. (3.2).

$$2x - 2a + 2y\frac{\mathrm{d}y}{\mathrm{d}x} - 2b\frac{\mathrm{d}y}{\mathrm{d}x} = 0 \tag{3.2}$$

Then, the constant *a* can be found using the *x* coordinate of the arch at the midpoint of the arch (*m*) from:

$$\left(\frac{\mathrm{d}y}{\mathrm{d}x}\right)_m = \frac{2a - 2x_m}{2y_m - b} = 0 \Rightarrow a = x_m = \frac{L}{2} \tag{3.3}$$

Substituting (*L/2*, *h*) for the midpoint of the arch into the general equation and using *a=L/2* gives: *h-b=R*. Moreover, substituting (0, 0) into the general equation leads to $a^2+b^2=R.^2$ Therefore, *b* and *R* are respectively equal to $\frac{h}{2}-\frac{L^2}{8h}$ and $\frac{h}{2}+\frac{L^2}{8h}$.

Having *a*, *b* and *R*, the general equation leads to the governing equation form for the circular arch, which is given by:

$$(x-\frac{L}{2})^2 + (y-\frac{h}{2}+\frac{L^2}{8h})^2 = (\frac{h}{2}+\frac{L^2}{8h})^2 \qquad \text{for } 0 \le y \le h \tag{3.4}$$

3.2.1.2. Parabolic form equation

To obtain the governing equation of a parabolic curve in terms of *L* and *h*, a similar method to that for deriving the circular shape is used.

The general equation of a parabola is expressed as Equ. (3.5) (mathwold.wolfram.com).

$$y = ax^2 + bx + c \tag{3.5}$$

in which *a*, *b* and *c* are constants. In order to convert a curve to an arch shape, *y* becomes *–y.*

$$y = -(ax^2 + bx + c), \text{ where at (0, 0), } c=0 \tag{3.6}$$

At the midpoint of the arch (*m*), $(\mathrm{d}y/\mathrm{d}x)_m = -(2ax_m + b) = 0$ in which x_m=*L*/2 and *b*=-*aL*. Additionally substituting (*L/2*, *h*) into the general equation, *a* and *b* are given respectively as $\frac{4h}{L^2}$ and $-\frac{4h}{L}$. Replacing *a*, *b* and *c* into the equation of general form for a parabolic arch gives Equ. (3.7).

$$y = \frac{4h}{L}(x - \frac{x^2}{L}) \qquad \text{for } 0 \le x \le L \tag{3.7}$$

3.2.1.3. Catenary form equation

The general equation for a catenary is $y = A'\cosh(x/A')$ (mathwold.wolfram.com). In this equation "*A'* " is a constant which requires the use of an iterative algorithm to be found for each curve. To have an arch profile from its curve shape, same as a parabola, *f*(*x*) must be converted to *–f*(*x*), in which *y*=*f*(*x*). The curve defined by this equation will cross the *y*-axis at "*-A'*." As seen in Figure 3.2 (c), the arch curve passes through (0,0); hence, a constant is required, which is defined as *A'*+*h*. By considering the maximum point on the arch curve to have the *x* coordinate of *L/2*, the general equation is derived as Equ. (3.8).

$$y = -A'\cosh(\frac{x - \frac{L}{2}}{A'}) + A' + h \qquad \text{for } 0 \le x \le L \tag{3.8}$$

By substituting any of the three known points of the arch in the above equation and using the *MATLAB* software, "*A'* " is calculated. The *MATLAB* codes are listed in Appendix C.

3.3. Project description

In this section the specifications of the studied two-pin arch forms, i.e. circular, parabolic, and catenary, are described.

3.3.1. Arch specifications

The two-pin arches to be analysed are of a constant rectangular cross-section of uniform lineal density, supporting a superstructure of uniform density (*UDL*) per unit span. Their span is 10 m in each case. Concrete is considered as the construction material, with the elastic modulus of 27 GPa, density 2400 kg/m^3 and the cross-section size of 300 mm (depth) by 1000 mm (width) which are assumed as the inputs of computational analysis using *GSA* software. To have a real arch specification, these cross-sectional dimensions are taken from the Gerrards Cross tunnel, although Gerrards Cross was a three-pin arch. A 30 m section of the 320 m of this tunnel collapsed in 2005 (*NCE* 2005). The displaced shape of the arch is simulated by *GSA* software, as a linear elastic analysis method considering small displacements, using parabolic, catenary, and circular shapes. Comparing the displacement shape of the three known shapes of arches subjected to *UDL* plus *SW*, it was found that the circular form matched the actual failure mode of the tunnel (see Figure 3.3). One of the explanations for the destruction of Gerrards Cross tunnel considers the altered sequence of applying surcharge loading; instead of being placed over the sloping sides of the arch, it was placed on the top first. The collapse of this tunnel could probably have been prevented by using an arch form that was less sensitive to disproportionate loading. However, in post-failure

assessments on small-scale arches, the question of form was not raised. The effect of arch form on structural behaviour is investigated in this chapter.

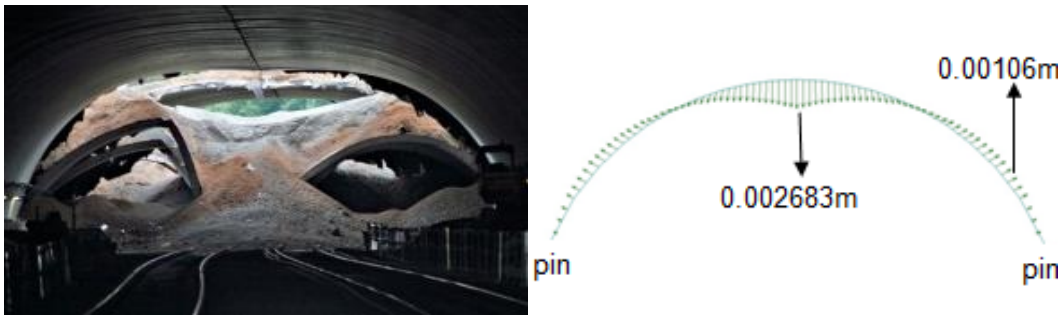

Figure 3.3. Collapsed section of tunnel at Gerrards Cross (*LHS*) (*NCE* 2005) – *FE*: Displacement of circular arch when subjected to a *UDL* +*SW* (*RHS*)

3.3.2 Load cases

The *SW* of studied arches with defined specification in Section 3.3.1 is equal to 7.2 kN/m. In order to achieve different ratios of *UDL*:*SW*, multiple load cases are applied to the arches, as listed below:

- *A1*: *UDL* of 20 kN/m applied across the full span of the arch plus *SW*.
- *A2*: *UDL* of 20 kN/m applied across the full span of the arch added to *SW*, plus an additional *UDL* of 20 kN/m applied to half the span.
- *A3*: *SW* only.
- *A4*: *UDL* of 20 kN/m applied across the full span of the arch only.

The reason of assuming *UDL* equal to 20 kN/m is to apply *UDL:SW*>1 to the arch which is a significant load case having a rib arch supporting a deck. The behaviour of different arch shapes is also evaluated for other load cases when *SW*≥*UDL* in this chapter which might be interesting as an architectural view point. It is important to consider the anticipated application of an arch when the loads are applied. In general, the arch is supposed to support its self-weight, the weight of a superstructure, and traffic passing over it. The first two loads are assumed as

permanent ones in a design situation and the last one as a variable action. There are also other variable loads such as wind and snow loads that are less important to consider in the imposing load configurations. The permanent loads are basically applied as a *UDL* across the full span of the arch. In order to apply the variable loads, the location of the imposing load has to be determined beforehand. The results of preliminary analysis indicated that the loading of half of the span is the critical loading pattern of the arches in terms of structural actions. To show this, the *UDL* of 20 kN/m is placed firstly across half the span (Figure 3.4) and secondly on the central 40% of the known shape of the arches (Figure 3.5). The maximum bending moment values for these load cases plus *SW* were then compared with the relevant results from the combination of *SW* and the *UDL* of 20 kN/m applied across the full span of the arches (Figure 3.6). Figures 3.4 to 3.6 demonstrate these load patterns diagrammatically. The short vectors for applied load displayed in each figure are referred to the *SW* of 7.2 kN/m and the longer vectors are for load of *SW* plus *UDL*. The studied arches are analysed for *L:h* ratios between 2 and 10. The maximum bending moment results from this analysis are presented in Table 1.

Figure 3.4. *FE*: The load pattern of 20 kN/m *UDL* applied across the half span of the arch plus *SW*

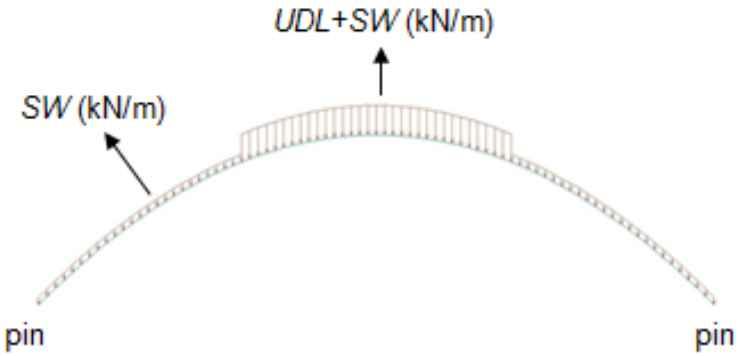

Figure 3.5. *FE*: The load pattern of 20 kN/m *UDL* applied across the central 40% of the arch plus *SW*

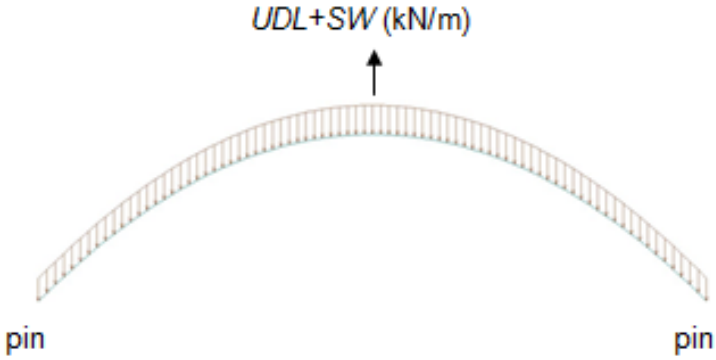

Figure 3.6. *FE*: The load pattern of 20 kN/m *UDL* applied across the full span of the arch plus *SW*

Table 3.1. The value of maximum bending moment (kNm) caused by *SW* plus differently positioned *UDL* of 20 kN/m applied on different arch shapes

L:h	Parabolic arch with *UDL*:			Catenary arch with *UDL*:			Circular arch with *UDL*:		
	Full span	Centre span	Half span	Full span	Centre span	Half span	Full span	Centre span	Half span
2	3.55	12.79	32.99	8.96	22.1	32.81	50.24	51.12	51.74
3	2.11	13.73	32.33	4.97	18.37	32.05	26.01	30.51	38.89
4	1.57	14.13	32.17	3.52	16.87	31.55	14.20	23.36	35.00
5	1.44	14.47	32.20	3.03	16.27	31.47	8.71	20.29	33.26
6	1.60	14.84	32.34	3.03	16.10	31.82	6.71	18.84	33.21
7	2.08	15.27	32.57	3.32	16.20	32.18	5.98	18.18	31.57
8	2.85	15.76	32.86	3.81	16.47	32.56	5.82	17.96	32.05
9	3.69	16.30	33.22	4.45	16.87	32.98	6.02	18.03	32.55
10	4.61	16.91	33.62	5.22	17.37	33.42	6.48	18.30	33.06

It can be seen in Table 3.1 that in most cases, loading across the half span of the arch generates the highest bending moment, which is presumed as the worst case for bending moments. As a result, a variable load or 'patch load' is applied across the half span of the arches as a critical load condition. The relevant studied load pattern is shown diagrammatically in Figure 3.7.

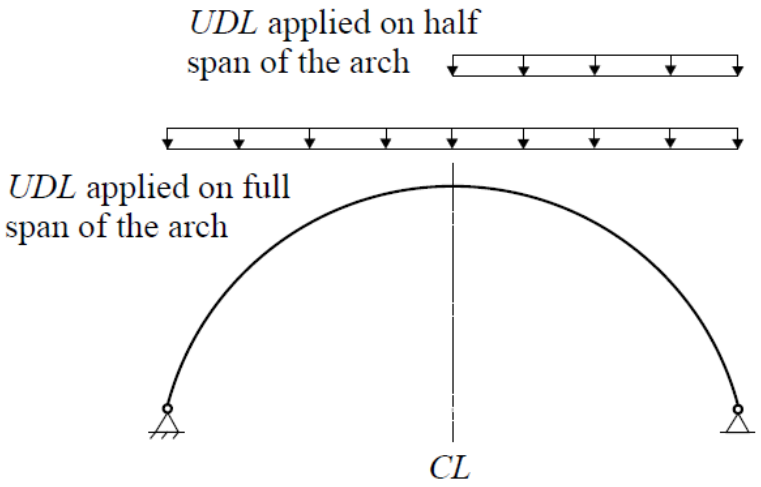

Figure 3.7. Visual representation of load patterns

3.3.3. Assessment of arch stability over considered *L:h* ratios

As stated earlier, the known shapes of arches are analysed for *L:h* ratios ranging from 2 to 10. This range of *L:h* ratio is chosen based on the common range of *L:h* ratios in which arch bridges have been built using concrete and masonry material (Salonga and Gauvreau 2010). The geometries of parabolic, catenary and circular arches with *L:h* ratios of 2, 3, 5, 7 and 10 are shown in Figure 3.8. The geometrical differences of each arch form are significant when the *L:h* ratio is varied from 2 to 5. As shown, the geometrical differences of each form then become almost indistinguishable above the *L:h* ratio of 7. The maximum percentage difference between the *y* coordinates of the catenary and parabolic arches for the same span is 14% when *L:h*=2 . It reduces to 2% for an *L:h* ratio equal to 7.

Being more precise in detail, there are still some differences in the geometry of the three arch shapes for *L:h* ratios less than 10. At this ratio, parabolic and catenary arches have practically the same geometry. The maximum percentage difference between the *y* coordinates for the same *x* coordinate of each pair of arch geometries is presented in Table 3.2. This table shows that the *y* coordinates of the parabolic and circular forms display the maximum difference.

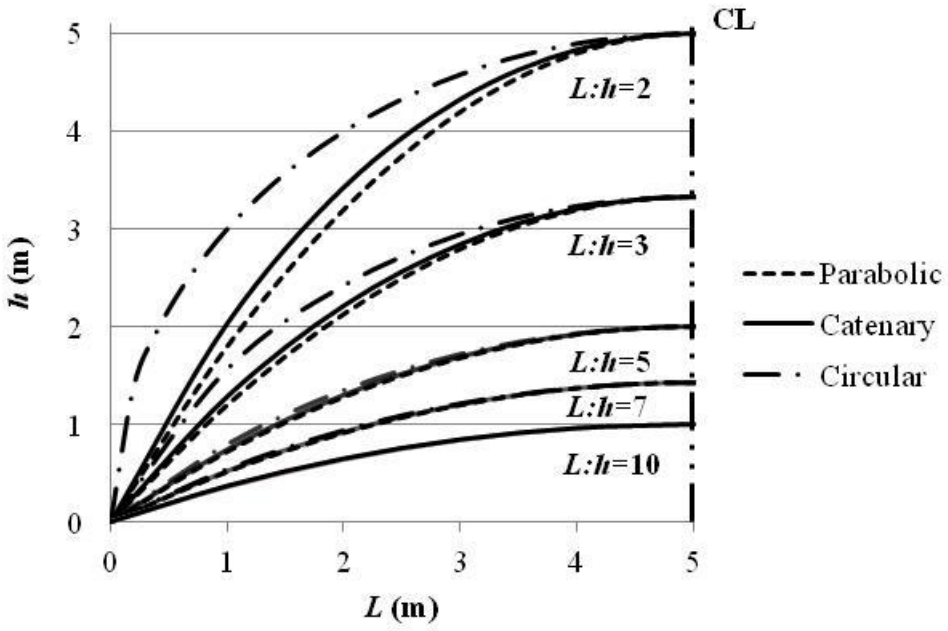

Figure 3.8. Geometric differences between arches for *L:h* ratios of 2, 3, 5, 7 and 10

Table 3.2. Maximum percentage difference between the *y* coordinates of each pair of arch shapes

L:h	Parabolic and catenary	Parabolic and circular	Catenary and circular
2	14.3%	56.4%	49.2%
3	8.4%	32.0%	25.8%
4	5.4%	19.1%	14.5%
5	3.7%	12.5%	9.1%
6	2.7%	8.8%	6.3%
7	2.0%	6.5%	4.6%
8	1.6%	5.0%	3.5%
9	1.3%	3.9%	2.7%
10	1.0%	3.2%	2.2%

Decreasing the height of the arches increases the axial deformations and bending moments in them. By increasing the external load applied to shallow arches, the in-plane structural actions such as axial forces and bending moments develop into nonlinear mode. This means that the in-plane behaviour of arches can turn into either an asymmetric bifurcation or a symmetric snap-through buckling mode (Bradford et al. 2007). To obtain the critical value of the intensity of loading (w_{cr}) that causes this buckling, the following Timoshenko stability equation for arches can be used (Timoshenko and Gere 1961).

$$w_{cr} = \gamma_2 \frac{EI}{L^3} \tag{3.9}$$

In the Equ. (3.9), *E* and *I* are: the modulus of elasticity and the second moment of area, respectively. The numerical factor γ_2 defined by Timoshenko and Gere for each *L:h* ratio. The results of the w_{cr} for the parabolic arch under load case *A4* are presented in Table 3.3.

Table 3.3. The critical values of the intensity of the load for the parabolic arch under *UDL* only applied across the span of the arch (Timoshenko and Gere 1961)

L:h	γ_2	w_{cr}(kN/m)	w_{cr}:*UDL*
2	38.4	2330	117
2.5	43.9	2670	133
3.33	46.5	2820	141
5	45.4	2760	138
10	28.5	1730	86

The *UDL* of 20 kN/m that is the applied load across the full span of the arch can be compared with w_{cr} for the parabolic arch in Table 3.3. As shown above, even for an *L:h* ratio of 10 the critical load is 86 times greater than the applied *UDL*. The same can be concluded for other arch forms in this study for the *UDL* only load case. This analysis can be conducted when the general combination of *UDL* and *SW* (load

case *A1*) is applied to the arches in the case of a shallow arch. The arch cross-sectional dimension and material density are given previously in Subsection 3.3.1. Since for flat arches *UDL* and *SW* are adopted, the imposed load can be presumed as the sum of *UDL*+*SW*, which is equal to 27.2 kN/m in this study. Therefore, for flat arches which Timoshenko and Genre (1961) noted as flat parabolic when *L:h*>5, the loading is still significantly smaller than the critical buckling load. It is concluded that arches are stable for the range of *L:h* ratios between 2 and 10 in this study.

3.4. Assessment criterion

There are many parameters that need to be considered when designing a structure. The most efficient structural form for a masonry arch is the one that shows the lowest bending moment and combined stress due to bending and thrust.

As bending moments have a direct effect on deflections, shear forces, and combined bending moment stresses plus compressive stress, reducing the bending moment is likely to produce a more efficient structure. Furthermore, wherever bending moment alone or the combination of bending moment and axial force is present, there is varying stress over the cross-section. If the stress distribution consists of a tensile region, depending on the material and its application, reinforcement is required. As concrete or masonry material is the centre of attention of this research, it is important to highlight the advantages and disadvantages of the properties of them. The benefits of using concrete and masonry materials include their flexibility, durability, and high compressive strength, all of which explain their extensive use in construction and civil engineering structures. Besides, they can amplify the thermal mass of a structure and have a high resistance to fire. Masonry or concrete is a non-linear material owing to its weakness in tension. However, it is relatively strong in compression. Due to the lack of tensile strength of masonry material, minimizing the bending moment also minimizes the internal tensile forces.

On the other hand, the fact that arch shapes are a pure compression form is in accordance with using concrete/masonry material to construct arch structures.

The criterion of minimum combined stress is used to evaluate the structural performance of arch forms.

3.5. Methodology

The methodology concentrates on the influence of arch shape and the span-to-height ratio on the resulting effect of structural action. It focuses on the form of the arch that presents the lowest combined stress – a criterion used to assess whether the structure is optimal.

To analyse the three most common forms of arches, the computational finite element method provided by the *GSA* software is used. This computational method is based on the Approximate Minimum Degree algorithm for the static analysis of two- and three-dimensional structures. For linear analysis, the stiffness matrix method in *GSA* is used. The static analysis of two-pin arches gives the displacement {**u**} as a solution of the linear system of (3.10).

$$\{u\} = [K]^{-1}\{f\} \tag{3.10}$$

in which [**K**] is the stiffness matrix of the arch, and {**f**} is the load or force vector derived from the applied load. To find the forces, Timoshenko's beam theory is used, which means that the bending moment in the specific direction is based on the stress in that direction.

The curved structures were modelled by a series of straight elements. In order to find a suitable number of elements to model the arch curves, a sensitivity analysis was carried out using variation of bending moments in an arch subjected to load case *A1*, as a function of the number of elements used. The circular arch was

modelled with between 10 and 110 elements. As shown in Figure 3.9, the change in the value of the bending moment at *L:h* ratio of 80 and 90 at the crown of the circular arch is less than 0.1% which is negligible difference. Hence, 81 nodes are found to be adequate to represent a given arch shape.

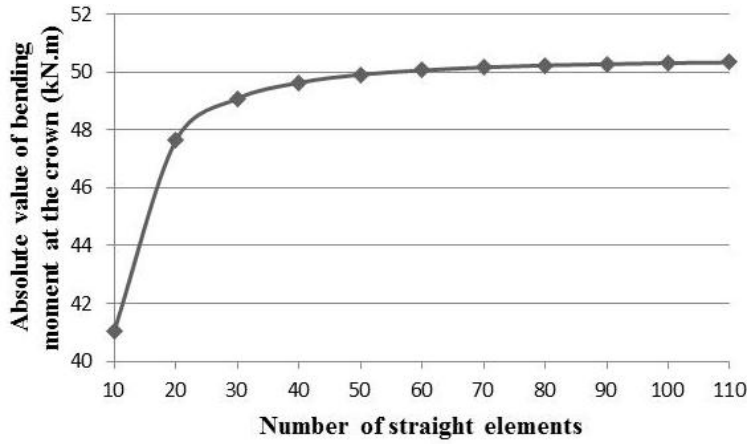

Figure 3.9. *FE*: Sensitivity analysis on circular arch with *L:h* of 2

To compare the different arch forms, as well as the influence of the *L:h* ratio on the structural action effects, the bending moments, combined stresses, compressive forces, displacements, shear forces, horizontal reaction forces, and arch mass are studied and presented in subsections 3.5.1 to 3.5.7.

To validate the results from *GSA*, all analyses in this chapter was carried out using *SAP2000* software. Consequently, the same results were obtained compared to *GSA* software.

3.5.1. Bending moments

Low bending moments lead to smaller variations in stress distribution, deflection and shear forces. Thus, the arch shape and *L:h* ratio at which the bending moment is minimum is assumed as an analysis benchmark in this subsection.

Variations of the maximum sagging and hogging bending moments with *L:h* ratios and their location for load case *A1* are presented in Tables 3.4 and 3.5 respectively.

The section dimensions and material properties were given in subsection 3.3.1 with constant arch span of 10 m. The ratio of *UDL:SW* for each arch shape and the *L:h* ratio are also given in Table 3.4. Concerning load case *A1*, due to the symmetry of the geometry and loading, the locations of the maximum bending moments and maximum combined stresses are presented for half of the span in the relevant tables.

In general, the circular arch presents the minimum *UDL:SW* due to its greater weight than the catenary and parabolic arches for the same *L:h* ratio and *UDL.*

Table 3.4. Maximum sagging bending moments (kNm), their locations along the span (m) and *UDL:SW* of the parabolic, catenary, and circular arches, load case *A1*

L:h	Maximum bending moment, (location), *UDL:SW*		
	Parabolic	Catenary	Circular
2	3.55, (1.3), 1.878	8.96, (5), 1.857	50.24, (5), 1.768
3	2.11, (1.4), 2.231	4.97, (5), 2.219	21.44, (5), 2.180
4	1.57, (1.56), 2.420	3.52, (5), 2.414	12.27, (5), 2.396
5	1.44, (1.8), 2.529	3.03, (5), 2.526	8.45, (5), 2.517
6	1.60, (2.4), 2.597	3.03, (5), 2.595	6.71, (5), 2.590
7	2.08, (3.8), 2.640	3.32, (5), 2.639	5.98, (5), 2.637
8	2.85, (5), 2.670	3.81, (5), 2.670	5.82, (5), 2.668
9	3.69, (5), 2.692	4.45, (5), 2.691	6.02, (5), 2.690
10	4.61, (5), 2.707	5.22, (5), 2.707	6.48, (5), 2.706

The parabolic arch shows the maximum *UDL:SW* amongst the three arch shapes. Comparing the maximum bending moments of the three arches in Table 3.4, the one with the lower weight (higher *UDL:SW*) behaves in a more efficient way. The maximum sagging bending moment of the parabolic and catenary arches decreases with the increase of *L:h* from 2 to 5. The trend of decreasing bending moments is then reversed above this ratio. In the case of the circular arch, the minimum sagging bending moment of 5.82 kNm is observed at *L:h*=8.

Table 3.5. Maximum hogging bending moments (kNm) and their locations along the span (m) of the parabolic, catenary, and circular arches, load case *A1*

L:h	Maximum bending moment, (location)		
	Parabolic	Catenary	Circular
2	3.52, (5)	8.11, (1.25)	60.96, (0.37)
3	1.31, (5)	4.64, (1.25)	26.01, (0.87)
4	0.22, (5)	2.78, (1.25)	14.20, (1.12)
5	NA	1.64, (1.12)	8.71, (1.12)
6	NA	0.88, (0.87)	5.67, (0.87)
7	NA	0.37, (0.62)	3.74, (0.87)
8	NA	0.07, (0.12)	2.40, (0.75)
9	NA	NA	1.43, (0.8)
10	NA	NA	0.72, (0.62)

- NA indicates that there is no hogging bending moment.

Comparing the results in Tables 3.4 and 3.5, the maximum sagging and hogging bending moments of the catenary and circular arches occurred at approximately the same location, contrary to the location of the maximum sagging and hogging bending moments of the parabolic arch. Compared to the hogging bending moment, the sagging bending moment is dominant for any *L:h* ratio for parabolic and catenary arches. The hogging bending moments of circular arches are higher when *L:h*<6. This shows that the tensile forces in circular arches are higher than compression for *L:h*<6 when the loading is the general combination of *UDL* and *SW*. It is interesting to compare the bending moments of circular arches with the other two forms for high *L:h* ratios. The differences in geometry of the three arch shapes are indistinguishable for *L:h* above 7 (see Figure 3.8). However, there are still differences in the bending moment result. The differences in bending moment distribution for the three arches with load case *A1* and *L:h* ratios of 2, 4, and 6 are illustrated in Figure 3.10.

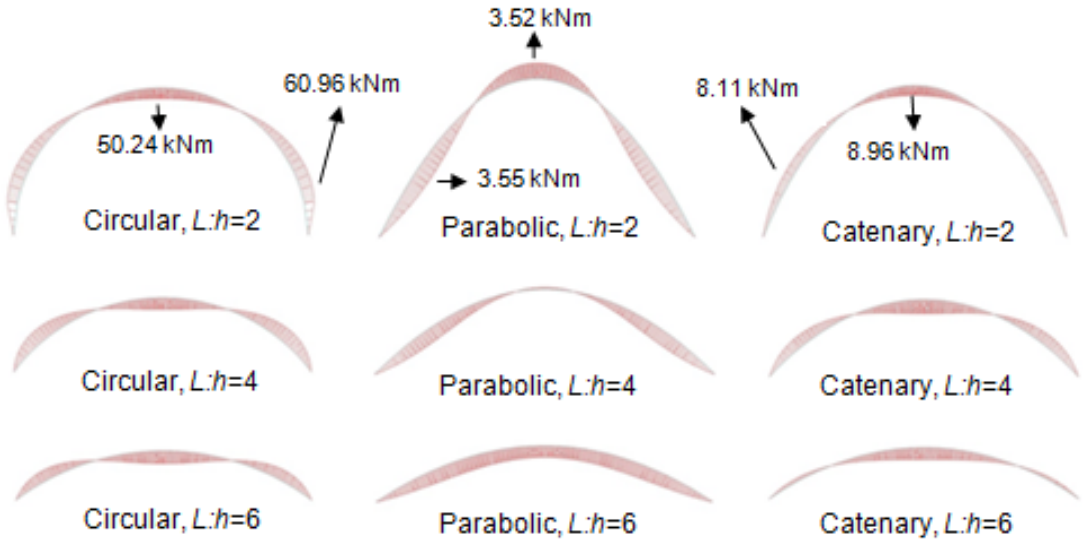

Figure 3.10. *FE*: Bending moments of three arches for *L:h* ratios of 2, 4 and 6 and load case *A1*

The overall change in the maximum bending moment for the three arches is shown in Figure 3.11. The *L:h* ratio for which the absolute value of the maximum bending moment reaches its minimum is considered in this subsection as the optimum *L:h* ratio to compare different shapes of arches. To illustrate the optimum range of the *L:h* ratio, diagrams of the maximum bending moment of each curve are given on the right hand side of Figure 3.11.

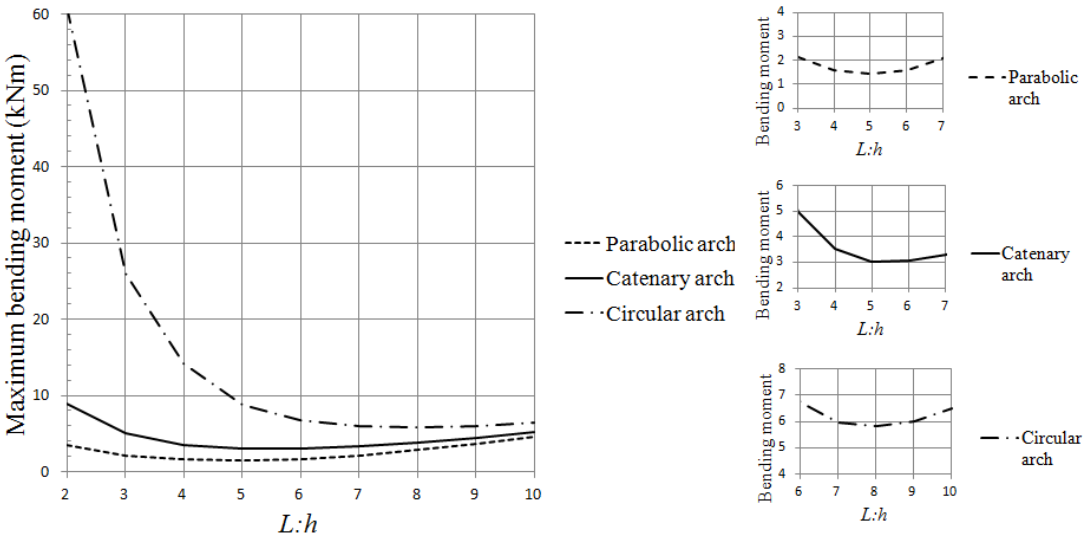

Figure 3.11. *FE*: The absolute value of maximum bending moment against *L:h* ratio for load case *A1*

The bending moment performance of the three arches is then investigated for load case *A2* (patch loading), which this load pattern was shown in Figure 3.7. The maximum sagging and hogging bending moments and their locations within the arches are reported in Tables 3.6 and 3.7.

Table 3.6. Maximum sagging bending moments (kNm) and their locations along the span (m) of the parabolic, catenary, and circular arches for load case *A2*

L:h	Maximum bending moment, (location)		
	Parabolic	Catenary	Circular
2	33.12, (7.81)	32.81, (6.69)	79.33, (5.94)
3	32.59, (7.69)	30.80, (7.06)	43.80, (6.28)
4	32.63, (7.69)	30.98, (7.31)	34.70, (6.56)
5	32.89, (7.69)	31.61, (7.31)	32.30, (6.81)
6	33.33, (7.56)	32.36, (7.44)	32.02, (6.96)
7	33.91, (7.56)	33.17, (7.44)	32.53, (7.06)
8	34.61, (7.56)	34.03, (7.44)	33.37, (7.19)
9	35.41, (7.56)	34.95, (7.44)	34.33, (7.31)
10	36.32, (7.56)	35.96, (7.44)	35.42, (7.31)

Table 3.7. Maximum hogging bending moments (kNm) and their locations along the span (m) of the parabolic, catenary, and circular arches for load case *A2*

L:h	Maximum bending moment		
	Parabolic	Catenary	Circular
2	30.15, (2.75)	38.27, (1.75)	95.30, (0.75)
3	30.13, (2.63)	34.73, (2)	56.37, (1.25)
4	29.97, (2.63)	32.85, (2.13)	43.55, (1.5)
5	29.67, (2.5)	31.63, (2.25)	37.84, (1.88)
6	29.23, (2.5)	30.64, (2.25)	34.66, (2)
7	28.66, (2.5)	29.73, (2.38)	32.59, (2.13)
8	27.98, (2.38)	28.85, (2.38)	30.99, (2.25)
9	27.23, (2.38)	27.92, (2.38)	29.62, (2.25)
10	26.38, (2.38)	26.96, (2.38)	28.34, (2.25)

Comparing the numerical predictions in Tables 3.6 and 3.7 the sagging bending moments for the parabolic arch are higher than hogging for any *L:h* ratio. However, the catenary and circular arches present higher hogging bending moments than

sagging ones when the *L:h* ratio is less than 6 and 8, respectively. Concerning the results for the maximum bending moment, the parabolic arch is preferred. The circular shape is the less desirable form for masonry and concrete arches.

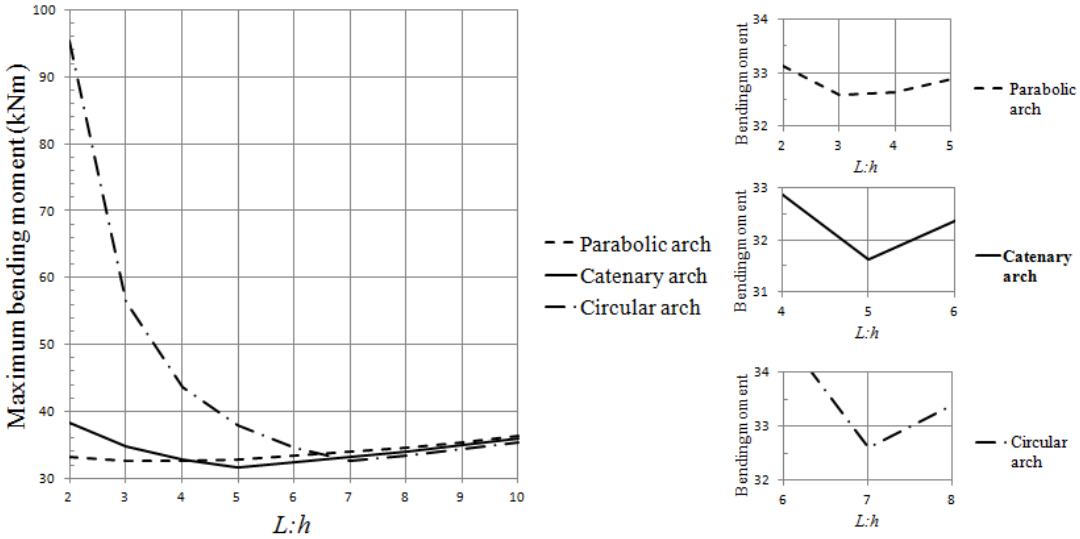

Figure 3.12. *FE*: The absolute value of maximum bending moment against *L:h* for load case *A2*

The absolute maximum bending moment values of the three arches under load case *A2* are shown in Figure 3.12.

In theory, catenary and parabolic arches can be assumed to be momentless for *SW* only, and *UDL* only, respectively (Megson 2006; Millais 2005). This is true only when ignoring the arch shortening/deformation in statical calculations. The *FE* modelling, based on a deformable arch model, where the 2nd order effects are included, produced results that show the catenary arch developing some moments for *SW* only load condition, which increase with the *L:h* ratio (Figure 3.13). A similar observation can be made with respect to load case *A4* and the parabolic arch (Figure 3.14), which also develops small bending moments. In both of these cases, if a non-deformable model were used, the bending moments would be equal to zero.

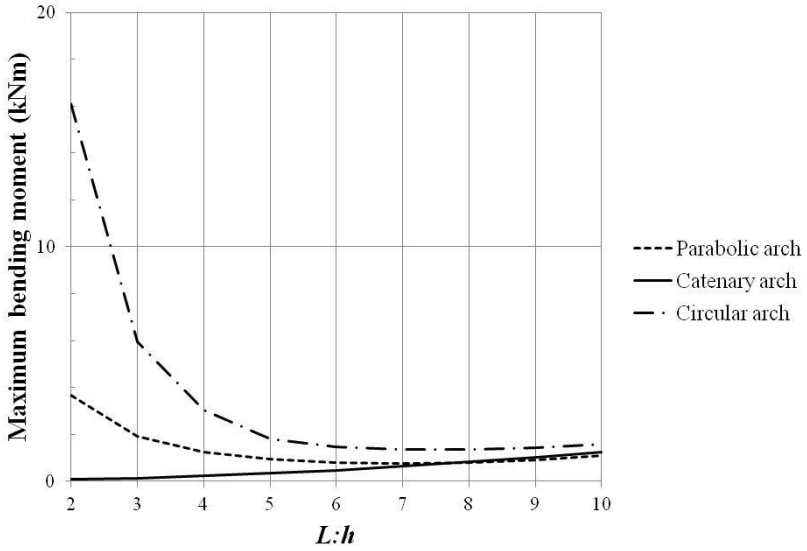

Figure 3.13. *FE*: The absolute value of maximum bending moment against *L:h* ratio for load case *A3* (*SW* only)

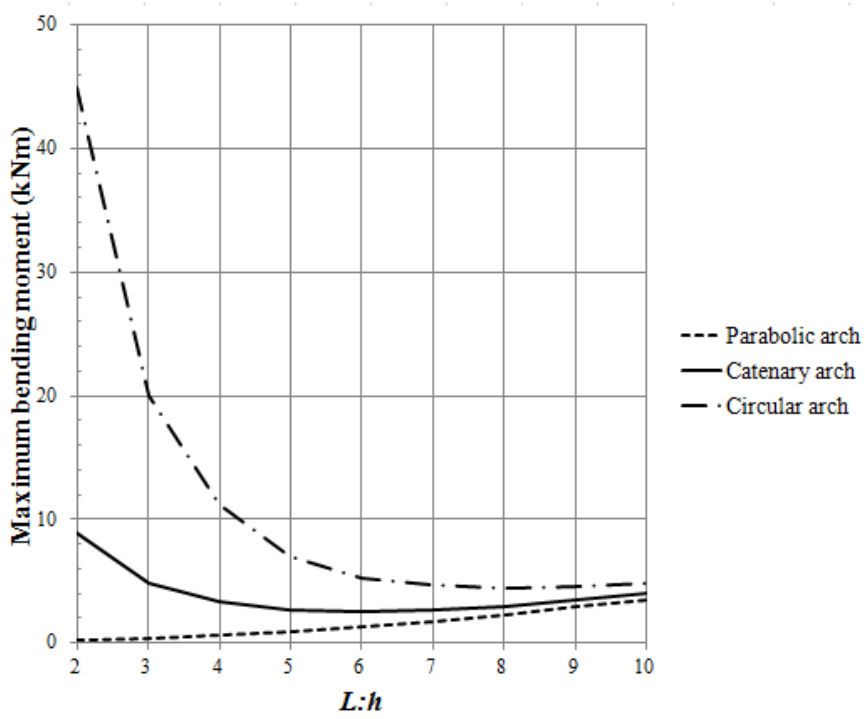

Figure 3.14. *FE*: The absolute value of maximum bending moment against *L:h* ratio for load case *A4* (*UDL* only)

The three curves in Figure 3.8 confirm that the geometries of the three arches converge above *L:h* ratios of 7. However, the maximum bending moment of the circular shape is approximately 50% more than the parabola and catenary curves

for load cases *A1*, *A3* and *A4* at this ratio. As a result, small changes in form may have a significant influence on the action effects. As expected, the maximum bending moment for load case *A2* is approximately twice that of load case *A1*. Generally, the maximum bending moment of a circular arch decreases when *L:h* increases to approximately 8 for all load cases. Beyond this ratio, the maximum bending moment trend is reversed to increasing, even though this increase is small, until the *L:h* ratio of 10. Therefore, the optimum *L:h* ratio of a circular arch appears to be between 7 and 8 concerning maximum bending moment. The same behaviour is observed for parabolic and catenary arches; however, the maximum bending moment starts to increase at *L:h* ratios between 4 and 5. Taking into account all the load cases, parabolic arches generally show a lower bending moment than catenary and circular arches.

For every high *L:h* ratio, an arch becomes a beam. Figure 3.15 illustrates the trend of maximum bending moments beyond the *L:h* ratio of 10. The results of maximum bending moments are obtained from analysing the circular arch under different load cases due to the similar structural actions of parabolic, catenary and circular arches in this range of *L:h* ratio. The maximum bending moments of the equivalent beam with the specification of these arches are 338.8, 463.3, 88.26 and 250 kNm for load cases *A1, A2, A3* and *A4* respectively. Figure 3.15 indicates that the maximum bending moments for each load case at *L:h* ratio of 300 are close to the ones calculated for the beam. The *FE* results showed that the maximum bending moments in the three arches at *L:h*=10 were found to be mostly less than 10% of the maximum bending moment of the equivalent beam (when the *L:h* ratio was taken as 300). The latter applies to all load cases.

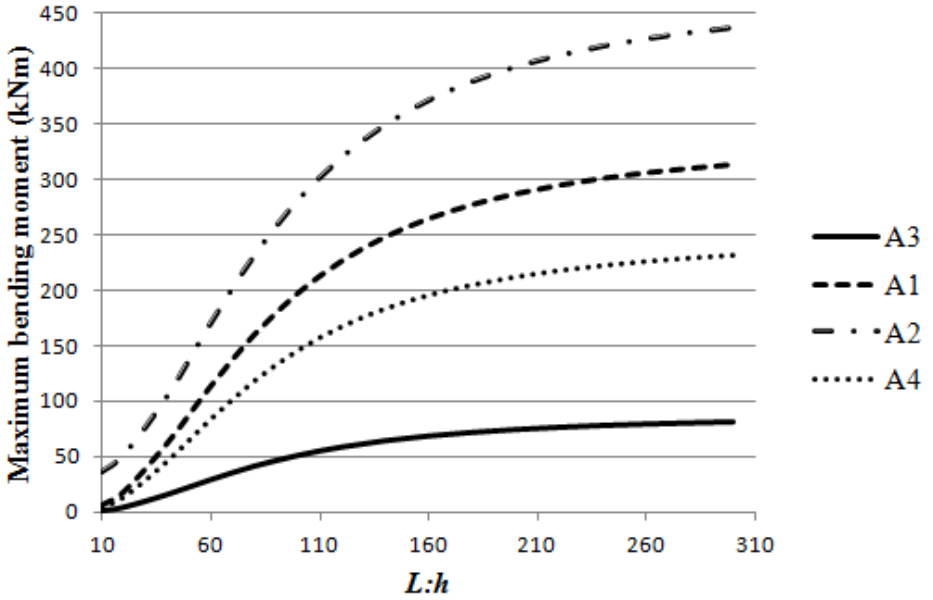

Figure 3.15. *FE*: The value of maximum bending moments against *L:h* ratio between 10 and 300 for all load cases

3.5.2. Combined stresses

As stated previously, the *L:h* ratio at which the combined stress due to bending and compressive axial force reaches its minimum is considered as optimal in this study. The results of the maximum combined stress against the *L:h* ratio and their location within the arch for the three arch shapes and load cases *A1* and *A2* are reported respectively in Tables 3.8 and 3.9. Since the compressive combined stresses are higher than tensile ones, the maximum combined stresses presented in these tables are compression.

Comparing the results in Tables 3.4 and 3.5 with the results of combined stresses for load case *A1* from Table 3.8, the values of both the maximum bending moment and maximum combined stress do not occur at the same *L:h* ratio for each arch shape. From Tables 3.8 and 3.9 the results for the maximum combined stress with the circular arch differ significantly from the results for the parabola and catenary shapes, particularly for *L:h* ratios below 5. The circular arch shows high sensitivity to

changes in the span-to-height ratio and the maximum combined stress reaches a minimum value at *L:h* ratios between 4 and 6.

Table 3.8. Maximum combined stresses (MPa) and their locations along the span (m) of the parabolic, catenary, and circular arches for load case *A1*

L:h	Maximum combined stress, (location)		
	Parabolic	Catenary	Circular
2	0.69, (1)	0.99, (1)	4.54, (0.5)
3	0.65, (1)	0.82, (1)	2.24, (1)
4	0.69, (1)	0.77, (1)	1.52, (1)
5	0.76, (1)	0.79, (1)	1.25, (1)
6	0.85, (1)	0.88, (4.75)	1.14, (1)
7	0.96, (1.5)	1.01, (4.75)	1.18, (4.75)
8	1.09, (3)	1.15, (4.75)	1.28, (4.75)
9	1.25, (5)	1.30, (4.75)	1.40, (4.75)
10	1.42, (5)	1.46, (4.75)	1.54, (4.75)

Table 3.9. Maximum combined stresses (MPa) and their locations along the span (m) of the parabolic, catenary, and circular arches for load case *A2*

L:h	Maximum combined stress, (location)		
	Parabolic	Catenary	Circular
2	2.70, (7.75)	3.05, (2)	6.92, (0.5)
3	2.76, (7.75)	2.91, (2)	4.38, (1)
4	2.88, (7.75)	2.90, (2)	3.63, (1.5)
5	3.03, (7.75)	2.95, (2)	3.37, (2)
6	3.20, (7.75)	3.12, (7.25)	3.30, (2)
7	3.38, (7.75)	3.32, (7.25)	3.30, (2)
8	3.57, (7.25)	3.53, (7.25)	3.47, (7.25)
9	3.77, (7.25)	3.73, (7.25)	3.68, (7.25)
10	3.98, (7.25)	3.95, (7.25)	3.90, (7.25)

The minimum combined stresses of parabolic and catenary arches are observed at *L:h* ratios between 2 and 4 when both *UDL* and *SW* are applied. In general, the parabolic arch shows a lower bending moment and combined stress than the catenary and circular arches. Parabolic arches experience a dramatic increase in

combined stress for load case *A2* (load case *A1* + patch load). Here, their performance does not differ much from that of the other two types of arches.

The arches are made of concrete, a material known to have low tensile strength. Therefore, it is worth examining whether the maximum combined stresses become tensile. The results are presented in Table 3.10. Assuming the maximum tensile strength of concrete to be 3 MPa (for concrete of characteristic strength of ~ 30 MPa), the results demonstrate that the tensile stresses in all the arches are lower than the maximum tensile strength of the material, except for the case of a circular arch under load cases *A1* and *A2* and the *L:h* ratio of 2. This has implications for both the design and the method of analysis, because we cannot assume that the material is behaving elastically at this level of tension. However, these are isolated load cases, which can be dealt with by using a higher *L:h* ratio in the design.

Table 3.10. Combined tensile stresses (MPa) of parabolic, catenary, and circular arches for all load cases

L:h	Parabolic arch				Catenary arch				Circular arch			
	A1	A2	A3	A4	A1	A2	A3	A4	A1	A2	A3	A4
2	NA	1.73	0.17	NA	0.36	2.06	NA	0.43	3.59	5.78	0.92	2.67
3	NA	1.60	0.01	NA	NA	1.73	NA	0.08	1.23	3.14	0.25	0.98
4	NA	1.48	NA	NA	NA	1.48	NA	NA	0.38	2.18	0.05	0.33
5	NA	1.36	NA	NA	NA	1.29	NA	NA	0.01	1.67	NA	0.04
6	NA	1.25	NA	NA	NA	1.19	NA	NA	NA	1.33	NA	NA
7	NA	1.14	NA	NA	NA	1.10	NA	NA	NA	1.08	NA	NA
8	NA	1.04	NA	NA	NA	1.01	NA	NA	NA	0.98	NA	NA
9	NA	0.95	NA	NA	NA	0.93	NA	NA	NA	0.90	NA	NA
10	NA	0.87	NA	NA	NA	0.85	NA	NA	NA	0.82	NA	NA

- NA indicates that there is no tensile stress.

3.5.3. Compressive force (thrust)

As an arch is a pure compression form of structure, its axial force is referred to the compressive force of arches. It is demonstrated that the differences of maximum

axial force (thrust) for the three studied arches are smaller than 5% with a higher thrust for parabolic arch than two other shapes. Furthermore, the maximum thrust of arches has an almost linear relationship with the *L:h* ratios. The maximum values of thrust for these load cases are also presented in Table 3.11. The location of the maximum value of thrust for all load cases is at the arch supports.

Table 3.11. Maximum thrust (kN) for parabolic, catenary, and circular arches

L:h	Load case *A1*			Load case *A2*		
	Parabolic	Catenary	Circular	Parabolic	Catenary	Circular
2	168.8	168	161.2	247	246.5	238.1
3	178.3	177.3	172.3	260.7	260	255.1
4	197	196	192.8	285.2	284.4	281.5
5	220.3	219.3	216.9	315.6	314.8	312.5
6	246.2	245.4	243.4	349.8	348.9	347
7	273.8	273.1	271.4	386.3	385.5	383.8
8	302.5	301.8	300.3	424.5	423.8	422.1
9	331.8	331.2	329.9	463.8	463.1	461.6
10	361.5	360.9	359.8	503.7	503	501.6

3.5.4. Displacements and deflections

The movement of a structure or its components from their original position is always important for a designer. If the deflection of a structure is excessive under a certain loading, cracking can occur. Consequently, it is important for a designer to determine the displacement and strains caused by the loads. The bending action caused by different loads is the primary reason generating the arch displacement. However, for a beam with a high cross-sectional area compared to span, shear forces are to be considered when calculating the deformation.

The ratio of the resultant maximum displacement to arch span (*u:L*) for the three types of arches is presented in Figures 3.16 and 3.17 for load cases *A1* and *A2*, respectively. The arch has a constant 10 m span and the resultant displacement (mm) is the sum of vertical and horizontal components. As expected, the catenary

and parabolic arches display lower resultant displacements when the loading is *SW* only (*A3*), and *UDL* only (*A4*), respectively.

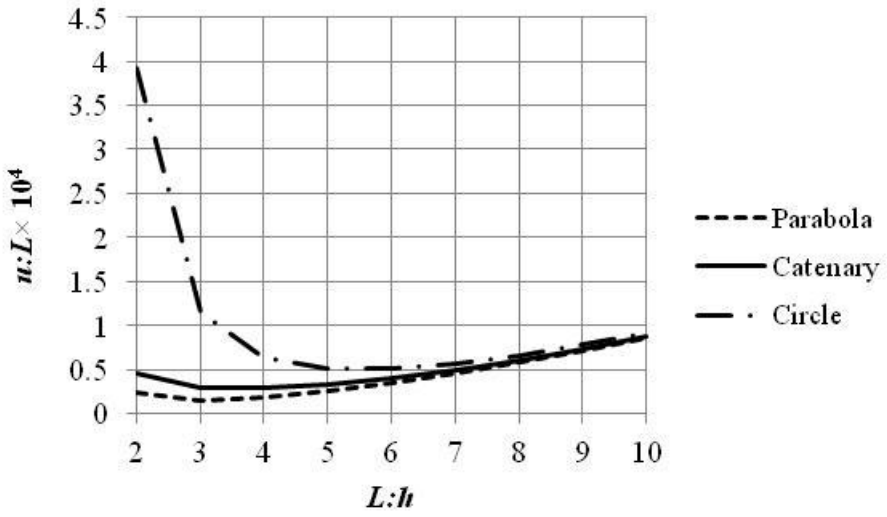

Figure 3.16. *FE*: Maximum resultant displacements against *L:h* ratio, load case *A1*

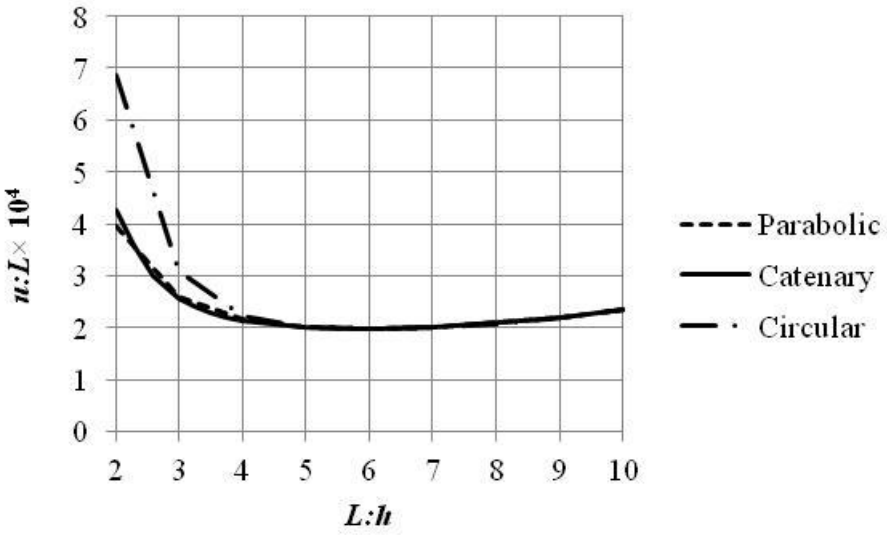

Figure 3.17. *FE*: Maximum resultant displacements against *L:h* ratio, load case *A2*

It can be seen that the variation of *u:L* ratio with *L:h* ratio follows a similar trend for load cases *A1* and *A2*. It has been found that the trend for load cases *A3* and *A4* is similar.

The circular form, when *L:h* ratio is between 2 and 5, shows the highest maximum resultant displacements compared with the other two forms. For parabolic and catenary arches under the load case *A1*, the difference in displacement between the two falls from 50% at the *L:h* ratio of 2, to 21% at the *L:h* ratio of 5. In general, the parabolic arch shows a lower displacement than the catenary and circular forms. The differences between the resultant displacements of the parabolic and catenary arches are negligible for load case *A2.*

The deformed shapes of circular, parabolic, and catenary arches for load case *A1* and *L:h* ratios of 2, 4 ,and 6 are illustrated with thick line in Figure 3.18.

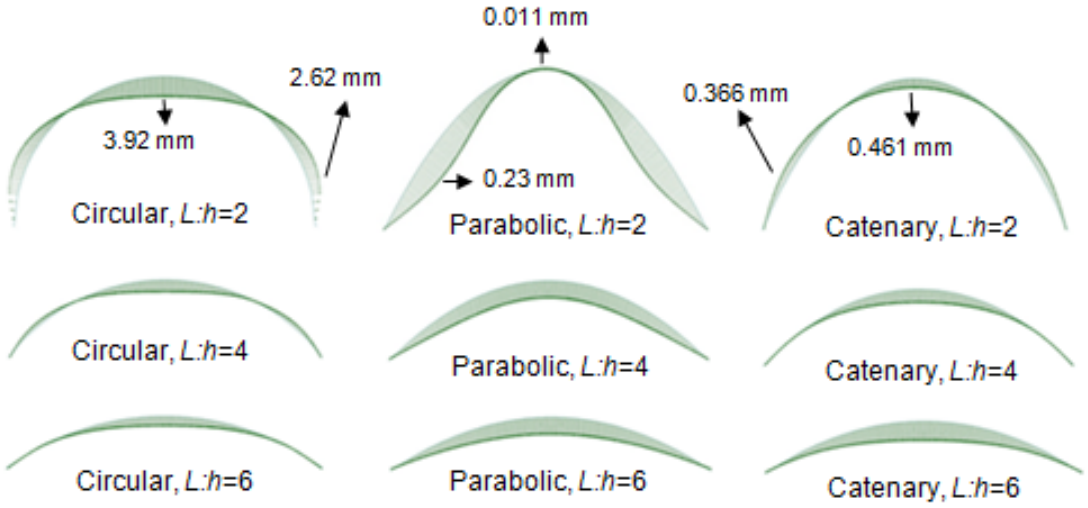

Figure 3.18. *FE*: Deformed shapes of circular, parabolic, and catenary arches for load case *A1* and *L:h* of 2, 4, and 6

The catenary and circular arches deform in the same way with the sides deforming outwards, but differ significantly from the parabolic arch (see Figure 3.18). This indicates that the failure mode of the parabolic arch can be expected to be completely different from the failure mode of the other two arches depending on arch material. Comparing Figures 3.10 and 3.18, the distribution of the bending moment is similar to the displaced form for each arch shape.

The parabolic arch deforms in the same way for all load cases *A1*, *A3*, and *A4*. However, the magnitudes of displacement are different. With regard to load case *A2* (presence of patch load), the arch displaces much more, and in a different shape from that of the other load cases. All three types of arches show a similar deformed shape under this load case. At the *L:h* ratio of 4 the differences in the displaced shapes of the arches are small but still significant, and this ratio has therefore been chosen to show the deformation of the parabolic arch. The deformed shape of the parabolic arch under load case *A2* for *L:h*=4 is shown in Figure 3.19.

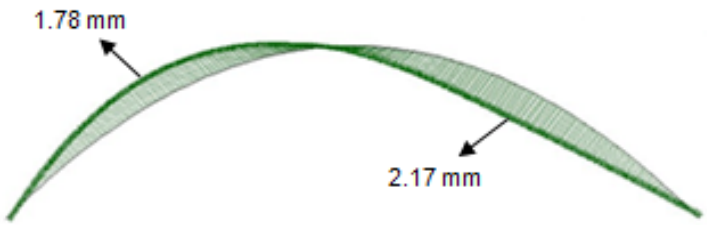

Figure 3.19. *FE*: Deformed shape of parabolic arch for load case *A2* and *L:h* = 4

3.5.5. Shear forces

The absolute value of the maximum shear force against the *L:h* ratio for load cases *A1* and *A2* is presented in Figure 3.20.

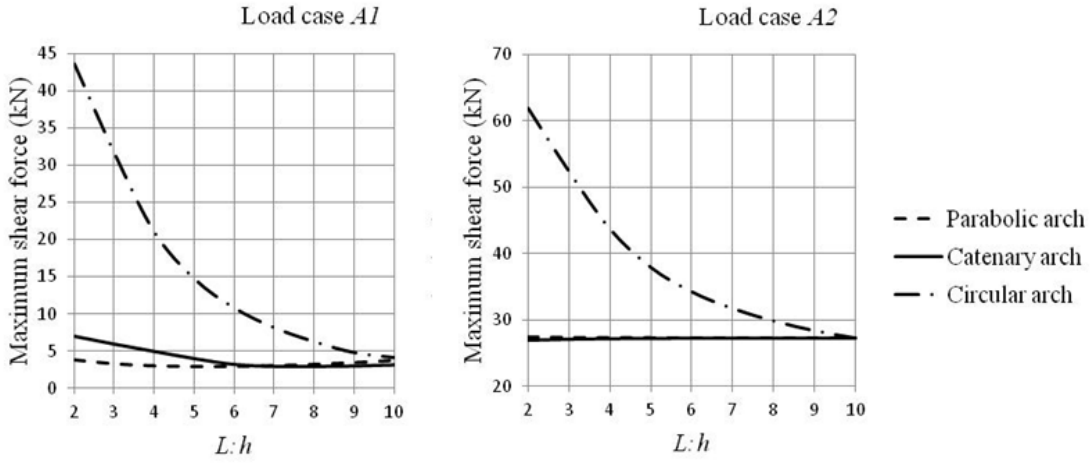

Figure 3.20. *FE*: Absolute value of maximum shear force against *L:h* ratio for load cases *A1* and *A2*

Concerning shear forces, circular arches exhibit a high sensitivity to changes in the *L:h* ratio, where the percentage differences between *L:h* ratios of 2 and 4 are about 52% for load case *A1* and 29% in load case *A2*. The catenary and parabolic arches show a very similar behaviour for the absolute value of the maximum shear forces. The parabolic arch shows a lower shear force than the catenary arch in the case of the general combination of *UDL* and *SW* (load case *A1*). In the presence of patch loading (load case *A2*), the parabolic and catenary forms have just 2% difference at *L:h* ratio of 2 and this difference falls to <1% for *L:h*= 4. Beyond the *L:h* ratio of 4, the maximum shear forces of the catenary and parabolic arches converge towards each other. The trends of shear forces for load cases *A3* and *A4* are similar to load case *A1*. However, the shear forces of the catenary and parabolic arches are negligible for load cases *A3* and *A4* respectively. The trend of the absolute value of shear force is analogous to the trend of the absolute values of maximum bending moment for all load cases. This conclusion is associated with the close relationship between bending moments, shear forces, and deflections.

3.5.6. Horizontal reaction force

Figure 3.21 illustrates the horizontal reaction forces in all three types of arches for load case *A1.* The results show a linear dependence on the *L:h* ratio and slight differences in the reactions for *L:h* ratios below 5. Above this ratio, the horizontal reaction forces are similar in all arches, and yet the maximum bending moments (Tables 3.4 and 3.5) and maximum combined stresses (Table 3.7) show significant differences. Such behaviour suggests that very small variations in horizontal reactions have a substantial influence on the behaviour of each structure.

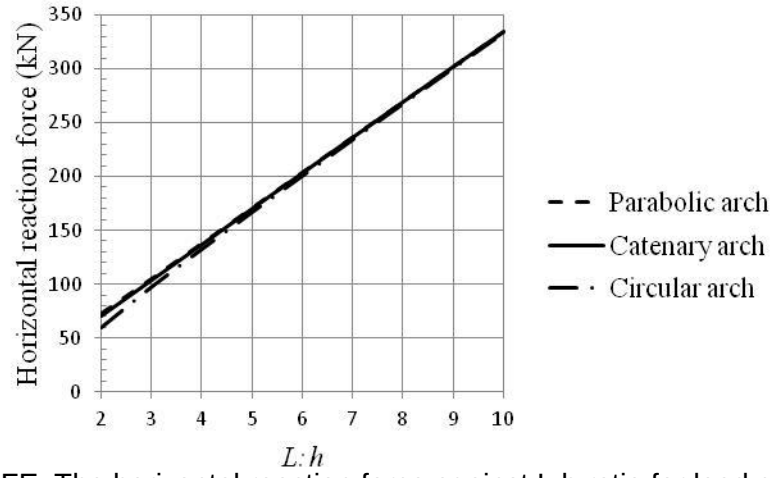

Figure 3.21. FE: The horizontal reaction force against L:h ratio for load case A1

3.5.7. Arch mass

The masses of the three forms of arches present a non-linear decrement with increase in the *L:h* ratio, see Figure 3.22. For a constant *L*, it is concluded that the *L:h* ratio is a dominant factor in arch mass. For *L:h* ratios above 5, the mass of the arches varies slightly with change in the *L:h* ratio. The magnitudes of the mass results for each arch shape are very close to the other shapes for any *L:h* ratio. The maximum percentage difference of arch mass is 5.8% for *L:h*=2 and the circular and parabolic forms. Moreover, the percentage difference of arch mass becomes less than 1% when *L:h*≥4. However, the circular arch seems to be slightly heavier, while the parabolic form is the lightest arch.

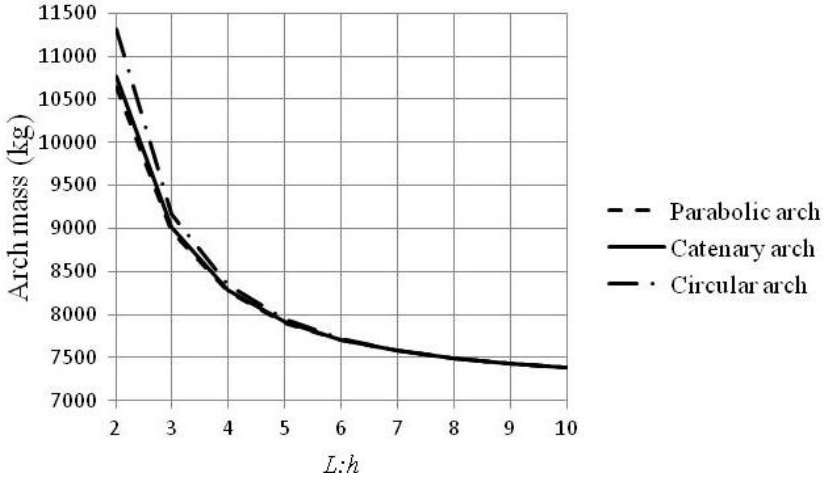

Figure 3.22. *FE*: Arch mass against *L:h* ratio for each form

3.6. Arches of steel material

For a general conclusion on the optimal arch form and *L:h* ratio, a hollow steel cross-section with a width of 200 mm, depth of 400 mm, and thickness of 13 mm was also analysed using the *GSA* software. This cross-section gives a flexural rigidity *EI*, that is the same as a concrete solid cross-section. The elastic modulus and density of the steel material are assumed to be 205 GPa and 7850 kg/m^3 respectively. It should be noted that the weight of concrete arches is 6 times greater than the weight of arches of the steel material with the properties given in this section. This means that the *UDL:SW* ratio of the three forms of arches constructed from steel is 6 times larger than the *UDL:SW* of the three studied shapes of concrete arches for any *L:h* ratio.

As stated previously, the optimal range to the *L:h* ratio is found when the maximum value of the combined stress reaches its minimum. Results to the absolute values of the maximum combined stress against *L:h* ratio under load case *A1* are plotted in Figures 3.23 and 3.24 using concrete and steel as the construction material, respectively.

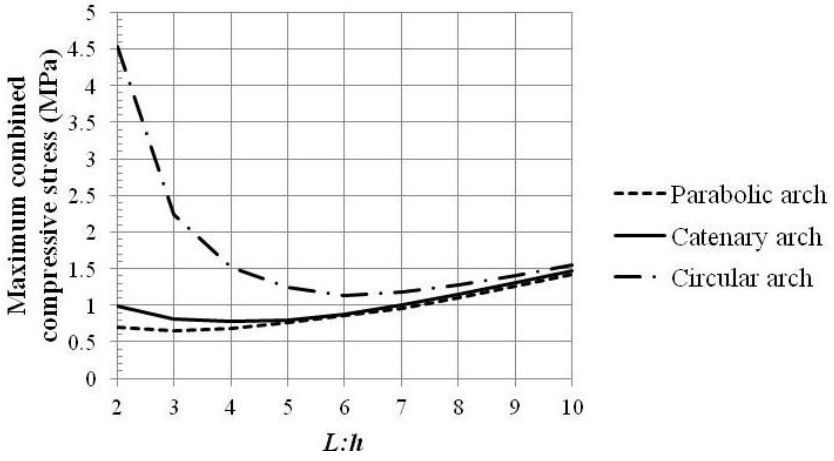

Figure 3.23. *FE*: The absolute value of the maximum combined stresses against *L:h* ratio using concrete material for load case *A1*

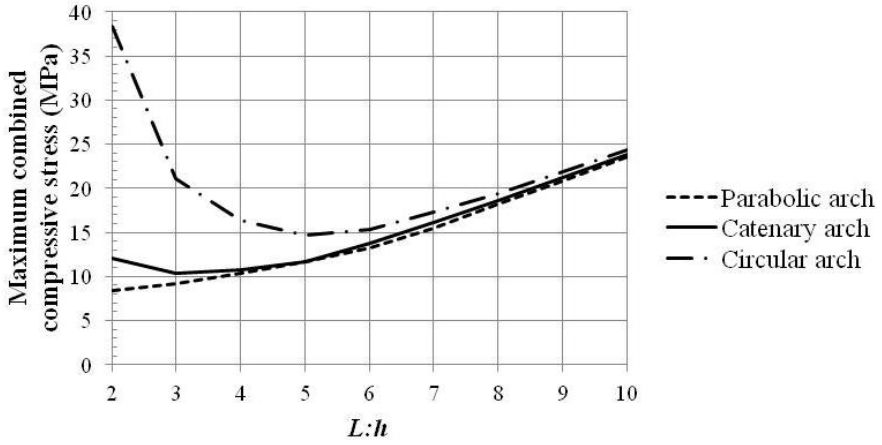

Figure 3.24. *FE*: The absolute value of the maximum combined stresses against *L:h* ratio using steel material for load case *A1*

The results of the maximum combined stress for the circular arch differ significantly from the results of the parabolic and catenary forms, particularly for *L:h* ratios below 5 for arches of both steel and concrete material. In general, the maximum combined stress reaches its minimum at *L:h* ratios between 2 and 4 for the parabolic and catenary arches under all load cases. Meanwhile, the optimal *L:h* ratio of the circular shape is between 4 and 6. The behaviour of both steel and concrete arches is the same under each load case. The magnitudes of the structural actions obtained from steel arches are different from those assuming arches built of concrete. The arches made of steel shows about 90% higher combined stresses than concrete arches for different *L:h* ratios.

3.7. Exploring the effect of different ratios of *UDL:SW*

The effect of different ratios of *UDL:SW* on structural actions, such as the maximum bending moment, maximum displacement, and maximum combined stress is explored in this section. It was stated that the behaviour of arches is affected by the shape, *L:h* ratio and the applied load. The effect of multiple load cases was investigated by applying different combinations of *SW* and *UDL* to the known shapes of arches. Although the considered load cases represent different *UDL:SW* ratios, the effect of the *UDL:SW* ratios cannot be studied appropriately using those

load cases. It was shown in Table 3.4 that the *UDL:SW* of the three shapes of arches increases with the *L:h* ratio for load case *A1*. However, the *UDL:SW* ratio is greater than 1 for all *L:h* ratios for the general combination of *SW* plus *UDL*. To explore the effect of different *UDL:SW* ratios, the behaviour of parabolic, catenary, and circular arches is studied when *UDL:SW*>1, *UDL:SW*=1, and *UDL:SW*<1. The analysis carried out for arches subjected to load case *A1* has covered the first load condition (*UDL:SW*>1) so far. To apply the other two load conditions *UDL:SW*=1 and *UDL:SW*<1, the *UDL* of 7.2 kN/m and 2.6 kN/m are respectively applied across the full span of the arches plus *SW*. The arch specification remains the same as the one defined in subsection 3.3.1, which ensures that *SW* is equal to 7.2 kN per unit arc length. Therefore, the maximum bending moment, maximum displacements, and maximum combined stress of the parabolic, catenary, and circular arches when *UDL:SW*=2.78, *UDL:SW*=1, and *UDL:SW*=0.36 are presented in Tables 3.12, 3.13, and 3.14.

Table 3.12. Maximum bending moment (kNm) of parabolic, catenary, and circular arches subjected to the general combination of *SW* plus *UDL* for different *UDL:SW* ratios

L:h	*UDL:SW*=2.78			*UDL:SW*=1			*UDL:SW*=0.36		
	Parabolic	Catenary	Circular	Parabolic	Catenary	Circular	Parabolic	Catenary	Circular
2	3.55	8.96	60.96	3.35	2.61	26.88	3.28	0.96	18.12
3	2.11	4.97	26.01	1.83	1.49	10.59	1.73	0.61	6.86
4	1.57	3.52	14.20	1.25	1.08	5.48	1.13	0.51	3.48
5	1.44	3.03	8.71	1.05	1.03	3.39	0.90	0.55	2.13
6	1.60	3.06	6.71	1.04	1.18	2.71	0.85	0.69	1.73
7	2.08	3.32	5.98	1.20	1.49	2.71	0.93	0.92	1.75
8	2.85	3.81	5.82	1.47	1.86	2.84	1.05	1.19	1.85
9	3.69	4.45	6.02	1.86	2.23	3.00	1.24	1.46	1.98
10	4.61	5.22	6.48	2.36	2.66	3.28	1.56	1.76	2.18

The circular arch shows a significant variation of maximum bending moment over *L:h* ratios between 2 and 10 in all three load cases. The maximum bending moment of the circular arch is at least 5 times greater than those of the parabolic and catenary arches at the *L:h* ratio of 2. The difference in the maximum bending moment of the different shapes of arches decreases when the *L:h* ratio increases. The parabolic arch shows the smallest magnitude of the maximum bending moment when *UDL:SW*=2.78. In the case of *UDL:SW*=0.36, the minimum value of the maximum bending moment is observed for the catenary arch with *L:h* ratios less than 8. The difference in the maximum bending moments of the catenary and parabolic arches is less than 1 kN/m for the full practical range of *L:h* ratios, and is negligible when *UDL:SW*=1.

Table 3.13. Maximum displacement (mm) of parabolic, catenary, and circular arches subjected to the general combination of *SW* plus *UDL* for different *UDL:SW* ratios

L:h	*UDL:SW*=2.78			*UDL:SW*=1			*UDL:SW*=0.36		
	Parabolic	Catenary	Circular	Parabolic	Catenary	Circular	Parabolic	Catenary	Circular
2	0.23	0.46	3.92	0.20	0.17	1.72	0.19	0.08	1.15
3	0.14	0.30	1.15	0.10	0.13	0.54	0.09	0.07	0.35
4	0.17	0.28	0.64	0.10	0.14	0.31	0.07	0.08	0.20
5	0.25	0.32	0.51	0.13	0.16	0.26	0.08	0.11	0.17
6	0.35	0.39	0.51	0.18	0.20	0.26	0.17	0.13	0.17
7	0.45	0.49	0.57	0.24	0.25	0.30	0.16	0.17	0.20
8	0.58	0.60	0.66	0.30	0.32	0.34	0.20	0.21	0.23
9	0.71	0.73	0.78	0.38	0.38	0.41	0.25	0.26	0.27
10	0.87	0.88	0.91	0.46	0.46	0.48	0.31	0.31	0.32

The maximum displacements of the catenary and circular arches are about 50% and 94% respectively greater than the maximum displacement of the parabolic arch for the *L:h* ratio of 2 when *UDL:SW*>1. The difference between the maximum displacements of the different shapes of arches decreases with increase of *L:h* ratio.

However, the maximum displacements of the parabolic arch remain smaller than the maximum displacements of the catenary and circular arches over all *L:h* ratios when *UDL:SW*>1. The differences between the maximum displacements of the parabolic and catenary arches are negligible for *UDL:SW*=1. Meanwhile, the circular arch shows about 88% greater maximum displacement than both the other arch shapes for the *L:h* ratio of 2. This percentage difference becomes smaller when the *L:h* ratio is increased. The difference between the maximum displacements of the catenary and parabolic arches is negligible for *UDL:SW*<1.

Table 3.14. Maximum combined stress (MPa) of parabolic, catenary, and circular arches subjected to the combination of *SW* plus *UDL* for different *UDL:SW* ratios

L:h	*UDL:SW*=2.78			*UDL:SW*=1			*UDL:SW*=0.36		
	Parabolic	Catenary	Circular	Parabolic	Catenary	Circular	Parabolic	Catenary	Circular
2	0.69	0.99	4.54	0.47	0.43	2.28	0.40	0.25	1.55
3	0.65	0.81	2.24	0.40	0.37	1.08	0.31	0.23	0.71
4	0.69	0.77	1.52	0.40	0.37	0.74	0.30	0.24	0.49
5	0.76	0.79	1.25	0.43	0.39	0.62	0.31	0.27	0.41
6	0.85	0.88	1.14	0.47	0.44	0.57	0.33	0.30	0.38
7	0.96	1.01	1.18	0.52	0.51	0.60	0.37	0.34	0.40
8	1.09	1.15	1.28	0.59	0.59	0.66	0.41	0.40	0.44
9	1.25	1.30	1.40	0.66	0.68	0.73	0.45	0.46	0.49
10	1.42	1.46	1.54	0.75	0.77	0.81	0.51	0.52	0.55

Similar to the results of the maximum bending moment and maximum displacements, the maximum combined stresses for the parabolic arch are smaller than for the other two arch shapes when *UDL:SW*=2.78. Again, the circular arches show the highest magnitude of the maximum combined stress amongst the three arch shapes for all load conditions. In general, the catenary arch presents lower combined stress than the parabolic arch when *UDL:SW*<1. The differences between the maximum combined stresses of the catenary and parabolic arches are

negligible when *UDL:SW*=1, with a slightly lower combined stress for the catenary arch when *L:h*≤7.

Overall, the parabolic arch is more efficient, exhibiting lower bending, displacements, and combined stresses than the other two arches when *UDL:SW*>1. The catenary arch is preferable when *UDL:SW*<1 considering the minimum structural action effect criterion. The differences in the results of structural actions are negligible between the catenary and parabolic arches for *UDL:SW*=1. Finally, the circular arch demonstrates the least desirable results for any ratios of *UDL:SW.*

3.8. Exploring the effect of arch thickness

To meet the strength and stability requirements for arch structures with an aesthetic effect, some rules were formulated. One of these rules was to assign a thickness for the arch that is required for construction stability. Many researchers have proposed an empirical formulation to obtain the arch thickness as a function of *L* depending on the type and application of the arch. In 1876, Castigliano stated that thickness of the arch can be formulated as $0.15\sqrt{L}$, based on the minimum thickness referable to any kind of arch (Timoshenko 1986). Using Castigliano's equation gives 470 mm to the minimum thickness of the studied arches with *L*=10 m. Since the thickness was assigned as 300 mm from the outset in this study based on the dimensions of the Gerrards Cross tunnel, the influence of the thickness of the arch rib on the results of the horizontal reaction forces and bending moments is reviewed in this section. It has been shown that the parabolic and circular arches are respectively the most and least preferable shapes in terms of structural engineering performance. For this reason, these two shapes of arches were modelled in *GSA* considering three different thicknesses (*d*) of 200, 300, and 400 mm. To compare bending moments at a specific location, the values of bending moment at the crown are reported. The results of the horizontal reaction force (kN) and the values of

bending moment (kNm) at the crown of a parabolic arch with *L:h* ratios between 2 and 10 under load case *A1* are presented in Table 3.15. The same investigation was carried out for the circular arch and the results are given in Table 3.16. Comparing the *GSA* outputs in Tables 3.15 and 3.16 it is seen that the horizontal reaction force and bending moments increase with increase thickness. In general, this effect is independent of the arch form.

Table 3.15. Horizontal reaction force and bending moment at the crown of parabolic arch for load case *A1*

L:h	Horizontal reaction force (kN)			Values of bending moment at the crown (kNm)		
	d=200mm	*d* =300mm	*d*=400mm	*d*=200mm	*d*=300mm	*d*=400mm
2	65.62	73.41	81.18	2.43	3.544	4.57
3	95.63	105.89	116.09	1.00	1.295	1.42
4	125.98	138.84	151.58	0.35	0.195	0.25
5	156.48	171.97	187.24	0.07	0.601	1.56
6	187.03	205.12	222.86	0.42	1.326	2.84
7	217.58	238.22	258.29	0.75	2.063	4.18
8	248.10	271.19	293.45	1.09	2.85	5.63
9	278.56	303.98	328.25	1.45	3.69	7.22
10	308.94	336.56	362.63	1.84	4.61	8.95

Table 3.16. Horizontal reaction force and bending moment at the crown of circular arch for load case *A1*

L:h	Horizontal reaction force (kN)			Values of bending moment at the crown (kNm)		
	d=200mm	*d* =300mm	*d*=400mm	*d*=200mm	*d*=300mm	*d*=400mm
2	54.43	60.41	66.37	46.36	50.24	55.14
3	88.94	98.32	107.66	19.73	21.44	23.57
4	121.22	133.53	145.75	11.05	12.27	13.82
5	152.78	167.90	182.84	7.26	8.45	9.96
6	184.01	201.86	219.41	5.35	6.71	8.39
7	215.05	235.54	255.58	4.32	5.98	7.95
8	245.94	268.98	291.37	3.77	5.82	8.17
9	276.69	302.18	326.77	3.51	6.02	8.83
10	307.32	335.14	361.75	3.45	6.48	9.80

It is seen that the bending moment at the crown of parabolic arch for *L:h*=4 is decreasing when the arch thickness is increasing from 200 to 300 mm. Then, the bending moment at arch crown is increasing when the thickness is increasing from 300 to 400 mm for this *L:h* ratio. But, the bending moment of parabolic arch with thickness of 400 mm is still lower that this action when the thickness of parabolic arch is 200 mm. The magnitude of the bending moment at the crown of parabolic arch at *L:h* ratio of 4 is less than 0.4 kNm for all the considered thicknesses. Hence, this trend is ignored because of the small magnitude of bending moment at the crown of parabolic arch for all assumed thicknesses at this *L:h* ratio. The effect of thickness on the bending moment of the parabolic arch subjected to *UDL* only (load case *A4*) is shown in Figure 3.25.

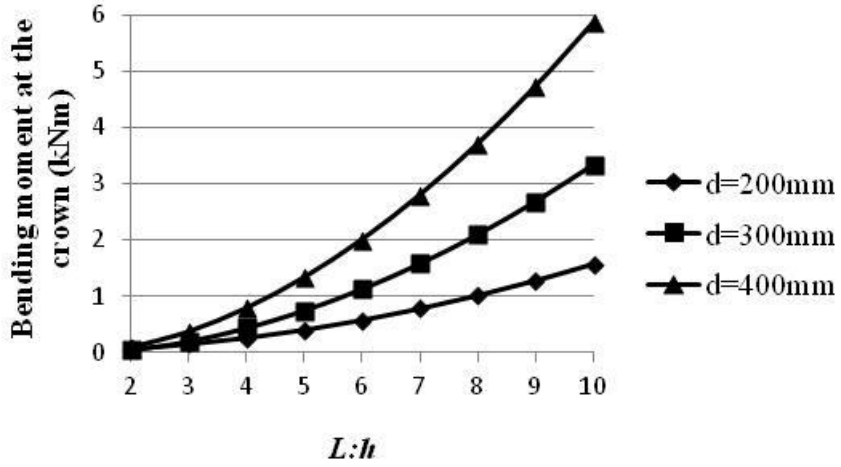

Figure 3.25. *FE*: Values of bending moment at the crown of parabolic arch with different arch depths for load case *A4* (*UDL* only)

The arch is subjected to *UDL* only and the effect of thickness in *SW* is not considered In Figure 3.25. Also, the parabolic arch is momentless in theory for any *L:h* ratio when subjected to *UDL* only. Meanwhile, it can be seen that the bending moment at the crown of the parabolic arch increases sharply with the increase of thickness especially for *L:h* ratios above 5. The reason for assuming the parabolic

arch is momentless for the *UDL* only load case is ignoring the section properties such as, gyration radius in calculating the horizontal reaction force in static theory.

3.9. Exploring the effect of shortening of the arch

In pin-ended arches, a compressive force in an arch rib causes that arch rib to be shortened, which will in turn release part of the horizontal thrust. This effect, called shortening, is not generally considered in arch analysis. However, in the case of shallow arches the shortening effect has a substantial impact on the results of the horizontal reaction force. Therefore, depending on the limit of the arch's shallowness, the effect of rib shortening can be either taken into consideration or neglected. The effect of shortening the arch rib on the results from arch analysis is investigated using *GSA* in this section.

3.9.1. Comparison of horizontal reaction force from *GSA* with other methods

In a study of the process of changing the horizontal reaction force with increase of the *L:h* ratio, Ghigliotty (2012) conducted a relevant investigation. He assumed that a two-pin parabolic arch is subjected to *UDL* only. A computer program named *BERNI90* was used to calculate the horizontal reaction force. The software was developed in 1990 to analyse frame structures using the finite element approach. In this software, the frame elements are considered to possess six degrees of freedom and the supports are restrained elastically.

The horizontal reaction forces of the two-pin parabolic arch with specifications defined by Ghigliotty are obtained via *GSA* software in this section. The horizontal reaction force of the two-pin parabolic arch under *UDL* only is also obtained using static theory, and is equal to $wL^2/8h$. In this equation, *w* is the imposed *UDL.* The shortening effect is not considered when calculating the horizontal reaction force using static theory. Consequently, the horizontal reaction forces of the two-pin parabolic arch using *BERNI90*, *GSA*, and static theory are compared against each

other in Table 3.17. The comparison leads to specification of the limit of the *L:h* ratio at which the shortening of the arch rib has a substantial effect on the results of the horizontal reaction force. The specification for the studied arch is given in Figure 3.26 from Ghigliotty study for comparison reason. The span of the parabolic arch was a constant 30.48 cm, while *h* decreased from about 6 m to 0.

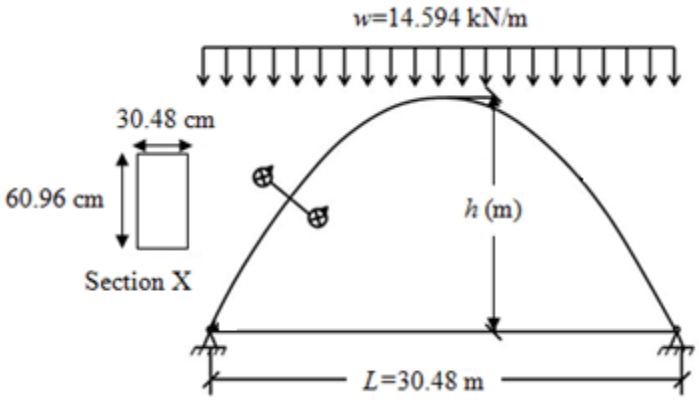

Figure 3.26. Arch specification (Ghigliotty 2012)

Table 3.17. Horizontal reaction force (kN) of parabolic arch subjected to *UDL* only

h	*L:h*	Horizontal reaction force (kN)		
		BERNI90	*GSA*	$H=wL^2/(8h)$
6.10	5	277	277.7	278
3.05	10	552	552.8	556
1.52	20	1085	1085	1112
1.22	25	1338	1338	1390
0.61	50	2402	2405	2780
0.30	100	3465	3423	5560
0.24	125	3571	3517	6950
0.18	166.67	3456	3388	9267
0.12	250	2947	2834	13900
0.06	500	1732	1672	27800
0	∞	0	0	∞

It can be seen in Table 3.17 that $H = wL^2/8h$ loses meaning when the *L:h* ratio exceeds 125 and the results from static theory grow to be very unsatisfactory. The reason for this deviation is the neglect of the axial deformation of the arch rib in

calculating the horizontal reaction force in static theory. The results from both finite element analyses demonstrate that the trend of increasing horizontal reaction force with the *L:h* ratio is inverted to decreasing for *L:h* ratios above 125. The fair comparison for the results of the horizontal reaction force from *BERNI90* and *GSA* proves the reliability of the results obtained using *GSA* software. However, the results of *H* obtained using two software slightly diverge for *L:h*>125 due to the numerical error.

Concerning the shortening effect, to ensure acceptable precision in calculating the horizontal reaction force of the arch based on static theory, Gaylord & Gaylord (1990) suggested the follow expression having the rib shortening coefficient *v'.*

$$H = \frac{wL^2}{8h}\upsilon' \text{ in which } \upsilon' = \frac{1}{1+\frac{(15/8)I}{Ah^2}} \tag{3.11}$$

In Equ. (3.11) *v'* is an adjustment made to the previous equation used in the past to obtain the horizontal reaction force of pin-ended parabolic arches subjected to the *UDL* only. For this reason, the horizontal reaction force obtained using Equ. (3.11) is labelled as 'adjusted' in this study. The adjustment factor was then applied to obtain horizontal reaction forces that are compared with static theory values in Table 3.18.

The adjusted factor suggested by Gaylord decreases from about 1 to 0 with the increase of *L:h* ratio till the arch becomes a straight beam. Therefore, the horizontal reaction force decreases above *L:h* ratios greater than 125 when the adjustment factor is applied to static theory, see Table 3.18. Thus, the results of the horizontal reaction force considering this factor are in very good agreement with those from *GSA*.

For a visual demonstration of the comparison of the horizontal reaction force using different approaches, these reactions are plotted against the *L:h* ratio in Figure 3.27.

Table 3.18. Horizontal reaction force (kN) of parabolic arch subjected to *UDL* only

h	*L:h*	Horizontal reaction force (kN)		
		$H= wL^2/(8h)$	Adjustment factor	Adjusted static theory
6.10	5	278	0.998	277
3.05	10	556	0.994	553
1.52	20	1112	0.976	1085
1.22	25	1390	0.962	1338
0.61	50	2780	0.865	2405
0.30	100	5560	0.615	3422
0.24	125	6950	0.506	3516
0.18	166.67	9267	0.366	3387
0.12	250	13901	0.204	2833
0.06	500	27801	0.060	1674
0	∞	∞	0	0

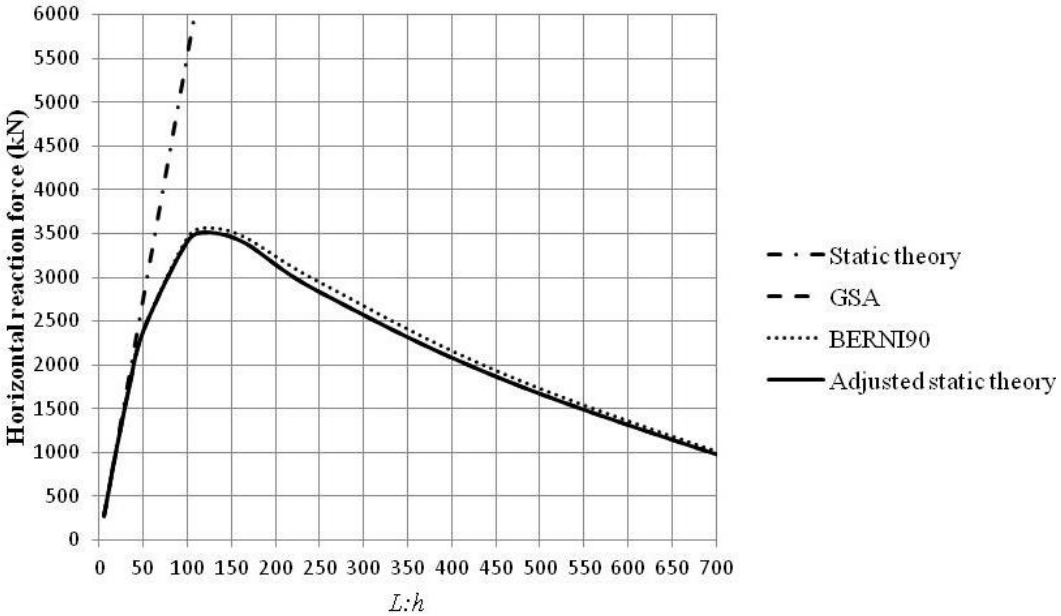

Figure 3.27. Comparison of the horizontal reaction forces using different methods

Figure 3.27 illustrates that the results of adjusted static theory match well with the results of *GSA*. Moreover, the results of the horizontal reaction force using *BERNI90* exhibit less than 4% difference with those obtained by *GSA* for the full range of *L:h* ratios. In addition, the horizontal reaction force increases towards infinity with increase of the *L:h* ratio. Therefore, consideration of the shortening effect is deemed

to be crucial when analysing shallow arches. These results are satisfactory, due to obtaining a horizontal reaction force of zero once the arch height becomes zero.

Most arches are constructed with the *L:h* ratio less than 10. Consequently, an *L:h* ratio limit such as 125 seems inapplicable due to the possibility of elastic buckling at this *L:h* ratio for the studied arch.

3.9.2. Threshold range of *L:h* ratio of arch shallowness

There are many investigations through the typical range of *L:h* ratios of arches. However, there is no valid reference as to the *L:h* ratio that should be considered the limit for the shallowness of arches at which the arch action is assured. Increase of the arch shallowness has a transforming effect on the behaviour of pure arch to pure beam behaviour. The commonly used range of *L:h* ratios for arch bridges as suggested by Gaylord (1990) and Merrit (1976) was between 4.5 and 6, in which there is no need to consider the rib shortening effect. However, there exists a concrete arch bridge with the highest *L:h* ratio equal to 11.2 (Fonesca and Mato 2005). The practical limits of the *L:h* ratio of masonry arch structures under permanent loads are an essential part of the design. This limit can be presumed as the effective behaviour of arch structures, beyond which the arch behaviour is reduced due to flexural response. This is because of the linear relationship of arch shallowness to axial deflections and bending moments. However, masonry arch bridges were frequently built in past centuries at *L:h* ratios of between 3 and 8 (Salonga and Gauvreau 2010).

To find the limit of the shallowness of the arch shapes in this study with the arch specifications set out in subsection 3.3.1, Table 3.19 presents the arc length (*S*) for a *L* of 10 m.

From Table 3.19, the percentage difference between the arc length and the span length of the three shapes of arches becomes less than 1% for *L:h* ratios above 16.

This shows that the arches are becoming so shallow that they can be considered as beams in practice for this *L:h* ratio. Moreover, the arc lengths of the three arch shapes are the same for *L:h*>16, which shows that they do not keep their own shape properties. Therefore, the arch shapes in this study are assumed as flat ones when *L:h*>16. Since the arches are analysed for the range of *L:h* ratios between 2 and 10, the effect of arch rib shortening is not seen when calculating the horizontal reaction force.

Table 3.19. Percentage difference between arch length *(S)* and horizontal distance between the supports *(L)* of known shape of arches

L:h	Parabolic arch		Catenary arch		Circular arch	
	Arc length *S*, (mm)	Percentage difference between *S* and *L*	Arc length *S*, (mm)	Percentage difference between *S* and *L*	Arc length *S*, (mm)	Percentage difference between *S* and *L*
2	14789	32.38%	14958	33.15%	15708	36.34%
3	12453	19.70%	12520	20.13%	12740	21.51%
4	11478	12.88%	11508	13.10%	11591	13.73%
5	10982	8.94%	10997	9.07%	11035	9.38%
6	10698	6.52%	10706	6.59%	10725	6.76%
7	10520	4.95%	10525	4.99%	10536	5.08%
8	10402	3.87%	10405	3.89%	10412	3.95%
9	10320	3.10%	10322	3.12%	10326	3.16%
10	10261	2.54%	10262	2.55%	10265	2.58%
11	10216	2.12%	10217	2.12%	10219	2.14%
12	10182	1.79%	10183	1.80%	10184	1.81%
13	10156	1.53%	10156	1.54%	10157	1.55%
14	10134	1.33%	10135	1.33%	10136	1.34%
15	10117	1.16%	10118	1.16%	10118	1.17%
16	10103	1.02%	10103	1.02%	10104	1.03%
17	10092	0.91%	10092	0.91%	10092	0.91%

3.10. Concluding Remarks

It was stated in Chapter 2 that there are some articles in the literature about the optimum range of *L:h* ratio for circular arches. However, no published research was

found on analysing the differences in the behaviour of the three studied shapes of arches. The results of analysing different arch shapes have shown that circular arches represent the least optimal shape over a typical range of load cases and span-to-height ratios. They exhibit higher combined stresses, displacements and bending moments, particularly for the *L:h* ratio of 2 (semi-circular arch). This shape is also the most sensitive to changes in the *L:h* ratio for all load cases. The optimum *L:h* ratio for a circular rib arch is between 4 and 6, but the stresses that develop in it are still higher than in parabolic or catenary shaped arches. The minimum combined compressive stresses in parabolic and catenary arches are observed at *L:h* ratios between 2 and 4, with the parabolic arch exhibiting the best performance. From the structural behaviour results of all three arch shapes it is concluded that arches are becoming shallow for *L:h*>5. It was seen that maximum combined stress and bending moments are increasing when *L:h* ratio increases above 5. The *L:h* ratio in which arches are known as flat in this study is 16. The effect of arch thickness on its behaviour showed the influence of changing in arch thickness on structural action effect when the arch is subjected to *UDL* only. This result highlighted the importance of considering section properties such as, gyration radius when analysing arch structures. The parabolic and catenary arch demonstrated lower structural action effects when respectively *UDL>SW* and *SW>UDL*. As a known fact, parabolic arch is momentless if it is subjected to *UDL* only and the *SW* is ignored in theory. Meanwhile, the catenary arch is considered as a momentless one when subjected to *SW* only. Moreover, for any other loading conditions, the existence of bending moments is inevitable for the studied arch shapes. However, it is possible to find a momentless arch geometry subjected to both self-weight and *UDL*.

Overall, the findings demonstrate that the response of two-pin arch forms to applied loading is critically dependent on the arch form and its shape governed by the *L:h* ratio.

Chapter 4 : Comparison of different methods of two-pin arch analysis

4.1. Introduction

In this chapter the approximate methods, which are currently in use in the analysis of two-pin arches are compared with the accurate method. Thus, the potential problems of the inaccuracy of the approximate analysis methods can be studied. To do so, an energy method based on Castigliano's second theorem for analysing the linearly elastic two-pin arches is explored. The results from the previous chapter have shown that circular and parabolic arches represent the least and most optimal shapes for typical load cases and *L:h* ratios. Therefore, the effects of form on the structural response of circular and parabolic arches are presented using theoretical analysis based on engineering beam theory in conjunction with the Castigliano's second principle (Timoshenko 1986). The analysis was used to varying degrees of refinement, i.e., bending action only, bending, thrust and shear, and bending, thrust, shear, and coupling between bending and thrust. The results are compared with each other, and with approximate methods of analysis, including virtual work, finite element solutions provided by *GSA*, and the masonry design method. In doing so, parabolic and circular arches were subjected to the general combination of *UDL* and *SW* (load case *A1*, defined in Chapter 3) and *UDL* only (load case *A4*). The specifications of these arches were defined in subsection 3.3.1 with a range of *L:h* ratios between 2 and 10. The purpose of this analysis is to assess the validity of different approximate methods of arch analysis. The effect of different actions of strain energy in Castigliano's theorem is evaluated too.

4.2. Theoretical analysis method

Since the two-pin arch has four components of reactions at the supports, the structure is statically indeterminate to degree one, see Figure A.1. Only vertical reactions can be obtained from the three equilibrium equations. To find the horizontal reaction force, a further equation in addition to equilibrium equations is required. This can be obtained using a number of alternative methods. A classical method applicable to linear elastic structures is based on Castigliano's second theorem (Timoshenko 1986). In this case, it is possible to consider the strain energy *U* due to bending *M*, shear *F*, thrust *T* and coupling of bending and thrust (Timoshenko 1986).

$$U = \frac{1}{2}\int_0^S \frac{M^2}{EI}\,\mathrm{d}s + \frac{1}{2}\int_0^S \frac{T^2}{EA}\,\mathrm{d}s + \frac{1}{2}\int_0^S \frac{F^2}{kGA}\,\mathrm{d}s + \int_0^S \frac{MT}{AER}\,\mathrm{d}s \qquad (4.1)$$

R is the radius of curvature of the structure (varying over the length of the arch, except for circular arches), and *k* is the shear reduction factor on area. The factor *k* is used to correct for the non-uniform distribution of shear over the arch cross-section. Also, *G* is the shear modulus, which is equal to $E/2(1+\upsilon)$ for an isotropic material and υ is the Poisson's ratio.

Using Castigliano's theorem, the horizontal deflection of an arch (here analysed as a curved bar) is equal to the derivative of strain energy with respect to the horizontal reaction at a pin. As pin-ended arches are assumed to have no horizontal deflections, the derivative of strain energy with respect to the horizontal reaction force, as defined by Equ. (4.2), will be zero at the supports (Timoshenko 1986).

(Bending action) (Thrust and shear terms)

$$\frac{\partial U}{\partial H} = \frac{1}{EI}\int_0^S M\frac{\partial M}{\partial H}\,\mathrm{d}s + \frac{1}{EA}\int_0^S T\frac{\partial T}{\partial H}\,\mathrm{d}s + \frac{1}{kGA}\int_0^S F\frac{\partial F}{\partial H}\,\mathrm{d}s + \underbrace{\frac{1}{AER}\int_0^S T\frac{\partial M}{\partial H}\,\mathrm{d}s + \frac{1}{AER}\int_0^S M\frac{\partial T}{\partial H}\,\mathrm{d}s} \tag{4.2}$$

(Coupling of bending and thrust terms)

To study the effect of each term of the strain energy equation, this method is divided into three categories in order to analyse the arch structures. They are:

- Bending action only: in general this assumption is valid when the radius of curvature from its centre line is much greater than the cross-sectional dimensions of a bar. The classic virtual work method leads to the same result.
- Bending action plus the shear and thrust terms: the strain energy is assumed to result from the theory of the elastic behaviour of a rib arch, which approximates the Euler–Bernoulli assumption.
- Full structural actions: as above plus a term arising from the coupling of bending and thrust term. This analysis is used as a benchmark for the results from the approximate methods of analysis.

The arch forms which are mostly used in design are circular, parabolic, and catenary. Due to the close structural response of parabolic and catenary arches for general load conditions, this method is applied to the circular and parabolic arches. The processes of finding the horizontal reaction force of circular and parabolic arches using Castigliano's second theorem are outlined in Appendix A and Appendix B respectively.

The results of the theoretical analysis are compared with those obtained by *FE*.

Previous arch analysis based on Castigliano's theorem (Bridle and Hughes, 1990; Clemente et al., 2001) have included some assumptions, such as ignoring the shear action because of its small effect on the strain energy equation. The effect of all actions are considered and assessed in this study.

4.3. Approximate analytical methods

The circular and parabolic arches have been analysed by alternative 'hand calculation' methods, which use simplifying assumptions to calculate the reaction forces. These methods are of two types; the first, based on the virtual work principle and presented by Megson (2006), is named 'virtual work' in this study; the second is the 'masonry design' method (Curtin et al., 2006). The effects of the assumptions used in these methods are evaluated. Both of these methods are commonly used for practical analysis of arch structures. Therefore, examining their underlying assumptions will enable designers to become aware of the advantages and disadvantages of using them. It is interesting to note that the masonry design method has not been changed in the Structural Masonry Designers' Manual between its 1982 and 2006 editions, despite its approximate nature. The reason is probably in providing a conservative design solution using masonry design method. The two methods are discussed below, starting with the masonry design method.

4.3.1. Masonry design method

To calculate the horizontal reaction force using the masonry design method, it is assumed that the thrust at the crown runs through the centre of the thickness of the arch rib. This leads to having a zero bending moment at its crown, which has a remarkable effect on the results of the horizontal reaction force. As a result, the arch acts like a three-pin arch in the masonry design method. This method is generally used to draw the thrust line of the arch based on the force diagram of Bow's notation. The location of the thrust line within the arch ring then determines the

stress zones in the arch. To have dominant compressive stresses in the masonry material, the thrust line is required to lie in the middle third of the arch cross-section (Curtin et al. 2006). A further approximation in the method is due to the level of discretisation of the arch into individual segments to which self-weight and *UDL* are applied, as shown in Figure 4.1.

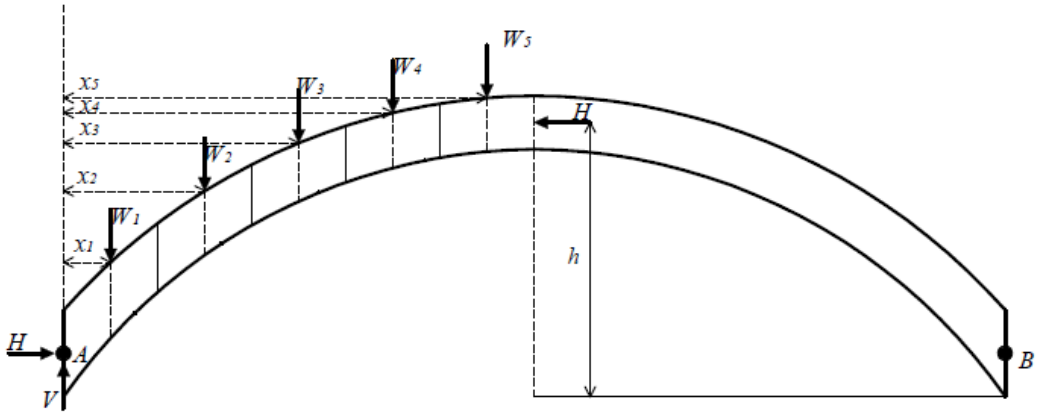

Figure 4.1. Masonry design method (arch is divided into several segments)

According to the masonry design method, the arch is split into segments with *SW* and *UDL* applied as a series of point loads, W_i. Therefore, the horizontal reaction force, *H*, is calculated using:

$$M_A = \sum W_i x_i - Hh = 0 \Rightarrow H = \frac{\sum W_i x_i}{h} \tag{4.3}$$

where M_A is the bending moment at point *A* (depending on the loading), x_i is defined as the horizontal distance between where loads W_i act and *A*, *h* is also the height of the arch. Having *V* as the vertical reaction force at point *A*, the internal bending moment for the arch at any arbitrary point $p(x_p, y_p)$, is expressed as:

$$M_p = Vx_p - Hy_p - [W_1(x_p - x_1) + W_2(x_p - x_2) + ...] \quad (4.4)$$

4.3.2. Virtual work method presented by Megson

According to this method, the virtual work of all forces acting on a body including external and internal force is zero if the body is in static equilibrium. The application of the virtual work method to two-pin arches is presented by Megson (2006). When applying the virtual work approach to two-pin arches, it is assumed that only bending produces displacements and this approach ignores the effect of thrust on them. Therefore, the assumption for calculating reaction forces is that arches work in bending only. To obtain a real displacement, a virtual force is imposed on a deformable body in the virtual work method. In order to have a statically determinate structure, a release is chosen at one support (see Figure 4.2). Then the unit load is applied to that support, which induces internal forces and displacements.

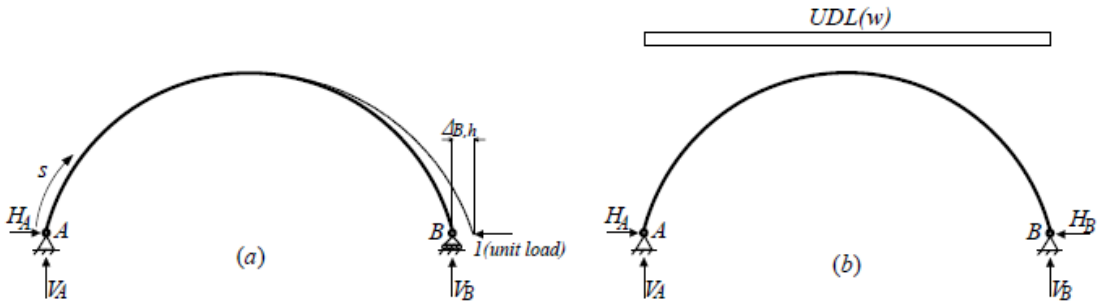

Figure 4.2. Application of the virtual work method (using a unit load) to the two-pin arch

Thus to find the displacement, the support "*B*" needs to be released as shown in Figure 4.2 (a). The imposed *UDL* results in deformation, while the horizontal reaction force H_B is not present. Since the virtual work approach assumes that arches work in bending only and ignore thrust, for compatibility with the horizontal displacement at support *B*, $\Delta_{B,h}$ is expressed by H_B in.

$$\Delta_{B,h} = a' H_B \tag{4.5}$$

In Equ. (4.5) '*a'* ' is the flexibility coefficient of the arch. To find $\Delta_{B,h,}$ a unit horizontal load should be imposed at *B*. The external virtual work of the system, W_e is given by:

$$W_e = 1\Delta_{B,h} \tag{4.6}$$

The internal virtual work, W_i from the derivation of the expression for internal work for bending moment leads to:

$$W_i = \int_{Profile} \frac{M_A M_1}{EI} ds \tag{4.7}$$

where M_A is the bending moment distribution due to the applied loading and M_1 is obtained by removing all the external loads and moments and just considering the unit horizontal load at the support *B*. The distance round the profile from *A* is '*S*'. The horizontal displacement at that support can be obtained using work–equilibrium relationships, i.e. $W_e = W_i$, which yields:

$$\Delta_{B,h} = \int_{Profile} \frac{M_A M_1}{EI} ds \tag{4.8}$$

Also the flexibility coefficient is defined using (Megson 2006):

$$a' = \int_{profile} \frac{M_1^{\,2}}{EI} ds = \int_{profile} \frac{y^2}{EI} ds \tag{4.9}$$

Substituting *a'* and $\Delta_{B,h}$ from the above equations into Equ. (4.5) and substituting M_1 for the moment from the unit load enables determination of the horizontal reaction force from:

$$H_B = \frac{\int_{\text{profile}} \frac{M_A y}{EI} \mathrm{d}s}{\int_{\text{profile}} \frac{y^2}{EI} \mathrm{d}s} \tag{4.10}$$

Consequently, the internal bending moment for the arch at any arbitrary point $p(x_p,y_p)$ is expressed as:

$$M_p = Vx_p - Hy_p - \frac{wx^2}{2} \tag{4.11}$$

where '*w*' is the uniformly distributed load and '*V*' is the vertical reaction force which can be found from the static equilibrium.

When analysing arches of shapes other than the semi-circular profile, to avoid complicated integrals in the process of finding a horizontal reaction force, the secant assumption is required. If the term ds/*I* in Equ. (4.10) is replaced by a term that is a function of either *x* or *y*, the solution can be simplified. Assuming an elemental length *δs* of an arch as shown in Figure 4.3, *ds* will be equal to d*x*sec*θ* when $\delta s \to 0$

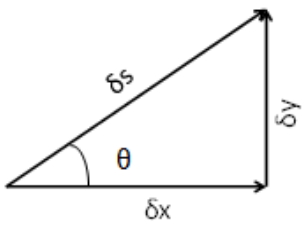

Figure 4.3. Elemental length, *δs*, split into *x* and *y* components *δx* and *δy*

Based on the secant assumption, a second moment of area is assumed to vary around the arch profile $(I = I_0 \sec\theta)$, in which I_0 is the second moment of area at the crown of the arch. Therefore, the horizontal reaction force of parabolic and catenary arches is obtained from Equ. (4.12).

$$H = \frac{\int_{x_1}^{x_2} M_A y \mathrm{d}x}{\int_{x_1}^{x_2} y^2 \mathrm{d}x} \tag{4.12}$$

The horizontal reaction force from the virtual work method for a linear-elastic system is equal to the one obtained from Castigliano's second theorem assuming bending action only.

4.4. Comparison of different methods of analysis

The different analysis methods of two-pin arches which were summerized in Sections 4.2 and 4.3 are applied to the studied shapes of arches. For this reason, the general combination of *UDL* and *SW* (load case *A1*) is applied to the circular and parabolic arches, and the previously described methods of arch analysis are used. The aim is to compare the results from these methods with the results provided by the most accurate method, based on the Castigliano principle and full structural action, including the "coupling of bending and thrust" term (Equation 4.2). Within the Castigliano-based approach, further comparisons are also given for cases of bending action only (*M* only), and bending+ shear+ thrust (*M*, *F*, and *T*). This provides a comprehensive assessment of methods for arch analysis based on the findings of previous work.

The horizontal reaction forces and maximum bending moments in a circular arch subjected to load case *A1* and analysed by different methods are given in Tables

4.1 and 4.2, respectively when *L*=10 m. The location of the maximum bending moment for a circular arch obtained using the different methods is also reported in Table 4.2. Table 4.3 presents the maximum thrust of the circular arch for load case *A1*. Table 4.4 gives a comparison of the maximum combined compressive stresses of the circular arch from Castigliano's analysis and from the *FE* analysis for load case *A1*.

Table 4.1. Horizontal reaction force of circular arch (kN) subjected to the *UDL* of 20 kN/m plus *SW* (*A1*)

L:*h*	*GSA*	masonry design	Castigliano (*M* only)	Castigliano (*M*, *F* and *T*)	Castigliano (Full actions)
2	60.14	70.55	60.44	60.41	60.45
3	97.80	104.80	98.45	98.32	98.41
4	132.80	138.46	133.83	133.53	133.67
5	167.00	172.11	168.46	167.90	168.11
6	200.70	205.83	202.82	201.86	202.15
7	234.20	239.61	237.04	235.54	235.89
8	267.40	273.43	271.19	268.98	269.35
9	300.30	307.28	305.29	302.18	302.50
10	333.00	341.16	339.38	335.14	335.27

- Results from the virtual work method are identical to those from Castigliano, bending action only

Table 4.2. Maximum bending moments (M) and their locations along the span (*x*) of circular arch subjected to the *UDL* of 20 kN/m plus *SW* (*A1*)

L:*h*	*GSA*		masonry design		Castigliano (M only)		Castigliano (M, F and T)		Castigliano (Full actions)	
	M (kNm)	*x* (m)	*M* (kNm)	*x* (m)	*M* (kNm)	*x* (m)	*M* (kNm)	*x* (m)	*M* (kNm)	*x* (m)
2	-60.96	0.5	-83.38	0.5	-61.35	0.5	-61.27	0.5	-61.37	0.5
3	-26.01	1	-35.91	1.0	-25.96	1	-25.76	1	-25.89	1
4	-14.20	1	-19.46	1.5	-14.56	1	-14.24	1	-14.39	1
5	-8.713	1	-12.49	1.5	-9.21	1	-8.76	1	-8.92	1
6	6.71	5	-8.67	1.5	-6.33	1	6.62	5	6.14	5
7	5.98	5	-6.36	1.5	-4.62	1	5.81	5	5.31	5
8	5.815	5	-4.86	1.5	-3.52	1	5.56	5	5.09	5
9	6.02	5	-3.84	1.5	-2.77	1	5.67	5	5.32	5
10	6.48	5	-3.11	1.5	-2.26	1	6.02	5	5.89	5

Table 4.3. Maximum thrust (kN) of circular arch subjected to the *UDL* of 20 kN/m plus *SW* (*A1*)

L:h	*GSA*	Castigliano (*M* only)	Castigliano (*M*, *F* and *T*)	Castigliano (Full actions)
2	161.2	156.55	156.55	156.55
3	172.3	172.51	172.46	172.49
4	192.8	193.68	193.50	193.58
5	216.9	218.35	217.94	218.09
6	243.4	245.42	244.65	244.88
7	271.4	274.12	272.85	273.15
8	300.3	303.98	302.03	302.36
9	329.9	334.66	331.84	332.12
10	359.8	365.95	362.03	362.16

Table 4.4. Maximum combined compressive stresses of circular arch (σ) and their locations along the span of the arch (x) subjected to the *UDL* of 20 kN/m plus *SW* (*A1*)

L:h	*GSA*		Castigliano (*M* only)		Castigliano (*M*, *F* and *T*)		Castigliano (Full actions)	
	σ(MPa)	x(m)	σ(MPa)	x(m)	σ(MPa)	x(m)	σ(MPa)	x(m)
2	4.54	0.5	3.57	5	3.58	5	3.57	5
3	2.24	1	1.74	5	1.77	5	1.75	5
4	1.52	1	1.22	5	1.27	5	1.24	5
5	1.25	1	1.05	5	1.12	5	1.09	5
6	1.14	1	1.01	5	1.11	5	1.08	5
7	1.18	5	1.03	5	1.17	5	1.14	5
8	1.28	5	1.09	5	1.27	5	1.24	5
9	1.40	5	1.16	5	1.38	5	1.36	5
10	1.54	5	1.25	5	1.52	5	1.51	5

In general, the results of Castigliano with bending, shear, and thrust are in good agreement with those obtained from *FE*. There are small differences between the results of these two methods, such as the location of the maximum combined stress for *L:h* lower than 6. Since the results of the virtual work method and Castigliano with bending action only are the same, the virtual work method results are not separately given in the above tables. In Table 4.1 the horizontal reaction force of the

circular arch grows with the *L:h* ratio for load case *A1*. The masonry design method gives the horizontal reaction force as the maximum, while the minimum of this force is obtained from Castigliano's theorem based on bending, shear, and thrust. The horizontal reaction force of Castigliano with bending action only is the maximum when Castigliano's approach with different categories is investigated. However, Castigliano based on bending, shear, and thrust calculates the horizontal reaction force as the minimum amongst the three categories of Castigliano's theorem. The maximum bending moment values of the circular arch for load case *A1* decrease when the *L:h* ratio is increased from 2 to 8 using *FE*, Castigliano's approach based on bending, shear, and thrust, and Castigliano's approach with full structural action. Then, the decreasing trend of the maximum bending moment is reversed to increase above this ratio using these methods of analysis (see Table 4.2). The maximum bending moment in the circular arch has a decreasing trend over the full range of *L:h* ratios when masonry design, virtual work, and Castigliano's theorem based on bending action only are applied. Also, these methods produce the maximum bending moment as hogging for the full range of *L:h* ratios. However, the maximum bending moment becomes sagging after an *L:h* ratio of 5 when other methods of analysis are applied. The location of the maximum bending moment of the circular arch using all methods is near the supports when the *L:h* ratio is below 6. The location of the maximum bending moment is seen near the supports for *L:h* ratios between 2 and 10 using masonry design, virtual work, and Castigliano with bending action only. But, this location is at the crown of the circular arch for $L{:}h \geq 6$ using other methods. Furthermore, the masonry design method predicts the maximum bending moment as the highest in comparison to the other methods of analysis for *L:h* ratios between 2 and 7. The minimum value of this bending moment is given by Castigliano due to bending, shear, and thrust when the *L:h* ratio is between 2 and 5. The results of the maximum bending moment of the circular arch using all the methods in Table 4.2 show the sensitivity of the circular arch to

changes in the *L:h* ratio. Table 4.3 presents the thrust of the circular arch using different methods of analysis for the general combination of *UDL* and *SW* applied across the full span of the arch (*A1*). The masonry design method is neglected in Table 4.3 due to the large differences of the results obtained using this method and other analysis methods. The thrust values are the maximum when Castigliano with bending action only is used, while Castigliano based on bending, shear, and thrust gives the minimum thrust. The maximum combined compressive stresses are presented in Table 4.4. It can be seen that *FE* and Castigliano with bending, shear, and thrust produce the maximum combined compressive stress amongst all the methods. Again, the masonry design method is not being evaluated in Table 4.4. Castigliano with bending action gives the minimum combined stress values. The location of maximum combined stress using Castigliano's theorem is at the crown. However, the location of the maximum combined stress obtained from *FE* is near the supports for *L:h*≤6, while above this ratio the location of the maximum combined stress is at the crown. The same analysis was carried out for the parabolic arch and the results are presented in Tables 4.5 to 4.8.

Table 4.5. Horizontal reaction force of parabolic arch (kN) subjected to the *UDL* of 20 kN/m plus *SW* (*A1*)

L:h	*GSA*	masonry design	Castigliano (*M* only)	Castigliano (*M*, *F* and *T*)	Castigliano (Full actions)
2	72.97	72.70	73.46	73.41	73.45
3	105.30	105.50	106.04	105.89	105.95
4	138.10	138.76	139.17	138.84	138.93
5	171.10	172.27	172.60	171.97	172.08
6	204.10	205.92	206.20	205.13	205.27
7	237.00	239.66	239.91	238.22	238.39
8	269.80	273.47	273.68	271.19	271.38
9	302.40	307.31	307.50	303.98	304.19
10	334.90	341.18	341.35	336.56	336.79

- Results from the virtual work method are identical to those from Castigliano, bending action only

It is seen that similar to the circular arch, the horizontal reaction force of a parabolic arch (Table 4.5) grows when the *L:h* ratio is increased from 2 to 10.

Table 4.6. Maximum bending moments (*M*) and their location along the span (*x*) of parabolic arch subjected to the *UDL* of 20 kN/m plus *SW* (*A1*)

L:h	*GSA*		masonry design		Castigliano (*M* only)		Castigliano (*M*, *F* and *T*)		Castigliano (Full actions)	
	M (kNm)	*x* (m)	*M* (kNm)	*x* (m)	*M* (kNm)	*x* (m)	*M* (kNm)	*x* (m)	*M* (kNm)	*x* (m)
2	-3.55	5	5.29	1.5	-3.79	5	-3.54	5	-3.72	5
3	2.11	1.25	2.74	1.5	1.84	1	2.08	1.5	1.97	5
4	1.57	1.25	1.66	1.5	1.14	1	1.56	1.5	1.44	1.5
5	1.44	1.25	1.10	1.5	0.77	1	1.41	1.5	1.29	1.5
6	1.60	1.75	0.78	1.5	0.55	1	1.59	2.5	1.42	2
7	2.08	2.75	0.58	1.5	0.41	1	2.07	4	1.86	3.5
8	2.85	4.75	0.45	1.5	0.32	1	2.85	5	2.61	5
9	3.69	4.75	0.36	1.5	0.26	1	3.70	5	3.46	5
10	4.61	4.75	0.29	1.5	0.21	1	4.63	5	4.39	5

Table 4.7. Maximum thrust (kN) of parabolic arch subjected to the *UDL* of 20 kN/m plus *SW* (*A1*)

L:h	*GSA*	Castigliano (*M* only)	Castigliano (*M*, *F* and *T*)	Castigliano (Full actions)
2	168.8	169.92	169.89	169.91
3	178.3	179.49	179.39	179.43
4	197	198.34	198.1	198.16
5	220.3	221.95	221.45	221.54
6	246.2	248.4	247.51	247.62
7	273.8	276.7	275.23	275.38
8	302.5	306.25	304.02	304.19
9	331.8	336.70	333.48	333.68
10	361.5	367.80	363.34	363.56

Table 4.8. Maximum combined compressive stresses of parabolic arch (σ) and their location along the span of the arch (x) subjected to the *UDL* of 20 kN/m plus *SW*

L:h	*GSA*		Castigliano (*M* only)		Castigliano (*M*, *F* and *T*)		Castigliano (Full actions)	
	σ(MPa)	x(m)	σ(MPa)	x(m)	σ(MPa)	x(m)	σ(MPa)	x(m)
2	0.69	1	0.69	1	0.70	1	0.69	1
3	0.65	1	0.64	0.5	0.65	1	0.65	1
4	0.69	1	0.68	0.5	0.69	1	0.69	0.5
5	0.76	1	0.75	0.5	0.76	1	0.76	0.5
6	0.85	1	0.83	0.5	0.86	1	0.85	1
7	0.96	1.5	0.92	0	0.97	1.5	0.96	1.5
8	1.09	3	1.02	0	1.10	3	1.10	2.5
9	1.25	5	1.12	0	1.26	5	1.24	5
10	1.42	5	1.23	0	1.43	5	1.41	5

Comparing the equivalent set of results in Tables 4.1 and 4.5, the horizontal reaction force for a parabolic arch at *L:h*=2 is about 17.5% higher than the semi-circular arch using the different methods of analysis, except for the masonry design method. This difference decreases when the arches become shallower, and the parabolic arch shows about 0.5% higher horizontal reaction force than the circular one for *L:h*=10. In the case of masonry design method the differences is < 1% for *L:h*>2. This shows a weakness in using the masonry design method for analysing arches in which the effect of the arch form is not being recognized. The horizontal reaction force is at its maximum using Castigliano's theorem with bending action only and the virtual work method for the parabolic arch and load case *A1*. The effect of including the coupling term in the results of the horizontal reaction force obtained from Castigliano's theorem increases with the increase of the *L:h* ratio from 2 to 7 when compared with Castigliano's theorem due to bending, shear, and thrust. This trend is similar for both parabolic and circular arches. Above the *L:h* ratio of 7, the differences between the horizontal reaction force obtained from Castigliano with full structural action and Castigliano with bending, thrust, and shear decreases. Obviously, when the different methods of analysis are compared, the findings of the

FE method are analogous to those acquired using Castigliano's theorem when the strain energy is arising from bending, shear, and thrust (see Tables 4.2 to 4.6). The value of the maximum bending moment of parabolic and circular arches decreases with the increase of the *L:h* ratio when masonry design, virtual work, and Castigliano due to bending action only are applied to analyse the arches. This proves the deficiency of using these methods for analysing arch structures. The decreasing trend of the maximum bending moment with the increase of the *L:h* ratio is unsatisfactory for a high value of *L:h* ratio when applying these methods. But, the decreasing trend of the maximum bending moment is reversed to increasing using *FE* and Castigliano's method derived from other actions in addition to the bending term. Therefore, once the height becomes very small, the bending moment becomes greatest owing to the behaviour of a curved beam in elevation rather than the behaviour of a pure arch. The optimal range of the *L:h* ratio of the parabolic arch, with the minimum value of the maximum bending moment, occurs at the *L:h* ratio of about 5 using the *FE* method, Castigliano's theorem based on bending, thrust, and shear, and Castigliano's theorem with full structural actions. The thrust of the parabolic arch using the considered methods of analysis is higher than the thrust of the circular arch (from Tables 4.3 and 4.7). But the difference between the magnitude of the thrust of parabolic and circular arches becomes less with the increase of the *L:h* ratio. It can be seen from Tables 4.3 and 4.7 that the thrust of the parabolic arch is less than 1% higher than the circular one for *L:h* ratios above 6. Similar to the results of the horizontal reaction force in the case of using Castigliano's theorem, the thrust of the circular and parabolic arches is the maximum and minimum when Castigliano is based on bending action only and bending, shear, and thrust respectively. Moreover, the effect of the coupling term is less than 0.1%, which is negligible over the full range of *L:h* ratios when comparing the last two columns of Table 4.3 and similarly in Table 4.7. The maximum combined compressive stresses for the parabolic arch are presented in Table 4.8,

while the masonry design method is ignored because of the great difference of the results calculated from the masonry design method and other methods. Using all methods, the location of the maximum combined stress of the parabolic arch is near the supports for *L:h* ratios less than 8. Then this location moves to the crown, except in the case of Castigliano with bending action only, which from Table 4.6 gives the location of the maximum combined stress near the supports for all *L:h* ratios. It is interesting that the trend of decreasing maximum combined stress with increase of the *L:h* ratio reversed when applying Castigliano with bending only for both the circular and parabolic arches. The reason for this finding is the significant effect of increasing thrust with the *L:h* ratio in the calculation of the combined stresses. This confirms the necessity of considering the thrust action of the arch through its analysis. The maximum combined stress reaches its minimum at *L:h* ratios of 6 and 3 for the circular and parabolic arches individually using *FE* and the Castigliano approach (see Tables 4.4 and 4.8). The trend of change in the combined stress with increasing *L:h* ratio is the same for all categories of the Castigliano approach. However, the differences between the magnitude of the maximum combined stress from Castigliano with bending action only and the other two categories of Castigliano increase from less than 1% to about 13% and 18% when the *L:h* ratio increases from 2 to 10 in the case of the parabolic and circular arches, respectively. Over the full range of *L:h* ratios the effect of the coupling term is less than 2% and 3% for the parabolic and circular arches when Castigliano with bending, shear, and thrust is compared with Castigliano with full structural action. Since the maximum combined stress and maximum bending moment of the parabolic arch reach their minimum for *L:h* ratios between 2 and 4 and *L:h* ratios between 3 and 5, respectively, the effect of each term of the strain energy in Castigliano's theorem is examined for *L:h*=4. The results from the Castigliano approach based on bending, shear, and thrust give horizontal reactions that are 0.24% lower than the horizontal reaction force in the case of bending action. The

term including shear and thrust actions has a 27% and 1.4% greater effect on the maximum bending moment and maximum combined compressive stress than Castigliano's theorem and bending action only at the *L:h* ratio of 4. The results are listed in Tables 4.6 and 4.8., which shows this effect increases with increasing *L:h* ratio.

To assess the effect of the coupling term on the parabolic arch, the structural reactions resulting from Castigliano based on full structural action and Castigliano arising from the linear combination of bending, shear and thrust are compared. The coupling term causes the horizontal reaction force to be 0.06% higher at *L:h*=4 (see Table 4.5), while the maximum bending moment and combined compressive stress from Tables 4.6 and 4.8 are lower by 7.4% and 0.4% at this geometric ratio. Generally, the bending/thrust coupling term has a slightly decreasing effect on the results of the bending moments from the Castigliano method including bending, shear, and thrust terms. Similar to the circular arch, the results from Castigliano due to bending action only match the results from the virtual work method. The favourable comparison of numerical prediction from *GSA* with the calculations from Castigliano's approach, considering bending, shear, and thrust shows the validity of the *FE* model to reliably simulate the response of parabolic and circular arches.

Comparing the results of the horizontal reaction force with the maximum bending moment suggests that even a 0.1% change in the value of the horizontal reaction force leads to a 10% change in the value of the maximum bending moment in the arch structures in this study.

The results of the horizontal reactions obtained from the Castigliano approach are next to be compared with those calculated using static theory. To do so, no *SW* is applied to the parabolic arch (load case *A4* defined in Chapter 3). The horizontal reaction force (*H*) for a parabolic arch under *UDL* only obtained from static theory is equal to $wL^2/8h$, which causes the parabolic arch to become momentless. The

comparison of the horizontal reaction force obtained from the methods used in this research and static theory for the parabolic arch subjected to load case *A4* is given in Table 4.9. The same comparison is carried out for the maximum bending moments in the parabolic arches obtained from the aforementioned methods for load case *UDL* only. The results are presented in Table 4.10.

Table 4.9. Horizontal reaction force of parabolic arch (kN) subjected to the *UDL* of 20 kN/m only

L:h	*GSA*	masonry design	Castigliano (*M* only)	Castigliano (*M*, *F* and *T*)	Castigliano (Full actions)	Static theory $H=wL^2/(8h)$
2	49.97	50	50	49.97	49.99	50
3	74.9	75	75	74.89	74.94	75
4	99.77	100	100	99.76	99.8	100
5	124.6	125	125	124.54	124.6	125
6	149.2	150	150	149.22	149.3	150
7	173.8	175	175	173.77	173.9	175
8	198.2	200	200	198.18	198.3	200
9	222.5	225	225	222.42	222.6	225
10	246.5	250	250	246.49	246.7	250

- Results from the virtual work method are identical to those from Castigliano, bending action only

Table 4.6 shows that the horizontal reaction forces calculated from statics is in agreement with calculation by the masonry design and virtual work methods, and the Castigliano approach presuming bending action only. This is because in the energy approach (Castigliano based on bending action only and virtual work) the horizontal reaction force (*H*) is obtained from Equs. (4.13) and (4.14). Substituting the bending moment at any cross-section of the arch, which is $M = M_0 - Hy$ into Equs. (4.2) and (4.12) in the case of using Castigliano's theorem and virtual work respectively.

Table 4.10. Maximum bending moment in parabolic arch (kNm) subjected to the *UDL* of 20 kN/m only

L:h	*GSA*	masonry design	Castigliano (*M* only)	Castigliano (*M*, *F* and *T*)	Castigliano (Full actions)	Static theory $H=wL^2/(8h)$
2	0.17	0	0	0.17	0.05	0
3	0.36	0	0	0.35	0.21	0
4	0.61	0	0	0.60	0.44	0
5	0.93	0	0	0.92	0.75	0
6	1.31	0	0	1.31	1.13	0
7	1.76	0	0	1.76	1.58	0
8	2.28	0	0	2.28	2.10	0
9	2.87	0	0	2.86	2.69	0
10	3.52	0	0	3.51	3.34	0

- Results from the virtual work method are identical to those from Castigliano, bending action only

The horizontal reaction force is given as below. It should be noted that when applying virtual work Equ. (4.2), only the first term for flexural energy is taken into account.

$$M = M_0 - Hy \;\&\; M_0 = (\frac{w}{2})x(L-x) \rightarrow$$
$$\frac{1}{EI}\int_0^S \left((\frac{w}{2})x(L-x) - H\frac{4h}{L}(x-\frac{x^2}{L})\right)\left(-\frac{4h}{L}(x-\frac{x^2}{L})\right)\mathrm{d}s = 0 \Rightarrow H = \frac{wL^2}{8h} \qquad (4.13)$$

$$M = M_0 - Hy \;\&\; M_0 = (\frac{w}{2})x(L-x) \rightarrow$$
$$H = \frac{\int_0^S \frac{M_0 y}{EI}\mathrm{d}s}{\int_0^S \frac{y^2}{EI}\mathrm{d}s} = \frac{\int_0^S (\frac{w}{2})x(L-x)\frac{4h}{L}(x-\frac{x^2}{L})\mathrm{d}s}{\int_0^S \left(\frac{4h}{L}(x-\frac{x^2}{L})\right)^2 \mathrm{d}s} = \frac{wL^2}{8h} \qquad (4.14)$$

where *y* is the parabolic function of $\left((4h/L)(x-x^2/L)\right)$.

Accordingly, the parabolic arch is momentless for any *L:h* ratio using these methods (see Table 4.10). When arches become shallow the arch behaviour transfers to that of a horizontal beam. Hence, there would be a moment for shallow arches and it is predicted that the bending moments will grow with increase of the *L:h* ratio in the

case of shallow arches. The reason for having a zero bending moment for all *L:h* ratios of the parabolic arch under *UDL* when using masonry design, virtual work, and the Castigliano principle with bending action only is that these methods ignore the section properties for non-deformable bodies. Since in the linear elastic small displacement static theory it is presumed that the structure remains undeformed, the moments are not estimated well by this theory for shallow arches. For the problem analysed the maximum bending moment is < 1 kNm for *L:h* ratios < 6 using *GSA* and the Castigliano approach with bending, shear, and thrust, and the Castigliano approach with full structural action. This can be taken as a negligible moment. Therefore, the parabolic arch can be considered as momentless using all the methods of analysis when *L:h*<6. Since the optimum range of the *L:h* ratio with the criterion of minimum combined stress is found to be between 2 and 4, it can be recommended for practice to use the parabolic arch generally in this *L:h* ratio range.

In general, concerning the masonry design method, the assumption that an arch acts like a three-pin arch has a significant impact on the results of bending moment; in particular, once bending moments are considered near the crown of the arch. The number of discretisations of the arch into segments also produces a numerical error. In the case of applying the virtual work method to two-pin arches, the assumption that displacements are only caused by bending inevitably leads to inaccuracies in the computed horizontal reaction forces. As shown in Tables 4.1 to 4.10, the results from *FE* work strongly correlate with those obtained from Castigliano's theory due to bending, shear and thrust. Finally, despite the 'reasonable agreement' of the numerical prediction for the horizontal reaction force, the same cannot be said of the bending moment and combined compressive stress; the results have shown that the different analysis methods predicted different values of the maximum bending moment and maximum combined stress at different locations within the arch. Overall, it can be concluded that, when having an arch behaviour (*L:h*<6 for the

parabolic arch in this study due to producing zero bending moment when the parabolic arch is subjected to the *UDL* only load case), static analysis assuming the arch as a rigid unreformed body is applicable, while, in the case of shallow arches, the moments are not estimated well by linear elastic static theory.

4.5. Exploring the thickness effect on horizontal reaction force using the Castigliano approach

The effect of the arch thickness on the horizontal reaction force and bending moment was studied in Section 3.8 using *GSA* analysis. Regarding this effect, the different terms in the Castigliano principle were assessed. The results obtained using Castigliano's approach are then compared with the *FE* results. Next, the horizontal reaction force of circular and parabolic arches with 200, 300, and 400 mm thickness are calculated.

Table 4.11. Horizontal reaction force (kN) of circular arch with different thicknesses (mm) using Castigliano approach with different categories (*A1*)

L:h	Castigliano (*M* only)			Castigliano (*M*, *F* and *T*)			Castigliano (Full actions)		
	d=200	*d*=300	*d*=400	*d*=200	*d*=300	*d*=400	*d*=200	*d*=300	*d*=400
2	54.44	60.44	66.44	54.43	60.41	66.37	54.45	60.45	66.47
3	89.00	98.45	107.91	88.94	98.32	107.66	88.98	98.41	107.83
4	121.34	133.83	146.32	121.22	133.53	145.75	121.27	133.67	146.02
5	153.01	168.46	183.92	152.78	167.90	182.84	152.86	168.11	183.24
6	184.41	202.82	221.22	184.01	201.86	219.41	184.13	202.15	219.96
7	215.67	237.04	258.40	215.05	235.54	255.58	215.19	235.89	256.25
8	246.86	271.19	295.51	245.94	268.98	291.37	246.09	269.35	292.08
9	278.00	305.29	332.59	276.69	302.18	326.77	276.82	302.50	327.38
10	309.11	339.38	369.65	307.32	335.14	361.75	307.37	335.27	362.05

The analysis is conducted for the general load combination of *UDL* and *SW* (load case *A1*), and *UDL* only (load case *A4*) conditions. The same procedure is carried out to calculate the bending moment at the crown of the circular and parabolic arches. The results of the horizontal reaction force are presented in Tables 4.11 and

4.12 for load case *A1*. In this analysis, the strain energy is derived, firstly upon bending action only (*M* only), then due to bending, shear, and thrust action (*M*, *F*, and *T*), and finally with full structural action.

Table 4.12. Horizontal reaction force (kN) of parabolic arch with different thicknesses (mm) using Castigliano approach with different categories (*A1*)

L:h	Castigliano (*M* only)			Castigliano (*M*, *F* and *T*)			Castigliano (Full actions)		
	d=200	*d*=300	*d*=400	*d*=200	*d*=300	*d*=400	*d*=200	*d*=300	*d*=400
2	65.64	73.46	81.28	65.62	73.41	81.18	65.63	73.45	81.25
3	95.69	106.04	116.38	95.63	105.89	116.09	95.66	105.95	116.21
4	126.12	139.17	152.23	125.98	138.84	151.58	126.02	138.93	151.75
5	156.74	172.60	188.47	156.48	171.97	187.24	156.53	172.08	187.46
6	187.47	206.20	224.94	187.03	205.12	222.86	187.09	205.27	223.13
7	218.27	239.90	261.54	217.58	238.22	258.29	217.65	238.39	258.61
8	249.12	273.68	298.24	248.10	271.19	293.45	248.18	271.38	293.81
9	280.00	307.50	335.00	278.56	303.98	328.25	278.65	304.19	328.65
10	310.90	341.35	371.80	308.94	336.56	362.63	309.04	336.80	363.07

For load case *A1* the results of bending moment at the crown of the circular and parabolic arches are then reported in Tables 4.13 and 4.14. It can be seen that changing the arch thickness has the same effect on both the circular and parabolic arches, except for bending moment at the crown of parabolic arch and a *L:h* ratio of 4. (*L:h* =4 is highlighted in the Table 4.14)

Table 4.13. Bending moment at the crown (kNm) of circular arch with different thicknesses (mm) using Castigliano approach with different categories (*A1*)

L:h	Castigliano (*M* only)			Castigliano (*M*, *F* and *T*)			Castigliano (Full actions)		
	d=200	*d*=300	*d*=400	*d*=200	*d*=300	*d*=400	*d*=200	*d*=300	*d*=400
2	46.29	50.54	54.78	46.36	50.72	55.14	46.26	50.48	54.66
3	19.56	21.14	22.72	19.73	21.57	23.57	19.62	21.29	22.99
4	10.75	11.57	12.39	11.05	12.31	13.82	10.91	11.97	13.13
5	6.79	7.30	7.80	7.26	8.43	9.96	7.09	8.01	9.14
6	4.69	5.02	5.36	5.35	6.62	8.39	5.15	6.14	7.47
7	3.43	3.67	3.92	4.32	5.81	7.95	4.11	5.31	6.99
8	2.62	2.80	2.99	3.77	5.56	8.17	3.58	5.09	7.27
9	2.06	2.21	2.35	3.51	5.67	8.83	3.37	5.32	8.14
10	1.67	1.79	1.90	3.45	6.02	9.80	3.41	5.89	9.50

Table 4.14. Bending moment at the crown (kNm) of parabolic arch with different thicknesses (mm) using Castigliano approach with different categories (*A1*)

L:h	Castigliano (*M* only)			Castigliano (*M*, *F* and *T*)			Castigliano (Full actions)		
	d=200	*d*=300	*d*=400	*d*=200	*d*=300	*d*=400	*d*=200	*d*=300	*d*=400
2	2.53	3.79	5.06	2.43	3.54	4.57	2.50	3.72	4.92
3	1.20	1.79	2.39	1.00	1.29	1.42	1.08	1.50	1.83
4	0.69	1.03	1.38	**0.35**	**0.19**	**0.25**	**0.44**	**0.42**	**0.18**
5	0.45	0.67	0.89	0.07	0.60	1.56	0.03	0.37	1.12
6	0.31	0.47	0.62	0.42	1.33	2.84	0.32	1.09	2.38
7	0.23	0.35	0.46	0.75	2.06	4.18	0.65	1.82	3.72
8	0.18	0.27	0.35	1.09	2.85	5.63	0.99	2.61	5.18
9	0.14	0.21	0.28	1.45	3.70	7.22	1.36	3.46	6.77
10	0.11	0.17	0.23	1.84	4.63	8.95	1.75	4.39	8.50

The horizontal reaction forces for both arch shapes increases with increase of the arch thickness for all categories of Castigliano, as seen by the results in Tables 4.11 and 4.12. This increment falls from about 10% to 7% as the *L:h* ratio grows from 2 to 10. The effect of each term of the Castigliano approach is significant when bending moments are considered at the crown of the circular and parabolic arches. Comparing the numbers in Tables 4.13 and 4.14 it is seen that the effect of using different arch thicknesses on the bending moments at the arch crown is far greater for the parabolic arch than the circular one. In the case of bending action only and the circular arch, each 100 mm increase in the arch thickness results in a roughly 6–8% increase in the bending moment, while this increase lessens with growth of the *L:h* ratio. The bending moment at the crown of the parabolic arch increases constantly, by 33% and 25% for all *L:h* ratios, when the thickness of the arch changes from 200 to 300 mm and from 300 to 400 mm respectively for Castigliano with the bending action considered. It is found that the bending moment at the crown of the parabolic arches is decreasing on increasing arch thickness at *L:h* ratio of 4, using Castigliano approach with full structural actions. Also, the bending moment is decreasing when the thickness is increasing from 200 to 300 mm using *FE* and Castigliano theorem based on bending, thrust and shear forces. This trend

is ignored due to the low level of bending moment at the crown of parabolic arch for *L:h* ratio of 4. The bending moment at the crown of both types of arch decreases with increase of the *L:h* ratio when the strain energy in the Castigliano principle with bending action only. When the thickness of the arch is increased by 100 mm, coupling of bending and thrust generally has a decreasing effect on the bending moments at the crown of both the circular and parabolic arches compared with Castigliano due to bending, shear, and thrust. The coupling term has the maximum effect when the thickness of the arch is changed, for *L:h* ratio of 5for the parabolic and 8 for the circular arch. Above these ratios, the effect of the coupling term on the crown bending moment starts to decrease. Also, it is seen from the tabulated results that the bending moment at the crown of the circular arch reaches its minimum at different *L:h* ratios for load case *A1* when the arch thickness is increased. The same can be said in the case of the parabolic arch. From Table 4.13 the minimum bending moment is seen to occur at a *L:h* ratio of between 9 and 10 for the circular arch and an arch thickness of 200 mm, whereas the location where the bending moment reaches its minimum changes to *L:h* equal to 8 or 7 for thicknesses of 300 or 400 mm, respectively. Similarly, the location of the minimum bending moment at the crown of the parabolic arch is *L:h*=5 for an arch thickness of 200 mm. Then this location moves to the *L:h* ratio equal to 4 for the 400 mm arch thickness. In order to evaluate each category of Castigliano when there is no self-weight, the effect of changing the thickness is studied when the self-weight of the arch is ignored. Tables 4.15 and 4.16 list the horizontal reaction forces of circular and parabolic arches for load case *A4*.

For load case *A4* Tables 4.17 and 4.18 illustrate the variations in bending moment at the crown of the circular and parabolic arches.

Table 4.15. Horizontal reaction force (kN) of circular arch with different thicknesses (mm) using Castigliano approach with different categories (*A4*)

L:*h*	Castigliano (*M* only)			Castigliano (*M*, *F* and *T*)			Castigliano (Full actions)		
	d=200	*d*=300	*d*=400	*d*=200	*d*=300	*d*=400	*d*=200	*d*=300	*d*=400
2	42.44	42.44	42.44	42.43	42.42	42.40	42.44	42.44	42.44
3	70.08	70.08	70.08	70.04	69.99	69.92	70.06	70.04	70.00
4	96.36	96.36	96.36	96.26	96.13	95.96	96.30	96.22	96.12
5	122.10	122.10	122.10	121.91	121.67	121.33	121.97	121.81	121.59
6	147.60	147.60	147.60	147.26	146.84	146.27	147.35	147.05	146.64
7	172.94	172.94	172.94	172.41	171.75	170.84	172.53	172.01	171.30
8	198.20	198.20	198.20	197.41	196.43	195.07	197.53	196.70	195.54
9	223.41	223.41	223.41	222.28	220.88	218.96	222.36	221.08	219.30
10	248.57	248.57	248.57	247.02	245.11	242.49	247.02	245.11	242.49

Table 4.16. Horizontal reaction force (kN) of parabolic arch with different thicknesses (mm) using Castigliano approach with different categories (*A4*)

L:*h*	Castigliano (*M* only)			Castigliano (*M, F* and *T*)			Castigliano (Full actions)		
	d=200	*d*=300	*d*=400	*d*=200	*d*=300	*d*=400	*d*=200	*d*=300	*d*=400
2	50	50	50	49.98	49.97	49.94	50	49.99	49.98
3	75	75	75	74.95	74.89	74.81	74.97	74.94	74.89
4	100	100	100	99.89	99.76	99.57	99.92	99.82	99.69
5	125	125	125	124.79	124.54	124.18	124.83	124.62	124.33
6	150	150	150	149.65	149.22	148.61	149.70	149.32	148.80
7	175	175	175	174.45	173.77	172.83	174.51	173.89	173.04
8	200	200	200	199.19	198.18	196.79	199.25	198.32	197.03
9	225	225	225	223.85	222.42	220.47	223.92	222.58	220.74
10	250	250	250	248.43	246.49	243.83	248.51	246.66	244.13

In contrast with load case A1, the horizontal reaction forces of the parabolic and circular arches reduce with the increasing thickness for load case A4, although this reduction is very small.

Table 4.17. Bending moment at the crown (kNm) of circular arch with different thicknesses (mm) using Castigliano approach with different categories (*A4*)

L:h	Castigliano (*M* only)			Castigliano (*M*, *F* and *T*)			Castigliano (Full actions)		
	d=200	*d*=300	*d*=400	*d*=200	*d*=300	*d*=400	*d*=200	*d*=300	*d*=400
2	37.79	37.79	37.79	37.85	37.92	38.02	37.79	37.79	37.79
3	16.39	16.39	16.39	16.53	16.70	16.94	16.46	16.54	16.65
4	9.11	9.11	9.11	9.36	9.67	10.09	9.26	9.45	9.70
5	5.79	5.79	5.79	6.18	6.66	7.33	6.05	6.37	6.82
6	4.01	4.01	4.01	4.57	5.26	6.22	4.41	4.91	5.61
7	2.94	2.94	2.94	3.70	4.64	5.94	3.53	4.27	5.29
8	2.24	2.24	2.24	3.24	4.47	6.16	3.09	4.13	5.57
9	1.77	1.77	1.77	3.03	4.58	6.71	2.93	4.36	6.33
10	1.43	1.43	1.43	2.98	4.89	7.51	2.98	4.89	7.51

Table 4.18. Bending moment at the crown (kNm) of parabolic arch with different thicknesses (mm) using Castigliano approach with different categories (*A4*)

L:h	Castigliano (*M* only)			Castigliano (*M*, *F* and *T*)			Castigliano (Full actions)		
	d=200	*d*=300	*d*=400	*d*=200	*d*=300	*d*=400	*d*=200	*d*=300	*d*=400
2	0.00	0.00	0.00	0.08	0.17	0.30	0.08	0.05	0.08
3	0.00	0.00	0.00	0.16	0.35	0.63	0.16	0.21	0.36
4	0.00	0.00	0.00	0.27	0.60	1.07	0.27	0.44	0.78
5	0.00	0.00	0.00	0.41	0.92	1.63	0.41	0.75	1.33
6	0.00	0.00	0.00	0.58	1.31	2.31	0.58	1.13	2.01
7	0.00	0.00	0.00	0.78	1.76	3.10	0.78	1.58	2.80
8	0.00	0.00	0.00	1.02	2.28	4.01	1.02	2.10	3.71
9	0.00	0.00	0.00	1.28	2.86	5.04	1.28	2.69	4.73
10	0.00	0.00	0.00	1.57	3.51	6.17	1.57	3.34	5.87

It was expected that the horizontal reaction of arches does not change when the thickness of the arch in each category of the Castigliano approach is varied in the case of the *UDL* only load condition. But, this is true, just for case of Castigliano and bending action only. This shows the effect of thickness in the calculation of the horizontal reaction force when thrust, shear and the coupling of bending and thrust are all taken into account. The reason for the change in the horizontal reaction force with the changes in arch thickness when the arch is assumed to be weight-less, relates to the gyration of radius, which is considered in the other categories of

Castigliano's theorem in addition to the bending action only category. Subsequently, as can be seen in Equ. (4.15), changing the thickness (*d*) of the rectangular cross-section of the arches in this study affected the gyration of radius (g^2), hence, all the terms related to the gyration radius in the strain energy will be changed.

$$\frac{1}{g^2} = \frac{A}{I} = \frac{bd}{\frac{bd^3}{12}} \Rightarrow \frac{1}{g^2} = \frac{12}{d^2} \tag{4.15}$$

The horizontal reaction force decreases when increasing the arch thickness for both types of arches for load case *A4* (see Tables 4.15 and 4.16). However, this decrease is less than 1% for the full range of *L:h* ratios for both arches. The bending moment at the crown of the circular arch is the same for any arch thickness for Castigliano and bending action only in the case of the *UDL* only load condition. Since the parabolic arch is momentless under *UDL* only, the Castigliano approach with bending action only presents the bending moment of the parabolic arch at the crown as zero. Meanwhile, the bending moment at the crown of the parabolic arch from Table 4.18 increases with the arch thickness when the structure is deformable. This bending moment is mostly < 1 kNm for *L:h* ratios less than 5 which is negligible for practice. The behaviour of change in the bending moment at the crown for both the circular and parabolic arches is similar to load case *A1*.

Moreover, changing the depth of the arch rib causes the *UDL* to self-weight (*UDL:SW*) ratio to change. The changing of the *UDL:SW* ratio with the arch rib thickness is shown in Figure 4.4. As a result, the relation of the *UDL:SW* ratio and the horizontal reaction force (*H*) is found from comparing results in Figure 4.4 and Table 4.16.

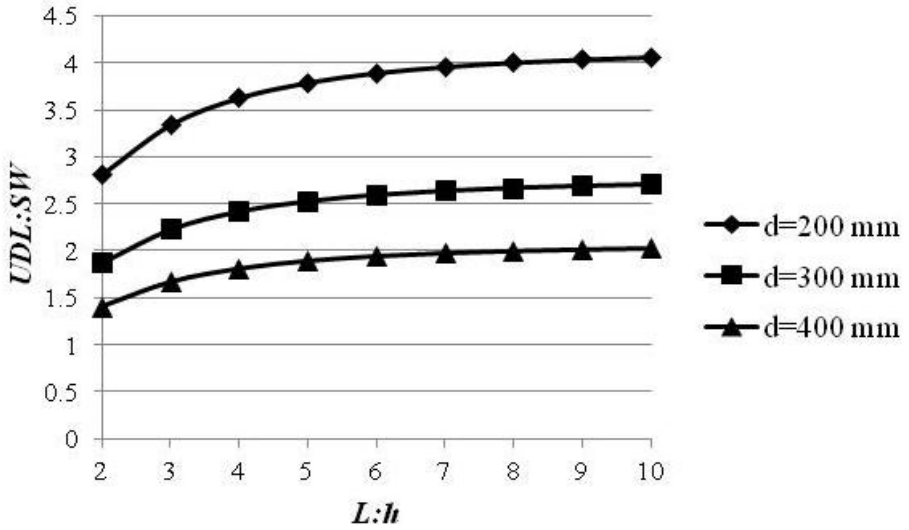

Figure 4.4. The *UDL:SW* ratio against *L:h* ratio for different rib thicknesses of a parabolic arch subjected to 20 kN/m *UDL* only

In general, change in the *UDL:SW* ratio has a major impact on the value of the horizontal reaction force. As displayed in Figure 4.4, increase in the *L:h* ratio causes the *UDL:SW* ratio to grow as well, which is associated with the decreasing trend of the arc lengths. In this study when thickness is 300 mm, the range of change in the *UDL:SW* ratio is between 1.87 and 2.7 for *L:h* from 2 to 10. It can also be seen that reducing the *UDL:SW* ratio, which is preceded by increasing the thickness of the arch rib for each *L:h* ratio, causes the horizontal reaction force to increase. Finally, it is concluded that increasing the arch thickness generates a higher bending moment for the arch to resist. This finding is applicable to any arch form, *L:h* ratio, and applied load. However, increase in the arch thickness results in higher bending moments when the *L:h* ratio is increased. Therefore, reducing thickness leads to a reduction in the bending moment. The thickness has to meet the minimum limit for design based on material choice in order to carry the design loading safely over the design working life.

4.6. Exploring the shortening effect

It is seen that the horizontal reaction force of the arches obtained using all the analysis methods has an increasing trend with *L:h* ratios from 2 to 10. The force also increases for any load case and any arch thickness with increase of the *L:h* ratio. Tables 4.1, 4.5, 4.9, and 4.11 show this the rising horizontal reaction force for load cases *A1* and *A4*. But, as shown in Section 3.9 this reaction force for the parabolic arch for the *UDL* only load case, obtained using the *FE* method, will decrease for *L:h* ratios > 125. It was stated in Section 3.9 that the reason for this force decrease is related to the shortening effect. To explore whether the analysis methods include the effect of arch shortening or not, the horizontal reaction forces for the parabolic arch with the specifications defined in subsection 3.3.1 and load case *A1* are calculated for *L:h* ratios ranging from 2 to infinity. Table 4.19 compares the results from this parametric study.

As stated previously, the results from Castigliano with bending action only and the virtual work method are identical. It can be seen from the information in Table 4.19 that the horizontal reaction force increases with ratio *L:h* when applying the methods of the masonry design, virtual work, and Castigliano with bending. The effect of rib shortening is not considered in these aforementioned methods. It can be concluded that the predictions using any of these methods are not satisfactory for shallow arches.

The outcome is analogous for the results of the horizontal reaction force when using elastic linear static theory. The 1427 kN reaction force of the parabolic arch under load case *A1* reaches its maximum at 1434 kN for the *L:h* ratio of 85 in the case of applying Castigliano with bending, shear, and thrust, Castigliano with full structural action, and the *FE* method. For higher ratios the force starts to decrease until it vanishes when the shallow arch becomes a horizontal beam. Since shallow arches have approximately the same geometry, this conclusion can be applied to all types

of arch shapes. This analysis was also conducted for the parabolic arch and load case *A4*. The trend of changing horizontal reaction force with *L:h* ratio, when ignoring *SW,* matches the findings when considering load case *A1*. Therefore, the *FE* method, like the Castigliano approach due to bending, shear, and thrust, and Castigliano with all structural actions, involves the effect of rib shortening. This conclusion can be generalized for any load case and all three types of arches.

Table 4.19. Horizontal reaction force of parabolic arch (kN) subjected to the *UDL* of 20 kN/m plus *SW* (*A1*) using different methods of analysis

L:h	*GSA*	masonry design	Castigliano (*M* only)	Castigliano (*M*, *F* and *T*)	Castigliano (Full actions)
2	72.97	72.70	73.46	73.41	73.45
20	642.20	680.60	680.68	644.35	644.77
40	1106.00	1360.30	1360.34	1110.57	1111.03
60	1349.00	2040.20	2040.23	1354.94	1355.12
80	1425.00	2720.15	2720.17	1432.44	1432.26
85	1427.00	2890.14	2890.16	1434.44	1434.18
90	1424.00	3060.13	3060.15	1431.51	1431.17
100	1406.00	3400.12	3400.14	1414.06	1413.59
120	1342.00	4080.10	4080.11	1349.95	1349.29
200	1017.42	5070.70	6800.07	1027.59	1026.75
300	742.70	7606.10	10200.05	747.86	747.13
400	574.40	10141.90	13600.04	579.48	578.89
500	467.50	12678.17	17000.02	470.81	470.31

4.6.1. Shortening effect of flat arches

It was shown in Chapter 3 that the arches in the range of *L:h* ratios between 2 and 10 have their own shape properties which cannot be presumed as flat ones which could carry 90% of the applied load by developing bending moment. But for an in-depth exploration of both the arch behaviour and the analysis method, the shortening effect is discussed in the case of flat arches in this section. It was illustrated in Section 3.9 that the general form of Castigliano's approach (having full structural action for arches and with bending, shear, and thrust for beams) to

analyse arches involves the effect of rib shortening. Furthermore, the *FE* method in this research, which is based on Timoshenko's beam theory, includes a shortening effect as well. The arches were analysed using these methods for *L:h* ratios above 500. It was observed that the horizontal reaction force becomes smaller when increasing the *L:h* ratio beyond 500. There was no specific value for the *L:h* ratio at which the horizontal reaction force becomes zero. Also, the arch is expected to become a straight beam rather than a curved beam at the *L:h* ratio of 500. As a result, the horizontal reaction force at *L:h*=500 should be lower than the values given in Table 4.19. Consequently, there should be appropriate consideration of shallow arches. According to the theory, for a two-pin flat arch the last two terms of the general equation for the strain energy, i.e., Equ. (4.1), can be ignored (Timoshenko 1986). The strain energy is then expressed based on the bending and axial compression actions. As a result, the governing equation to calculate the horizontal reaction force or the thrust of the flat arch (Timoshenko 1986).

$$\frac{\partial U}{\partial H} = \frac{\mathrm{d}}{\mathrm{d}H}\int_0^s \left(\frac{M^2}{2EI} + \frac{T^2}{2EA}\right)\mathrm{d}s = 0 \tag{4.16}$$

Concerning a flat arch, a compression force *T* is assumed to be equal to the horizontal reaction force *H*. With this assumption and substituting expression for *M* into Equ. (4.16), the horizontal reaction force is by (Timoshenko 1986).

$$-\int_0^S \frac{(M_0 - Hy)y\mathrm{d}s}{EI} + \int_0^S \frac{H\mathrm{d}s}{AE} = 0 \Rightarrow H = \frac{\int_0^S \frac{M_0 y\mathrm{d}s}{EI}}{\int_0^S \frac{y^2\mathrm{d}s}{EI} + \int_0^S \frac{\mathrm{d}s}{AE}} = \frac{\int_0^S M_0 y\mathrm{d}s}{\int_0^S y^2\mathrm{d}s + g^2\int_0^S \mathrm{d}s} \tag{4.17}$$

where g^2 is the gyration of radius of the arch cross-section and M_0 is the bending moment calculated for a beam equivalent to the arch subjected to the same loading. The second term in the denominator of Equ. (4.17) corresponds to the effect of the

longitudinal compression or shortening in the flat arch. There is no specific approach to find the *L:h* ratio in which the arch can be counted as flat. But, as discussed in subsection 3.9.2, arches in this research are taken to be flat when *L:h* exceeds 16. Thus, Equ. (4.17) is applied to find the horizontal reaction force of the studied arches with *L:h*>16. The horizontal reaction force of the circular arch for load case *A1* is found using Castigliano with bending action only, Castigliano with bending and thrust action, and the Castigliano approach for flat arches, i.e., from Equ. (4.17) when *L:h*>16. The horizontal reaction forces using these methods are plotted in Figure 4.5. It can be seen that the force is very different for the case of flat arches. Equ. (4.17) has not been used in this previous PhD work because of the upper limit on the *L:h* ratio of 10.

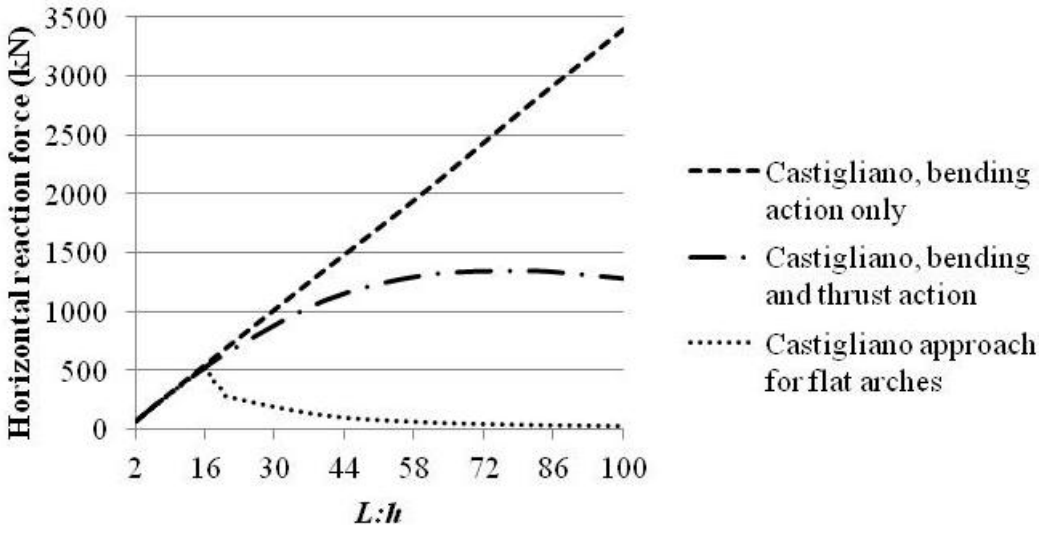

Figure 4.5. Effect of rib shortening to calculate the horizontal reaction force of a two-pin circular arch based on Castigliano's theory for load case *A1*

Figure 4.5 shows that the horizontal reaction force using Castigliano's method due to bending action only as given by dashed line increases with ratio *L:h*. When thrust action is also considered the trend given by the long dash dot line has reversed when ratio *L:h* reaches about 80. The same behaviour was seen in subsection 3.9.1

when the horizontal reaction force was obtained from *FE* analysis. Figure 4.5 also illustrates that the horizontal reaction force of the arch decreases dramatically when Equ. (4.17) is applied for the flat arch case. Also, as the arch height is reduced to 0.1 m, the horizontal reaction for the 10 m span shallow arch vanishes. Meanwhile, the acquired horizontal reaction force when the strain energy is based on bending and thrust action is >1000 kN for the *L:h* =100. Therefore, obtaining the limit of the arch shallowness allowed a conclusion to be drawn as to which equation is required to find the horizontal reaction force.

Results for the horizontal reaction force using all of the analysis methods are very close to each other when the *L:h* ratio < 10. One conclusion this finding establishes is that there is no need to consider rib shortening effect for the working range of *L:h* ratios in this study. This is because the arches are not considered as flat ones in this range of *L:h* ratios. Furthermore, the importance of taking the thrust and shear action into account in Castigliano's method in order to calculate the horizontal reaction force is greater for higher *L:h* ratios. It has been shown that small changes in the horizontal reaction force have a significant influence on the results of structural action effects such as, bending moment, combined stresses, and displacements.

4.7. Concluding Remarks

In this chapter different analysis methods were compared against each other. As the findings from analysis of different arch shapes using multiple methods show, the resulting effects of structural actions are notably influenced by both the arch shape and the span-to-height ratio.

Comparing the different methods of arch analysis, it was shown that Castigliano's approach considering strain energy due to full structural actions is a comprehensive analysis method. This method was used to validate the approximate methods of

arch analysis. Therefore, *GSA* software is deemed to be a credible analysis method for arch structures. However, arch shapes are modelled by means of series of straight lines in this finite element analysis software, which unavoidably led to some numerical approximations. The results from the approximate analytical methods were also unsatisfactory because of the assumptions made in their models for the arch problem. When the masonry design method is taken into consideration, the assumption that the arch acts like a three-pin arch has a significant impact on the results. In particular, once the internal moments are considered near the crown of the arch, the effect of this assumption is highlighted. Furthermore, the assumption that arches work only in flexural, in order to find the reaction forces, inevitably leads to inaccuracies related to the results acquired using the virtual work method. In addition, for arches with other than a semi-circular profile, to avoid complicated integrals in the process of finding the horizontal reaction force, the second moment of area (*I* value) of the cross-section is assumed to vary across the span of the arch.

The effect of arch thickness on the horizontal reaction force and bending moment at arch crown was studied. Consequently, it was demonstrated that generally bending moment at the crown increases with increase of the arch thickness. It was correspondingly shown that the effect of introducing rib shortening into Castigliano's theory should be considered when calculating the horizontal reaction force of flat arches. The limit of the ratio *L:h* from subsection 3.9.2 at which an arch is assumed to become a curved beam in elevation is 16 in this study.

Moreover, good agreement has been achieved between the results produced by *GSA* finite element simulation and analytical treatment based on Castigliano's principle with full structural action. The worst performing analysis method to predict arch behaviour is masonry design.

Chapter 5 : Analytical form-finding of two-pin arch

5.1. Introduction

The focus of this investigation is on the prediction of the shape for momentless arches involving an analytical form-finding approach. The purpose of studying the behaviour of known shapes of arches in the Chapters 3 and 4 was the basis of finding the optimal arch shape. This exploration is carried out for two-dimensional pin-ended arches with a constant cross-section. In the traditional procedure of designing an arch structure, the shape is determined from the outset (Curtin et al. 2006). However, this method of design may lead to an inefficient form. The optimal form of arches is required, not just to prevent the collapse under the applied load, but to make them durable and safe under environmental loading as well as cost effective and aesthetically pleasing. So far, it has been shown in previous chapters that the structural response is directly related to the shape of the arch as well as the *L:h* ratio. The fact that small changes in the arch shape may have a major effect on the behaviour of the arch was also discussed. It was demonstrated in Section 3.7 of that the parabolic arch produces the minimum magnitude of bending moment, combined stresses, and maximum displacements when the uniformly distributed load (*UDL*) is greater than the self-weight (*SW*), that is, *UDL:SW* > 1, for the full range of *L:h* ratios. Hence, when the deck weight or *UDL* is much greater than the arch weight or *SW*, the parabolic form is preferred in design, using the criterion of minimum bending moments and minimum combined stresses. In contrast, it was shown in Chapter 3 that the structural actions of the catenary arch are smaller than two other known shapes of arches when *UDL:SW* < 1. In particular, when the weight of the arch significantly exceeds *UDL*, the catenary arch is the preferable form of arch, assuming a purely thrust structure as a principle of optimality. It was also shown in Section 3.7 that, in the case of *UDL:SW* = 1, the parabolic arch

behaves similarly to the catenary arch. The aforementioned comparisons illustrated which arch shape is preferable under a given load condition.

The optimal forms of arch structures that are momentless are determined in this chapter. To find the optimal form of structures, structural optimization is a well known approach which relies on science and is generally based on existing rigid structures. However, form-finding requires creativity as well as engineering science in favour of finding an optimal form. The form-finding methodology presents new insights and advances impressive prospects for the safe and durable design of arch forms. Pin-ended arches are to be subjected to static loading, including the general combination of *SW* and *UDL*. An analytical method that was presented by Brew (2013) was used by the author to obtain numerical predictions for the form-fining of momentless arches for any *L:h* ratio and three categories of *UDL*:*SW* ratios. The categories are: (1) *UDL*:*SW* > 1 or the *UDL*-dominant condition; (2) *UDL* = *SW*; (3) *UDL*:*SW* < 1 or the *SW*-dominant condition. Each category gives one functional relationship for arch shape as a function of loading.

To find the momentless arch shape, it is assumed that any point on the arch is in equilibrium. The equilibrium equations consist of equilibrium in the *x* and *y* directions, and rotational equilibrium is used to demonstrate the necessary and sufficient condition for a momentless arch. In this regard, the principle of zero bending action will be applied in rotational equilibrium, which ensures zero shear force when establishing the vertical equilibrium equations. The vertical equilibrium equation is then solved by an iterative process with the characteristic of the optimal known shape arch for considered boundary conditions and load case as initial inputs. The optimal two-pin rib arch is investigated based on the assumption that the weight of the supporting structure between arch and deck is negligible. The arch structure is presumed to be stiff enough that linear elastic deflections under imposed loading do not have an impact on the arch profile. Finally, the preference of

using the momentless arch is shown through comparing its maximum deflection and first failure of the arch cross-section with those for the parabolic arch in the case of *UDL:SW* > 1.

5.2. Optimality criterion of two-pin arches

The efficiency of arches is when they transmit loads to the foundations in compression. The optimal shape of arch can be achieved when the bending moments are diminished. This leads to an arch that resists loading by developing compressive forces in a state of pure compression. A momentless arch is suitable when using concrete as a construction material because of its relatively strong compressive strength. Moreover, decreasing the magnitude of the bending moment in arches leads to a smaller stress distribution, deflection, and shear forces.

Since arch structures are diagnosed as compressive forms, a momentless shape of arch has to be considered as the optimal form. It has been stated previously in subsection 3.5.1 that, in theory, catenary and parabolic arches are assumed to be momentless for *SW* only and *UDL* only, respectively, and, therefore, they may be assumed to have an optimal form (Megson, 2006; Millais, 2005). This is true only when ignoring arch shortening and actual deformation. As a result, for the combined load cases, where *SW* and *UDL* are together actions on the arches, none of the known shapes represent the optimal arch form with the criterion of a zero bending moment distribution. The existence of bending moments is inevitable for known shapes of arches when both *SW* and *UDL* are applied to them. Although obtaining an optimal form for each probable load case is not feasible, momentless arches can be derived by using a form-finding technique for different ratios of *UDL:SW*. The resultant purely thrust structure should take as an intermediate arch shape between the parabola and catenary shapes.

5.3. Equilibrium of any point on the arch

The two-pin arch to be analysed is taken to be a rib arch of constant cross-section with uniform linear density (*q*) for the *SW*. The arch is supporting a superstructure of uniform density (*w*) per unit span for the *UDL*. The pins are assumed to be non-yielding supports and the section is presumed to be materially and geometrically uniform. The arch profile with the general imposed loading and the horizontal and vertical reactions *H* and *V*, respectively, at the pins is shown in Figure 5.1. As can be seen in this figure, the applied loading and the geometry of the arch are presumed to be symmetric about the crown of the arch. Therefore, the vertical reaction at the left support, V_A, is equal to the vertical reaction at the right support, V_B. Similarly, the horizontal reaction forces at the left support, H_A, and at the right support, H_B, are equal because of the symmetry. Because of the geometry and loading symmetry, the analysis can be conducted for half of the arch, from support *A* to the arch crown. The arch is assumed to act as an elastic rib and the displacements are assumed to be small. Figure 5.2 shows the sign convention for thrust, *T*, which is parallel to the tangent line of the arch curve, the shear force, *F*, and the bending moment, *M*, for an infinitesimal piece of arch length, d*s*. The infinitesimal piece of arch length can be defined in terms of infinitesimal horizontal and vertical directions as $ds^2=dx^2+dy^2$. With the use of the definition of *y'* as d*y*/d*x*, the infinitesimal piece of arch length can be expressed as $\mathrm{d}s = \sqrt{1+y'^2}\,\mathrm{d}x$. Since d*s* represents an infinitesimal piece of the arch length, the total length of arch can be achieved by integrating d*s* over the full length *S* from the left support to the right one. Consequent, the total length of arch is defined as $S = \int_0^L \sqrt{1+y'^2}\,\mathrm{d}x$, where *L* is the span length of the arch. The analytical methodology from Brew (2013) that is presented in Sections 5.3 and 5.4 gives the primary Equs. (5.1) to (5.4) and (5.11).

All the mathematical solutions reported in this chapter using these equations are from the author's work.

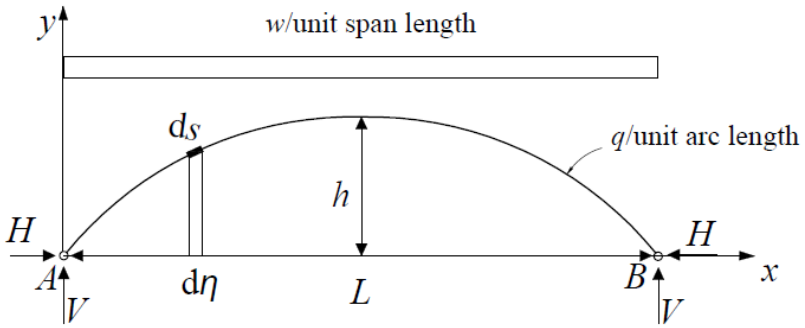

Figure 5.1. The two-pin arch specification

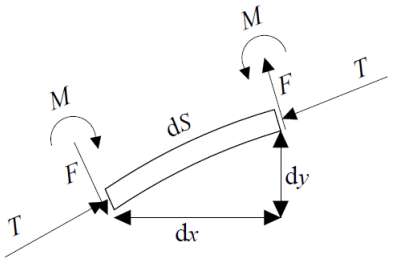

Figure 5.2. Sign convention of the forces acting on the infinitesimal piece of the arch

The vertical reaction of the arch can be calculated from static equilibrium. From Figure 5.1, the vertical equilibrium of the arch yields the vertical reaction force of the arch as:

$$\sum (F_y)_{\text{arch}} = 0: \; V_A + V_B = \int_0^L w\mathrm{d}x + \int_0^S q\mathrm{d}s \rightarrow V_A = V_B = \frac{1}{2}\left(wL + \int_0^S q\mathrm{d}s \right)$$

$$V = \frac{wL}{2} + \frac{q}{2}\int_0^L \sqrt{1+y'^2}\,\mathrm{d}x = \frac{wL}{2} + q\int_0^{L/2} \mathrm{d}s \tag{5.1}$$

where w and q are, respectively, the deck weight per unit span length and the self-weight of the arch per unit arc length.

From Figure 5.3, the slope of a smooth curve is tan*α* and it is equal to d*y*/d*x*=*y*' (mathworld.wolfram.com). Moreover, from trigonometry, d*y*/d*s*=sin*α* and d*x*/d*s*=cos*α*. Since d*s* is a function of *y'*, sin*α* and cos*α* can be written in terms of *y'*; that is, $\sin\alpha = y'/\sqrt{1+y'^2}$ and $\cos\alpha = 1/\sqrt{1+y'^2}$.

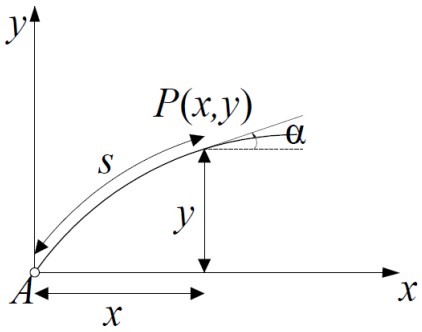

Figure 5.3. Trigonometry of the arch slope

The general equations of static equilibrium at point *P* can be used to obtain the thrust, shear, and bending moment acting on the right hand side of the arch element *AP* (see Figure 5.4).

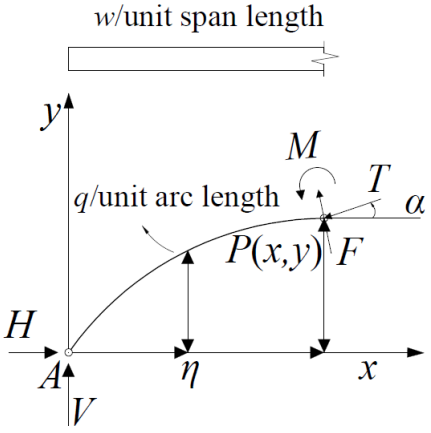

Figure 5.4. The forces acting on the arch segment *AP*

In above figure, *η* is the variable defined alongside the *x*-axis for calculating the lever arm for arch length d*s* relative to arch *SW*. The vertical and horizontal equilibrium of segment *AP* yields the shear force, *F*, and thrust, *T*. Also, the bending

moment at point *P* is given by the rotational equilibrium of segment *AP* about point *P*. Vertical, horizontal, and rotational equilibrium gives:

$$\sum (F_y)_P = 0: \ \rightarrow V - T\sin\alpha + F\cos\alpha - wx - \int_0^x q\sqrt{1+y'^2_\eta}\,\mathrm{d}\eta = 0 \tag{5.2}$$

$$\sum (F_x)_P = 0: \ \rightarrow H - T\cos\alpha - F\sin\alpha = 0 \tag{5.3}$$

$$\sum (M)_P = 0: \ \rightarrow M - Vx + Hy + \frac{wx^2}{2} + \int_0^x q(x-\eta)\mathrm{d}s = 0 \tag{5.4}$$

To find *T* and *F*, Equs. (5.2) and (5.3) should be solved together, via.

$$\left\{\begin{array}{c} (5.2)\times\cos\alpha \rightarrow V\cos\alpha - T\sin\alpha\cos\alpha + F\cos^2\alpha \\ -wx\cos\alpha - \int_0^x q\cos\alpha\sqrt{1+y'^2_\eta}\,\mathrm{d}\eta = 0 \\ (5.3)\times(-\sin\alpha) \rightarrow -H\sin\alpha + T\sin\alpha\cos\alpha + F\sin^2\alpha = 0 \end{array}\right\}$$

$(5.2)\times\cos\alpha + (5.3)\times(-\sin\alpha)$:

$$F = \frac{1}{\sqrt{1+y'^2}}\left(Hy' - V + wx + \int_0^x q\sqrt{1+y'^2_\eta}\,\mathrm{d}\eta\right) \tag{5.5}$$

Subsequently, the thrust *T* can be obtained by substituting *F* from Equ. (5.5) into Equ. (5.3) in parallel with using trigonometry. The expression is:

$$T = \left(y'/\sqrt{1+y'^2}\right)\left(-Hy' + V - wx - \int_0^x q\sqrt{1+y'^2_\eta}\,\mathrm{d}\eta\right) + H\sqrt{1+y'^2} \tag{5.6}$$

Substituting the vertical reaction force *V* from Equ. (5.1) into Equs. (5.4), (5.5), and (5.6) gives the bending moment, shear force, and thrust, respectively, as:

$$M-\left(\frac{wL}{2}+q\int_0^{L/2}\mathrm{d}s\right)x+Hy+\frac{wx^2}{2}+\int_0^x q(x-\eta)\mathrm{d}s=0$$

$$M=\left(Lx-x^2\right)(w/2)-Hy-q\int_0^x(x-\eta)\mathrm{d}s+xq\int_0^{L/2}\mathrm{d}s \tag{5.7}$$

$$F=\frac{1}{\sqrt{1+y'^2}}\left(Hy'-q\int_x^{L/2}\mathrm{d}s+w\left(x-L/2\right)\right) \tag{5.8}$$

$$T=\frac{1}{\sqrt{1+y'^2}}\left(H+y'\left[w\left(L/2-x\right)+q\int_x^{L/2}\mathrm{d}s\right]\right) \tag{5.9}$$

The derivative of the bending moment equation with respect to *x* is presented by Equ. (5.10).

$$M=\left(Lx-x^2\right)(w/2)-Hy-q\int_0^x(x-\eta)\mathrm{d}s+xq\int_0^{L/2}\mathrm{d}s$$

$$\frac{\partial M}{\partial x}=-Hy'+\left(L-2x\right)(w/2)-q\int_0^x\mathrm{d}s+q\int_0^{L/2}\mathrm{d}s=-Hy'+\left(L-2x\right)(w/2)+q\int_x^{L/2}\mathrm{d}s \tag{5.10}$$

The derivative of the bending moment with respect to *x* provides the shear force (Krenk and Hogsberg 2013).

$$\frac{\partial M}{\partial x}=-F\sqrt{1+y'^2}\ ,\ \mathrm{d}s=\sqrt{1+y'^2}\mathrm{d}x\ \rightarrow\ \frac{\mathrm{d}M}{\mathrm{d}x}=-F\frac{\mathrm{d}s}{\mathrm{d}x}\Rightarrow\ \frac{\mathrm{d}M}{\mathrm{d}s}+F=0 \tag{5.11}$$

Therefore, to have a momentless arch, it is required that the shear force in the two-pin rib arch becomes zero everywhere within the span. Having thrust force everywhere, the arch will be a pure thrust structure.

5.4. Geometry of the momentless arch

The shape of the optimal arch is now investigated when both *SW* and *UDL* are applied using the general Equ. (5.8). It is expected that having a zero shear force when *UDL* and *SW* are applied will not lead to a closed form solution. A parametric solution for coordinates *x* and *y* is presented in subsections 5.4.1 and 5.4.2 from applying the analytical approach by Brew (2013).

$$F = 0 \rightarrow \frac{1}{\sqrt{1+y'^2}}\left(Hy' - q\int_{x}^{L/2} \mathrm{d}s + w\left(x - L/2\right)\right) = 0$$
$$\rightarrow Hy' - q\int_{x}^{L/2} \sqrt{1+y'^2}\,\mathrm{d}\eta + w\left(x - L/2\right) = 0 \qquad (5.12)$$

To drop the integral from Equ. (5.12), the equation is differentiated with respect to the *x*.

$$Hy' + q\int_{L/2}^{x} \sqrt{1+y'^2}\,\mathrm{d}\eta + w\left(x - L/2\right) = 0 \;\rightarrow Hy'' + q\sqrt{1+y'^2} + w = 0$$
$$\Rightarrow\; y'' = -\left\{\frac{w}{H} + \frac{q}{H}\sqrt{1+y'^2}\right\} \qquad (5.13)$$

5.4.1. Finding the '*x*' coordinate of the momentless arch

To solve the above second-order differential equation for the *x* coordinate, another parameter *t* is defined to simplify the integrals as $y' = t$; hence $y'' = \mathrm{d}y'/\mathrm{d}x = \mathrm{d}t/\mathrm{d}x = t'$. Therefore, the general integral for *x* is given by:

$$t' = \frac{\mathrm{d}t}{\mathrm{d}x} = -\left\{\frac{w}{H} + \frac{q}{H}\sqrt{1+t^2}\right\} \rightarrow\; x(t) = -\int \frac{\mathrm{d}t}{\frac{w}{H} + \frac{q}{H}\sqrt{1+t^2}} \qquad (5.14)$$

Therefore, *x* can be expressed in terms of *t* by solving the integral above. The general form of *x*(*t*) when applying the boundary condition that at *x* = *L*/2, *y* = *h* is found to be:

$$x(t) = -\frac{H}{q}\left(\sinh^{-1}(t) + \frac{w}{\sqrt{q^2 - w^2}} \left(\begin{array}{l} \tan^{-1}\left(\dfrac{wt}{\sqrt{1+t^2}\sqrt{q^2 - w^2}} \right) \\ -\tan^{-1}\left(\dfrac{qt}{\sqrt{q^2 - w^2}} \right) \end{array} \right) \right) + \frac{L}{2} \qquad (5.15)$$

It can be seen from the Equ. (5.15) that the solution for *x* depends upon the term $q^2 - w^2$. Obviously, *x*(*t*) has a real answer when $q^2 - w^2 > 0$, which means *UDL:SW* < 1. However, to get a real solution, in the case of $q^2 - w^2 < 0$, which gives *UDL:SW* > 1, $\tan^{-1}$ is to be replaced by $\tanh^{-1}$ in the process of integrating. To simplify the integral, *w/q* is replaced by *k*, which is a known parameter since the loading is defined from the beginning. Hence, the function of *x* is written in terms of *k*. The solutions for *x* for different ratios of *UDL:SW* are given next.

- For *UDL:SW* < 1, which is the *SW*-dominant loading condition ($k^2 < 1$),

$$x(t) = -\frac{H}{q}\left(\sinh^{-1}(t) + \frac{k}{\sqrt{1-k^2}} \left(\begin{array}{l} \tan^{-1}\left(\dfrac{t}{\sqrt{1+t^2}} \dfrac{k}{\sqrt{1-k^2}} \right) \\ -\tan^{-1}\left(\dfrac{t}{\sqrt{1-k^2}} \right) \end{array} \right) \right) + \frac{L}{2} \qquad (5.16)$$

- For *UDL:SW* = 1 or ($k^2 = 1$),

$$x(t) = \frac{H}{q}\left(\frac{\sqrt{1+t^2} - t\sinh^{-1}(t) - 1}{t} \right) + \frac{L}{2} \qquad (5.17)$$

- For *UDL:SW* > 1, which is the *UDL*-dominant loading condition ($k^2 > 1$),

$$x(t) = -\frac{H}{q}\left(\sinh^{-1}(t) + \frac{k}{\sqrt{k^2-1}}\left(-\tanh^{-1}\left(\frac{t}{\sqrt{1+t^2}}\frac{k}{\sqrt{k^2-1}}\right) + \tanh^{-1}\left(\frac{t}{\sqrt{k^2-1}}\right)\right)\right) + \frac{L}{2} \qquad (5.18)$$

5.4.2. Finding the '*y*' coordinate of the momentless arch

In this subsection, Equ. (5.13) is solved for the *y* coordinate using the transformation that *y'* = *t*; thus, $y(t) = \int \frac{\mathrm{d}x}{\mathrm{d}t}.t.\mathrm{d}t$. d*x*/d*t* from Equ. (5.14) is substituted into the equation representing *y*(*t*). Solving the integral for *y* in terms of *t* with the boundary condition, that *t* = 0 for *y* = *h*, leads to:

$$y(t) = \int -\frac{t.\mathrm{d}t}{\frac{w}{H} + \frac{q}{H}\sqrt{1+t^2}} = -\frac{H}{q}\left(\sqrt{1+t^2} - 1 + \frac{w}{q}\ln\left(\frac{w+q}{w+q\sqrt{1+t^2}}\right)\right) + h \qquad (5.19)$$

As can be seen from Equ. (5.19), it is applicable for any ratio of *UDL* to *SW*.

5.4.3. Finding the shape of momentless arch

Using Equs. (5.16) to (5.19) it is noted that the *x* and *y* coordinates are for half of the arch from the left support to the crown. The necessary condition for constructing the arch shape is that the value of *t* must be found. Then, the horizontal reaction force *H* can be determined by having *t* and *k* as known values, and using the appropriate boundary conditions. Now by using Equ. (5.19) and Equs. (5.16) to (5.18) the arch shape can be obtained for different *UDL:SW* ratios. It was stated previously that *k* = *w*/*q*, in which *w* and *q* are prescribed from the outset, and hence *k* is a known parameter. From the definition of *t* and the constraint of the two-pin arch, *t* at the

crown of the arch is zero; that is, $t(x = L/2) = 0$. Moreover, the maximum magnitude of *t* occurs at the supports because the slope of the arch has its maximum value at these points. Then *t* can be specified for each nodal location on the arch's shape by choosing the number of equally spaced nodes from *A* to *B* in Figure 5.1. The procedure involves dividing the difference between the maximum value of *t* and zero by the number of nodes in half the span. Each node will have a specific *t* value. The number of nodes can be defined by a designer on the basis of the desired numerical accuracy. The horizontal reaction force, *H*, which is another determinative parameter for finding the optimal shape of the arch, can be calculated from the boundary condition at *A* of $x = 0$ then $y = 0$. This indicates that finding *H* is associated with calculating the maximum value of the *t* parameter. The essential requirement for finding the geometry of the momentless arch is calculating the *t* parameter at the supports of the optimal arch. To find the maximum value of the *t* parameter (t_{max}), the condition at *A* is applied to the Equ. (5.19) for *y* coordinate and to the Equs. (5.16) to (5.18) depends upon the ratio of *UDL:SW* for *x* coordinate. Then, dividing Equs. (5.16) to (5.18) with $x=0$ by Equ. (5.19) with $y=0$ yields an equation in which the only unknown is t_{max}. The outcome of applying the boundary condition at *A* to the *x* and *y* coordinates for the optimal arch for any load condition is calculated by the author.

- When *UDL:SW* < 1 or $k^2 < 1$,

$$\frac{L}{2h} = \frac{\left(\sinh^{-1}(t_{\max}) + \frac{k}{\sqrt{1-k^2}} \left(\tan^{-1}\left(\frac{t_{\max}}{\sqrt{1+t_{\max}^{\ 2}}} \frac{k}{\sqrt{1-k^2}} \right) - \tan^{-1}\left(\frac{t_{\max}}{\sqrt{1-k^2}} \right) \right) \right)}{\left(\sqrt{1+t_{\max}^{\ 2}} - 1 + k \ln\left(\frac{k+1}{k+\sqrt{1+t_{\max}^{\ 2}}} \right) \right)} \quad (5.20)$$

- When *UDL:SW* = 1 or $k^2 = 1$,

$$\frac{L}{2h} = \frac{\left(\frac{\sqrt{1+t_{\max}{}^2} - t_{\max}\sinh^{-1}(t_{\max}) - 1}{t_{\max}}\right)}{\left(\ln\left(\frac{1+\sqrt{1+t_{\max}{}^2}}{2}\right) - \sqrt{1+t_{\max}{}^2} + 1\right)} \tag{5.21}$$

- When *UDL:SW* > 1 or $k^2 > 1$,

$$\frac{L}{2h} = \frac{\left(\sinh^{-1}(t_{\max}) + \frac{k}{\sqrt{k^2-1}}\left(\tanh^{-1}\left(\frac{t_{\max}}{\sqrt{k^2-1}}\right) - \tanh^{-1}\left(\frac{t_{\max}k}{\sqrt{1+t^2\sqrt{k^2-1}}}\right)\right)\right)}{\left(\sqrt{1+t_{\max}{}^2} - 1 + k\ln\left(\frac{k+1}{k+\sqrt{1+t_{\max}{}^2}}\right)\right)} \tag{5.22}$$

It can be seen that *H* has been removed by dividing *x* by the *y* coordinate, and so Equs. (5.20) to (5.22) are independent of this unknown parameter. Moreover, since ratio *L:h* and ratio *UDL:SW* are defined from the beginning the equation can be solved. The three equations are nonlinear in terms of an unknown parameter t_{max} that can be calculated using an iterative process. The initial value of t_{max} for the required iteration depends on the ratio of *UDL:SW*. As stated previously, parabolic and catenary arches are likely to behave more efficiently when *UDL:SW* > 1 and *UDL:SW* < 1 respectively. Also, in the case of the loading condition of *UDL:SW* = 1, parabolic and catenary arches behave similarly. Therefore, the initial value of t_{max} is derived from the governing equation of the parabolic arch when *UDL:SW* ≥ 1. Meanwhile, the equation of an inverted catenary is used to find the initial value of t_{max} for *UDL:SW* < 1. The initial value of t_{max} can be obtained as below.

5.4.4. Determination of the initial value of t_{max} when *UDL:SW* ≥ 1

In this case, the governing equation of a parabolic arch, $y = \frac{4h}{L^2}\left(Lx - x^2\right)$, is applied to find the initial value of t_{max}, in which t is equal to y'. Subsequently, t can be determined for x = 0 at the arch support, which gives its maximum initial value, which can be used to solve Equs. (5.21) and (5.22). Applying the boundary condition at *A* to the governing equation for t gives:

$$y' = \frac{4h}{L^2}\left(L - 2x\right) \xrightarrow{x=0} y' = \frac{4h}{L} \Rightarrow t_{(\max)\text{initial}} = \frac{4h}{L} \tag{5.23}$$

It can be seen that the initial value of t_{max} is related to the *L:h* ratio, which is a known value. To find the desired value of t_{max}, Equs. (5.21) and (5.22) can be solved using the iterative process with the initial value for t_{max} from Equ. (5.23). Hence, the required value of t_{max} can be achieved using an iterative process programmed in *MATLAB* (Appendix C).

5.4.5. Determination of the initial value of t_{max} when *UDL:SW* < 1

The equation of the inverted catenary is applied when the load case is *SW*-dominant. The function of the catenary arch is given by $y = -A'\cosh\left(\frac{(L/2 - x)}{A'}\right) + h + A'$, considering the left support has coordinates x = 0 and y = 0. As stated in subsection 3.2.1.3, *A'* is a constant that can be found using an iterative algorithm for each catenary curve and coded in *MATLAB*, as listed in Appendix C for $k^2 < 1$. Having the function of the catenary arch, the initial value of t can be calculated for x = 0 as.

$$y' = \sinh\left(\frac{(L/2 - x)}{A'}\right) \xrightarrow{x=0} y' = \sinh\left(\frac{L}{2A'}\right) \Rightarrow t_{(\max)\text{initial}} = \sinh\left(\frac{L}{2A'}\right) \tag{5.24}$$

It is seen in Equ. (5.24) that the initial value of t_{max} depends only upon the span of the arch and constant *A'* when the self-weight of the arch is greater than the imposed *UDL*.

5.4.6. Determination of horizontal reaction force

Once t_{max} is known, *H* can be calculated using any of Equs (5.16) to (5.18) for each load case with the boundary condition of $x = 0$ or using Equ. (5.19) with $y = 0$. Here, the governing equation for the *y* coordinate when $y = 0$ is applied to find the horizontal reaction force. *H* for any ratio of *UDL:SW* can be calculated from:

$$H = \frac{qh}{\left(k\ln\left(\frac{k+1}{k+\sqrt{1+t_{\max}{}^2}} \right) + \sqrt{1+t_{\max}{}^2} - 1 \right)} \tag{5.25}$$

Since only *H* is required to determine the shape of the rib arch, the geometry of the momentless arch can be found. The whole process of finding the form of the momentless arch for any *L:h* ratio and any ratio of *UDL:SW* is programmed in *MATLAB*, as listed in Appendix C.

5.5. Comparing the geometry of the momentless arch with known shapes of arches

It was shown in Figure 3.8 the differences in the geometry of known shapes of arches become indistinguishable when the *L:h* ratio is increased. It is known that, small changes to the geometry have a significant effect on arch structural response. To compare the geometry of the momentless arch with known shapes, the geometries for circular, parabolic, and catenary arches with specification introduced in subsection 3.3.1 are plotted in Figure 5.5, for *L:h* ratios of 2, 3, and 5. Since the

three geometries is become similar as the *L:h* ratio increases, using a higher *L:h* ratio than *S* has little effect. The best behaviour of parabolic and catenary arches was found for an *L:h* ratio between 2 and 4 for constant *L*=10 m. Only half of the arch need to be modelled because of the symmetry of the arch material, and *UDL*. As stated, the arch specification is taken from arches studied in Chapter 3, which had *SW* equal to 7.2 kN/m with a *UDL* of 20 kN/m applied across the full 10 m span of the arch. The imposed loading for which the shape of the momentless arch is obtained is load case *A1*. Since load case *A1* consisted of a general combination of *SW* plus a *UDL* of 20 kN/m the ratio of *UDL:SW* is 2.78. For this problem, the *MATLAB* file in Appendix C was run with $k^2 > 1$, in combination with changing *h* for the three cases of *L:h*=2, 3, or 5. The shapes of circular, catenary, and parabolic arches are plotted in Figure 5.5 with the momentless arch for the same specifications.

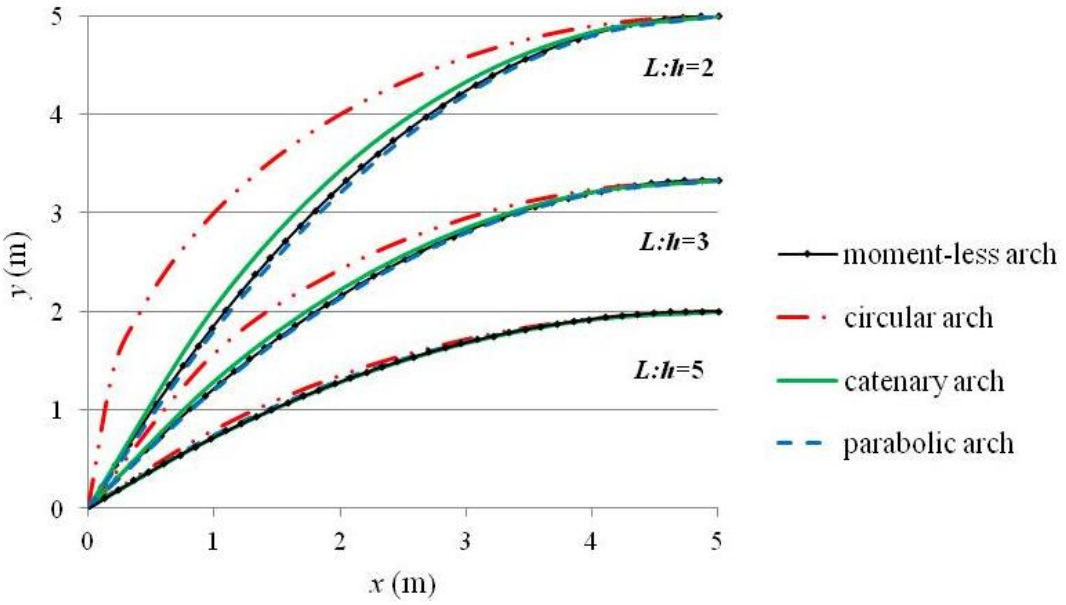

Figure 5.5. Geometry differences between momentless arch and known shapes of arches for *L:h* ratios of 2, 3, and 5 when *UDL:SW* > 1

From the curves in the Figure 5.5, it is seen that the geometry of the momentless arch when *UDL:SW* > 1 is much closer to the geometry of the parabolic arch for all considered *L:h* ratios. However, the differences between the geometries of arches

are less than 7% for an *L:h* ratio of 5. To perform a deeper investigation when comparing the geometry of the momentless arch with known shapes of arches, different ratios of *UDL:SW* are applied to them. In this regard, firstly an *UDL* of 7.2 kN/m is applied to all arches, which gives *UDL:SW* = 1 (k^2 = 1). Secondly, to achieve *UDL:SW* < 1, a *UDL* of 3 kN/m is imposed over the full span of the arch (k^2 < 1). The shape of the momentless arch is then obtained using the *MATLAB* program shown in Appendix C for each load case. The geometries of the half-arches are then plotted for an *L:h* ratio of 2 in Figure 5.6 and compared with each other.

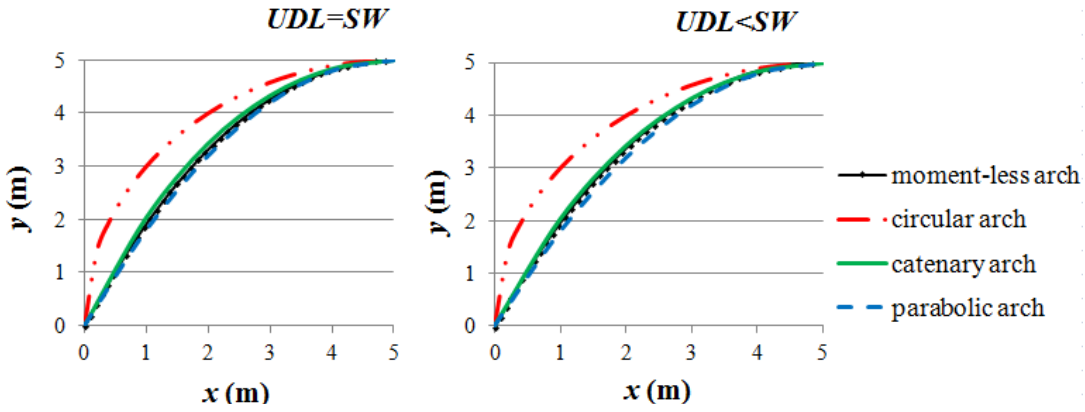

Figure 5.6. Geometry differences between momentless arch and known shapes of arches for *UDL:SW* = 1 and *UDL:SW* < 1 when *L:h* = 2

It is seen that the geometry of the momentless arch is between the geometry of the parabolic and catenary arch shapes when *UDL* = *SW*. As a result, the optimal shape of arch for the general combination of *UDL* plus *SW* is the shape between the parabolic and catenary forms but far from a circular shape. From the above figure, it can be seen that the geometry of the momentless arch becomes close to the catenary form when k^2 < 1 (*UDL:SW* < 1). This also validates the calculated shape for the optimal arch, as it was shown in Section 3.7 that the best arch performance is achieved by the catenary arch when the *SW* of the arch is much greater than the imposed *UDL*. Meanwhile, the parabolic arch form is the best shape due to the criterion of the minimum bending moment for *UDL:SW* > 1. As previously stated, the

obtained momentless shape is optimal because the bending moment and shear forces are zero everywhere along the arch. This is illustrated in Figure 5.7. It can be seen in this figure that the loading can be carried using only axial forces in the arch and that the arch shows purely thrust behaviour. Consequently, the deflection of the arch and the combined stress due to the axial forces and bending moments will be lower than those of known shapes of arches.

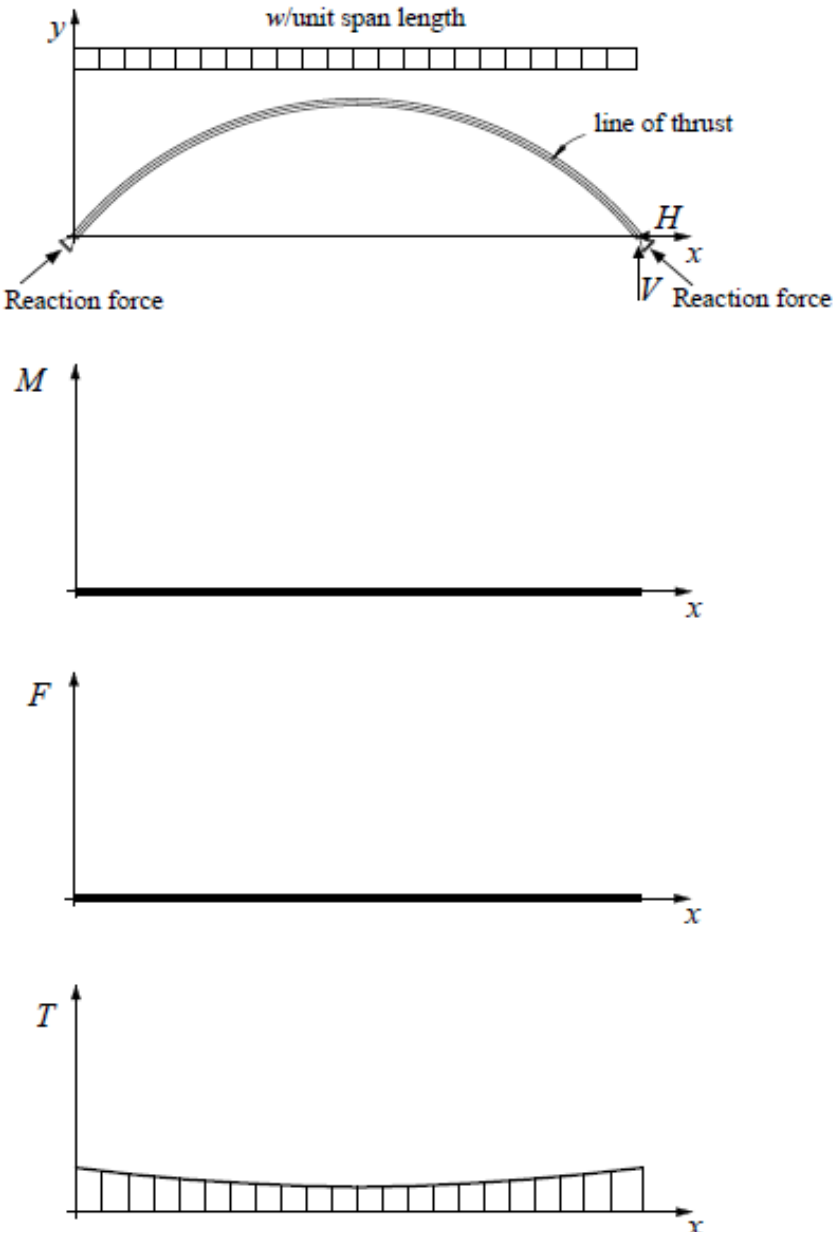

Figure 5.7. Diagram of forces in optimal arch shape subjected to *UDL* plus *SW* (Salonga 2010)

5.6. Case study

The excellence of the momentless arch is investigated in this section. To illustrate the advantages of using the momentless arch instead of known shapes of arches, the behaviour of the parabolic arch and the momentless one are compared when *UDL:SW* > 1. It is also noted that the parabolic arch is the best known arch shape for this load case. To assess the structural behaviour, the deflection and the first failure of the concrete section of the parabolic arch are compared with those of the momentless arch.

To compare the structural response of the momentless arch with known shapes of arches, a rib concrete arch bridge is chosen and analysed. The analysis is carried out for a hypothetical bridge with some of the basic dimensions of the studied arch are taken from a concrete arch-bridge traffic overpass in Daugavpils in Latvia (Taurenis et al. 2013). This bridge is a carriageway with a parabolic shape and was constructed in 2011 to improve the transportation infrastructure. To have a more pronounced difference between the geometries of the parabolic arch and the momentless form, the *L:h* ratio is assumed to be equal to 3. Regarding other assumptions, the bridge is considered as a two-pin arch bridge with a constant cross-section. The loading configuration is estimated based on EN1991-2: 2003 for a highway bridge in a harsh urban environment. The span of the arch (*L*) is 60 m, and to have an *L:h* ratio of 3, the height of the arch (*h*) is 20 m. The deck width is 13.5 m, consisting of a 9 m carriageway with two sidewalks of 1.5 m. The deck is linked to the arch rib with the support of piers (vertical members). The distance between piers is 6.5 m, except over the middle interval at the crown where the sepaqration is 8 m. The arch bridge is made of C50/60 concrete with a covering of asphalt concrete for both carriageway and sidewalks. The properties of this type of concrete consist of 25 kN/m^3 cylinder weight per unit volume and modulus of elasticity (E_c) of 37 GPa. The specified concrete compressive strength is 50 MPa.

To find the ratio of *UDL* to *SW*, the weight of the arch rib, arch deck and piers are estimated. The weight of the deck and piers is presumed to comprise the *UDL* applied to the rib arch. Moreover, the traffic load is calculated and estimated as the imposed *UDL*. The ratio of *UDL:SW* is therefore specified. Previously in Section 3.7, it was shown that the parabolic arch is the best known shape of arch when the loading condition is *UDL*-dominant. Therefore, in the case of *UDL:SW* > 1, the best known shape of arch will be compared with the momentless form. The parabolic arch and the momentless one are then modelled in *SAP2000* (2012). The arches are then analysed for the general combination of *SW* and *UDL* having the same cross-section and similar properties. Thus, the required reinforcement for the parabolic and momentless arches can be calculated using the results of forces and bending moments from *FE* using *SAP2000* software for linear static analysis assuming small displacements.

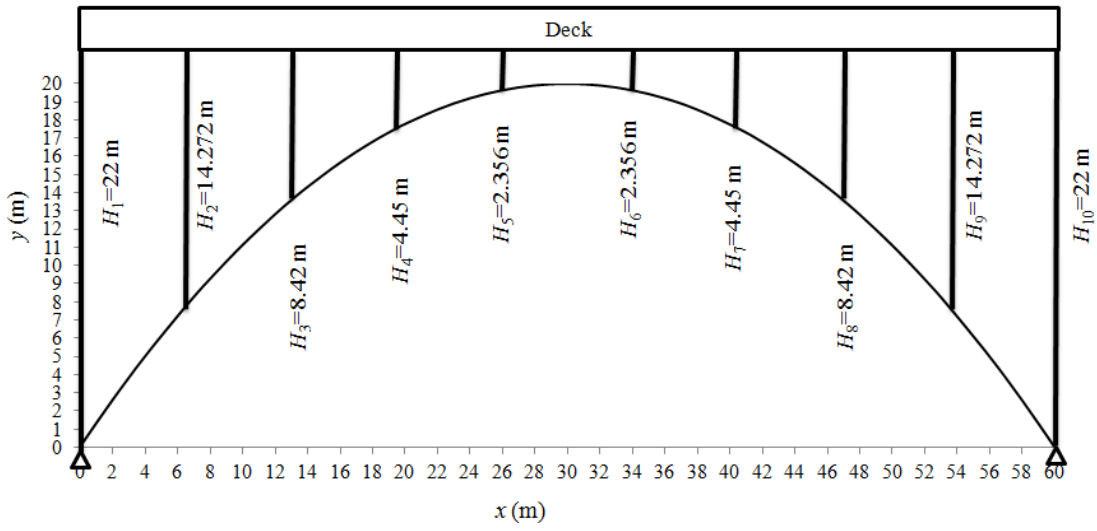

Figure 5.8. Shape of the studied arch bridge

The general shape of the arch is given in Figure 5.8. Although most dimensions and specifications are taken from a real overpass bridge, many assumptions are made, especially when calculating the applied load. The dimensions of the arch are reasonable in reality; for this hypothetical illustrative example. The reason is that the

effect of the shape of the arch on its resistance is going to be assessed. As the first step, the loading is calculated as below.

5.6.1. Calculating the weight of the arch rib

Based on the geometry data of the arch overpass in Daugavpils, the cross-section of the rib arch is 5000 mm wide (b_a) and about 650 mm thick (d). Hence, the effective depth of the arch cross-section (d_a) is considered to be equal to 600 mm. It is assumed that the thickness of the arch is constant over the full span of the arch. The specific weights of steel and concrete are taken as 78 and 25 kN/m^3, respectively, based on EN1991-1-1:2002. To estimate the weight of the arch rib, it is assumed that the cross-section of the arch is made of concrete material with the minimum required steel reinforcement of 0.2% in the tension zone of the cross-section. The weight of the arch rib is the summation of the weight of the minimum steel reinforcement plus the concrete and the calculation for the reinforcement is based on a conventional reinforced concrete design (Mosely et al. 2007).

The $A_{s(min)}$ is then calculated as the maximum of $0.00016f'^{2/3}_c b_a d_a$=6515 mm^2 and $0.0013\ b_a d_a$=3900 mm^2 that results the weight of steel and concrete part to be respectively $6515\times10^{-6}\times78$=0.51 kN/m and $(5\times0.65-(6515\times10^{-6}))\times25$=81.1 kN/m, where A denotes the area and the subscripts $_S$ and $_C$ indicate steel and concrete material respectively. According to EN1990: 2000, the weight of the arch rib can be obtained using partial factors for concrete and steel weights equal to 1.35 and 1.2, respectively. The factored weight of the arch (SW) is to be $A_{arch}=1.2A_S+1.35A_C$ =110.1 kN/m. Pier and weight of concrete weight of steel kN

5.6.2. Calculating the weight of the vertical members (piers)

Based on the information from the traffic overpass bridge in Latvia (Taurenis 2013), the width of the piers is 4500 mm and their thickness is 400 mm. To avoid large

bending moments, the vertical members are assumed to be flexible. For this reason, to have enough flexibility in the longitudinal direction, the piers are linked to the deck and arch rib using hinge connections. The specifications of concrete and steel material are the same as those considered for the arch rib. Therefore, the weight of steel and concrete for each pier is estimated, as for the arch cross-section to be the maximum of $0.00016f'^{2/3}_{c}b_a d_a$=3421 mm^2 and $0.0013\ b_a d_a$=2047.5 mm^2 that results the weight of steel and concrete part to be respectively $3421\times10^{-6}\times78$=0.27 kN/m and $(4.5\times0.4-(3421\times10^{-6}))\times25$=45 kN/m,

Consequently, the weight of each pier can be calculated knowing the height of each pier; H_1 to H_{10} was given in Figure 5.8. The weight of piers consists of the weight of concrete and steel. The steel reinforcement is estimated as the minimum required area for the cross-sections. Similarly to the rib arch calculation, the weight of each pier can be obtained as below. The chosen value for each pier is similar to the height value that is shown in Figure 5.8.

$$\text{Pier 1 and 10:}$$
$$\left.\begin{array}{l}\text{weight of concrete}: 45\times22\cong990\ \text{kN}\\ \text{weight of steel}: 0.27\times22=5.94\ \text{kN}\end{array}\right\}$$
$$\Rightarrow W_{1,10}\cong1.35\times990+1.2\times5.94=1343.6\ \text{kN}$$

$$\text{Pier 2 and 9:}$$
$$\left.\begin{array}{l}\text{weight of concrete}: 45\times14.272=642.24\ \text{kN}\\ \text{weight of steel}: 0.27\times14.272=3.85\ \text{kN}\end{array}\right\}$$
$$\Rightarrow W_{2,9}\cong1.35\times642.24+1.2\times3.85=871.6\ \text{kN}$$

$$\text{Pier 3 and 8:}$$
$$\left.\begin{array}{l}\text{weight of concrete}: 45\times8.422=379\ \text{kN}\\ \text{weight of steel}: 0.27\times8.422=2.27\ \text{kN}\end{array}\right\}$$
$$\Rightarrow W_{2,9}\cong1.35\times379+1.2\times2.27=514.4\ \text{kN}$$

$$\text{Pier 4 and 7:}$$
$$\left.\begin{array}{l}\text{weight of concrete}: 45\times 4.45 = 200.25\ \text{kN}\\ \text{weight of steel}: 0.27\times 4.45 = 1.2\ \text{kN}\end{array}\right\}$$
$$\Rightarrow W_{4,7} \cong 1.35\times 200.25 + 1.2\times 1.2 = 271.8\ \text{kN}$$

$$\text{Pier 5 and 6:}$$
$$\left.\begin{array}{l}\text{weight of concrete}: 45\times 2.356 = 106\ \text{kN}\\ \text{weight of steel}: 0.27\times 2.356 = 0.64\ \text{kN}\end{array}\right\}$$
$$\Rightarrow W_{5,6} \cong 1.35\times 106 + 1.2\times 0.64 = 144\ \text{kN}$$

The arrangement of the applied loads resulting from the pier effect is visualized in Figure 5.9.

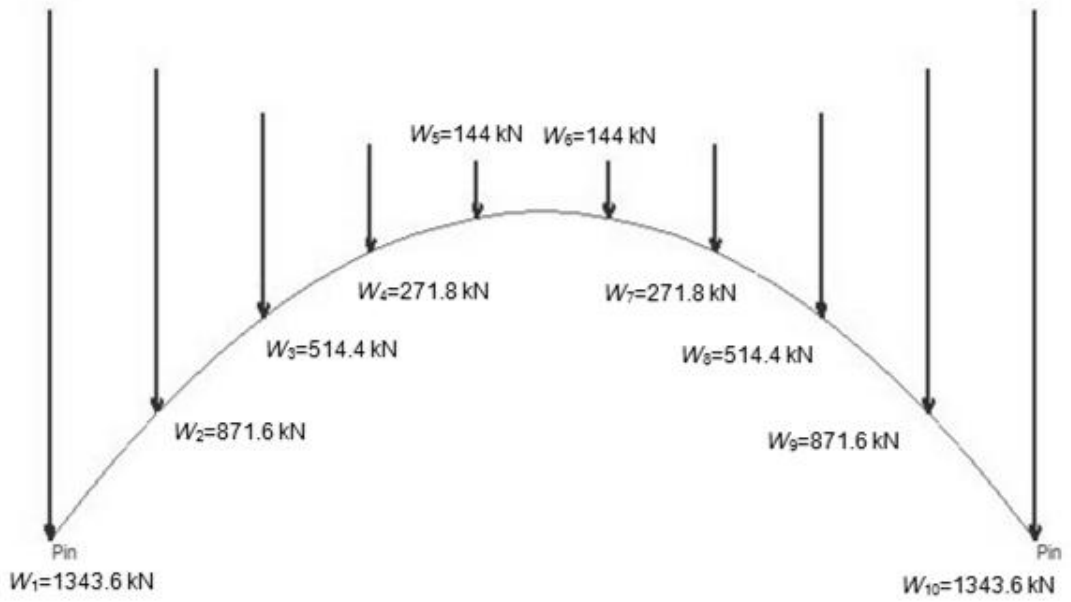

Figure 5.9. Configuration of the applied loads on the pin-ended arch because of the piers

To estimate the effect of piers with the *UDL*, the parabolic arch subjected to its *SW* and applied point loads was analysed in *SAP2000*. Then, multiple magnitudes of *UDL* plus *SW* were applied to the parabolic arch and modelled in *SAP2000* as *FEA*.

It was seen that a *UDL* of 264 kN/m can be assumed to be the applied loading, replacing the effect of the 10 piers over the bridge's span. Hence, the piers effect is estimated with *UDL*, as a similar behaviour of the arch occurs under both types of loadings. If the number of piers is high enough for them, they can be considered as a continuous wall in reality. Thus, the weight and effect of the continuous wall representing the pier effect can be seen in the relevant equations in Section 5.3 when investigating the general case to find the optimal arch shape. Here, to apply a *UDL* and an *SW* to the arch, this simplification is used. The combination of *SW* and *UDL* of 264 kN/m gives maximum hogging and sagging bending moments similar to the ones when the arch is subjected to the point loads from the effect of piers and *SW*. A diagram of the bending moment of a parabolic arch subjected to the combination of *SW* and the pier effect (as point loads) is presented in Figure 5.10. Figure 5.11 shows the bending moment diagram of a parabolic arch under *SW* plus a *UDL* of 264 kN/m applied across the full span of the arch.

Comparing the two figures below, the bending moment behaviour of the parabolic arch in this study is the same under two different loadings. Consequently, the piers are replaced by a *UDL* of 264 kN/m.

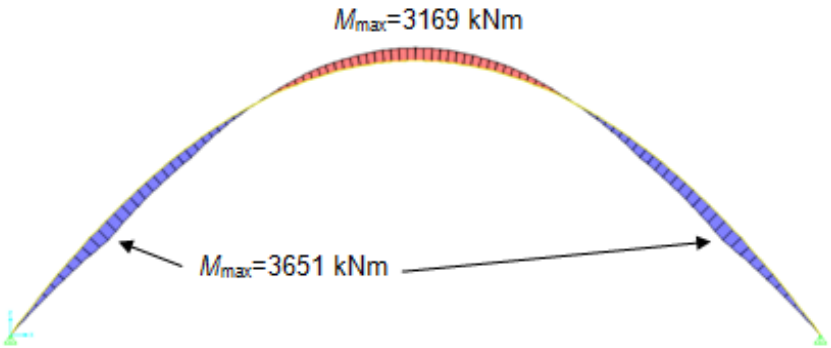

Figure 5.10. *SAP2000*: Bending moment of parabolic arch subjected to *SW* plus point loads from piers

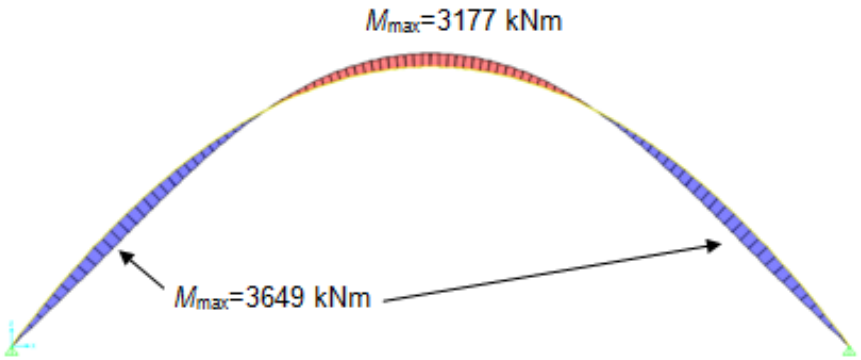

Figure 5.11. *SAP2000*: Bending moment of parabolic arch subjected to *SW* plus *UDL* of 264 kN/m

5.6.3. Calculating the weight of the deck (superimposed dead load)

The deck width is 13500 mm, which consists of a 9000-mm carriageway and two pavements of 1500 mm. The surface layer of the deck consists of asphalt with a thickness of 100 mm. The weight of this thickness of asphalt and the weight of the parapet are taken as 2.2 kN/m^2 and 0.5 kN/m, respectively, based on the EN1991-2: 2003. It is assumed that a steel beam supports a 200-mm concrete deck; hence, the weight of the steel beam is assumed to be 15 kN/m. The weight of concrete is calculated as 0.2×13.5×25=67.5 kN/m. The weight of the deck is estimated as the *UDL* applied across the full span of the arch as: $W_{Deck}=1.2W_{Parapet}+1.35W_{Surfacing}+1.35W_{Concrete}+1.2W_{Steel}=150$ kN/m.

5.6.4. Calculating the traffic load

In reality, the axle loading from vehicles has a great impact on the loading configuration. However, for the purpose of comparison between the behaviour of parabolic and momentless arches, the traffic load must be applied on both arches as the *UDL* in this section under some assumptions. According to Table 4.1 of the EN1991-2: 2003, the carriageway of 9000 mm has three lanes, each with the national lane width of 3000 mm. The load model 1 (*LM*1) is assumed for the effect

of traffic in ultimate limit state (*ULS*). This load model involves a double-axle concentrated load and a uniformly distributed load of $\alpha_q q_k$. α_q is the adjustment factor and is assumed to be equal to 1 due to the absence of a specification. To analyse the arches under the *UDL*-only condition, the effect of variable loads is not considered. Hence, a *UDL* of 9 kN/m^2 for two lanes and 2.5 kN/m^2 for the other lane is imposed on the arch based on Table 4.2 of EN1991-2. The loading for the remaining width of 1500 mm is referred to as $\alpha_q q_k$. The *UDL* applied to the 9000-mm carriageway plus the remaining width of 1500 mm is calculated as $UDL = 9 \times 3 \times 2 + 2.5 \times 3 + 2.5 \times 1.5 = 65.25\,\text{kN/m}$.

There are also pavements of 1500 mm with a characteristic *UDL* of 5 kN/m^2. Hence, another applied *UDL* for the carriageway is equal to $UDL = 5 \times 1.5 \times 2 = 15\,kN/m$.

In total, all live imposed loads on the arch bridge are estimated by the summation of the above two values of *UDL*, which is equal to 80.25 kN/m. In order to ignore the concentrated load, the *UDL* of 93 kN/m is applied to arches as a traffic load.

5.6.5. Arch model

From subsection 5.6.1, the self-weight of the arch rib was estimated to be equal to 110.1 kN/m. The imposed load on the arch rib was approximated as a summation of the weight of piers and the deck plus traffic load. The weight of piers is obtained by summation of Equations 5.38 to 5.42 in Section 5.6.2. The weights of the deck and traffic were calculated in Sections 5.6.3 and 5.6.4, respectively. Therefore, accumulating the estimated *UDL* from Sections 5.6.2 to 5.6.4 gives a total *UDL* of 507 kN/m, which is considered as the load applied to the arches in this study. Having an *SW* of 110.1 kN/m and a *UDL* of 507 kN/m, the ratio of *UDL:SW* is 4.6. Therefore, the behaviour of the best known shape of arch, that is, a parabolic arch, is compared with the momentless form for this loading configuration. The parabolic arch is then modelled with the specification defined in *SAP2000* and subjected to its

SW plus *UDL* of 507 kN/m from the live load and accumulated weight of the deck with piers. The reason for using *SAP2000* instead of *GSA* software is the limitation of the new version of *GSA* software in modelling arches with more than 50 nodes. Similarly to *GSA* software, the curve is modelled using straight elements such as beams in *SAP2000*. Thus, sensitivity analysis is carried out to find what number of nodes is sufficient for modelling a parabolic arch bridge. Therefore, the parabolic arch is modelled and analysed using different numbers of nodes/straight elements for a combination of *SW* equal to 110.1 kN/m and *UDL* of 507 kN/m. To perform the sensitivity analysis, the results of the maximum and minimum bending moment when the parabolic arch is modelled with 31 nodes or 30 straight elements, 61 nodes, 103 nodes, and finally 121 nodes are given in Table 5.1.

Table 5.1. Maximum/minimum bending moments in parabolic arch when modelled in *SAP2000* using different numbers of nodes

Number of nodes used for modelling		Bending moment (kNm)
31	max	1265.7
	min	–1208.1
61	max	1113.7
	min	–1003.4
103	max	1081.6
	min	–958.8
121	max	1076.5
	min	–952.3

The maximum bending moment of the parabolic arch is sagging and is located at both sides of the arch. Comparing the maximum sagging bending moment of the parabolic arch subjected to *UDL* plus *SW*, the percentage difference between the maximum sagging bending moments of the arch modelled with 61 and 31 nodes is 12%. The percentage difference between the maximum sagging bending moments of the arch modelled with 61 and 103 nodes decreased to 2.88%. Then, increasing

the number of nodes from 103 to 121 nodes caused the maximum sagging bending moment to decrease by 0.47%, which can be considered negligible. Therefore, the trend of the change in maximum bending moment becomes roughly a straight horizontal line when the arch is modelled with more than 103 nodes. The *x* and *y* coordinates for parabolic and momentless arch are given in Table 5.2 for half span.

Table 5.2. Coordinates of parabolic and momentless arch for the half span

n	Parabolic arch		Momentless arch		*n*	Parabolic arch		Momentless arch	
	x(m)	*y*(m)	*x*(m)	*y*(m)		*x*(m)	*y*(m)	*x*(m)	*y*(m)
1	0.00	0.00	0.00	0.00	27	15.29	15.19	14.83	14.97
2	0.59	0.78	0.55	0.74	28	15.88	15.57	15.43	15.36
3	1.18	1.54	1.10	1.46	29	16.47	15.93	16.02	15.73
4	1.76	2.28	1.65	2.18	30	17.06	16.28	16.62	16.09
5	2.35	3.01	2.20	2.88	31	17.65	16.61	17.22	16.43
6	2.94	3.73	2.76	3.57	32	18.24	16.92	17.82	16.76
7	3.53	4.43	3.32	4.25	33	18.82	17.22	18.42	17.07
8	4.12	5.11	3.87	4.91	34	19.41	17.51	19.02	17.37
9	4.71	5.78	4.43	5.56	35	20.00	17.78	19.62	17.65
10	5.29	6.44	5.00	6.20	36	20.59	18.03	20.23	17.92
11	5.88	7.07	5.56	6.82	37	21.18	18.27	20.83	18.17
12	6.47	7.70	6.13	7.44	38	21.76	18.49	21.44	18.40
13	7.06	8.30	6.70	8.03	39	22.35	18.70	22.04	18.62
14	7.65	8.90	7.27	8.62	40	22.94	18.89	22.65	18.83
15	8.24	9.47	7.84	9.19	41	23.53	19.07	23.26	19.01
16	8.82	10.03	8.41	9.75	42	24.12	19.23	23.87	19.18
17	9.41	10.58	8.99	10.30	43	24.71	19.38	24.48	19.34
18	10.00	11.11	9.56	10.83	44	25.29	19.51	25.09	19.48
19	10.59	11.63	10.14	11.34	45	25.88	19.62	25.71	19.60
20	11.18	12.13	10.72	11.85	46	26.47	19.72	26.32	19.71
21	11.76	12.61	11.31	12.34	47	27.06	19.81	26.93	19.80
22	12.35	13.08	11.89	12.81	48	27.65	19.88	27.54	19.87
23	12.94	13.53	12.48	13.27	49	28.24	19.93	28.16	19.93
24	13.53	13.97	13.06	13.72	50	28.82	19.97	28.77	19.97
25	14.12	14.39	13.65	14.15	51	29.41	19.99	29.39	19.99
26	14.71	14.80	14.24	14.57	52	30	20	30	20

Here, *n* denotes the node numbers and 103 nodes or 102 straight elements are chosen to model the arches. As a result, parabolic and momentless arches are analysed for the general combination of *SW* and *UDL* while modelling in *SAP2000* using 103 nodes. The required reinforcement of both arches can be obtained using forces and bending moment results found from the analysis of arches by *SAP2000*.

5.6.6. Calculating the required reinforcement

Having f'_c as the concrete strength, the concrete design stress in compression, f_{cd}, is equal to $0.85 f_c^{'} / \gamma_c$, where γ_c is the concrete partial factor of safety and is equal to 1.5 (Mosely et al. 2007). Since f'_c for C50/60 concrete is equal to 50000 kN/m^2, the design concrete strength is calculated as 28.3 MPa. It was also previously stated that the width of the arch cross-section, b_a, is equal to 5000 mm. Therefore, the minimum reinforcement for both parabolic and momentless arches in the tension and compression zones can be calculated:

1) The minimum reinforcement area for the tension zone of the cross-section for both parabolic and momentless arches was calculated in Section 5.6.1 as 6515 mm^2.
2) The minimum reinforcement area for the compression zone of the cross-section of the parabolic and momentless arches is: $A_{s2(\min)} = 0.002 b_a d \Rightarrow A_{s(\min)} = 6500 \ \text{mm}^2$

It is seen that the minimum required reinforcements are calculated to be about 6515 and 6500 mm^2, respectively, for the lower and upper parts of the cross-section. Therefore, the minimum required reinforcements in the tension and compression zones are almost similar and are taken as 6515 mm^2. Then, the required reinforcement of the arch cross-section for maximum bending moment can be obtained as follows. It should be noted that although the bending moment is zero everywhere for a momentless arch in theory, the momentless arch shows bending

moments when using *SAP2000*. However, the maximum bending moment obtained using *SAP2000* for the momentless arch is negligible in comparison with the maximum bending moment of the parabolic arch. From Table 5.3, the maximum bending moment produced by *SAP2000* for parabolic arch is 95% more than momentless arch. Moreover, the maximum bending moment is only seen for the longest straight element of the momentless arch curve, which is at arch crown, and the bending moments decrease for short elements. Hence, bending moments occur for the momentless arch because the arch is modelled using straight elements in the software, but the magnitude of the maximum bending is small. The maximum sagging and hogging bending moments in both arches obtained from a *SAP2000* analysis are presented in Table 5.3.

Table 5.3. Maximum bending moments of both arches obtained from *SAP2000*

Maximum bending moment (kNm)	Parabolic arch	Momentless arch
Maximum sagging bending	1082	57
Maximum hogging bending	–959	0

The design ultimate bending moment (M_{rd}) for the cross-sections of the parabolic and momentless arches is equal to $M_{rd} = 0.168 f'_c bd^2 = 15120 \text{ kNm}$. It is seen in Table 5.2 that the design bending moment (M_d) of the parabolic arch from *SAP2000* is equal to 1082 kNm. Based on the concrete design, if $M_{rd} > M_d$, the cross-section needs to be singly reinforced, which means no reinforcement is desired in the compression part of the cross-section. It was calculated that the minimum compressive reinforcement needs to be 6500 mm^2.

To calculate the essential bars in the tension zone of the arch cross-section, the lever arm *z* is calculated first. Thus, assuming the effective depth of the cross-

section to be equal to 600 mm, the lever arm z for flexure is obtained for this section as $z = d - (0.4 \times 0.45d) = 0.82d = 492\,\text{mm}$.

Hence, the required reinforcement of the parabolic arch in the tension zone can be calculated as: $A_S = \dfrac{M_d}{0.87 f_{yk} z} \Rightarrow A_{S(\min)} \cong 5056\,\text{mm}^2$

where f_{yk} is the steel strength, which is assumed to be equal to 500 MPa. It is seen that the reinforcement calculated for the parabolic arch is less than the minimum reinforcement of the cross-section. The same can be concluded in the case of the momentless arch and obviously the minimum reinforcement is considered for the momentless arch. Therefore, the minimum reinforcement of 6515 mm^2 is applied for both parabolic and momentless arches in both compression and tension zones. Consequently, 32 bars of 18-mm diameter with a bar spacing of 150 mm are considered in both the upper and lower sections of the arch cross-section. The confinement bars are assumed to be 12 mm in diameter with a bar spacing of 150 mm. The same configuration for confinement bars is assigned for parabolic and momentless arch shapes. The reason for having low reinforcement for the parabolic arch in theory refers to the usage of arch shapes in design that have less bending moment than beams.

Although the geometry of the momentless arch is close to the geometry of the parabolic arch for *UDL:SW* > 1, small differences in the geometry of arches lead to significant differences in result and structural actions. The difference in the geometry of these arches also has an effect on the designed dimension of the arch cross-section. The length of the parabolic arch (*S'*) is found to be equal to 74717 mm when the arch is modelled using straight elements, while the length of the momentless arch (*S*) is equal to 74792 mm. Therefore, if the concrete volumes of the parabolic and momentless arches are supposed to be equal, then the cross-

sectional depth of the momentless arch can be reduced. However this reduction is negligible in this study.

To compare the behaviour of the momentless arch with the parabolic one for the applied loading, the deflections and first failures of the arch cross-section of both arches are compared with each other in the following sections.

5.6.7. Comparing the deflections of parabolic and momentless arches

To compare the deflection of the parabolic arch with that of the momentless one, it is assumed that both arches are of the same material and have similar general properties. Both arches are subjected to a *UDL* of 507 kN/m plus *SW*. The self-weight of the two arches are assumed to be the same and equal to the value calculated in subsection 5.6.1. Then the parabolic and momentless arches are modelled in *SAP2000* and analysed for the general combination of *SW* and *UDL*. The deflections of the parabolic and momentless arches are shown in Figures 5.12 and 5.13.

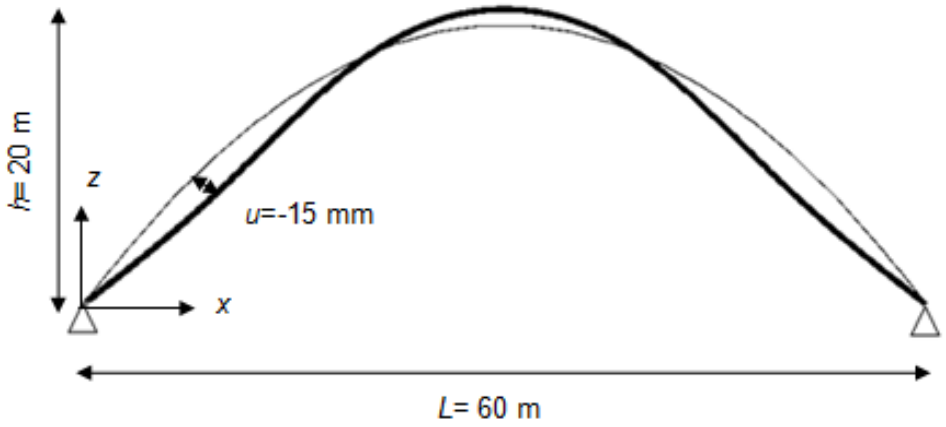

Figure 5.12. *SAP2000*: Deformed shape of parabolic arch subjected to *UDL* of 507 kN/m plus *SW* of 110.1 kN/m

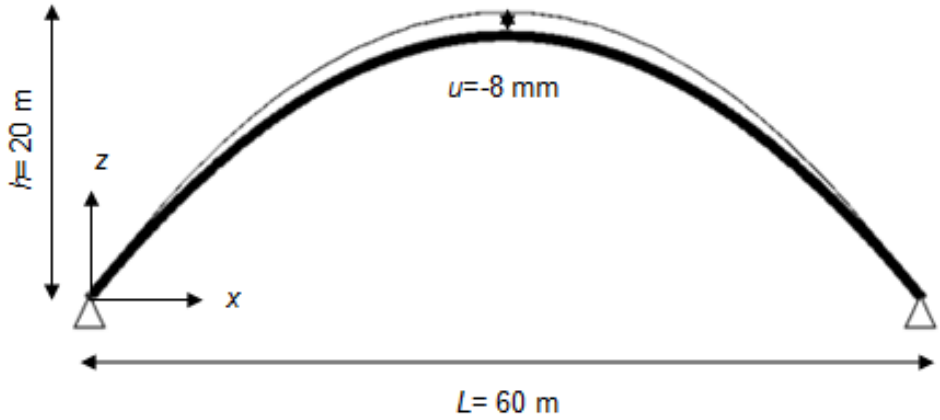

Figure 5.13. *SAP2000*: Deformed shape of momentless arch subjected to *UDL* of 507 kN/m plus *SW* of 110.1 kN/m

The thin line represents the original shape of the arch and thick line is for the deformed shape. It can be seen that the momentless arch deforms vertically and maintains its original geometric shape under the applied load. The maximum displacement of momentless arch is seen at its crown equal to -8 mm. However, parabolic arch deforms noticeably with the maximum displacements equal to -15 mm at both sides of the arch.

The maximum vertical displacement of the momentless arch is about half of that of the parabolic one. It is expected that the true maximum displacement for the momentless arch will be smaller than that obtained owing to the *SAP2000* modelling of the momentless arch having straight finite elements. In order to have the same vertical displacement with the momentless and the parabolic arches, the thickness of the cross-section of the momentless arch is decreased gradually. The required thickness is that when the maximum displacement in the *z* direction reaches -15 mm is chosen. Table 5.4 reports the vertical displacements (*u*) for momentless arches having different thicknesses (*d*) from 0.35 to 0.65 m.

Table 5.4. Maximum displacements of momentless arch obtained from *SAP2000* using different arch thicknesses (*d*)

Momentless arch thickness(m)	*u* in *z* direction (mm)
0.65	–8.205
0.45	–11.695
0.40	–13.068
0.35	–14.785

As can be seen, decreasing the thickness of the momentless arch cross-section makes the maximum displacement increase. This is in accordance with the study carried out by Altunişik et al. (2015). In reality the thickness of the arch should meet the minimum limit of arch thickness. Since the momentless arch is compared with the parabolic option, the former thickness can decrease without considering design regulations. It is observed that the maximum displacement in the *z* direction for the cross-section of the momentless arch with a thickness of 0.35 m is close to that of the parabolic one with a thickness of 0.65 m. Nevertheless, the parabolic arch displays 1.5% more displacement in the *z* direction than the momentless arch. It is also seen that the displacement in the *x* direction does not vary significantly with decreasing *d*. Overall, the momentless arch experiences almost 50% less deflection. To have the same deflection, the momentless arch thickness for a constant rectangular cross-section can be approximately half of the thickness in the parabolic arch. It should be noted that the parabolic arch has the minimum deflection compared to circular and catenary arches for this load case, that is, *UDL:SW* > 1.

The reduction in momentless arch thickness leads to the arch mass decrease. The momentless arch shape mass is equal to 619 kNs^2/m for *d*=0.65m. To have a similar maximum vertical displacement, the momentless arch mass is reduced to 334 kNs^2/m with *d*=0.35m. The mass reduction is important for the construction cost and material saving.

5.6.8. Comparing the first failure of the cross-sections of the parabolic and momentless arches

One of the reasons for searching for an optimized shape of the arch is to establish greater resistance. In other words, a favourable arch structure is one that carries a specified design load case or cases for the minimum weight of the construction material. Concerning other applications of the momentless arch, the first failure of the section of the momentless arch is evaluated with the first failure of the section of the parabolic arch. The first failure of arch cross-section is emerged under ultimate load beyond the initial yield.

For the first step of finding the failure of these arches, the *OpenSees* program (http://*OpenSees*.berkeley.edu/) was used. *OpenSees* is an interactive Tool Command Language (*Tcl*) software framework in which the commands can be changed at any time and performed at the *MS-DOS/Unix* prompt. This program works in parallel with *MATLAB* as a post-processing tool generated by means of *Tcl* scripting language. Each *Tcl* command is bound with a *C*++ procedure. Therefore, this finite element analysis is executed to simulate the response of the arch structure to the applied loading. Both parabolic and momentless arches are modelled using straight elements, which are defined as displacement-based beam-column elements. Since this programme performs as displacement control, the displacement increased by 1 mm at the crown of the arch. As a result, the required structural responses are achieved at each displacement increment using *OpenSees*. The first input to the *OpenSees* program is the nodes that define the arch curve. Parabolic and momentless arch shapes are established by the positions of *x*-*y* nodes, as described in subsection 5.6.5. The other input is the material where, arches are assumed to be reinforced concrete. The area of the reinforcement for arch cross-section is assumed to be 193396 mm^2 that gives A_s=95%A_c. The amount of reinforcement is considered for both arch shapes for

comparison reason having the same section across arch length. However, the momentless arch doesn't require any reinforcement. Having set the pin as arch constraints in the program, the third input is the nodal masses. The nodal masses are produced by the summation of nodal weight caused by *SW* and *UDL* at each individual node. The final step is the introduction of the desirable outputs that involve reactions, displacements, all forces, and bending moments. Furthermore, a final vertical displacement of 10000 mm at the crown of the parabolic and momentless arches is chosen in the *OpenSees* programme. The *MATLAB* file for this analysis can be run for a targeted vertical displacement at the arch crown. Finally, the reactions, forces, and bending moments at the nodes are obtained at each displacement for parabolic and momentless arches.

The second step of finding the first failure of the arch cross-section is accomplished by using an interaction curve between the axial forces and bending moments. Hence, the obtained axial forces and bending moments from *OpenSees* are plotted. This diagram is plotted for each displacement. To do so, a programme was written in *Excel* as "*Visual Basic*" that only requires a vertical displacement at the arch crown as input and gives a diagram of the axial force and bending moment for that displacement. The interaction curve of the arch cross-section can be plotted based on finding some points on the curve such as, the points relevant to the squash load, decompression, balance, and pure moment (EN1992-1-1: 2004). These points are calculated using dimension, reinforcement, and material properties of the cross-section for each arch. The generated interaction curve of each arch is then plotted on the same diagram of axial force and bending moments. To have a safe cross-section, the diagram of axial forces and bending moments of the arch must be under the interaction curve of the arch cross-section. Therefore, the displacement at which the diagram of axial forces and bending moments from *OpenSees* crosses the interaction curve of the cross-section is considered as the first failure of the

cross-section. The parabolic arch shows the first failure of the cross-section when the vertical displacement at the arch crown is 3950 mm; see Figure 5.14. Meanwhile, from Figure 5.15, the first failure of the cross-section of the momentless arch is seen for a vertical displacement of 5200 mm at the arch crown.

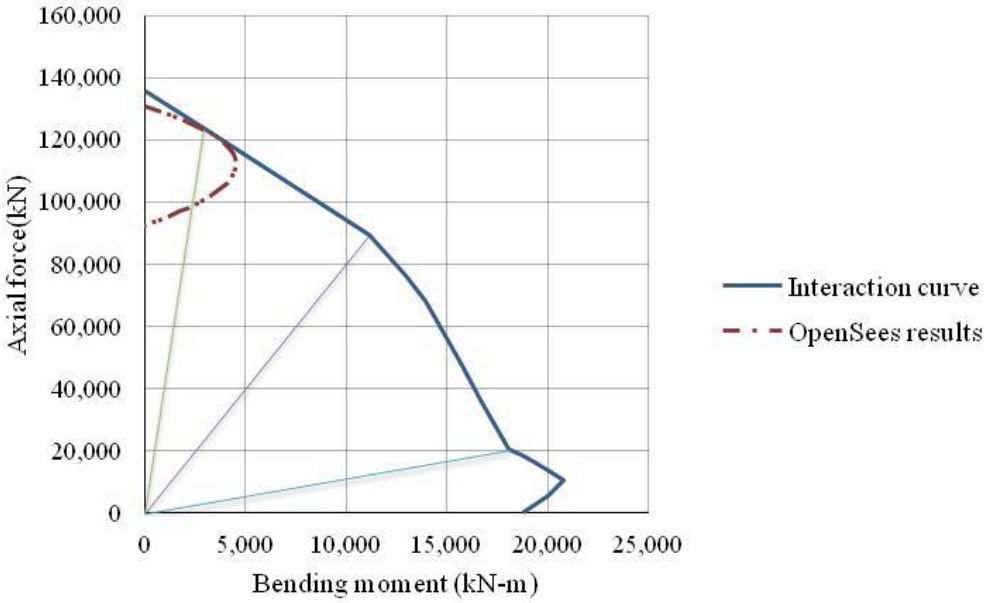

Figure 5.14. Comparison of the interaction curve of the parabolic arch cross-section and diagram of the axial force and bending moment results from *OpenSees* when the vertical displacement at the arch crown is 3950 mm

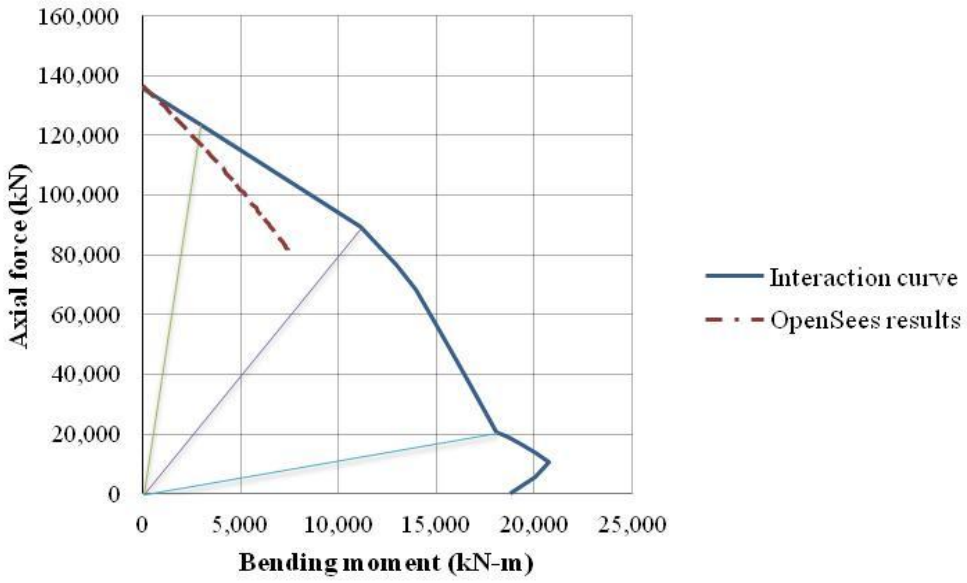

Figure 5.15. Comparison of the interaction curve of the momentless arch cross-section and diagram of axial force and bending moment results from *OpenSees* when the vertical displacement at the arch crown is 5200 mm

The green, purple, and blue straight lines in Figures 5.14 and 5.15 connect the minimum eccentricity, decompression, and nominal balance points to the origin. The minimum eccentricity point shows the maximum moment strength at the maximum axial compression load permitted by Eurocode. The decompression point shows compression and moment strength at zero strain in the tension side reinforcement. The nominal balance point presents compression and moment strength at 50% strain in the tension side reinforcement. The interaction curve crosses the axial force axis at the squash load point that gives the axial compression at zero moment. The interaction curve also crosses the bending moment axis at pure moment point when the axial force is zero.

Although the interaction curve of the parabolic arch is similar to that of the momentless arch, the axial force and bending moment diagrams from *OpenSees* are completely different for these two arches. According to the *OpenSees* results, the total load that causes first failure of the parabolic arch is 211992 kN. First failure of the momentless arch is initiated at 221722 kN. Comparing the first failures of the parabolic and momentless arches, the momentless arch could carry 5% higher load before reaching the first cross-sectional failure.

5.7. Concluding Remarks

An analytical form-finding procedure that can optimize shape is used to find the shape of a momentless two-pin arch. The shape of the momentless form has been investigated using equilibrium equations from Brew (2013) for a pin-ended arch with constant cross-section. The geometry of the momentless arch is then obtained using the equation of zero shear force having axial force only for any *L:h* ratio.

A functional relationship is found that represents the *x* and *y* coordinates individually for the three categories of loading, that is, *UDL:SW* < 1, *UDL:SW* = 1, and *UDL:SW* > 1. The unknown parameters in the governing equations of *x* and *y* coordinates is

solved by iterative method using the boundary condition. The parabolic arch function is used to calculate the initial value in the case of *UDL:SW* > 1. Meanwhile, the initial value in the iterative procedure of finding the *x* and *y* coordinates is chosen from the equation of a catenary arch when *UDL:SW* < 1. Consequently, the geometry of the optimal arch is given as a function of loading for any *L:h* ratio and any ratio of *UDL:SW* via the analytical form-finding technique. However, the effect of arch shape is more tangible for arches of *L:h*≤5.

The application of the momentless arch was shown by comparing a momentless arch and a parabolic one in a theoretical case study. This study was carried out for *UDL:SW* > 1, when the parabolic arch is the best known arch shape. The momentless arch was compared with the parabolic arch, both made of concrete which is relatively weak in tension subjected to the same loading for *L:h*=3.

Case study shows that the maximum vertical displacement of momentless arch to be almost half of the maximum vertical displacement of the parabolic arch for a similar load case. To have the same maximum displacement, the thickness of the momentless arch could be reduced to half of its initial value. This leads to mass reduction in the case of momentless arch down to about half on its initial mass.

From case study, momentless arch could also carry 5% greater load before reaching the first cross-sectional failure compared to the parabolic form under the same conditions. The momentless arch shows this first failure for 24% higher vertical displacement at the arch crown compared to the parabolic one.

Overall, the comparison confirmed the superiority of using the momentless arch in practice which demonstrates the significant effect of shape on structural response.

Chapter 6 : Discussion and Conclusions

The core of this research is finding the momentless shape of a two-pin arch with the use of static equilibrium, highlighting the excellence of its application, which has not been attempted hitherto. This work has been preceded by the assessment of known shapes of arches that advances understanding the behaviour of two-pin arches as a function of chosen arch form. A comprehensive assessment of known arch shapes and a comparison of their structural performance are carried out numerically, which has not hitherto been done. The degree of credibility of approximate analysis methods of two-pin arches consisting of masonry design (Curtin et al. 2006) and virtual work based on bending action only (Megson, 2005), is also evaluated for the first time.

In this chapter, the principal findings of the author's PhD work in association with the effect of arch form on its structural action and the optimal form of two-pin rib arches are presented. The general behaviour of a two-pin arch of constant cross-section is presented in Section 6.1. Section 6.2 scopes a comparison of two alternative approximate methods of arch analysis with a numerical method using *GSA* software and the second theorem of Castigliano. A concise review of analytical finding of the form of a momentless two-pin arch and the application of a momentless arch are given in Section 6.3. Section 6.4 is used to present conclusions from the new contribution to knowledge and understanding. Finally, various research areas for future work are presented in Section 6.5.

6.1. Discussion of the general behaviour of the two-pin arch

The behaviour of two-pin arches of known shapes was studied comprehensively and compared to each other in Chapter 3. Although the behaviour of a circular arch and comparison of the buckling load of known arch shapes have been investigated

widely, the inclusive performance of arch structures based on their structural form has received little attention. The collapse of Gerrards Cross Tunnel (*NCE* 2005) in 2005 was an example of the importance of choosing the best arch shape, depending on load cases during execution and operation

Common arch shapes including catenary, parabolic and circular forms with constant cross-sections of concrete were statically analysed numerically using *GSA* finite element software for different ratios of *UDL:SW*, and for *L:h* ratios between 2–10 in Section 3.5. According to the Timoshenko stability equation (Timoshenko and Gere 1961), the arches were stable for the considered applied loading. The arches were then modelled using 80 straight elements following a sensitivity analysis for the variation of bending moments. The criterion of developing minimum combined stress due to bending and thrust was used to find the optimal common arch shape and best range of *L:h* ratio. The three arch forms were evaluated using four different load cases. The maximum sagging bending moment with parabolic and catenary arches reduced when *L:h* increased from 2 to 5 and for higher ratios the maximum bending moments increased. The minimum sagging bending moment of circular arch was observed at *L:h* = 8. It was seen that increasing the *L:h* ratio to 300 led the maximum bending moment to grow and be close to that of the equivalent horizontal beam. The maximum sagging and hogging bending moments for the catenary and circular arches occurred at approximately the same location which are respectively at arch crown and at both sides, different for the parabolic arch. The sagging bending moments of parabolic and catenary arches are greater than the hogging ones for any *L:h* ratio. However, in the case of the circular arch, the maximum hogging bending moment was higher than maximum sagging bending moment when *L:h* < 6, showing the dominance of tensile forces when the loading was a general combination of uniformly distributed load (*UDL*) and self-weight (*SW*). The absolute value of maximum bending moment of the parabolic and catenary arches reached its minimum for an *L:h* ratio between 4–5; this ratio was between 7–8 for

the circular arch. The displacement and shear forces for the arches gave distributions over the arch shape that are similar in shape to that of the bending moment. Since the deformation of the parabolic arch with *UDL+SW* was different to the catenary and circular arches, the parabolic arch is expected to fail with the different mode. The deformed shape of each arch was similar for any load condition, excluding the patch loading condition. The geometry of different arch forms became almost identical for *L:h* ratios abovef 7. However, it was shown that thereremains differences in the structural response, even at the *L:h* ratio of 10. One important finding from the author's work is that small changes in shape may noticeably affect the structural results. The presence of tensile stress in the arch was inevitable when the load case had the patch load over half of the arch length. In general, the maximum stress for the parabolic and catenary arches had its minimum when $2 < L{:}h < 4$; it was between 4–6 for the circular arch. This range of *L:h* ratios was referred to as the optimal ratios. To generalise this result, the arch made of a hollow steel cross-section that had the same second moment of area as the concrete solid cross-section was analysed with load case *UDL+SW*. Although the magnitude of the combined stresses from the steel arch was different to that of the concrete one, the overall behaviour was the same.

The relation between the maximum thrust of the arches and the *L:h* ratios was almost linear, with the maximum value of thrust at the supports. The difference in the horizontal reaction forces for the three arch shapes was indistinguishable when ratio *L:h* exceeded 5. There were noticeable differences for the bending moments and combined stresses. This indicates the importance of calculating the horizontal reaction force. Since the horizontal reaction force has an increasing linear relation with increasing *L:h* ratio, a lower *L:h* ratio is preferable to design for this action. It has been shown that the arch mass is not largely affected by shape, and that it decreases with increasing *L:h* ratio. The best range of *L:h* ratios assuming mass

saving will be between 4–5. The structural performance of an arch shape with increasing *L:h* was observed to be similar for each load case i.e., any ratio of *UDL:SW*. The values of the maximum bending moment, maximum displacements and maximum combined stress for the parabolic, catenary, and circular arches when *UDL:SW* > 1, *UDL:SW* = 1, and *UDL:SW* < 1 can be used to demonstrate the preference for the parabolic or catenary shape when *UDL:SW* > 1 and *UDL:SW* < 1, respectively. Results for catenary and parabolic arches when *UDL:SW* = 1. The circular arch gave the least desirable results for any ratios of *UDL:SW*. From the parametric studies in Chapter 3, it can be concluded that the circular and the parabolic arches are the least and most preferable shapes, respectively, for typical load cases and *L:h* ratios. A new finding is that the bending moment and horizontal reaction increase in magnitude with arch thickness, except for the parabolic arch with ratio *L:h* = 4 and load case *UDL+SW*.

Exploring the end-shortening effect shows that the horizontal reaction force obtained from static theory (Merritt 1976) increases with *L:h* ratio. However, it is critical to consider the effect of arch shortening when analysing shallow arches. As a known fact (Megson, 2005; Millais, 2005), the parabolic arch, when subjected to *UDL* only, is momentless, while the catenary arch when subjected to *SW* only, is considered to be momentless. The findings from the *FE* work show that catenary and parabolic arches do develop some moments for the *UDL* only and *SW* only load cases. Bending moment is found to increase with *L:h* ratio in both arches and, in particular, when *L:h* is > 5.

Finally, the arc length was compared to the arch span. It was seen that the percentage difference between the length and span of each arch was less than 1% for *L:h* > 16.

6.2. Discussion of the comparison of different methods of analysis

Different methods for the analysis of two-pin arches have been explored extensively in the past. However, the credibility of some existing analysis methods based on approximate models such as the masonry design and virtual work (depending on bending action only) had not yet been investigated. The effect of the assumptions made by these methods on the structural response of two-pin arch was explored in Section 4.3.

To find the horizontal reaction force for circular and parabolic arches, different methods of analysis were applied in Section 4.4. The methods involved: a theoretical analysis based on the second Castigliano principle; *FEM* using *GSA* software; virtual work (Megson, 2006) and the masonry design (Curtin et al., 2006). The studied arches were subjected to the general combination of *SW* plus *UDL*. When using Castigliano's theorem, to assess the effect of different actions in the strain energy formulation, the methodology was applied to divide the analysis: bending action only; bending plus shear and thrust action terms; full structural actions for the combination of bending, shear, thrust and coupling of bending and thrust. It was demonstrated that the shear and thrust contributions have an increasing effect on the maximum bending moment and maximum combined compressive stress, relative to the solution with bending action only. When evaluating different terms in Castigliano's approach, the differences in the combined stresses < 5% for $L:h < 8$, which is considered negligible. Generally, the presence of the bending/thrust coupling term slightly decreased the bending moments calculated.

Alternative analytical methods of virtual work and masonry design are based on a number of assumptions, with varying degrees of credibility. The effect of these assumptions was evaluated. In the masonry design method, it is assumed that the thrust at the crown passes the arch thickness centre that leads the arch to act like a

three-pin arch. This assumption has a significant impact on the resultant bending moment results; mostly near the crown of the arch. Furthermore, the level of discretisation over the arch's length into individual segments (to which *SW* and *UDL* are applied) is another approximation. It was shown that, generally, the results of structural actions obtained from using this method deviated significantly from those calculated using other methods. In the case of the virtual work approach, it is assumed that displacements are produced only by bending and so, the effect of thrust on arch deformation is ignored. Also, when analysing any arch other than those having a semi-circular profile, to avoid complicated integrals in the process of finding a horizontal reaction force, the secant assumption is used.

The results of the horizontal reactions obtained from the Castigliano approach were compared to those calculated from applying static theory to a parabolic arch subjected to *UDL* only. The horizontal reaction obtained confirmed that the parabolic arch shape is momentless for this load case. This is in agreement with the results calculated from the alternative analysis method and the Castigliano approach, using bending action only. This finding was due to the analysis methods ignoring the section properties because the arch is assumed to be non-deformable. Because arches are deformable the moments were not estimated well by applying these methods, in particular, when the $L{:}h > 5$. The results from the masonry design method and other methods depending on bending action only do not have adequate numerical precision in predicting arch structural action effects.

The good correlation between the results obtained from *FE* and Castigliano's theory due to bending, shear and thrust showed the validity of using *GSA* in the PhD work (providing a sufficient number of straight elements are used to model a two-pin arch). Different values of maximum bending moment and maximum combined stresses at different locations were obtained when using different methods of analysis.

In general, the horizontal reaction and bending moment at the crown of parabolic and circular arches subjected to a general load combination of *SW* and *UDL* are seen to increase with arch thickness. Probably, analysing the arches for other load case predominantly for patch loading could show the effect of each term of strain energy more specifically. The horizontal reaction forces of the studied arches decreased slightly with increasing arch thickness when only *UDL* was applied, although this action was found to be a constant with Castigliano having bending action only. This was due to a change in the gyration of radius with thickness, when other actions to bending were considered in the strain energy formulation.

Concerning the shortening effect, the horizontal reaction force obtained from the alternative methods and Castigliano with bending action only is seen to grow linearly with increasing *L:h* ratio. This outcome led to unsatisfactory results in the case of shallow arches, with the horizontal reaction force starting to decrease when *L:h* > 80 when using *FE* and Castigliano's method, with other actions in addition to bending.

6.3. Discussion of the optimal shape of two-pin arch

Despite many studies on structural optimisation, the optimal shape of a two-pin rib arch with constant cross section has not been investigated analytically based on the state of static equilibrium, probably because of the essential difficulties of mathematical analysis. The analytical form-finding of two-pin arch structures considering full structural actions of bending, shear, and thrust has not hitherto been published. The contribution of the momentless arch as an optimal two-pin rib arch form is presented here for the first time in Section 5.6.

As was shown in Chapter 3, the form of the arch can have a crucial influence on structural actions, which will inherently impair the long-term durability and safety of the arch made of masonry or concrete. The shape of the optimal two-pin arch with

constant cross-section was derived analytically using a form-finding approach based on the work done by Brew (2013). It is known that none of the circular, parabolic or catenary arch shapes is an optimal form when the arch is subjected to both *SW* and *UDL*. The geometry of the momentless arch was determined using the state of the static equilibrium of the arch (Brew, 2013). Therefore, the equation of shear force, which is the derivative of the moment equation, for any arbitrary point on the arch, was set to zero. The method was developed for any *L:h* ratio and any ratio of *UDL:SW*. The geometry of the optimal arch was found as one functional relationship representing the *y* coordinate for any *UDL:SW* ratio, and corresponding to the *x* coordinate for the three load cases of: *UDL:SW* < 1; *UDL:SW* = 1, and *UDL:SW* > 1. The functional relationships expressing the *x* and *y* coordinates involved the horizontal reaction force as an unknown parameter. The author made calculations by applying an iterative process with constraints for a two-pin arch. To find the initial values of the defined variable for finding the horizontal reaction force, the geometry for a parabolic and for a catenary arch was taken as an initial value for *UDL:SW* ≥ 1 and *UDL:SW* < 1, respectively. The process was coded in *MATLAB.* Starting with the ratios *L:h* ratio and *UDL:SW* the shape of the optimal momentless two-pin arch could be determined. The momentless arch application was then investigated numerically. First, the maximum displacement of momentless and parabolic arches was compared against each other for the same load and conditions, where *UDL:SW* > 1. Since the parabolic arch performed best for this load case against catenary or circular arch shape: the momentless arch compared to the best-known arch shape. To do so, both arches were modelled in *SAP2000* software using 102 straight elements. The parabolic arch deformed significantly, while the momentless arch kept its geometry. Furthermore, the maximum displacement of the parabolic arch was about twice that of the momentless arch. This was followed by a study on the first failure of the cross-section for concrete arches using the *OpenSees* programme. Calculated was the internal response for each 1 mm increment in

vertical displacement at the arch crown. The bending moment and axial forces calculated using *OpenSees* were then plotted using *Visual Basics* in *Excel* and compared to the *M-N* interaction curve for the arch cross-section. The comparison showed the contribution of the momentless arch in practice.

6.4. Conclusions

The principal conclusions are as follows:

- The response of two-pin arch forms to applied loading is critically dependent on the arch form and its shape governed by the *L:h* ratio.

- Circular arches are very sensitive to variations in ratio *L:h* and large differences in the arch's bending moments and combined (bending + thrust) stresses compared to parabolic and catenary arch forms.

- The minimum compressive stresses in parabolic and catenary arches were observed for *L:h* ratios between 2 and 4. Although the optimum *L:h* ratio for a circular arch, using the minimum combined stress criterion, is between 4 and 6, the stresses developed are still higher than with parabolic or catenary arches. This finding is acceptable when the arch is of masonry, concrete, or steel.

- Circular arches exhibit relatively high combined stresses and bending moments, particularly for the *L:h* ratio of 2 (i.e. a semi-circular arch).

- The difference of arch mass for different arch shapes is negligible when *L:h* ≥ 4. Moreover, the arch mass decreases when *L:h* is increased. The author recommends that an *L:h* ratio of about 4 can be chosen to save mass while also preserving the arch's structural efficiency.

- Even a 0.1% change in the value of the horizontal reaction of three known arch shapes can lead to a 10% change in the value of the maximum bending moment.

- The outcome of approximate methods for predicting bending moments is not positive, because of the limitations from the assumptions made in the analysis. It is noted that, these methods are currently used by design engineers to obtain the reaction forces in two-pin rib arches.

- Different analysis methods predict different values of maximum bending moment at different locations in the arch.

- For a rigorous analysis method the author formulated the Castigliano's approach (Timoshenko, 1986) that involved strain energy due to full structural actions (bending, shear, thrust, and coupling of bending and thrust).

- By using the full analysis it was found that by coupling thrust and bending there is a slightly decrease in the bending moments when compared with Castigliano's method without the coupling.

- The magnitude of the horizontal reaction force at the supports, and bending moment at the crown of the circular arch is found to grow on increasing the arch thickness for all *L:h* ratios, using any method of analysis and for all load conditions.

- The bending moment at the crown of the parabolic arch decreases on increasing arch thickness at an *L:h* ratio of 4 using Castigliano's method with full structural actions with both *SW* and *UDL*. This finding is opposite to what is found with other *L:h* ratios.

- The masonry design and other methods relying on bending action only produced the least reliable results. One reason for the prior performance is that these methods do not involve the effect of rib shortening.
- The results confirmed a known fact that the parabolic arch performs best for the load case of *UDL >> SW*, and the catenary for load case *UDL << SW* (Millais 2005), when minimizing the maximum bending moment and combined stresses are considered. In reality, when *SW* and *UDL* are combined, neither of known arch shapes represents an optimal form under a range of loading cases and *L:h* ratios.
- The optimal shape of two-pin rib arches that is momentless is obtained for any ratio of *UDL:SW* and *L:h* using an analytical form-finding technique (Brew, 2013).
- Case study shows that the maximum vertical displacement of momentless arch was found to be almost half of the maximum vertical displacement of the parabolic arch under the same load conditions when *UDL:SW* > 1.
- The momentless arch could carry greater loads to have the first cross-sectional failure than the parabolic arch for *UDL:SW* > 1 and the same load conditions in the case study.

6.5. Recommendations for future work

6.5.1. Further work on form-finding of arch structures

It would be interesting to expand the conducted work of analytical form-finding of two-pin arches to their three-dimensional equivalent of arches, such as domes and vaults/tunnels. Exploring the form of an optimal vault and domes has demonstrated the validity of the findings in this dissertation for the third dimension. Moreover, the structural behaviour could be evaluated for the effect of the third dimension. This

project will also give an in-depth understanding of the structural action of domes and vaults. Hence, the form-finding of tunnels and vaulted structures could be carried out in isolation as a novel topic. It is expected that this proposed research area will also indicate the significant effect of small changes to structural form on the structural behaviour; in particular, the stresses produced within the structure material.

This study was also carried out for static loading when the uniformly distributed load was applied across the full span of the arch. Therefore, another potential research area is the application of the proposed analytical form-finding technique for two-pin arches and *3D* dome and vault structures under transient loading. In this regard, the effect of dynamic loading on structural response could comprehensively be assessed. Thus, a vast amount of information could be collected to provide for arch-based structures that could carry their self-weight and transient loading. The project will test the hypothesis of ideal shapes of arch-based structures as momentless forms for variable loading, which advances their safety and durability compared to the existing equivalent structures. The contribution of finding the optimal form while applying variable loads could be studied for real cases with the criterion of finding the minimum collapse load. In view of the proliferation of studies on the collapse and buckling load of arches subjected to dynamic loading, the results of the proposed shape could then be compared to the available results of the corresponding form. This project could be defined separately for two-pin and fixed-ended arches, and also three-dimensional designs of arch structures. The effect of the imposed transient load on finding the optimal form of arch-based structures could be explored in parallel with considering the appropriate structural materials.

The work here was mainly analytical, which required numerical calculation to achieve the ultimate solution. On the other hand, an experimental approach could provide a solution that is more easily understood, due to the visualisation of

practical aspects. A new prospective project could be defined as finding the optimal form of two and three-dimensional arch structures individually using experimental tools.

6.5.2. Further work on different methods of analysis

The arches were analysed in Chapter 4 using the second theorem of Castigliano when strain energy was based on full structural action for static load. This work could be examined for other load cases, such as that involving patch loading, e.i., a uniformly distributed load applied on half of the arch span. The difference of applying different analysis methods might also be highlighted more in the presence of the patch load. Thus, more research could be carried out on the topic of different methods of arch analysis, indicating the amplitude of the different results. This work may lead to finding a specific load condition in which the obtained results using different analysis methods differ significantly from each other.

6.5.3. Further work on computational analysis of arch structures

Each form of common shape of arch, including catenary, parabolic, and circular, showed similar behaviour for the considered range of *UDL:SW* ratios. Only the magnitude of structural response varied when *UDL:SW* was changed in that determined range. It is however also possible to find a certain value of *UDL:SW* ratio, beyond which the arch behaves differently. This work also indicates the effect of *UDL:SW* on structural behaviour. Moreover, possible further effort lies in the comprehensive computational analysis of two- and three-dimensional arch structures under their self-weight and transient load conditions. Stress analysis of arch structures under static and dynamic loads could allow the designers to make informed choices in design using the appropriate arch form.

Glossary

Approximate method	A computational method which is based on assumptions to simplify the problem
Arch ring	The curved member that is the major supporting component in an arched structure. A single span arch may built of single- or multi-ring
Arch structure	A curved (concave down) structure spanning between two supports that carries a large amount of applied load in compression
Axial deflection	Arch structures can resist compressive stresses which produce compressive strains. These strains cause axial deflection and reduction in arch height because of crown deflection. This height reduction generates additional compressive forces in the arch.
Castigliano second theorem	The theorem used to calculate horizontal reaction force of statically indeterminate arch. The displacement at a point is equal to the derivative of strain energy with respect to a force acting at the point
Catenary shape	The shape of an inextensible chain that hangs under its own weight
Combined stress	Combination of axial stress and bending one
Coupling term	The term refers to the combination of axial force and bending moment in strain energy equation
Elastic material	The material that its deformation is in proportion to the applied load and the deformation is recoverable when the applied force is removed
Flat arch	The arch with high *L*:*h* ratio that could carry the most applied load (90%) using bending moments
Form	Correspondent to shape
Form-finding	A technique that uses optimization methods to find the optimal form of structure under a particular load condition (Otto, 1995)
Funicular	Derived from Latin word for “rope”. A cable subjected to load deforms depending upon the load. The acquired form is called funicular
Funicular structure	A structure that is in equilibrium state by adopting a form corresponding to the applied load
GSA	Finite element structural analysis software used to

	analysis arch structures
Hogging bending moment	The bending moment results in convexity upwards in beam which generates tension in top fibres of the beam; also called negative bending moment
Hunching	Consisting large coarse sandstone blocks possibly cemented together behind the arch above the springing
Load case	Illustrates the load situations used in analysis
L:h ratio	The ratio of span to height of the arch
Masonry design method	A design method used for arches laid out in the Structural Masonry Designers' Manual (Curtin et al, 2006)
Momentless	Having bending moment equal to zero within the structure
OpenSees	Finite element analysis software used in this study to simulate response of the arch
Optimal shape	An efficient structural shape that transfers loads while the magnitude of action effects is relatively small
Parabolic shape	The shape of a weightless chain that carries a uniformly distributed load along its span
Rib arch	An economical design in which the voussoirs are replaced by discreet arch rings. Rib arches comprise of either closed spandrels, with the ribs supporting solid spandrel walls, or open spandrels, with columns rising from the extrados to support the deck structure
Sagging bending moment	The bending moment results in concavity downwards in beam which generates compression in top fibres of the beam; also called positive bending moment
SAP	Finite element structural analysis software used to analysis arch structures
Semi-empirical method	A method used empirical corrections and data in parallel with additional approximations to speed up the calculations
Sensitivity analysis	An analysis to assess structure response when design variable changes
Shallow arch	The arch with high *L:h* ratio which is sensitive to axial deformation
Shearing resistance angle	It is a soil friction angle that derived from Mohr-Coulomb failure criterion and it is used to describe the friction shear resistance of the soil

Shortening	Increasing compressive forces in pin-ended arches due to increasing *L:h* ratio causes arch rib to be shortened
Slender	When the cross-sectional dimensions of the arch are small compared to the radius of curvature of arch centre line
Springing	Points/level at which the arch begins to rise from its supports
State of static equilibrium	When forces acting on an object which is at rest are balanced
Structural action effect	The resulting effects of structural actions such as; bending moments, displacements, and stresses
Ultimate passive deflection of soil	The deflection that is necessary to mobilize earth ultimate passive pressure. This pressure is the highest limiting lateral pressure developed at the onset of shear failure in the direction opposite to the direction of acting earth pressure
Virtual work method	An analysis method to calculate the horizontal reaction force of statically indeterminate structures
Voussoir	A wedged shape element typically a stone that used to construct arch structures

References

Altunişik, A.C., Kanbur, B. & Genç, A.F. (2016). The effect of arch geometry on the structural behavior of masonry bridges, *Smart Structures and Systems,* **16**(6), 1069-1089

Ambrose, J. & Tripeny, P. (2011). *Building Structures,* 3rd Edition, John Wiley & Sons, Inc., New Jersey, USA

Audenaerta, A., Fanning, P., Sobczak, L. & Peremans, H. (2008). 2-D analysis of arch bridges using an elasto-plastic material model, *Engineering Structures*, **30** (3), 845–855

Austin, W.J. & Ross, T.J. (1976). Elastic Buckling of Arches under Symmetrical Loading, *Journal of Structural Division ASCE*, **120**, 1085-1095

Barker, M. & Puckett, J.A. (2007). *Design of Highway Bridges*, 3rd Edition, John Wiley & Sons, Inc., New Jersey, USA

Barnes, M.R. (1977). *Form-finding and analysis of tension space structures by dynamic relaxation*, Thesis (PhD), City University London, UK

Bensalem, A., Sibbald, A. & Fairfield, C.A. (1998). The use of dynamic characteristics for the optimal design of arches, *Computers and Structures*, **68** (5), 461-472

Blasi, C. & Foraboschi, P. (1994). Analytical approach to collapse mechanisms of circular masonry arch, *Journal of Structural Engineering*, **120** (8), 2288-2309

Bletzinger K.-U. (2011). Form finding and morphogenesis. *In: Mungan I, Abel JF, Editors. Fifty years of progress for shell and spatial structures; Multi Science Publishing Company Limited*, 459–474

Bradford, M.A., Pi, Y.-L., & Tin-Loi, F. (2007). Nonlinear analysis and buckling of elastically supported circular shallow arches, *Solids and Structures,* **44** (7-8), 2401-2425

Brew, J. (2013). *Hand writing notes given by Professor W.J Lewis*, University of Warwick, UK

Bridle, R.J. & Hughes, T.G. (1990). An energy method for arch bridge analysis, Proceedings of the Institution of Civil Engineers, **89** (3), 375-385

BS EN 1991-1-1. (2002). *Eurocode 1: Actions on structures* – Part 1-1: General actions – Densities,self-weight, imposed loads for buildings

BS EN 1991-2. (2003). *Eurocode 1: Actions on structures* - Part 2: Traffic loads on bridges

BS EN 1992-1-1. (2004). *Eurocode 2. Design of Concrete Structures*. Part 1: General Rules and Rules for Buildings.

Byun, K.J. & Han, S.H. (1984). Shape optimization of arches, *Proceeding of the Korean Society of Civil Engineers*, **4**, 127-135

Casas, J. (2011). Reliability-based assessment of masonry arch bridges, *Construction and Building Materials,* **25** (4), 1621–1631

Castigliano, C.A.P. (1876). Nuova teoria intorno all'eqilibrio dei sistemi elastici, *Trans. Acad. Sci.,* Turin, Italy

Castigliano, C.A.P. (1879). Theorie de l'eqilibre des systems elastiques et ses applications, *F. A.Nero.,* Turin, Italy

Chenais, D., Rousslet, B. & Benedict. R. (1988). Design Sensitivity for Arch Structures with Respect to Midsurface Shape under Static Loading, *Journal of Optimization Theory and Application,* **58** (2), 225–239

Chilton, J. (2012). Form-finding and fabric forming in the work of Heinz Isler, *International Society of Fabric formwork,* 84–91

Choi, J.H. (2002). Shape design sensitivity analysis and optimization of general plane arch structures, *Finite Elements in Analysis and Design*, **39** (2), 119–136

Choi, K.K. & Seong, H.G. (1986). Design component method for sensitivity analysis of built-up structures, *Journal of Structural Mechanics,* **14** (3), 379-399

Choo, B.S. & Coutie, M. G. (1991). Finite-element analysis of masonry arch bridges using tapered elements. *Proceedings of the Institution of Civil Engineers,* **91**, 755-770

Clemente, P., Occhiuzzi, A. & Raithel, A. (2001). Discrete model for non-linear analysis of masonry arches Discrete model for non-linear analysis of masonry arches, *In Abdunur C. (ed) ARCH'01*, 417-422

Coenders, J.L. & Bosia, D. (2006). Computational tools for design and engineering of complex geometrical structures: From a theoretical and a practical point of view, *On Computer Games, Advanced Geometries, and Digital Technologies* , 271-279

Crisfield, M.A. (1984). *A finite element computer program for the analysis of masonry arches,* Transport and Road Research Laboratory, Crowthorne, UK

Cundall, P.A. & Hart, R.D. (1992). Numerical modelling of discontinua. *Eng Comput,* **9** (2), 101-113

Curtin, W.G., Shaw, G., Beck, J.K. & Bray, W.A. (2006). *Structural Masonry Designers' Manual,* 3rd Edition revised by Easterbrook, Blackwell Publishing Inc., Massachusetts, USA

Davis, L., Rippmann, M., Pawlofsky, T. & Block, P. (2012). Innovative funicular tile vaulting, *The Structural Engineer,* **90** (11), 46-56

Dems, K. & Mroz, Z. (1987). A variational approach to sensitivity analysis and structural optimization of plane arches, *Mech. Struct. Mach*, **15**, 297-321

Descamps, B. (2014). *Computational Design of Lightweight Structures: Form Finding and Optimization*, John Wiley & Sons, New York

Ding, Y. (1986). Shape Optimization of Structures-A Literature Review, *Computers Structures*, **24** (6), 985-1004

Dopker, B., Choi, K.K. & Benedict, R.L. (1988). Shape Design Sensitivity Analysis of Structures Containing Arches, *Computer Structures*, **28** (1), 1-13

Drosopoulos, G.A, Stavroulakis, G.E & Massalas, C.V. (2008). Influence of the geometry and the abutments movement on the collapse of stone arch bridges, *Construction and Building Materials*, **22**, 200–210

Fairfield, C.A. & Ponniah, D.A. (1994). Model tests to determine the effect of fill on buried arches, *Proceedings of the Institution of Civil Engineers - Structures and Buildings*, **104** (4), 471-482

Fanning, P.J. & Boothby,T.E. (2001). Three-Dimensional modelling and full-scale testing of stone arch bridges, *Computers and Structures*, **79** (29), 2645-2662

Farshad, M. (1976). On optimal form of arches, *Journal of the Franklin Institute*, **302** (2), 87-194

Foglar, M. & Křístek, V. (2012). Centre-line optimization of buried arch bridges – theoretical derivation and practical application, *Natural hazards (optimization of protection, interaction with structures),* 141-148

Fonseca A. & F. Mato. (2005). Infant Henrique Bridge over the River Douro, *Structural Engineering International*, **15** (2), 85-87

Gaylord E.H. & Gaylord C. N. (1990). *Structural Engineering Handbook.* McGraw-Hill Publishing Company, New York

Gencturk, B. & Kilic, S. A. (2006). Assessment of Historical Masonry Arch Bridges Using the Discrete Finite Elements Method, *Kandilli Observatory and Earthquake Research Institute*, Turkey

Ghigliotty, WL. (2012). *Compression-bending interaction and spring horizontal stiffness in structural arches,* Thesis (MSc), Polytechnic University of Puerto Rico

Gibbons, N. & Fanning, P.J. (2010). Ten stone masonry arch bridges and five different assessment approaches, *Proceedings of the ARCH'7 - 6th International Conference on Arch Bridges,* Fuzhou, China

Gilbert, M. (2007). Limit analysis applied to masonry arch bridges: state-of-the-art and recent developments, *Proceedings of the ARCH'7 -5th International Conference on Arch Bridges,*13-28

Gilbert, M. & Melbourn, C. (1994). Rigid block analysis of masonry structures, *The Structural Engineer,* **72** (21), 356-361

Gimena, F.N., Gonzaga, P. & Gimena, L. (2014). Analytical formulation and solution of arches defined in global coordinates, *Engineering Structures,* **60**, 189–198

Griva, I.A. & Vanderbei, R.J. (2003). Case Studies in Optimization: Centenary Problem, *Optimization and Engineering,* **6**, 463–482

GSA Analysis Version 8.6. Released (2012). *Oasys Ltd.*, London, UK.

Habbal, A. (1998). Direct Approach to the Minimization of the Maximal Stress over an Arch Structure, *Journal of optimization and application*, **97** (3), 551-578

Haftka,, R.T. & Grandhi R.V. (1986). Structural Shape Optimisation-A Survey, *Computer Methods in Applied Mechanics and Engineering,* **57** (1), 91-106

Harvey, W.J. & Smith, F.W. (1987). Semicircular arches, *Proceedings of the Institution of Civil Engineers*, **85** (4), 845- 849

Harvey, W. J. & Smith, F. W. (1991). The behavour and assessment of multispan arches, *The Structural Engineer,* **69** (24), 411-417

Harvey, W.J., Smith, F.W. & Vardy, A.E. (1990). Three-hinge analysis of masonry arches, the structural engineer, **68** (11), 203-207

Heyman, J. (1966). The stone skeleton, International Journal of Solids and Structures, **2** (1), 249-279

Heyman, J. (1969). The safety of Masonry arches, *International Journal of Mechanical Sciences*, **11** (4), 363-385

Heyman, J. (1982). The Masonry Arch, *Ellis Horwood,* Chichester, UK

Heyman, J. (2010). Equilibrium of masonry arches, *Proceedings of the Institution of Civil Engineers - Engineering and Computational Mechanics,* **163** (3), 129-133

Houšt, V., Elias, J. & Mica, L. (2013). Shape optimization of concrete buried arches, *Engineering Structures,* **48**, 716–726

Hsu, Y.L. (1994). A review of structural shape optimization, *Computers in Industry*, **26**, 3-13

Hughes, T.G., Davies, M.C.R. & Taunton, P.R. (1998). Small scale modelling of brickwork arch bridges using a centrifuge, *Proc Instn Civil Eng Struct Build*, **128**, 49-58

Hughes, T.G. & Pritchard, R. (1998). In situ measurement of dead and live load stresses in a masonry arch, *Engineering Structures*, **20** (1), 5-13

Isler, H. (1994). Concrete shells derived from experimental shapes, *Structural Engineering International,* **3**, 142-147

Killian, A., & Ochsendorf, J. (2005). Particle-Spring Systems for Structural Form Finding, *Journal of the International Association for Shell and Spatial Structures,* **46** (2), 77–84

Kim, I.Y. & Kwak, B.M. (1993). Shape design sensitivity analysis and optimization of general shape arches, *Computers & Structures,* **48** (17), 1025–1031

Koohestani, K. (2014). Nonlinear force density method for the form-finding of minimal surface membrane structures, *Communications in Nonlinear Science and Numerical Simulation,* **19** (6), 2071–2087

Krenk, S. & Høgsberg, J. (2013). *Statics and Mechanics of Structures.* Springer

MATLAB and Statistics Toolbox, Release 2012b, *The MathWorks, Inc.*, Natick, Massachusetts, United States.

Megson, T. H. G. (2006). *Structural and Stress Analysis*, 2nd Edition, Elsevier, Oxford, UK

Merritt F. S. (1976). *Standard Handbook for Civil Engineers,* McGraw-Hill Book Company, New York

Michell, A.G.M. (1904). The limits of Economy of Material in Frame-structures., *Philosophical Magazine S6,* **8** (47), 589-597

Millais, M. (2005). *Building Structures: from concepts to design*, 2nd Edition, Spon Press, Abingdon, UK

Miller, A.B., Kenneth, M.C. & Mathew C.G. (2000). *A Survey of Masonry and Concrete Arch Bridges in Virginia,* Virginia Transportation Research Council, Virginia, USA

Moon, J., Yoon, K.Y, Lee, T.H. & Lee, H.E. (2007). In-plane elastic buckling of pin-ended shallow parabolic arches, *Engineering Structures,* **29** (10), 2611-2617

Mosely, B., Bungey, J., Husle, R. (2007). *Reinforced concrete design to Eurocode 2,* 6th Edition, Palgrave Macmillan

Ng, K. (1999). *Analysis of masonry arch bridges*, Thesis (PhD), Napier University

Ng, K.-H. & Fairfield, C.A. (2004). Modifying the mechanism method of masonry arch bridge analysis, *Construction and Building Materials*, Vol **18** (2), 91–97

Oliveira, D. V., Lourenco, P. B. & Lemos, C. (2010). Geometric issues and ultimate load capacity of masonry arch bridges from the northwest Iberian, *Engineering Structures*, **32** (12), 3955–3965

Osserman, R. (2010). How the gateway arch got its shape, *Nexus Network Journal*, **12**, (2), 176-189

Otto, F. & Rasch, B. (1995). *Finding Form: Towards an Architecture of the Minimal*, 3rd Edition (Edition Axel Menges), Deutsche Werkbund Bayen

Oxman, R. & Oxman, R. (2010). The new structuralism, Architectural design, *Wiley*, **80** (4), 14-23

Pintucchi, B. & Zani, N. (2009). Effects of material and geometric non-linearities on the collapse load of masonry arches, *European Journal of Mechanics A/Solids,* **28** (1), 45-61

Pippard, A.J.S. & Ashby, K. J. (1939). An experimental study of the voussoir arch, *Journal of the Institution of Civil Engineers,* **10** (3), 383-404

Pippard, A.J.S. & Chitty, L. (1951). A study of the Voussoir arch, *National Building Studies Research Paper* (11)

Pippard, A.J.S., Tranter, E. & Chitty, L. (1936). The Mechanics of the Voussoir Arch, *Journal of the Institution of Civil Engineers,* **4** (2), 281-306

Proske, D. & Pieter, V.G. (2009). *Safety of historical stone arch bridges*, Springer

Rizzi, E., Rusconi, F. & Cocchetti, G. (2014). Analytical and numerical DDA analysis on the collapse mode of circular masonry arches, *Engineering Structures,* **60**, 241–257

Salonga, J. A. (2010). *Innovative systems for arch bridges using ultra high-performance fibre-reinforced concrete*, Thesis (PhD), University of Toronto

Salonga, J. & Gauvreau, P. (2010). Span-to-rise ratios in concrete arches: threshold values for efficient behaviour', *ARCH'10 – 6th International Conference on Arch Bridges,* 665-673

SAP2000. (2012). *Integrated Finite Element Analysis and Design of Structures*, Computers and Structures, Inc., CSI, Berkeley, California

Serra, M. (1994). Optimal Arch: Approximate Analytical and Numerical Solutions,

Smith, F. W. (1991). *Load path analysis of masonry arches,* Thesis (PhD), University of Dundee

Smith, F.W., Harvey, W.J. & Vardy, A.E. (1990). Three-hinge analysis of masonry arches, *The structural engineer*, **68** (11), 203-207

Tadjbakhsh, I.G. (1981). Stability and optimum design of arch-type structures, *International Journal of Solids & Structures,* **17** (6), 565-574

Tadjbakhsh, I. & Farshad, M. (1973). On conservatively loaded funiular arches and their optimal design, *Proceedings of IUTAM Symposium on Optimization in Structural Design,* Warsaw

Taysi, N., Gögüs, M.T. & Özakça, M. (2008). Optimization of arches using genetic algorithm, *Computational Optimization and Applications,* **41** (3), 377–394

Taurenis, M., Linde, A., Gruberts, R. & Straupe, V. (2013). Examples of construction of new reinforced concrete arch bridges in Latvia, *XXVIII International Baltic Road Conference*, Lithuania

The official site for the State of Maryland. (2015). Historical Development :Metal Arch Bridges, *Available: https://www.roads.maryland.gov/OPPEN/VIII-HDm.pdf.*

Timshenko, S.P. (1986). *Strength of Materials.* 3rd Edition, CBS Publishers, New Delhi

Timoshenko, S.P. & Gere, J.M. (1961). *Theory of Elastic Stability,* 2nd Edition, McGraw Hill, New York

Timoshenko, S.P. & Young, D.H. (1961). *Theory of Structures,* McGraw Hill, New York

Tomlow, J., Graefe, R., Otto, F. & Szeemann, H. (1989). *Das Modell / The Model / El Modelo. Number 34 in Mitteilungen des Instituts fr Leichte Flchentragwerke (IL),* Institut für Leichte Flächentragwerke, Stuttgart

Tóth, A.R., Orban, Z. & Bagi, K. (2009). Discrete element analysis of a stone masonry arch, *Mechanics Research Communications*, **36** (4), 469–480

Tyas, B., Pichugin, A.V. & Gilbert, M. (2011). Optimum structure to carry a uniform load between pinned supports: exact analytical solution, *Proceedings of the Royal Society A: Mathematical, Physical and Engineering Sciences,* **467** (2128), 1101-1120

Vanderplaats, G.N. & Han, H. (1986). A general-purpose optimization program for engineering design, *Int. J. Comput. Struct,* **24**, 13-21

Vanderplaats, G.N. & Sugimoto, S.H. (1990). Arch shape optimization using force approximation methods, *Structural Optimization,* **2** (4), 193-201

Veenendaal, D. & Block, P. (2012). An overview and comparison of structural form finding methods for general networks, *International Journal of Solids and Structures,* **49** (26), 3741–3753

Appendix A: Theoretical analysis of a two-pin circular arch using Castigliano's approach

The circular rib arch of uniform lineal density *q* supporting a superstructure of uniform density *w* per unit span is analysed using the second theorem of Castigliano. The half of two-pin circular arch with the loading applied to it and all forces acting along the arch is presented in Figure A.1. Thrust, shear, and bending action are denoted with *T*, *F*, and *M* at point *P* along the length in this figure. The height, half span length and the radius of the circular arch are shown by *h*, *l*=*L*/2, and *R*. Therefore $b=R-h=RSin(\gamma)$, in which γ is defined as the angle between the arch support and horizontal axis. The coordinates of the origin are set at the left support of the arch. The angles are defined in the figure below, in which angles θ and φ are related to the infinitesimal length of arch *ds*, and angle β is related to the location of arbitrary point *P*. Because of the symmetry in loading and in arch geometry, the analysis is carried out for half of the arch span starting from the left support (point *A*) to the crown of the arch.

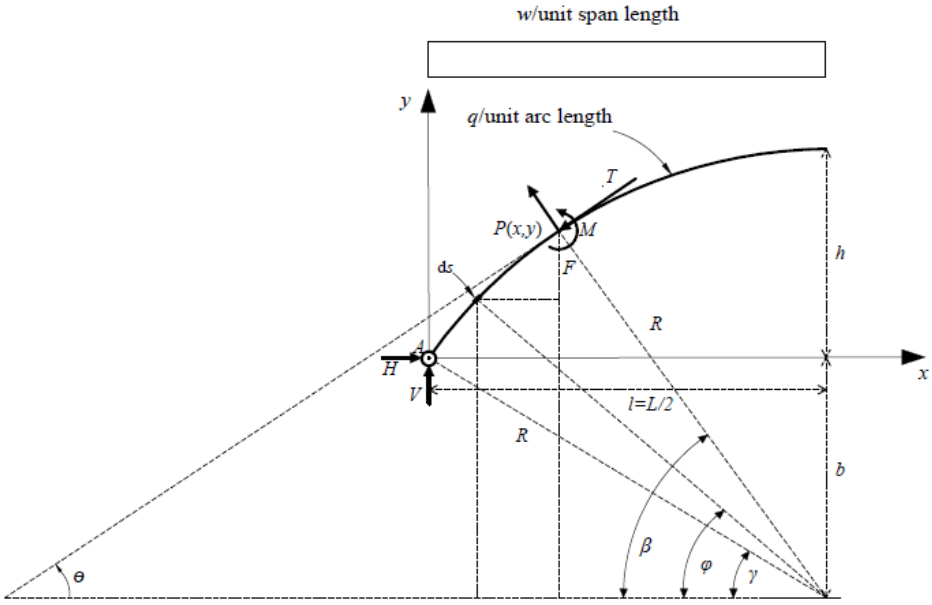

Figure A. 1. The two-pin circular arch specification

The important parameter is the span-to-height ratio, which is demonstrated as *L:h=r*. The radius of circular arch (*R*) can be found from the intersecting chord theorem as below.

$$h\left(2R-h\right)=l^2 \rightarrow \frac{2R}{l}-\frac{h}{l}=\frac{l}{h} \rightarrow R=\frac{l}{2}\left(\frac{l}{h}+\frac{h}{l}\right) \tag{A.1}$$

Substituting *l=L/2* and *L:h=r* gives the radius of the circular arch in terms of the arch span and *L:h* ratio.

$$R=\frac{L}{4}\left(\frac{r}{2}+\frac{2}{r}\right) \; and \; \gamma=\cos^{-1}\frac{l}{R} \tag{A.2}$$

To calculate the vertical reaction force (*V*), the vertical equilibrium of the circular arch subjected to its self-weight (*q*) and uniformly distributed load (*w*) is used.

$$\sum\left(F_y\right)_{\text{arch}}=0 \rightarrow 2V-2wl-2qR\left(\frac{\pi}{2}-\gamma\right)=0 \rightarrow V=wl+qR\left(\frac{\pi}{2}-\gamma\right) \tag{A.3}$$

To find the horizontal reaction force (*H*), a further equation in addition to the equilibrium equations is required due to the arch's statical indeterminacy of degree one. This equation can be obtained using Castigliano's theorem for a linear elastic structure. Hence, *H* is found by setting the partial derivative of the strain energy, *U*, with respect to *H*, to zero, i.e., $\frac{\partial U}{\partial H}=0$.

The assumption made to derive the strain energy is that the rib arch behaves elastically in a manner that roughly approximates the Euler–Bernoulli assumption. However, coupling of bending and thrust is also considered in the strain energy derivation in this study. Hence, the strain energy is a linear combination of terms arising from bending, shear, thrust, and the coupling of bending and thrust. The strain energy from the Castigliano method is then obtained by integrating full structural actions over the entire arch length *S*. To explore the effect of each term in

Castigliano's theorem, the strain energy can be assumed based on firstly bending action only, secondly bending, shear, and thrust, and finally full structural action. In this appendix the strain energy arises from the full structural action which can be used as a base for other investigations, as given in Equ. (A.4).

$$U = \frac{1}{2}\int_0^s \frac{M^2}{EI}\,\mathrm{d}s + \frac{1}{2}\int_0^s \frac{T^2}{EA}\,\mathrm{d}s + \frac{1}{2}\int_0^s \frac{F^2}{kGA}\,\mathrm{d}s + \int_0^s \frac{MT}{AER}\,\mathrm{d}s \tag{A.4}$$

The positive sign in the moment/axial force coupling term is appropriate when the axial force is compressive. Since the arch shapes are assumed concave down, the sign of coupling term is considered as positive. The horizontal reaction force is calculated assuming that the section is materially and geometrically uniform, and that the pins are of non-yielding supports.

$$\begin{aligned}\frac{\partial U}{\partial H} = 0 = \frac{1}{EI}\int_0^s M\,\frac{\partial M}{\partial H}\,\mathrm{d}s + \frac{1}{EA}\int_0^s T\,\frac{\partial T}{\partial H}\,\mathrm{d}s + \frac{1}{kGA}\int_0^s F\,\frac{\partial F}{\partial H}\,\mathrm{d}s \\ + \frac{1}{AER}\int_0^s T\,\frac{\partial M}{\partial H}\,\mathrm{d}s + \frac{1}{AER}\int_0^s M\,\frac{\partial T}{\partial H}\,\mathrm{d}s\end{aligned} \tag{A.5}$$

where *E* is the Young's modulus, *A*- the cross-section area, *k*- the shear reduction factor on area to account for the non-uniform distribution of shear over the arch cross-section, and *G*- the shear modulus. Assuming isotropic linear elasticity, $G = \frac{E}{2(1+\upsilon)}$, where υ is the Poisson's ratio.

The bending moment *M*, thrust *T*, and shear force *F* can be determined with the use of equations of equilibrium for any arbitrary point *P* shown in Figure A.1. The vertical, horizontal, and rotational equilibrium at point *P* yields Equs. (A.6), (A.7), and (A.8) respectively.

$$\sum\left(F_y\right)_P = 0 \rightarrow V - wx - qR(\beta - \gamma) - T\sin\theta + F\cos\theta = 0 \tag{A.6}$$

$$\sum (F_x)_P = 0 \rightarrow H - T\cos\theta - F\sin\theta = 0 \tag{A.7}$$

$$\sum (M)_P = 0 \rightarrow M + Hy - Vx + \frac{wx^2}{2} + \int_{\gamma}^{\beta} q\,\mathrm{ds}(R\cos\varphi - R\cos\beta) = 0 \tag{A.8}$$

To solve the integral in the rotational equation, $R\mathrm{d}\varphi$ is substituted for ds; hence, the above integral in Equ. (A.8) becomes $qR\left[R\sin\varphi - \varphi R\cos\beta\right]_{\gamma}^{\beta}$ which leads to Equ. (A.9).

$$M + Hy - Vx + \frac{wx^2}{2} + qR\left[R(\sin\beta - \sin\gamma) - R(\beta - \gamma)\cos\beta\right] = 0 \tag{A.9}$$

Therefore, Equs. (A.6) to (A.8) are rewritten using $\theta = \frac{\pi}{2} - \beta$.

$$V - wx - qR(\beta - \gamma) = T\cos\beta - F\sin\beta \tag{A.10}$$

$$H = T\sin\beta + F\cos\beta \tag{A.11}$$

$$M = -Hy + Vx - \frac{wx^2}{2} - qR^2\left[(\sin\beta - \sin\gamma) - (\beta - \gamma)\cos\beta\right] \tag{A.12}$$

From Equ. (A.3), $V = wl + qR\left(\frac{\pi}{2} - \gamma\right)$. Substituting for *V* in the above equations and re-arranging gives

$$T\cos\beta - F\sin\beta = w(l - x) + qR\left(\frac{\pi}{2} - \beta\right) \tag{A.13}$$

$$T\sin\beta + F\cos\beta = H \tag{A.14}$$

$$\begin{aligned} M &= -Hy + w\left(lx - \frac{x^2}{2}\right) + qR\left(\frac{\pi}{2} - \gamma\right)x \\ &\quad - qR^2\left[\left(\sin\beta - \sin\gamma\right) - \left(\beta - \gamma\right)\cos\beta\right] \\ &= -Hy + w\left(lx - \frac{x^2}{2}\right) \\ &\quad + qR\left[\left(\frac{\pi}{2} - \gamma\right)x - R\left(\sin\beta - \sin\gamma\right) + R\left(\beta - \gamma\right)\cos\beta\right] \end{aligned} \tag{A.15}$$

To find the thrust and shear force, Equs. (A.13) and (A.14) are solved with each other.

$$T = \left[w(l-x) + qR\left(\frac{\pi}{2} - \beta\right)\right]\cos\beta + H\sin\beta \tag{A.16}$$

$$F = -\left[w(l-x) + qR\left(\frac{\pi}{2} - \beta\right)\right]\sin\beta + H\cos\beta \tag{A.17}$$

Therefore, the derivative of bending, thrust, and shear with respect to the horizontal reaction are respectively: $\frac{\partial M}{\partial H} = -y$, $\frac{\partial T}{\partial H} = \sin\beta$, $\frac{\partial F}{\partial H} = \cos\beta$. Substituting these derivatives and *M*, *T*, and *F* from the above equations in Equ. (A.5) yields the required equation to find *H*.

$$\begin{aligned} 0 = {} & \frac{1}{EI}\int_0^s \left\{-Hy + w\left(lx - \frac{x^2}{2}\right) + qR\left[\left(\frac{\pi}{2} - \gamma\right)x - R(\sin\beta - \sin\gamma) + R(\beta - \gamma)\cos\beta\right]\right\}(-y)\mathrm{d}s \\ & + \frac{1}{EA}\int_0^s \left\{\left[w(l-x) + qR\left(\frac{\pi}{2} - \beta\right)\right]\cos\beta + H\sin\beta\right\}\sin\beta\mathrm{d}s \\ & + \frac{1}{kGA}\int_0^s \left\{-\left[w(l-x) + qR\left(\frac{\pi}{2} - \beta\right)\right]\sin\beta + H\cos\beta\right\}\cos\beta\mathrm{d}s \\ & + \frac{1}{AER}\int_0^s \left\{\left[w(l-x) + qR\left(\frac{\pi}{2} - \beta\right)\right]\cos\beta + H\sin\beta\right\}(-y)\mathrm{d}s \\ & + \frac{1}{AER}\int_0^s \left\{-Hy + w\left(lx - \frac{x^2}{2}\right) + qR\left[\left(\frac{\pi}{2} - \gamma\right)x - R(\sin\beta - \sin\gamma) + R(\beta - \gamma)\cos\beta\right]\right\}\sin\beta\mathrm{d}s \end{aligned} \tag{A.18}$$

To find *H*, Equ. (A.18) is grouped on the terms with *H*.

$$
\begin{aligned}
0 = {} & \frac{1}{EI}\int_0^s \left\{ -wy\left(lx-\frac{x^2}{2}\right) - qRy\left[\begin{array}{l}\left(\frac{\pi}{2}-\gamma\right)x - R(\sin\beta-\sin\gamma)\\ +R(\beta-\gamma)\cos\beta\end{array}\right]\right\}\mathrm{d}s \\
& + \frac{1}{EI}\int_0^s Hy^2\mathrm{d}s + \frac{1}{EA}\int_0^s H\sin^2\beta\mathrm{d}s + \frac{1}{EA}\int_0^s\left[w(l-x)+qR\left(\frac{\pi}{2}-\beta\right)\right]\cos\beta\sin\beta\mathrm{d}s \\
& + \frac{1}{kGA}\int_0^s H\cos^2\beta\mathrm{d}s - \frac{1}{kGA}\int_0^s\left[w(l-x)+qR\left(\frac{\pi}{2}-\beta\right)\right]\sin\beta\cos\beta\mathrm{d}s \\
& - \frac{2}{AER}\int_0^s Hy\sin\beta\mathrm{d}s - \frac{1}{AER}\int_0^s\left[w(l-x)y+qRy\left(\frac{\pi}{2}-\beta\right)\right]\cos\beta\mathrm{d}s \\
& + \frac{1}{AER}\int_0^s\left\{w\left(lx-\frac{x^2}{2}\right)\sin\beta + qR\sin\beta\left[\begin{array}{l}\left(\frac{\pi}{2}-\gamma\right)x - R(\sin\beta-\sin\gamma)\\ +R(\beta-\gamma)\cos\beta\end{array}\right]\right\}\mathrm{d}s
\end{aligned}
\tag{A.19}
$$

To find *H*, Equ. (A.19) is grouped on the terms with *H*, as *H=N/D*, where *N* and *D* are expressed below.

$$
\begin{aligned}
N = {} & \frac{1}{EI}\int_0^s \left\{ wy\left(lx-\frac{x^2}{2}\right) + qRy\left[\begin{array}{l}\left(\frac{\pi}{2}-\gamma\right)x\\ -R(\sin\beta-\sin\gamma)+R(\beta-\gamma)\cos\beta\end{array}\right]\right\}\mathrm{d}s \\
& + \left(-\frac{1}{EA}+\frac{1}{kGA}\right)\int_0^s\left[w(l-x)\cos\beta\sin\beta + qR\left(\frac{\pi}{2}-\beta\right)\cos\beta\sin\beta\right]\mathrm{d}s \\
& + \frac{1}{AER}\int_0^s\left[w(l-x)y+qRy\left(\frac{\pi}{2}-\beta\right)\right]\cos\beta\mathrm{d}s \\
& - \frac{1}{AER}\int_0^s\left\{w\left(lx-\frac{x^2}{2}\right)\sin\beta + qR\sin\beta\left[\begin{array}{l}\left(\frac{\pi}{2}-\gamma\right)x\\ -R(\sin\beta-\sin\gamma)+R(\beta-\gamma)\cos\beta\end{array}\right]\right\}\mathrm{d}s
\end{aligned}
\tag{A.20}
$$

$$
D = \frac{1}{EI}\int_0^s y^2\mathrm{d}s + \frac{1}{EA}\int_0^s \sin^2\beta\mathrm{d}s + \frac{1}{kGA}\int_0^s \cos^2\beta\mathrm{d}s - \frac{2}{AER}\int_0^s y\sin\beta\mathrm{d}s \tag{A.21}
$$

Substituting $x = l - R\cos\beta$, $y = R\sin\beta - b$, and $\mathrm{d}s = R\mathrm{d}\beta$ and then using the symmetry (i.e., β from the left support to the arch crown and from the arch crown to the right support is respectively in the range of $(\gamma, \pi/2)$ and $(\pi/2, \pi-\gamma)$), both *N*

and *D* have a common factor, 2*R*, which will drop out from the equation presenting *H*. Then *N* and *D* can be expressed in terms of an independent variable β.

$$
\begin{aligned}
N = {} & \frac{w}{2EI}\int_{\gamma}^{\frac{\pi}{2}}\left(R\sin\beta - b\right)\left(l^2 - R^2\cos^2\beta\right)\mathrm{d}\beta \\
& + \frac{qR}{EI}\int_{\gamma}^{\frac{\pi}{2}}\left\{\left(R\sin\beta - b\right)\left[\begin{array}{l}\left(\frac{\pi}{2} - \gamma\right)\left(l - R\cos\beta\right) \\ - R\left(\sin\beta - \sin\gamma\right) + R\left(\beta - \gamma\right)\cos\beta\end{array}\right]\right\}\mathrm{d}\beta \\
& + \left(-\frac{1}{EA} + \frac{1}{kGA}\right)\int_{\gamma}^{\frac{\pi}{2}}\left[wR\cos^2\beta\sin\beta + qR\left(\frac{\pi}{2} - \beta\right)\cos\beta\sin\beta\right]\mathrm{d}\beta \\
& + \frac{wR}{AER}\int_{\gamma}^{\frac{\pi}{2}}\left(R\sin\beta\cos^2\beta - b\cos^2\beta\right)\mathrm{d}\beta \quad + \frac{qR}{AER}\int_{\gamma}^{\frac{\pi}{2}}\left(R\sin\beta - b\right)\left(\frac{\pi}{2} - \beta\right)\cos\beta\mathrm{d}\beta \\
& - \frac{w}{2AER}\int_{\gamma}^{\frac{\pi}{2}}\left(l^2\sin\beta - R^2\cos^2\beta\sin\beta\right)\mathrm{d}\beta \\
& - \frac{qR}{AER}\int_{\gamma}^{\frac{\pi}{2}}\sin\beta\left[\begin{array}{l}\left(\frac{\pi}{2} - \gamma\right)\left(l - R\cos\beta\right) \\ - R\left(\sin\beta - \sin\gamma\right) + R\left(\beta - \gamma\right)\cos\beta\end{array}\right]\mathrm{d}\beta
\end{aligned}
\tag{A.22}
$$

$$
\begin{aligned}
D = {} & \frac{1}{EI}\int_{\gamma}^{\frac{\pi}{2}}\left(R\sin\beta - b\right)^2\mathrm{d}\beta + \frac{1}{EA}\int_{\gamma}^{\frac{\pi}{2}}\sin^2\beta\mathrm{d}\beta \\
& + \frac{1}{kGA}\int_{\gamma}^{\frac{\pi}{2}}\cos^2\beta\mathrm{d}\beta - \frac{2}{AER}\int_{\gamma}^{\frac{\pi}{2}}\left(R\sin\beta - b\right)\sin\beta\mathrm{d}\beta
\end{aligned}
\tag{A.23}
$$

Now to find *N* and *D*, the above integrals are solved forβ. The lower limit of β is γ and the upper limit is $\pi/2$. To do so, the integrals are split.

1. Numerator part

$$1.1\,\frac{w}{2EI}\quad term:\ \int_{\gamma}^{\frac{\pi}{2}} Rl^2\sin\beta\mathrm{d}\beta-\int_{\gamma}^{\frac{\pi}{2}} R^3\sin\beta\cos^2\beta\mathrm{d}\beta-\int_{\gamma}^{\frac{\pi}{2}} bl^2\mathrm{d}\beta+\int_{\gamma}^{\frac{\pi}{2}} R^2b\cos^2\beta\mathrm{d}\beta$$

$$1.1.1:\ \int_{\gamma}^{\frac{\pi}{2}} Rl^2\sin\beta\mathrm{d}\beta=-Rl^2\cos\beta\Big|_{\gamma}^{\frac{\pi}{2}}$$

$$1.1.2:\ \int_{\gamma}^{\frac{\pi}{2}} R^3\sin\beta\cos^2\beta\mathrm{d}\beta=-\frac{1}{3}R^3\cos^3\beta\Big|_{\gamma}^{\frac{\pi}{2}}=-\frac{1}{12}R^3\left(\cos(3\beta)+3\cos(\beta)\right)\Big|_{\gamma}^{\frac{\pi}{2}}$$

$$1.1.3:\ \int_{\gamma}^{\frac{\pi}{2}} bl^2\mathrm{d}\beta=bl^2\beta\Big|_{\gamma}^{\frac{\pi}{2}}$$

$$1.1.4:\ \int_{\gamma}^{\frac{\pi}{2}} R^2b\cos^2\beta\mathrm{d}\beta=\frac{1}{2}bR^2(\beta+\sin\beta\cos\beta)\Big|_{\gamma}^{\frac{\pi}{2}}$$

$$\Rightarrow N_1=\frac{w}{2EI}\left[-Rl^2\cos\beta+\frac{1}{3}R^3\cos^3\beta-bl^2\beta+\frac{1}{2}bR^2(\beta+\sin\beta\cos\beta)\right]\Big|_{\gamma}^{\frac{\pi}{2}}$$

$$N_1=\frac{w}{2EI}\begin{bmatrix}Rl^2\cos\gamma-\frac{1}{3}R^3\cos^3\gamma-bl^2\frac{\pi}{2}+bl^2\gamma\\+\frac{1}{2}bR^2(\frac{\pi}{2}-\gamma-\sin\gamma\cos\gamma)\end{bmatrix}\qquad(A.24)$$

$$1.2\quad\frac{qR}{EI}\quad term:\frac{qR}{EI}\int_{\gamma}^{\frac{\pi}{2}}\begin{Bmatrix}(R\sin\beta-b)(\frac{\pi}{2}-\gamma)(l-R\cos\beta)\\-R(R\sin\beta-b)(\sin\beta-\sin\gamma)+R(R\sin\beta-b)(\beta-\gamma)\cos\beta\end{Bmatrix}\mathrm{d}\beta$$

$$part\,1: \frac{qR}{EI}\int_{\gamma}^{\frac{\pi}{2}}(\frac{\pi}{2}-\gamma)[Rl\sin\beta - R^2\sin\beta\cos\beta - bl + Rb\cos\beta]\mathrm{d}\beta :$$

$$1.2.1: \int_{\gamma}^{\frac{\pi}{2}}(\frac{\pi}{2}-\gamma)(Rl\sin\beta)\mathrm{d}\beta = (\frac{\pi}{2}-\gamma)(-Rl\cos\beta)\Big|_{\gamma}^{\frac{\pi}{2}}$$

$$1.2.2: \int_{\gamma}^{\frac{\pi}{2}}(\frac{\pi}{2}-\gamma)(R^2\sin\beta\cos\beta)\mathrm{d}\beta = (\frac{\pi}{2}-\gamma)(-\frac{1}{4}R^2\cos(2\beta))\Big|_{\gamma}^{\frac{\pi}{2}}$$

$$1.2.3: \int_{\gamma}^{\frac{\pi}{2}}(\frac{\pi}{2}-\gamma)(-bl)\mathrm{d}\beta = (\frac{\pi}{2}-\gamma)(-bl\beta)\Big|_{\gamma}^{\frac{\pi}{2}}$$

$$1.2.4: \int_{\gamma}^{\frac{\pi}{2}}(\frac{\pi}{2}-\gamma)(Rb\cos\beta)\mathrm{d}\beta = (\frac{\pi}{2}-\gamma)(Rb\sin\beta)\Big|_{\gamma}^{\frac{\pi}{2}}$$

$$\xrightarrow{Total}(I): \frac{1}{2}(2\gamma-\pi)(Rl\cos\beta - \frac{1}{4}R^2\cos(2\beta) + bl\beta - Rb\sin\beta)\Big|_{\gamma}^{\frac{\pi}{2}}$$

$$part\,2: \frac{qR}{EI}\int_{\gamma}^{\frac{\pi}{2}}(-R^2\sin^2\beta + R^2\sin\beta\sin\gamma + Rb\sin\beta - Rb\sin\gamma)\mathrm{d}\beta :$$

$$1.2.5: \int_{\gamma}^{\frac{\pi}{2}}R^2\sin^2\beta\mathrm{d}\beta = (\frac{R^2\beta}{2} - \frac{1}{4}R^2\cos(2\beta))\Big|_{\gamma}^{\frac{\pi}{2}}$$

$$1.2.6: \int_{\gamma}^{\frac{\pi}{2}}R^2\sin\beta\sin\gamma\mathrm{d}\beta = (-R^2\sin\gamma\cos\beta)\Big|_{\gamma}^{\frac{\pi}{2}}$$

$$1.2.7: \int_{\gamma}^{\frac{\pi}{2}}Rb\sin\beta\mathrm{d}\beta = -Rb\cos\beta\Big|_{\gamma}^{\frac{\pi}{2}}$$

$$1.2.8: \int_{\gamma}^{\frac{\pi}{2}}Rb\sin\gamma\mathrm{d}\beta = Rb\beta\sin\gamma\Big|_{\gamma}^{\frac{\pi}{2}}$$

$$\xrightarrow{Total}(II): (-\frac{R^2\beta}{2} + \frac{1}{4}R^2\cos(2\beta) - R^2\sin\gamma\cos\beta - Rb\cos\beta - Rb\beta\sin\gamma)\Big|_{\gamma}^{\frac{\pi}{2}}$$

$$part\,3: \frac{qR}{EI}\int_{\gamma}^{\frac{\pi}{2}} (R^2\beta\cos\beta\sin\beta - Rb\beta\cos\beta - R^2\gamma\sin\beta\cos\beta + Rb\gamma\cos\beta)\mathrm{d}\beta\ :$$

$$1.2.9: \int_{\gamma}^{\frac{\pi}{2}} R^2\beta\cos\beta\sin\beta\mathrm{d}\beta = (-\frac{1}{8}R^2(2\beta\cos(2\beta) - \sin(2\beta)))\Big|_{\gamma}^{\frac{\pi}{2}}$$

$$1.2.10: \int_{\gamma}^{\frac{\pi}{2}} Rb\beta\cos\beta\mathrm{d}\beta = (Rb(\beta\sin\beta + \cos\beta))\Big|_{\gamma}^{\frac{\pi}{2}}$$

$$1.2.11: \int_{\gamma}^{\frac{\pi}{2}} R^2\gamma\sin\beta\cos\beta\mathrm{d}\beta = (-\frac{1}{2}\gamma R^2\cos^2\beta)\Big|_{\gamma}^{\frac{\pi}{2}}$$

$$1.2.12: \int_{\gamma}^{\frac{\pi}{2}} Rb\gamma\cos\beta\mathrm{d}\beta = Rb\gamma\sin\beta\Big|_{\gamma}^{\frac{\pi}{2}}$$

$$\xrightarrow{Total}(III): (\frac{1}{4}R[\cos(\beta)(R\sin(\beta) - 4b) - (\beta - \gamma)(4b\sin\beta + R\cos(2\beta)])\Big|_{\gamma}^{\frac{\pi}{2}}$$

$$N_2 = (I) + (II) + (III)$$

$$N_2 = \frac{qR}{EI}\left[\begin{array}{l} bl\beta\gamma - bR\gamma\sin\beta + l\gamma R\cos\beta - \frac{1}{4}\gamma R^2\cos(2\beta) - Rb\beta\sin\gamma - Rb\sin\beta \\ -R^2\sin\gamma\cos\beta - \frac{R^2\beta}{2} + \frac{1}{4}R^2\sin(2\beta) + \frac{1}{4}R^2\cos\beta\sin\beta - Rb\cos\beta \\ -4\beta b\sin\beta - R\beta\cos(2\beta) + 4\gamma b\sin\beta + \gamma R\cos(2\beta) \end{array}\right]\Bigg|_{\gamma}^{\frac{\pi}{2}}$$

$$N_2 = \frac{qR}{EI}\left[\begin{array}{l} \frac{1}{2}[(-\frac{\pi}{2})(-2b\gamma l + 2bR\sin\gamma + bl\pi + R^2) \\ -\frac{1}{2}[(-\gamma)(-2b\gamma l + 2bR\sin\gamma + bl\pi + R^2) \\ -R\cos(\gamma)(4b - 2\gamma l + 2R\sin\gamma + l\pi) - (\sin\gamma)(bR)(2\gamma - \pi) \\ -\cos(2\gamma)(\frac{1}{4}R^2(2\gamma - \pi)) + \sin(2\gamma)(\frac{3}{4}R^2)] \end{array}\right]$$

$$N_2 = \frac{qR}{EI}\left[\begin{array}{l}\left(-(\frac{\pi}{2}-\gamma)(\frac{R^2}{2}+bl(\frac{\pi}{2}-\gamma))\right)-\left((\frac{\pi}{2}-\gamma)\frac{R^2}{4}\cos 2\gamma\right)\\ +\left(\frac{R^2}{8}\sin 2\gamma\right)-\left(2Rb(\frac{\pi}{2}-\gamma)\sin\gamma\right)\\ +\left(R\cos\gamma((\frac{\pi}{2}-\gamma)l+2b)\right)\end{array}\right] \qquad \text{(A.25)}$$

$$1.3\,(-\frac{1}{EA}+\frac{1}{kGA}) \quad term:(-\frac{1}{EA}+\frac{1}{kGA})\int_{\gamma}^{\frac{\pi}{2}}\left[wR\sin\beta\cos^2+qR(\frac{\pi}{2}-\beta)\sin\beta\cos\beta\right]\mathrm{d}\beta$$

$$1.3.1:\ \int_{\gamma}^{\frac{\pi}{2}} wR\sin\beta\cos^2\mathrm{d}\beta = -\frac{1}{3}R\cos^3\beta\Big|_{\gamma}^{\frac{\pi}{2}}$$

$$1.3.2:\left\{\begin{array}{l} same\ as\ 1.2.2:\ qR\int_{\gamma}^{\frac{\pi}{2}}\frac{\pi}{2}\sin\beta\cos\beta\mathrm{d}\beta = -\frac{\pi}{4}qR\cos^2\beta\Big|_{\gamma}^{\frac{\pi}{2}} \\ same\ as\ 1.2.9:\ qR\int_{\gamma}^{\frac{\pi}{2}}\beta\sin\beta\cos\beta\mathrm{d}\beta = \frac{1}{8}qR(\sin(2\beta)-2\beta\cos(2\beta))\Big|_{\gamma}^{\frac{\pi}{2}}\end{array}\right\}$$

$$1.3.1, 1.3.2 \Rightarrow N_3 = (-\frac{1}{EA}+\frac{1}{kGA})\left[\begin{array}{l}-\frac{1}{3}R\cos^3\beta-\frac{\pi}{8}qR\cos(2\beta)\\ +\frac{1}{8}qR\sin(2\beta)-\frac{1}{4}qR\beta\cos(2\beta)\end{array}\right]\Bigg|_{\gamma}^{\frac{\pi}{2}}$$

$$N_3 = (-\frac{1}{EA}+\frac{1}{kGA})\left[\begin{array}{l}\frac{qR}{8}\left((\pi-2\gamma)\cos(2\gamma)+\sin(2\gamma)\right)\\ +\frac{1}{4}Rw\cos\gamma+\frac{1}{12}Rw\cos(3\gamma)\end{array}\right] \qquad \text{(A.26)}$$

$$1.4\left(\frac{1}{AER}\right)\ \ term: \frac{1}{AER}\int_{\gamma}^{\frac{\pi}{2}}\left\{\left[w(R\cos\beta)+qR\left(\frac{\pi}{2}-\beta\right)\right]\cos\beta\right\}(R\sin\beta-b)R\mathrm{d}\beta$$
$$+\frac{1}{AER}\int_{\gamma}^{\frac{\pi}{2}} w\left[(l^2-lR\cos\beta)-\frac{(l-R\cos\beta)^2}{2}\right](-\sin\beta)R\mathrm{d}\beta$$
$$+\frac{1}{AER}\int_{\gamma}^{\frac{\pi}{2}} qR\begin{bmatrix}\left(\frac{\pi}{2}-\gamma\right)(l-R\cos\beta)\\ -R(\sin\beta-\sin\gamma)+R(\beta-\gamma)\cos\beta\end{bmatrix}(-\sin\beta)R\mathrm{d}\beta$$

Expanding *N* 1.4 results in Equ. (A.26) as below.

$$\frac{1}{AER}\int_{\gamma}^{\frac{\pi}{2}} w(R\cos\beta)\cos\beta(R\sin\beta)\mathrm{d}\beta+\frac{1}{AER}\int_{\gamma}^{\frac{\pi}{2}} qR\left(\frac{\pi}{2}-\beta\right)\cos\beta(R\sin\beta)\mathrm{d}\beta$$
$$+\frac{1}{AER}\int_{\gamma}^{\frac{\pi}{2}} w(R\cos\beta)\cos\beta(-b)\mathrm{d}\beta+\frac{1}{AER}\int_{\gamma}^{\frac{\pi}{2}} qR\left(\frac{\pi}{2}-\beta\right)\cos\beta(-b)\mathrm{d}\beta$$
$$+\frac{1}{AER}\int_{\gamma}^{\frac{\pi}{2}} (l^2-lR\cos\beta)(-\sin\beta)w\mathrm{d}\beta+\frac{1}{AER}\int_{\gamma}^{\frac{\pi}{2}} -\frac{(l-R\cos\beta)^2}{2}(-\sin\beta)w\mathrm{d}\beta$$
$$+\frac{1}{AER}\int_{\gamma}^{\frac{\pi}{2}} \left(\frac{\pi}{2}-\gamma\right)(l-R\cos\beta)qR(-\sin\beta)\mathrm{d}\beta$$
$$+\frac{1}{AER}\int_{\gamma}^{\frac{\pi}{2}} -R(\sin\beta-\sin\gamma)qR(-\sin\beta)\mathrm{d}\beta$$
$$+\frac{1}{AER}\int_{\gamma}^{\frac{\pi}{2}} R(\beta-\gamma)\cos\beta qR(-\sin\beta)\mathrm{d}\beta$$

$$1.4.1: \int_{\gamma}^{\frac{\pi}{2}} R^2 w\cos^2\beta\sin\beta\,\mathrm{d}\beta = (-\frac{w}{3})R^2\cos^3\beta\Big|_{\gamma}^{\frac{\pi}{2}} = (\frac{w}{3})R^2\cos^3\gamma$$

$$1.4.2: \int_{\gamma}^{\frac{\pi}{2}} q(\frac{\pi}{2}-\beta)(R^2\sin\beta\cos\beta)\mathrm{d}\beta = q\left[-\frac{\pi}{8}R^2\cos(2\beta)-\frac{1}{8}R^2\sin(2\beta)+\frac{1}{4}R^2\beta\cos(2\beta)\right]\Big|_{\gamma}^{\frac{\pi}{2}}$$

$$= q\left[\frac{\pi}{8}R^2\cos(2\gamma)+\frac{1}{8}R^2\sin(2\gamma)-\frac{1}{4}R^2\gamma\cos(2\gamma)\right]$$

$$1.4.3: \int_{\gamma}^{\frac{\pi}{2}} -wbR\cos^2\beta\,\mathrm{d}\beta = -w(bR)\left[\frac{\beta}{2}+\frac{1}{4}\sin(2\beta)\right]\Big|_{\gamma}^{\frac{\pi}{2}} = w(bR)\left[\frac{\gamma}{2}+\frac{1}{4}\sin(2\gamma)-\frac{\pi}{4}\right]$$

$$1.4.4: \int_{\gamma}^{\frac{\pi}{2}} -qRb(\frac{\pi}{2}-\beta)\cos\beta\,\mathrm{d}\beta = (q)(bR)\left[-\frac{\pi}{2}\sin\beta+\beta\sin\beta+\cos\beta\right]\Big|_{\gamma}^{\frac{\pi}{2}}$$

$$= (q)(bR)\left[\frac{\pi}{2}\sin\gamma-\gamma\sin\gamma-\cos\gamma\right]$$

$$1.4.5: \int_{\gamma}^{\frac{\pi}{2}} (l^2-lR\cos\beta)(-\sin\beta)w\,\mathrm{d}\beta = (w)(-\frac{l}{2})\cos\beta(R\cos\beta-2l)\Big|_{\gamma}^{\frac{\pi}{2}}$$

$$= (w)(\frac{l}{2})\cos\gamma(R\cos\gamma-2l)$$

$$1.4.6: \int_{\gamma}^{\frac{\pi}{2}} \frac{(l^2-2lR\cos\beta+R^2\cos^2\beta)}{2}(\sin\beta)w\,\mathrm{d}\beta = (\frac{w}{2})\left[-l^2\cos\beta+lR\cos^2\beta-\frac{1}{3}R^2\cos^3\beta\right]\Big|_{\gamma}^{\frac{\pi}{2}}$$

$$= (\frac{w}{2})\left[l^2\cos\gamma-lR\cos^2\gamma+\frac{1}{3}R^2\cos^3\gamma\right]$$

$$1.4.7: \int_{\gamma}^{\frac{\pi}{2}} (\frac{\pi}{2}-\gamma)(l-R\cos\beta)qR(-\sin\beta)\mathrm{d}\beta = (q)(-\frac{R}{2})(\pi-2\gamma)\left[\frac{1}{2}R\cos^2\beta-l\cos\beta\right]\Big|_{\gamma}^{\frac{\pi}{2}}$$

$$= (q)(\frac{R}{2})(\pi-2\gamma)\left[\frac{1}{2}R\cos^2\gamma-l\cos\gamma\right]$$

$$1.4.8: \int_{\gamma}^{\frac{\pi}{2}} R^2q(\sin\beta-\sin\gamma)(\sin\beta)\mathrm{d}\beta = (q)(R^2)\left[\sin\gamma\cos\beta+\frac{1}{2}\beta-\frac{1}{4}\sin(2\beta)\right]\Big|_{\gamma}^{\frac{\pi}{2}}$$

$$= (q)(R^2)\left[\frac{\pi}{4}-\sin\gamma\cos\gamma-\frac{1}{2}\gamma+\frac{1}{4}\sin(2\gamma)\right]$$

$$1.4.9: \int_{\gamma}^{\frac{\pi}{2}} -R^2q(\beta-\gamma)\cos\beta\sin\beta\,\mathrm{d}\beta = (q)(-R^2)\left[\frac{\gamma}{2}\cos^2\beta+\frac{1}{8}\sin(2\beta)-\frac{1}{4}\beta\cos(2\beta)\right]\Big|_{\gamma}^{\frac{\pi}{2}}$$

$$= (q)(-R^2)\left[\frac{\pi}{8}-\frac{\gamma}{2}\cos^2\gamma-\frac{1}{8}\sin(2\gamma)+\frac{1}{4}\gamma\cos(2\gamma)\right]$$

$$N_4 = (\frac{1}{AER})\begin{bmatrix} (\frac{w}{3})R^2\cos^3\gamma + q\left[\frac{\pi}{8}R^2\cos(2\gamma) + \frac{1}{8}R^2\sin(2\gamma) - \frac{1}{4}R^2\gamma\cos(2\gamma)\right] \\ + w(bR)\left[\frac{\gamma}{2} + \frac{1}{4}\sin(2\gamma) - \frac{\pi}{4}\right] + q(bR)\left[\frac{\pi}{2}\sin\gamma - \gamma\sin\gamma - \cos\gamma\right] \\ + w(\frac{l}{2})\cos\gamma(R\cos\gamma - 2l) + \frac{w}{2}\left[l^2\cos\gamma - lR\cos^2\gamma + \frac{1}{3}R^2\cos^3\gamma\right] \\ + q(\frac{R}{2})(\pi - 2\gamma)\left[\frac{1}{2}R\cos^2\gamma - l\cos\gamma\right] \\ + q(R^2)\left[\frac{\pi}{4} - \sin\gamma\cos\gamma - \frac{1}{2}\gamma + \frac{1}{4}\sin(2\gamma)\right] \\ + q(-R^2)\left[\frac{\pi}{8} - \frac{\gamma}{2}\cos^2\gamma - \frac{1}{8}\sin(2\gamma) + \frac{1}{4}\gamma\cos(2\gamma)\right] \end{bmatrix} \quad \text{(A.27)}$$

2. Denominator part

$$D = \frac{1}{EI}\int_{\gamma}^{\frac{\pi}{2}}(R\sin\beta - b)^2\mathrm{d}\beta + \frac{1}{EA}\int_{\gamma}^{\frac{\pi}{2}}\sin^2\beta\mathrm{d}\beta$$

$$+ \frac{1}{kGA}\int_{\gamma}^{\frac{\pi}{2}}\cos^2\beta\mathrm{d}\beta + \frac{2}{AER}\int_{\gamma}^{\frac{\pi}{2}}\sin\beta(-R\sin\beta + b)R\mathrm{d}\beta$$

$$2.1\,\frac{1}{EI}\,terms: \ \frac{1}{EI}\int_{\gamma}^{\frac{\pi}{2}}(R\sin\beta - b)^2\mathrm{d}\beta = \frac{1}{EI}\int_{\gamma}^{\frac{\pi}{2}}(R^2\sin^2\beta - 2Rb\sin\beta + b^2)\mathrm{d}\beta$$

$$2.1.1: \int_{\gamma}^{\frac{\pi}{2}}R^2\sin^2\beta\mathrm{d}\beta = \frac{R^2}{2}(\beta - \sin\beta\cos\beta)\Big|_{\gamma}^{\frac{\pi}{2}}$$

$$2.1.2: \int_{\gamma}^{\frac{\pi}{2}}2Rb\sin\beta\mathrm{d}\beta = -2Rb\cos\beta\Big|_{\gamma}^{\frac{\pi}{2}}$$

$$2.1.3: \int_{\gamma}^{\frac{\pi}{2}}b^2\mathrm{d}\beta = b^2\beta\Big|_{\gamma}^{\frac{\pi}{2}}$$

$$D_1 = \frac{1}{EI}\left[\frac{1}{2}(2b^2 + R^2)(\frac{\pi}{2} - \gamma) - 2bR\cos\gamma + \frac{1}{4}R^2\sin(2\gamma)\right] \quad \text{(A.28)}$$

$$2.2\,\frac{1}{EA}\,term:\ \frac{1}{EA}\int_{\gamma}^{\frac{\pi}{2}}\sin^2\beta\mathrm{d}\beta\ \rightarrow\int_{\gamma}^{\frac{\pi}{2}}\sin^2\beta\mathrm{d}\beta\ =\frac{1}{2}\left[\beta-\sin\beta\cos\beta\right]\Big|_{\gamma}^{\frac{\pi}{2}}$$

$$D_2=\frac{1}{EA}\left[\frac{\beta}{2}-\frac{1}{4}\sin(2\beta)\right]\Big|_{\gamma}^{\frac{\pi}{2}}$$

$$D_2=\frac{1}{EA}(\frac{\beta}{2}-\frac{1}{4}\sin(2\beta))\Big|_{\gamma}^{\frac{\pi}{2}}=\frac{1}{EA}\left[\frac{\pi}{4}-\frac{\gamma}{2}+\frac{1}{4}\sin(2\gamma)\right] \tag{A.29}$$

$$2.3\,\frac{1}{kGA}\,term:\ \frac{1}{kGA}\int_{\gamma}^{\frac{\pi}{2}}\cos^2\beta\mathrm{d}\beta\ \rightarrow\int_{\gamma}^{\frac{\pi}{2}}\cos^2\beta\mathrm{d}\beta\ =\frac{1}{2}\left[\beta+\sin\beta\cos\beta\right]\Big|_{\gamma}^{\frac{\pi}{2}}$$

$$D_3=\frac{1}{kGA}\left[\frac{\beta}{2}+\frac{1}{4}\sin(2\beta)\right]\Big|_{\gamma}^{\frac{\pi}{2}}$$

$$D_3=\frac{1}{kGA}(\frac{\beta}{2}+\frac{1}{4}\sin(2\beta))\Big|_{\gamma}^{\frac{\pi}{2}}=\frac{1}{kGA}\left[\frac{\pi}{4}-\frac{\gamma}{2}-\frac{1}{4}\sin(2\gamma)\right] \tag{A.30}$$

$$2.4\,\frac{1}{AER}\,term:\ \frac{1}{AER}\int_{\gamma}^{\frac{\pi}{2}}2\sin\beta(-R\sin\beta+b)\mathrm{d}\beta:\Rightarrow 2.5:\ \int_{\gamma}^{\frac{\pi}{2}}2\sin\beta(-R\sin\beta+b)\mathrm{d}\beta$$

$$D_4=-2b\cos\beta-R\beta+\frac{1}{2}R\sin(2\beta)\Big|_{\gamma}^{\frac{\pi}{2}}$$

$$D_4=(\frac{1}{AER})\left[-\frac{\pi}{2}R+2b\cos\gamma+R\gamma-\frac{1}{2}R\sin(2\gamma)\right] \tag{A.31}$$

Consequently, *N* is the summation of Equs. (A.24), (A.25), (A.26), and (A.27) and *D* is the summation of Equs. (A.28), (A.29), (A.30), and (A.31). Therefore, *H* for the general case when full structural actions are assumed in Castigliano's theorem can

be found by dividing *N* by *D*, presented as $H = N/D = (N_1 + N_2 + N_3 + N_4)/(D_1 + D_2 + D_3 + D_4)$. It can be seen from the split equation above that dividing Equs. (A.24) by (A.28), in which are presented the N_1 and D_1 respectively, leads to the horizontal reaction force when the strain energy is based on bending action only, i.e., $H = (N_1)/(D_1)$. This horizontal reaction is the same as the one obtained from virtual work method presented by Megson. To find the horizontal reaction force when the strain energy in Castigliano's theorem is the linear combination of bending, shear, and thrust terms, the summation of Equs. (A.24), (A.25), and (A.26) is divided by the summation of Equs. (A.28), (A.29), and (A.30), i.e., $H = (N_1 + N_2 + N_3)/(D_1 + D_2 + D_3)$.

The studied circular arch in Chapter 4 is analysed using Castigliano's theorem when the strain energy results from the full structural action. From Chapter 4, *w*=20000 N/m, *q*=7200 N/m, *L*=10 m, *k*=0.845, *υ*=0.2, *I*=0.00225 m^4, and *E*=2.7e10 Pa. Applying the above equations to the circular arch leads to finding the horizontal reaction force for *L:h* ratios from 2 to 10 as presented in Table A.1.

Table A. 1. Horizontal reaction force of circular arch (N) subjected to load case *A1*

L:h	*h*(m)	*R*	$\gamma=\cos^{-1}(l/R)$	*N*	*D*	*H*
2	5	5	0	1.95E-05	3.23E-10	60452.11
3	3.33	5.42	0.39	1.09E-05	1.11E-10	98408.81
4	2.5	6.25	0.64	6.67E-06	4.99E-11	133669.8
5	2	7.25	0.81	4.45E-06	2.64E-11	168107.2
6	1.67	8.33	0.93	3.16E-06	1.56E-11	202146.1
7	1.43	9.46	1.01	2.35E-06	9.97E-12	235892.4
8	1.25	10.62	1.08	1.82E-06	6.74E-12	269352.9
9	1.11	11.8	1.13	1.44E-06	4.77E-12	302496.4
10	1	13	1.18	1.17E-06	3.5E-12	335274.2

It can be seen from the table above that the results of the horizontal reaction force of the circular arch are the same as those presented in the last column of Table 4.1.

Appendix B: Theoretical analysis of a two-pin parabolic arch using Castigliano's approach

The two-pin parabolic arch to be analysed is geometrically and materially symmetric and subjected to the symmetric loading of the general combination of *UDL* plus *SW*, see Figure 5.1. The arch is of linearly elastic material with non-yielding supports. To find the horizontal reaction force of this parabolic arch using Castigliano theorem, the half of arch is analysed, hence, the starting point of the analysis is set at the left support. The arch with the external and internal forces is demonstrated in Figure 5.4. In that figure, η is substituted by ζ here which is the variable defined alongside the *x*-axis.

The general equation of the parabolic arch is $y = ax^2 + bx + c$ in which *a*, *b* and *c* can be obtained using boundary conditions. Therefore, the equation of parabolic arch considering *y*(0)=*0*, and *y*(*L/2*)=*h* is $y = 4h/L\,(x - x^2/L)$. Accordingly, to adapt the procedure of finding the horizontal reaction force for the parabolic arch, the length of the infinitesimal piece of the arch curve, ds, is defined depending on the angle of inclination of the *x* direction. Hence, the arch length (*S*) can be calculated as below.

$$ds = \sqrt{1 + y'^2}\,\mathrm{d}x = \sqrt{1 + (\frac{16h^2}{L^2})(1 - \frac{2x}{L})^2}\,\mathrm{d}x \;\rightarrow\; S = \int_0^L \mathrm{d}s$$

$$\rightarrow S = -\frac{1}{4}(L - 2x)\sqrt{\frac{16h^2(L-2x)^2 + L^4}{L^4}} - \frac{L^2}{16h}\arcsin h(\frac{4h(L-2x)}{L^2})\Big|_0^L \qquad \text{(B.1)}$$

The derivative of parabolic arch equation with respect to the *x* then gives $y' = 4h/L\,(1-2\,x/L)$. Followed by, sin(*α*) and cos(*α*) for *0≤α ≤π/2* are calculated using trigonometry.

$$\cos\alpha = \frac{\mathrm{d}x}{\mathrm{d}s} = \frac{1}{\sqrt{1+y'^2}}\ , \quad \sin\alpha = \frac{\mathrm{d}y}{\mathrm{d}s} = \frac{y'}{\sqrt{1+y'^2}} \tag{B.2}$$

A radius of parabola is different for every point of the curve other than its mirror point on the axis of symmetry. The radius of parabolic arch is:

$$\frac{1}{R} = \left|\frac{y''}{(1+y'^2)^{3/2}}\right| = \frac{8h}{L^2(1+(\frac{8hx}{L^2})^2)^{3/2}} \tag{B.3}$$

Similar to Appendix A, the vertical reaction force (*V*) of two-pin arch can be found from the equilibrium equations of the arch as shown in Equ. (B.4).

$$\sum(F_y)_{arch} = 0 \rightarrow V = \frac{wL}{2} + \frac{1}{2}\int_0^S q\mathrm{d}s = \frac{wL}{2} + \frac{q}{2}\int_0^L \sqrt{1+y'^2}\,\mathrm{d}x \tag{B.4}$$

The thrust, shear, and bending moment at any arbitrary point on the arch are then derived from the three equilibrium equations i.e. vertical, horizontal, and rotational equilibrium.

$$\sum(F_y)_P = 0 \rightarrow V - T\sin\alpha + F\cos\alpha - wx - \int_0^x q\sqrt{1+y_\zeta'^2}\,\mathrm{d}\zeta = 0 \tag{B.5}$$

$$\sum(F_x)_P = 0 \rightarrow H - T\cos\alpha - F\sin\alpha = 0 \tag{B.6}$$

$$\sum(M)_P = 0 \rightarrow M - Vx + Hy + \frac{wx^2}{2} + \int_0^x q(x-\zeta)\mathrm{d}s = 0 \tag{B.7}$$

To calculate *T* and *F*, Equs. (B.5) and (B.6) should be solved together, thus thrust and shear force are obtained and presented in Equ. (B.8) and (B.9) individually.

$$B.5\times\cos\alpha\rightarrow V\cos\alpha-T\sin\alpha\cos\alpha+F\cos^2\alpha-$$
$$wx\cos\alpha-\int_0^x q\cos\alpha\sqrt{1+y_\zeta{}'^2}\,\mathrm{d}\zeta=0$$
$$B.6\times(-\sin\alpha)\rightarrow -H\sin\alpha+T\sin\alpha\cos\alpha+F\sin^2\alpha=0$$

$$B.5\times\cos\alpha+B.6\times(-\sin\alpha)\Rightarrow\quad F=\frac{1}{\sqrt{1+y'^2}}\left[Hy'-V+wx+\int_0^x q\sqrt{1+y_\zeta{}'^2}\,\mathrm{d}\zeta\right] \quad \text{(B.8)}$$

$$B.5\times\sin\alpha\rightarrow V\sin\alpha-T\sin^2\alpha+F\sin\alpha\cos\alpha-$$
$$wx\sin\alpha-\int_0^x q\sin\alpha\sqrt{1+y_\zeta{}'^2}\,\mathrm{d}\zeta=0$$
$$B.6\times\cos\alpha\rightarrow H\cos\alpha-T\cos^2\alpha-F\cos\alpha\sin\alpha=0$$

$$B.5\times\sin\alpha+B.6\times\cos\alpha\Rightarrow\quad T=\frac{1}{\sqrt{1+y'^2}}\left[H+y'[V-wx-\int_0^x q\sqrt{1+y_\zeta{}'^2}\,\mathrm{d}\zeta]\right] \quad \text{(B.9)}$$

Also, substituting vertical reaction force from Equ. (B.4) in the equation of bending moment leads Equ. (B.7) to be simplified and presented as Equ. (B.10).

$$M=\frac{wx}{2}(L-x)+(\frac{qx}{2})\int_0^L\sqrt{1+y'^2}\,\mathrm{d}x-Hy-\int_0^x q(x-\zeta)\mathrm{d}s \quad \text{(B.10)}$$

As it was explained in Appendix A, the two-pin arches are statically indeterminate and a further equation is required to obtain the horizontal reaction force (*H*). This supplementary equation can be acquired using Castigliano's theorem for a linear elastic arch, see Equ. (A.5). In this regard the derivative of *T*, *F*, and *M* with respect to *H* is obtained.

$$\frac{\partial M}{\partial H}=-y\ ,\ \frac{\partial T}{\partial H}=\cos(\alpha)\ ,\ \frac{\partial F}{\partial H}=\sin(\alpha) \quad \text{(B.11)}$$

Substituting *F*, *T*, and *M* from Equs. (B.8), (B.9), and (B.10) and their derivations from Equ. (B.11) into Equ. (A.5) yields to calculating horizontal reaction force such as; $H = \frac{wW + qQ}{D}$. In this equation, *w* and *q* are *UDL* and *SW* respectively as shown in Figure 5.1. Derivative of strain energy with respect to *H* is shown below.

$$\frac{\partial U}{\partial H} = 0 = \frac{1}{EI}\int_0^s [\frac{wx}{2}(L-x) + (\frac{qx}{2})\int_0^L \sqrt{1+y_x{}'^2}\,\mathrm{d}x - Hy - \int_0^x q(x-\zeta)\mathrm{d}s\,](-y)\mathrm{d}s +$$
$$\frac{1}{EA}\int_0^s \frac{1}{\sqrt{1+y_x{}'^2}}[H + y'[V - wx - \int_0^x q\sqrt{1+y_\zeta{}'^2}\,\mathrm{d}\zeta]](\frac{1}{\sqrt{1+y_x{}'^2}})\mathrm{d}s +$$
$$\frac{1}{kGA}\int_0^s \frac{1}{\sqrt{1+y_x{}'^2}}[Hy' - V + wx + \int_0^x q\sqrt{1+y_\zeta{}'^2}\,\mathrm{d}\zeta]\frac{y'}{\sqrt{1+y_x'^2}}\mathrm{d}s +$$
$$\frac{1}{AE}\int_0^s (-y)\frac{1}{\sqrt{1+y_x{}'^2}}\frac{8h}{L^2(1+y'^2)^{\frac{3}{2}}}[H + y'[V - wx - \int_0^x q\sqrt{1+y_\zeta{}'^2}\,\mathrm{d}\zeta]]\mathrm{d}s +$$
$$\frac{1}{AE}\int_0^s \frac{1}{\sqrt{1+y_x'^2}}\frac{8h}{L^2(1+y'^2)^{\frac{3}{2}}}\left[\begin{array}{l}\frac{wx}{2}(L-x) + \\ (\frac{qx}{2})\int_0^L \sqrt{1+y_x{}'^2}\,\mathrm{d}x - Hy - \int_0^x q(x-\zeta)\mathrm{d}s\end{array}\right]\mathrm{d}s$$

On grouping the terms with *H* leads to:

$$(-H)[\frac{1}{EI}\int_0^S y^2\mathrm{d}s + \frac{1}{EA}\int_0^S \frac{\mathrm{d}s}{1+y_x{}'^2} + \frac{1}{kGA}\int_0^S \frac{y_x{}'^2}{1+y_x{}'^2}\mathrm{d}s - \frac{2}{AER}\int_0^S \frac{(y)}{\sqrt{1+y_x{}'^2}}\mathrm{d}s] =$$
$$\frac{1}{EI}\int_0^S (-\frac{wxy}{2}(L-x))\mathrm{d}s - \frac{1}{EI}\int_0^S (\frac{qxy}{2})(\int_0^L \sqrt{1+y_x{}'^2}\,\mathrm{d}x)\,\mathrm{d}s + \frac{1}{EI}\int_0^S qy(\int_0^x (x-\zeta)\mathrm{d}s)\mathrm{d}s +$$
$$\frac{1}{EA}\int_0^S \frac{y'}{1+y_x{}'^2} w(\frac{L}{2} - x)\mathrm{d}s + \frac{1}{EA}\int_0^S \frac{y'}{1+y_x{}'^2}(\frac{q}{2}\int_0^L (\sqrt{1+y_x{}'^2})\mathrm{d}x)\mathrm{d}s -$$
$$\frac{1}{EA}\int_0^S \frac{y'}{1+y_x{}'^2}(\int_0^x q\sqrt{1+y_\zeta{}'^2}\,\mathrm{d}\zeta)\,\mathrm{d}s + \frac{1}{kGA}\int_0^S \frac{y_x{}'}{1+y_x{}'^2} w(x - \frac{L}{2})\mathrm{d}s -$$
$$\frac{1}{kGA}\int_0^S \frac{y_x{}'}{1+y_x{}'^2}(\frac{q}{2}\int_0^L (\sqrt{1+y_x{}'^2})\mathrm{d}x)\mathrm{d}s + \frac{1}{kGA}\int_0^S \frac{y_x{}'}{1+y_x{}'^2}(\int_0^x q\sqrt{1+y_\zeta{}'^2}\,\mathrm{d}\zeta)\mathrm{d}s +$$

$$\frac{1}{AE}\int_0^S \frac{(-yy')}{\sqrt{1+y_x'^2}} \frac{8h}{L^2(1+y'^2)^{\frac{3}{2}}} w(\frac{L}{2}-x)\mathrm{d}s +$$

$$\frac{1}{AE}\int_0^S \frac{(-yy')}{\sqrt{1+y_x'^2}} \frac{8h}{L^2(1+y'^2)^{\frac{3}{2}}} (\frac{q}{2}\int_0^L (\sqrt{1+y_x'^2})\mathrm{d}x)\mathrm{d}s -$$

$$\frac{1}{AE}\int_0^S \frac{(-yy')}{\sqrt{1+y_x'^2}} \frac{8h}{L^2(1+y'^2)^{\frac{3}{2}}} (\int_0^x q\sqrt{1+y_\zeta'^2}\,\mathrm{d}\zeta)\mathrm{d}s +$$

$$\frac{1}{AE}\int_0^S \frac{1}{\sqrt{1+y_x'^2}} \frac{8h}{L^2(1+y'^2)^{\frac{3}{2}}} \frac{wx}{2}(L-x)\mathrm{d}s +$$

$$\frac{1}{AE}\int_0^S \frac{1}{\sqrt{1+y_x'^2}} \frac{8h}{L^2(1+y'^2)^{\frac{3}{2}}} (\frac{qx}{2}\int_0^L \sqrt{1+y_x'^2}\,\mathrm{d}x)\mathrm{d}s -$$

$$\frac{1}{AE}\int_0^S \frac{1}{\sqrt{1+y_x'^2}} \frac{8h}{L^2(1+y'^2)^{\frac{3}{2}}} (\int_0^x q(x-\zeta)\mathrm{d}s)\mathrm{d}s$$

Substituting $\mathrm{d}s = \sqrt{1+(\frac{16h^2}{L^2})(1-\frac{2x}{L})^2}\mathrm{d}x$, $y = \frac{4h}{L}(x-\frac{x^2}{L})$ and using *x* in the range of (0, *L*/2), gives the total equation becomes as below in which all terms have a common factor $\sqrt{1+(\frac{16h^2}{L^2})(1-\frac{2x}{L})^2}$ which drops out of the equation. On grouping the terms with *H* and using *x* as an independent variable, denominator and numerator (*H=N/D*) are found where numerator is the combination of *W* (terms related to *SW*) and *Q* (terms related to *UDL*). In equations below, $1/g^2$ is assumed as *A/I*, in which *g* is the radius of gyration of the cross-section.

$$W = w\left\{\begin{array}{l}\frac{1}{g^2}\int_0^{L/2}(-\frac{2xh}{L})(x-\frac{x^2}{L})(L-x)\mathrm{d}x+(1-\frac{2(1+\upsilon)}{k})\int_0^{L/2}\frac{2h(L-2x)^2}{L^2(1+\frac{16h^2}{L^4}(L-2x)^2)}\mathrm{d}x \\ +\int_0^{L/2}\frac{-64h^3(x-\frac{x^2}{L})(L-2x)^2}{L^5(1+\frac{16h^2}{L^4}(L-2x)^2)^2}\mathrm{d}x+\int_0^{L/2}\frac{4hx(L-x)}{L^2(1+\frac{16h^2}{L^4}(L-2x)^2)^2}\mathrm{d}x\end{array}\right\}$$

$$Q = q\left\{\begin{array}{l}-\frac{1}{g^2}\int_0^{L/2}[(\frac{2xh}{L})(x-\frac{x^2}{L})(C1)\mathrm{d}x+\frac{1}{g^2}\int_0^{L/2}\frac{4h}{L}(x-\frac{x^2}{L})(C3)\mathrm{d}x+ \\ \int_0^{L/2}\frac{2h(L-2x)}{L^2(1+\frac{16h^2}{L^4}(L-2x)^2)}(C1)\mathrm{d}x+ \\ (1+\frac{2(1+\upsilon)}{k})\int_0^{L/2}\frac{4h(L-2x)}{L^2(1+\frac{16h^2}{L^4}(L-2x)^2)}(C2)\mathrm{d}x- \\ \frac{(1+\upsilon)}{k}\int_0^{L/2}\frac{4h(L-2x)}{L^2(1+\frac{16h^2}{L^4}(L-2x)^2)}(C1)\mathrm{d}x+\int_0^{L/2}\frac{-64h^3(x-\frac{x^2}{L})(L-2x)}{L^5(1+\frac{16h^2}{L^4}(L-2x)^2)^2}(C1)\mathrm{d}x+ \\ \int_0^{L/2}\frac{128h^3(x-\frac{x^2}{L})(L-2x)}{L^5(1+\frac{16h^2}{L^4}(L-2x)^2)^2}(C2)\mathrm{d}x+\int_0^{L/2}\frac{4hx}{L^2(1+\frac{16h^2}{L^4}(L-2x)^2)^2}(C1)\mathrm{d}x- \\ \int_0^{L/2}\frac{8h}{L^2(1+\frac{16h^2}{L^4}(L-2x)^2)^2}(C3)\mathrm{d}x\end{array}\right\}$$

$$D = \left\{\begin{array}{l}-\frac{1}{g^2}\int_0^{L/2}\frac{16h^2}{L^2}(x-\frac{x^2}{L})^2\mathrm{d}x-\int_0^{L/2}\frac{1}{1+\frac{16h^2}{L^4}(L-2x)^2}\mathrm{d}x- \\ \frac{(1+\upsilon)}{k}\int_0^{L/2}\frac{32h^2(L-2x)^2}{L^4(1+\frac{16h^2}{L^4}(L-2x)^2)}\mathrm{d}x+\int_0^{L/2}\frac{64h^2(x-\frac{x^2}{L})}{L^3(1+\frac{16h^2}{L^4}(L-2x)^2)^2}\mathrm{d}x\end{array}\right\}$$

Where *C1*, *C2*, and *C3* are defined next.

$$C1=\int_0^L \sqrt{1+y'^2}\,\mathrm{d}x$$

$$C2=\int_0^x \sqrt{1+\frac{16h^2}{L^4}(L-2\zeta)^2}\,\mathrm{d}\zeta$$

$$=-\frac{1}{4}(L-2\zeta)\sqrt{\frac{16h^2(L-2\zeta)^2+L^4}{L^4}}-\frac{L^2\arcsin h(\frac{4h(L-2\zeta)}{L^2})}{16h}\Bigg|_0^x$$

$$C2=-\frac{1}{4}(L-2x)\sqrt{\frac{16h^2(L-2x)^2+L^4}{L^4}}-\frac{L^2\arcsin h(\frac{4h(L-2x)}{L^2})}{16h}+$$

$$\frac{L}{4}\sqrt{\frac{16h^2+L^2}{L^2}}+\frac{L^2\arcsin h(\frac{4h}{L})}{16h}$$

$$C3=\int_0^x (x-\zeta)\sqrt{1+(\frac{16h^2}{L^2})(1-\frac{2\zeta}{L})^2}\,\mathrm{d}\zeta$$

$$C3=\frac{1}{192h^2}\{6hL^2(L-2x)\arcsin h(\frac{4h(L-2x)}{L^2})-\sqrt{\frac{16h^2(L-2x)^2+L^4}{L^4}}(L^4-8h^2(L-2x)^2)\}-$$

$$\frac{1}{192h^2}\{6hL^2(L-2x)\arcsin h(\frac{4h}{L})-\sqrt{\frac{16h^2+L^2}{L^2}}(L^4-8h^2L(L-6x))\}$$

The *W* terms are calculated as below where *W1* is bending term, *W2* is thrust and shear term, and *W3* and *W4* are coupling terms.

$$W1=\frac{1}{g^2}\int_0^{L/2}(-\frac{2xh}{L})(x-\frac{x^2}{L})(L-x)\mathrm{d}x=\frac{1}{g^2}(-\frac{hL^3}{30})$$

$$W2=(1-\frac{2(1+\upsilon)}{k})\int_0^{L/2}\frac{2h(L-2x)^2}{L^2(1+\frac{16h^2}{L^4}(L-2x)^2)}\mathrm{d}x=-(1-\frac{2(1+\upsilon)}{k})(\frac{L^4}{64h^2}\arctan(\frac{4h}{L})-\frac{L^3}{16h})$$

$$W3=\int_0^{L/2}\frac{-64h^3(x-\frac{x^2}{L})(L-2x)^2}{L^5(1+\frac{16h^2}{L^4}(L-2x)^2)^2}\mathrm{d}x=(\frac{\mathrm{L}^2}{256h^2})(12hL-(16h^2+3L^2)\arctan(\frac{4h}{\mathrm{L}}))$$

$$W4=\int_0^{L/2}\frac{4hx(L-x)}{L^2(1+\frac{16h^2}{L^4}(L-2x)^2)^2}\mathrm{d}x==(\frac{L^2}{256h^2})(16h^2-L^2)\arctan(\frac{4h}{L})+4hL)$$

The *Q* terms regarding *SW* includes *Q1* and *Q2* as bending terms, *Q3*, *Q4*, and *Q5* as thrust plus shear terms and *Q6*, *Q7*, *Q8*, and *Q9* as coupling terms.

$$Q1= -\frac{1}{g^2}\int_0^{L/2}[(\frac{2xh}{L})(x-\frac{x^2}{L})(C1)\mathrm{d}x = -\frac{1}{g^2}(\sqrt{\frac{16h^2+L^2}{L^2}}(\frac{5hL^3}{192})+(\frac{5L^4}{768})\arcsin h(\frac{4h}{L}))$$

$$Q2= \frac{1}{g^2}\int_0^{L/2}\frac{4h}{L}(x-\frac{x^2}{L})(\int_0^{x}(x-\zeta)\sqrt{1+(\frac{16h^2}{L^2})(1-\frac{2\zeta}{L})^2}\,\mathrm{d}\zeta)\mathrm{d}x$$

$$= \frac{1}{g^2}\int_0^{L/2}\frac{4h}{L}(x-\frac{x^2}{L})(C3)\mathrm{d}x$$

$$Q2 = Q2_1 + Q2_2 + Q2_3 + Q2_4$$

$$Q2_1 = \frac{1}{g^2}\int_0^{L/2}[\frac{L}{8}(x-\frac{x^2}{L})(L-2x)\arcsin h(\frac{4h(L-2x)}{L^2})]\mathrm{d}x =$$

$$\therefore Q2_1 = -\frac{1}{g^2}(\frac{1}{524288})\begin{bmatrix}(384\frac{L^4}{h}+\frac{12L^6}{h^3})\sqrt{16h^2+L^2}- \\ (2048L^4+128\frac{L^6}{h^2}+3\frac{L^8}{h^4})\arcsin h(\frac{4h}{L})\end{bmatrix}$$

$$Q2_2 = -\frac{1}{g^2}\int_0^{L/2}[\frac{1}{48hL}(x-\frac{x^2}{L})\sqrt{\frac{16h^2(L-2x)^2+L^4}{L^4}}(L^4-8h^2(L-2x)^2)]\mathrm{d}x$$

$$\therefore Q2_2 = -\frac{1}{g^2}(\frac{1}{2359296})\begin{bmatrix}-(864\frac{L^6}{h^2}+15\frac{L^8}{h^4})\log_e(hL^2)+ \\ (-4096hL^3+1280\frac{L^5}{h}-60\frac{L^7}{h^3})\sqrt{\frac{16h^2+L^2}{L^2}} \\ +(864\frac{L^6}{h^2}+15\frac{L^8}{h^4})\log_e(h\sqrt{16h^2L^2+L^4}+4h^2L)\end{bmatrix}$$

$$\therefore Q2_3 = -\frac{1}{g^2}\int_0^{L/2}[\frac{L}{8}(x-\frac{x^2}{L})(L-2x)\arcsin h(\frac{4h}{L})]\mathrm{d}x = -\frac{1}{g^2}(\frac{L^4}{256})\arcsin h(\frac{4h}{L})$$

$$\therefore Q2_4 = \frac{1}{g^2}\int_0^{L/2}[\frac{1}{48h}(x-\frac{x^2}{L})(\sqrt{\frac{16h^2+L^2}{L^2}}(L^3-8h^2(L-6x))]\mathrm{d}x$$

$$= -\frac{1}{g^2}\sqrt{\frac{16h^2+L^2}{L^2}}(\frac{L}{1152h})(-14h^2L^2-2L^4)$$

$$Q3= \int_0^{L/2}\frac{2h(L-2x)}{L^2(1+\frac{16h^2}{L^4}(L-2x)^2)}(C1)\mathrm{d}x$$

$$= [-\frac{L^3\log_e(L^4)}{64h}+\frac{L^3\log_e(16h^2L^2+L^4)}{64h}][\sqrt{\frac{16h^2+L^2}{L^2}}+\frac{L}{4h}\arcsin h(\frac{4h}{L})]$$

$$Q4= (1+\frac{2(1+\upsilon)}{k})\int_0^{L/2}\frac{4h(L-2x)}{L^2(1+\frac{16h^2}{L^4}(L-2x)^2)}(C2)\,\mathrm{d}x,\quad Q4 = Q4_1 + Q4_2 + Q4_3$$

$$Q4_1 = (1+\frac{2(1+\upsilon)}{k})\int_0^{L/2}(\frac{\frac{4h}{L^2}(L-2x)}{1+\frac{16h^2}{L^4}(L-2x)^2})(-\frac{1}{4}(L-2x)\sqrt{\frac{16h^2(L-2x)^2+L^4}{L^4}})\,\mathrm{d}x$$

$$Q4_1 = (1+\frac{2(1+\upsilon)}{k})\left(\begin{array}{l}\frac{L^4\log_e(hL^2)}{256h^2} - \\ \frac{L^4\log_e(h\sqrt{16h^2L^2+L^4}+4h^2L)}{256h^2} + \frac{(16h^2L^3+L^5)}{64h\sqrt{16h^2L^2+L^4}}\end{array}\right)$$

$$Q4_2 = (1+\frac{2(1+\upsilon)}{k})\int_0^{L/2}(\frac{(2x-L)}{4(1+\frac{16h^2}{L^4}(L-2x)^2)})\arcsin h(\frac{4h(L-2x)}{L^2})\mathrm{d}x$$

$$Q4_3 = (1+\frac{2(1+\upsilon)}{k})\int_0^{L/2}\frac{4h(L-2x)}{L^2(1+\frac{16h^2}{L^4}(L-2x)^2)}(\frac{L}{4}\sqrt{\frac{16h^2+L^2}{L^2}}+\frac{L^2\arcsin h(\frac{4h}{L})}{16h})\mathrm{d}x =$$

$$Q4_3 = (1+\frac{2(1+\upsilon)}{k})(\sqrt{\frac{16h^4+h^2L^2}{L^4}}+\frac{1}{4}\arcsin h(\frac{4h}{L}))((\log_e(L^4)-\log_e(16h^2L^2+L^4))$$

$$Q5 = -\frac{(1+\upsilon)}{k}\int_0^{L/2}\frac{4h(L-2x)}{L^2(1+\frac{16h^2}{L^4}(L-2x)^2)}(C1)\mathrm{d}x$$

$$= \frac{(1+\upsilon)}{k}\frac{L^2C1}{16h}(\log_e(L^4)-\log_e(16h^2L^2+L^4))$$

$$Q6 = \int_0^{L/2}\frac{-64h^3(x-\frac{x^2}{L})(L-2x)}{L^5(1+\frac{16h^2}{L^4}(L-2x)^2)^2}(C1)\mathrm{d}x$$

$$= (-\frac{L^2C1}{64h})(\log_e(L^4)-\log_e(16h^2L^2+L^4)+\frac{16h^2}{L^2})$$

$$Q7 = \int_0^{L/2}\frac{128h^3(x-\frac{x^2}{L})(L-2x)}{L^5(1+\frac{16h^2}{L^4}(L-2x)^2)^2}(C2)\,\mathrm{d}x, Q7 = Q7_1+Q7_2+Q7_3$$

$$Q7_1 = \int_0^{L/2}-\frac{32h^3(x-\frac{x^2}{L})(L-2x)^2}{L^5(1+\frac{16h^2}{L^4}(L-2x)^2)^2}(\sqrt{\frac{16h^2(L-2x)^2+L^4}{L^4}})\mathrm{d}x$$

$$Q7_2 = \int_0^{L/2}-\frac{8h^2(x-\frac{x^2}{L})(L-2x)}{L^3(1+\frac{16h^2}{L^4}(L-2x)^2)^2}\arcsin h(\frac{4h(L-2x)}{L^2})\mathrm{d}x$$

$$Q7_3 = \int_0^{L/2}\frac{128h^3(x-\frac{x^2}{L})(L-2x)}{L^5(1+\frac{16h^2}{L^4}(L-2x)^2)^2}(\frac{L}{4}\sqrt{\frac{16h^2+L^2}{L^2}}+\frac{L^2\arcsin h(\frac{4h}{L})}{16h})\mathrm{d}x =$$

$$Q7_3 = (\frac{L^3}{128h})(\sqrt{\frac{16h^2+L^2}{L^2}}+\frac{L}{4h}\arcsin h(\frac{4h}{L}))(\log_e(L^4)-\log_e(16h^2L^2+L^4)+\frac{16h^2}{L^2})$$

$$Q8=\int_0^{L/2}\frac{4hx}{L^2(1+\frac{16h^2}{L^4}(L-2x)^2)^2}(C1)\mathrm{d}x=(\frac{LC1}{8})(\arctan(\frac{4h}{L}))$$

$$Q9=-\int_0^{L/2}\frac{8h}{L^2(1+\frac{16h^2}{L^4}(L-2x)^2)^2}(C3)\mathrm{d}x\ ,\ Q9=Q9_1+Q9_2+Q9_3+Q9_4$$

$$Q9_1=-\int_0^{L/2}\frac{(L-2x)}{4(1+\frac{16h^2}{L^4}(L-2x)^2)^2}\arcsin h(\frac{4h(L-2x)}{L^2})\mathrm{d}x$$

$$=(\frac{L^2}{256h^2})(\frac{L^4\arcsin h(\frac{4h}{L})}{16h^2+L^2}-\frac{4hL^2}{\sqrt{16h^2+L^2}})$$

$$Q9_2=\int_0^{L/2}\frac{(L^4-8h^2(L-2x)^2))}{L^2(1+\frac{16h^2}{L^4}(L-2x)^2)^2}(\frac{1}{24h})\sqrt{\frac{16h^2(L-2x)^2+L^4}{L^4}}\mathrm{d}x$$

$$Q9_2=\frac{L^4\log_e(hL^2)}{384h^2}+\frac{12L^5}{384h\sqrt{(16h^2L^2+L^4)}}-\frac{L^4\log_e(h\sqrt{16h^2L^2+L^4}+4h^2L)}{384h^2}$$

$$Q9_3=\int_0^{L/2}\frac{6hL^2(L-2x)\arcsin h(\frac{4h}{L})}{L^2(1+\frac{16h^2}{L^4}(L-2x)^2)^2}(\frac{1}{24h})\mathrm{d}x=\frac{L^4\arcsin h(\frac{4h}{L})}{16(16h^2+L^2)}$$

$$Q9_4=-\int_0^{L/2}\frac{(L^4-8h^2L(L-6x))}{L^2(1+\frac{16h^2}{L^4}(L-2x)^2)^2}(\frac{1}{24h}\sqrt{\frac{16h^2+L^2}{L^2}})\mathrm{d}x$$

$$=-\frac{\sqrt{16h^2+L^2}}{24hL^3}(-\frac{3L^5}{8}-\frac{5L^7+32h^2L^5}{8(16h^2+L^2)}-(\frac{L^6}{16h}+hL^4)\arctan(\frac{4h}{L}))$$

Then denominator (*D*) of *H* equation is derived as a combination of *D1* for bending term, *D2* and *D3* for thrust and shear terms, and *D4* for coupling term.

$$D1 = -\frac{1}{g^2}\int_0^{L/2}\frac{16h^2}{L^2}(x-\frac{x^2}{L})^2\,\mathrm{d}x = (\frac{1}{g^2})(-\frac{4Lh^2}{15})$$

$$D2 = -\int_0^{L/2}\frac{1}{1+\frac{16h^2}{L^4}(L-2x)^2}\mathrm{d}x = -\frac{L^2}{8h}\arctan(\frac{4h}{L})$$

$$D3 = -\frac{2(1+\upsilon)}{k}\int_0^{L/2}\frac{\frac{16h^2}{L^4}(L-2x)^2}{1+\frac{16h^2}{L^4}(L-2x)^2}\mathrm{d}x = \frac{(1+\upsilon)}{k}(\frac{L^2}{4h}\arctan(\frac{4h}{L})-L)$$

$$D4 = 2\int_0^{L/2}\frac{\frac{4h}{L}(x-\frac{x^2}{L})}{\sqrt{1+\frac{16h^2}{L^4}(L-2x)^2}}\frac{8h}{L^2(1+\frac{16h^2}{L^4}(L-2x)^2)^{\frac{3}{2}}}\mathrm{d}x = \frac{(16h^2-L^2)}{16h}\arctan(\frac{4h}{L})+\frac{L}{4}$$

The parameters used in above equations were defined previously in Appendix A.

Therefore, the horizontal reaction force of the parabolic arch when strain energy is based on full structural action is obtained by substituting *Wi, Qi*, and *Di* into Equ. (B.12).

$$H = \frac{\begin{array}{c}w(W1+W2+W3+W4)+\\ q(Q1+Q2+Q3+Q4+Q5+Q6+Q7+Q8+Q9)\end{array}}{D1+D2+D3+D4} \qquad \text{(B.12)}$$

The horizontal reaction force of parabolic arch when strain energy is the linear combination of bending, thrust, and shear can be calculated from Equ. (B.13).

$$H = \frac{w(W1+W2)+q(Q1+Q2+Q3+Q4+Q5)}{D1+D2+D3} \qquad \text{(B.13)}$$

Finally, the horizontal reaction force when strain energy is based on bending action only is calculated from Equ. (B.14).

$$H = \frac{w(W1)+q(Q1+Q2)}{D1} \qquad \text{(B.14)}$$

The studied parabolic arch in Chapter 4 is analysed using Castigliano's theorem when the strain energy results from the full structural action. Therefore using Equ.

(B.12) leads the horizontal reaction force of the parabolic arch to be obtained considering full structural action, when *w*=20kN/m, *q*=7.2kN/m, *L*=10m, *k*=0.845, *υ*=0.2, $1/g^2$=133.33m^{-2}, see Table B.1.

Table B. 1. Horizontal reaction force of parabolic arch (kN) subjected to load case *A1*

L:h	*h*(m)	*S*	*D*	*W*	*Q*	*H*
2	5	14.79	10943.72	27354.13	35650.35	73.45
3	3.33	12.45	4402.29	16495.04	18960.18	105.95
4	2.5	11.48	2374.90	11853.51	12898.14	138.93
5	2	10.98	1489.10	9278.88	9815.55	172.08
6	1.67	10.70	1022.88	7636.82	7948.13	205.27
7	1.43	10.52	747.06	6495.39	6691.76	238.39
8	1.25	10.40	570.24	5654.41	5786.12	271.38
9	1.11	10.32	450.02	5008.26	5100.85	304.19
10	1	10.26	364.53	4495.85	4563.39	336.79

It can be seen from the table above that the results of the horizontal reaction force of the parabolic arch are the same as those presented in the last column of Table 4.5.

Once the horizontal reaction force is found, the location of maximum bending moment can be calculated. In order to find the combined compressive stress, the substantial stress is considered at the outer surface of the arch beam cross-section. The combined stress (*σ*) is presented in Equ. (B.15) in which *T* and *M* are substituted from Equs. (B.9) and (B.10).

$$\sigma = \frac{Mz'}{I} + \frac{T}{A} \tag{B.15}$$

where *z'* is the distance of the surface from neutral axis in this equation. The location of maximum combined compressive stress then can be obtained.

Appendix C: Programming the momentless shape of two-pin arch

The geometry of the momentless arch is obtained using *MATLAB* code below that gives *x* and *y* coordinate of momentless arch by choosing a number of required nodes for the half of the arch; from left support to the mid-span. It is also assumed that *L:h* ratio, and loading are defined values. Using this code, the shape of the half of the arch will be plotted. The written program for *A'* when $k^2<1$ with the initial value of *A'* equal to 3, gives the constant for catenary arch form for any *L:h* ratio. However, *A'* is replaced by *Acat* in *MATLAB* script to avoid error when the program is running.

```
n= n ; %(number of nodes till half span)
L= L;
h= h ;
w= w;
q= q;
r=L/h;
k=w/q;

if (k^2)<1

Acat=3;

y1=0;
x1=0;
L=L;
h=h;
r=L/h

for i= 1: 100
```

```
b= Acat;
F= y1-h + b*cosh((L/2)/b)-b;
F1=cosh((L/2)/b) - (((L/2)*sinh((L/2)/b))/b) -1;
Acat = b- (F/F1);
i=i+1;
if abs(F/F1)<0.00000000001;
break
end
end
  i
format long
Acat
tmax0=sinh(L/(2* Acat))
syms tmax;
Ft=     (asinh(tmax)+(k/(1-k^2)^(0.5))*(atan(tmax*k/((1+tmax^2)^(0.5)*(1-k^2)^(0.5)))-atan(tmax/(1-k^2)^(0.5))))/((1+tmax^2)^(0.5)-1+k*log((k+1)/(k+(1+tmax^2)^(0.5))));
options= optimset('TolX',1e-18);
[tmax exitflag output]=fzero(@(tmax)eval(r/2-Ft), tmax0,options);
tmax
H=(q*h)/(k*log((k+1)/(k+(1+tmax^2)^(0.5)))+(1+tmax^2)^(0.5)-1)


for i=2 : n+1;


tsash=tmax/(n)
t0=tmax


t(1)=tmax-tsash
t(i)=t(i-1)-tsash
%Then for n number of nodes, n x and y should be found for each t…means t0 has x=0 and y=0 from below equations and t1…


x(1)=    (-H/q)*(asinh(t0)+(k/(1-k^2)^(0.5))*(atan(t0*k/((1+t0^(2))^(0.5)*(1-k^2)^(0.5)))-atan(t0/(1-k^2)^(0.5))))+(L/2);
y(1)=(-H/q)*((1+t0^(2))^(0.5)-1+k*log((k+1)/(k+(1+t0^2)^(0.5))))+h;


x(i)=          (-H/q)*(asinh(t(i-1))+(k/(1-k^2)^(0.5))*(atan(t(i-1)*k/((1+t(i-1)^(2))^(0.5)*(1-k^2)^(0.5)))-atan(t(i-1)/(1-k^2)^(0.5))))+(L/2);
y(i)=(-H/q)*((1+t(i-1)^(2))^(0.5)-1+k*log((k+1)/(k+(1+t(i-1)^2)^(0.5))))+h;
```

```
i+1;

format short
disp(x)
disp(y)
plot(x,y,'r')

end

else

   if k^2>1
tmax0=4/r;
syms tmax;
Ft=(asinh(tmax)+(k/(k^2-1)^(0.5))*(-atanh(tmax *k/((1+ tmax ^2)^(0.5)*(k^2-1)^(0.5)))+atanh(tmax /(k^2-1)^(0.5))))/((1+ tmax ^2)^(0.5)-1+k*log((k+1)/(k+(1+ tmax ^2)^(0.5))))
options= optimset('TolX',1e-18);
[tmax exitflag output]=fzero(@(tmax)eval(r/2-Ft), tmax0,options);
tmax
H=(q*h)/(k*log((k+1)/(k+(1+tmax^2)^(0.5)))+(1+tmax^2)^(0.5)-1)

for i=2 : n+1;

tsash=tmax/(n)
t0=tmax
t(1)=tmax-tsash
t(i)=t(i-1)-tsash
%Then for n number of nodes, n x and y should be found for each t…means t0 has x=0 and y=0 from below equations and t1…

x(1)=(-H/q)*(asinh(t0)+(k/(k^2-1)^(0.5))*(-atanh(t0*k/((1+t0^(2))^(0.5)*(k^2-1)^(0.5)))+atanh(t0/(k^2-1)^(0.5))))+(L/2);
y(1)=(-H/q)*((1+t0^(2))^(0.5)-1+k*log((k+1)/(k+(1+t0^2)^(0.5))))+h;

x(i)=(-H/q)*(asinh(t(i-1))+(k/(k^2-1)^(0.5))*(-atanh(t(i-1)*k/((1+t(i-1)^(2))^(0.5)*(k^2-1)^(0.5)))+atanh(t(i-1)/(k^2-1)^(0.5))))+(L/2);
y(i)=(-H/q)*((1+t(i-1)^(2))^(0.5)-1+k*log((k+1)/(k+(1+t(i-1)^2)^(0.5))))+h;
```

```
i+1;

format short
disp(x)
disp(y)
plot(x,y,'b')

end

   else

      %if (k^2)=1

tmax0=4/r;
syms tmax;
Ft=((1/tmax)*((1+tmax^2)^(0.5)-tmax*asinh(tmax)-1))/(1-
(1+tmax^2)^(0.5)+log((1+(1+tmax^2)^(0.5))/2))
options= optimset('TolX',1e-18);
[tmax exitflag output]=fzero(@(tmax)eval(r/2-Ft), tmax0,options);
tmax
H=(q*h)/(-log((1+(1+tmax^2)^(0.5))/2)+(1+tmax^2)^(0.5)-1)

for i=2 : n;

tsash=tmax/(n)
t0=tmax
t(1)=tmax-tsash
t(i)=t(i-1)-tsash
%Then for n number of nodes, n x and y should be found for each t…means t0 has
x=0 and y=0 from below equations and t1…

x(1)=(H/q)*((1/t0)*((1+t0^2)^(0.5)-t0*asinh(t0)-1))+(L/2);
y(1)=(H/q)*(log((1+(1+t0^2)^(0.5))/2)+1-(1+t0^2)^(0.5))+h;

x(i)=(H/q)*((1/t(i-1))*((1+t(i-1)^2)^(0.5)-t(i-1)*asinh(t(i-1))-1))+(L/2);
y(i)=(H/q)*(log((1+(1+t(i-1)^2)^(0.5))/2)+1-(1+t(i-1)^2)^(0.5))+h;
```

```
i+1;

format short
disp(x)
disp(y)
plot(x,y,'g')

end
      end
   end
```

Here, 41 nodes were chosen to plot the half of the arch. Moreover, the span and height of the arch are taken from studied arches in subsection 3.3.1 equal to 10 m and 5 m (*L:h*=2) with *SW*=7.2 kN/m and *UDL*=20 kN/m. Therefore, the arch will be plotted when k^2>1.

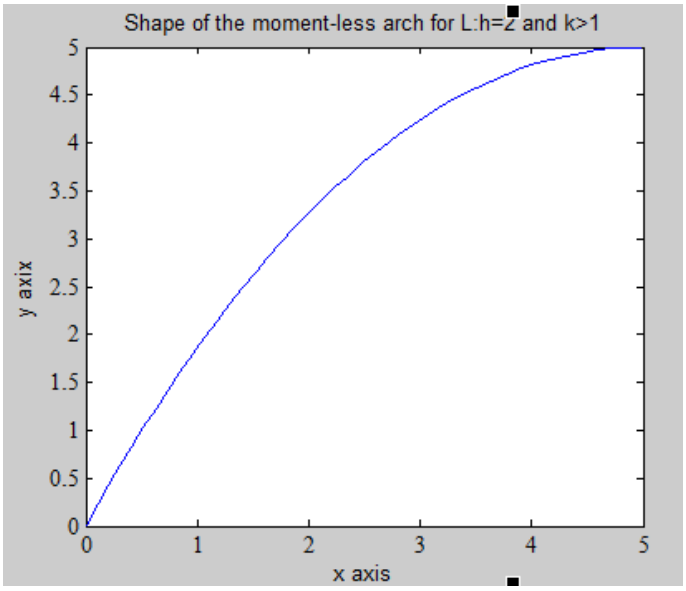

Figure C. 1. The shape of the momentless arch when *UDL:SW*>1 for half of the arch